UNIVERSITY OF STRATHCLYDE

DEPARTMENT OF BIOMEDICAL ENGINEERING

Prosthetic mechanobiology:

How prosthesis-related loading can influence skeletal muscle health

By

Marisa Sargent

2023

A thesis submitted in partial fulfilment of the

requirements for the degree of

DOCTOR OF PHILOSOPHY

Copyright

Signed: Date:

Acknowledgements

Thank you to everyone who has played a part throughout my PhD journey. It wouldn't have been possible without you.

To my supervisory team, thank you for your support and shared excitement about my project. To Dr. Arjan Buis for challenging me to think and step outside the box and helping me to grow as a researcher and a person. To Sarah Day for her invaluable clinical expertise that informed my project. A special thanks also to Dr. Alastair Wark for sharing so much of his time with me to support my imaging and writing endeavours.

To Dr. Mairi Sandison, Katie Henderson, Prof. Gail McConnell, and Prof. Erkan and Selda Oterkus for helping me navigate the various paths that my research took me on. Your willingness to discuss ideas and collaborate is greatly appreciated.

Thanks to my fellow PhD friends, including my peer support group and our newly formed mechanobiology research group, for lots of chat about everything PhD-related and beyond.

Thank you also to all my friends and my family back home. Your continuous love and moral support helped me through the tougher parts and made the ride a whole lot more enjoyable.

And finally, thank you to my own little family. You are my rock, and I truly don't know how I would have done any of this without you.

Abstract

The soft tissue of the residual limb in transtibial prosthetic users encounters unique biomechanical challenges. Although not intended to tolerate high loads and deformation, it becomes a weight-bearing structure within the residuum-prosthesis-complex. Consequently, skeletal muscles may be damaged, resulting in Deep Tissue Injury (DTI). While considerable effort has gone into DTI research on immobilised individuals and static loading conditions, only little is known about the effect of a dynamic loading environment as experienced by prosthetic users. The aim of this project was therefore to investigate the influence of prosthesis-related loading conditions on skeletal muscle tissue with the means of a newly developed *ex vivo* animal model.

Soleus and extensor digitorum longus muscles of male Sprague Dawley rats were dissected and transversely compressed with a flat-ended indenter. The generated compressive stress was predicted through finite element modelling. Five different protocols were tested: (a) static loading for 1h or 2h representing standing and sitting, (b) dynamic loading with a frequency of 1.42Hz for 1h or 2h representing walking, and (c) dynamic loading with a frequency of 4Hz for 1h representing running. Subsequently, dead cells were identified through fluorescent staining with Procion Yellow MX4R and quantified in a semi-automated process.

Extending the loading duration increased the amount of cellular damage significantly. Additionally, dynamic loading with a high frequency was more damaging than low frequency and static loading, suggesting the need to reconsider existing magnitude- and duration-based cell death thresholds. While a direct translation of these results to the prosthetic user is difficult, they provide important insights into the adaptive capabilities of skeletal muscle. This can contribute to further research into the role of soft tissue deformation in residual limb pain and could inform future directions for prosthetic socket design and user guidelines.

Publications

[1] Graser, M., Day, S. & Buis, A. Exploring the role of transtibial prosthetic use in deep tissue injury development: a scoping review. *BMC biomed eng* 2, 2 (2020). https://doi.org/10.1186/s42490-020-0036-6

[2] Graser, M. Aetiology and risk factors of deep tissue injury explained. *2nd Doctoral School Multidisciplinary Symposium 2020*, Glasgow, United Kingdom. 27th April 2020.

[3] Graser, M., Day, S. & Buis, A. Transtibial prosthetic users as a risk group for deep tissue injuries. *EPUAP Virtual Meeting: 2020 – The most challenging of times: Focusing on contemporary issues in pressure ulcer prevention and management (Virtual).* 24th September 2020.

[4] Graser, M., Wark, A., Day, S. & Buis, A. Development of an ex vivo model to study the response of skeletal muscle to transverse mechanical loading. *BioMedEng21.* Sheffield, United Kingdom. 6th – 7th September 2021.

[5] Graser, M., Day, S. & Buis, A. Prosthetic mechanobiology – how using a prosthesis can lead to deep tissue injuries. *ISPO 18th World Congress (Virtual).* 1st – 4th November 2021.

[6] Graser, M., Wark, A., Day, S. Sandison, M., McConnell, G. & Buis, A. Investigating the response of skeletal muscle to prosthesis-related loading conditions: an ex vivo animal model. *ISPO 18th World Congress (Virtual).* 1st – 4th November 2021.

[7] Sargent, M., Wark, A. & Buis, A. The effect of prosthesis-related loading on soft tissue health. *4th Doctoral School Multidisciplinary Symposium 2022*, Glasgow, United Kingdom. 8th – 10th June 2022.

[8] Sargent, M. Body-device interface interactions: Why you should know about mechanobiology. *ISPO 19th World Congress*, Guadalajara, Mexico, 24th – 27th May 2023.

Table of Contents

List of Figures

List of Tables

List of Abbreviations

ADL	Activities of daily living
ANOVA	Analysis of variance
ATP	Adenosine triphosphate
BABB	Benzyl alcohol benzyl benzoate
BAM	Bioartificial muscle
CAD	Computer aided design
CARS	Coherent anti-stokes Raman scattering
CFD	Computational fluid dynamics
CPK	Creatine phosphokinase
CRP	C-reactive protein
DT MRI	Diffusion-tensor magnetic resonance imaging
DTI	Deep tissue injury
ECM	Extracellular matrix
EDL	Extensor digitorum longus muscle
EPUAP	European Pressure Ulcer Advisory Panel
ESR	Energy storage and return (foot)
EtOH	Ethanol
FE	Finite element
FEA	Finite element analysis
FFPE	Formalin fixation and paraffin embedded
GRF	Ground reaction force
GUI	Graphical user interface
H&E	Haematoxylin and eosin
H-FABP	Heart-type fatty acid binding protein
IL-1α	Interleukin 1 alpha
IL-6	Interleukin 6
IR	Ischemia-reperfusion
LDH	Lactate dehydrogenase

LoD	Live-or-Dye™
mCRP	Monomer C-reactive protein
MDR	Method of dimensionality reduction
MRI	Magnetic resonance imaging
NBF	Neutral buffered formalin
NHS	National Health Services
NIR	Near infrared
NPIAP	National Pressure Injury Advisory Panel
OTC	Optical tissue clearing
PBS	Phosphate buffered saline
pCRP	Pentamer C-reactive protein
PFA	Paraformaldehyde
PI	Propidium Iodide
ProY	Procion Yellow MX4R
PTAH	Phosphotungstic acid haematoxylin
PTB	Patellar tendon bearing (socket design)
ROI	Region of interest
ROS	Reactive oxygen species
RPL	Residual limb pain
SCI	Spinal cord injury
SGR	Soft glassy rheology
SHG	Second-harmonic generation
SOL	Soleus muscle
SRS	Stimulated Raman scattering
TNF- α	Tumour necrosis factor alpha
TnI	Troponin-I
TSB	Total surface bearing (socket design)
TTA	Transtibial amputee
WHO	World Health Organisation

CHAPTER 1

Introduction

Problem statement - This project addresses the limited fundamental understanding of the influence of prosthetic use on soft tissue health.

Most people transferred to prosthetic services in the UK present with lower limb amputation [1]. Lower limb amputees in general are more successful in using a prosthesis with higher functional outcomes as compared to transfemoral amputation levels [2, 3]. However, this also puts them at risk of soft tissue damage from prosthetic use. This project therefore focusses on the skeletal muscles of the lower limb.

Increased need for quality prosthetics – We face an increasing need for quality prosthetics and prosthetic services across the world. In the UK, over 160 people undergo lower limb amputation surgery every week, caused by diabetes alone [4]. This extends to a global scale, with one individual losing a limb every 30 seconds because of complications of diabetes worldwide [5]. Considering our ageing population, the situation will probably worsen over the decades to come [6, 7]. Additionally, the World Health Organisation estimated that former and ongoing conflicts led to the deposit of over 110 million landmines in 70 countries over the last 65 years, causing limb loss for thousands of people [8]. Despite acts to prohibit the use of landmines like the Mine Ban Treaty in 1997 [9], ongoing conflicts like in Myanmar and the Ukraine continue to pose a threat [10, 11].

Amputation surgery - Under the described circumstances, amputation surgery is often needed, either as a life-saving procedure or as reconstructive intervention to improve functional outcomes [12]. During the surgery, the ankle-foot-complex and a part of the shank are removed (**Figure 1-1, II. a**). First, a skin incision is made to create a skin flap – either a long posterior flap, skew flap, or sagittal flap (**Figure 1-1, II. b**) [13]. Next, the muscles in the limb are transected and the bones, the tibia and fibula, cut with a bevelment at the end (**Figure 1-1, II. c**) [14]. The remaining muscles are reattached through myodesis (reattachment to the bone) or myoplasty (attachment to opposing muscles) before the surgical site is closed [15]. The remaining part of the leg is known as residual limb or residuum.

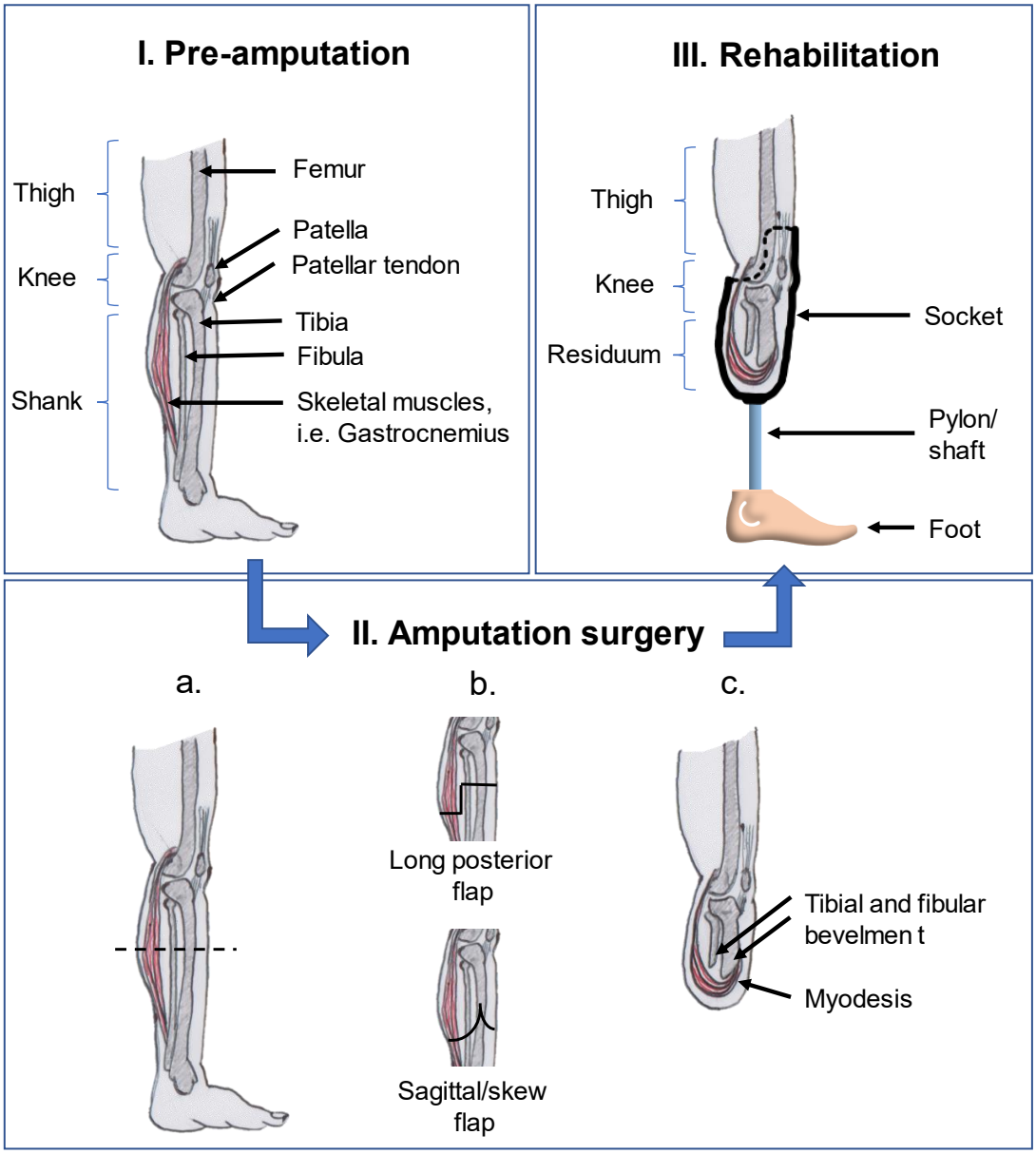

Figure 1-1: Transtibial amputation and rehabilitation process.

The importance of rehabilitation – Following surgery, amputees undergo an extensive rehabilitation programme. Restoring mobility and independence is key for the physical and mental well-being of amputees [16, 17]. Successful rehabilitation may also prevent conditions associated with immobility, such as venous stasis, skin pressure damage, falls, and obesity. These secondary conditions affect not only the individual but also the society and health and welfare services. Expenses for falls and pressure ulcers for example amount to over £2Bn each within the NHS [18, 19]. High quality prosthetic devices and services therefore play a crucial role in the rehabilitation process.

Fitting a prosthesis – An important part of the prosthetic system is the socket (**Figure 1-1, III.**). The socket forms the interface between prosthesis and limb. Its shape strongly influences the load transfer between bones, soft tissues, and prosthesis. Shaping and fitting a socket is usually performed manually by a prosthetist. The prosthetist takes a plaster cast of the residual limb to produce a negative mould of the residuum. Next, the mould is rectified, i.e. manually modified, around bony prominences and sensitive areas. A check socket, a clear test socket, is then often made from the mould to clinically evaluate the fit and get patient feedback. Once both prosthetist and prosthetic user are satisfied with the result, the user will receive a definite socket.

Problems with socket fit - Unfortunately, the iterative socket fitting procedure presents a considerable challenge within the rehabilitation process. Frequent changes in limb shape during daily use as well as over weeks and months complicate this procedure [20]. Amputees often complain about pain and discomfort caused by an ill-fitting socket, which can affect their daily life and reduce acceptance rates [21]. Extreme cases might even cause injury or increase the disability.

Soft tissue deformation - A major problem lies in the missing general agreement and understanding of what defines a “good” prosthetic fit. A well-fitting prosthesis should create a stiff mechanical coupling between the socket and the limb [20, 22, 23]. A tight fit will prevent vertical “pistoning” movement of the limb inside the socket and improve control and stability for the prosthetic user. On the other hand, the soft tissue of the residual limb has only limited weight-bearing capability. Balancing a tight fit against the risk for tissue injury is therefore a key challenge for successful socket design. However, the relationship between prosthesis-related mechanical loads and residual limb health is largely unknown.

Pressure Injuries – One area of research that could shine a light on these problems is pressure injuries, also known as pressure ulcers or decubitus. They develop when skin and/or soft tissues are damaged by mechanical loading [24]. A four-stage system classifies pressure injuries based on severity and clinical appearance. Over the last two decades, researchers and clinicians discovered a new category of pressure injuries originally classified as “unstageable ulcers”. Now known as “Deep Tissue Injury” (DTI), this pressure injury is caused by prolonged or acute deformation of deep soft tissue layers, leading to cell damage. The mechanical damage is exacerbated by a pressure-related impairment of the blood and lymphatic flow [25, 26]. If left

undetected and untreated, the damage might rapidly evolve into an open wound or resolve without tissue loss.

Skeletal muscle structures seem to be at high risk of tissue damage. When the body is in contact with a support surface, peak stresses and strains occur not at the body-support interface but within deep muscle layers near the bone [27–31]. Additionally, the fibrous structure of skeletal muscle is prone to shear-induced damage [32]. DTI is therefore a serious risk for skeletal muscle health.

Mechanobiology approach – To unravel the complex and interdependent interaction of soft tissue structures with a support surface, a mechanobiology-based approach has been adopted. The aim of mechanobiological research is to unveil the impact of the mechanical environment on cells and tissues, including their structural integrity, morphology, and dynamics. An integral part is the combination of information, techniques, concepts, and theories from different disciplines like biology, physiology, and biomechanics. Whilst this mechanobiological approach has been successfully applied to DTI research in general, its application to the field of prosthetics has been limited.

Interplay of pressure, stress, strain and cell death – The definition of cell-death thresholds marked a breakthrough in DTI research [33, 34]. These thresholds characterise how pressure and strain affect the integrity of skeletal muscle cells from short (minutes) to extended (hours) periods of time. The focus is thereby on immobilised individuals that experience static loading without the ability to shift their weight, i.e. people with spinal cord injury or wheelchair users. These thresholds also apply to prosthetic users to some extent. Putting on a prosthesis, also known as donning, applies a baseline direct stress to the residuum to achieve coupling stiffness. When standing on or sitting with the prosthesis, the static load increases. For the majority of time, however, individuals are actively moving with their prosthesis. This creates a dynamic loading environment with cyclic pressure application. The effect of dynamic loading on soft tissue health is yet unexplored.

Research question – As far back as in the 1970s, the Committee on Prosthetic Research and Development pointed at the relationship between pressure and soft tissue damage in prosthetic users [35]. They specifically recommended “further studies concerning the effects of frequency of application force”. Since then, other researchers also repeatedly highlighted the missing link between prosthesis-related mechanical loads and residual limb health [23, 36–38]. However, to the author’s

knowledge, little work has been done to close this research gap. This thesis is therefore centred around the following research question:

> How do dynamic, prosthesis-related loading conditions influence skeletal muscle health?

Significance of research – This thesis will contribute to build the knowledge base on the fundamentals of body-device interactions. The results will hopefully help to unravel and quantify the mechanisms that contribute to a tissue-safe prosthetic socket design. The methods developed for this project will also provide an adaptable framework for future research efforts in prosthetics and adjacent areas. On this basis, this thesis will be a steppingstone towards scientifically sound prosthetic socket design and clinical services of the future.

Structure of the thesis – This thesis revolves around the link between two areas of research: The mechanical environment of the body-device interface; and the biological response of the soft tissue structures. Both will be addressed over the following chapters:

- **Chapter 2:** Similarities and differences between pressure injuries and prosthetic use regarding the aetiology and risk factors for soft tissue damage will be identified and discussed. On this basis, a research aim will be formulated.
- **Chapter 3:** The basics of mechanobiology will be introduced and related research methods reviewed. From this, clear objectives for the concurrent research will be defined.
- **Chapter 4:** A suitable model system for experimental studies will be developed.
- **Chapter 5:** A robust data analysis workflow will be established.
- **Chapter 6:** Supplementary computational studies of the experimental setup will be performed.
- **Chapter 7:** The newly developed method will be verified in a small-scale study on the effect of static loading on skeletal muscle health.

- **Chapter 8:** The effect of different mechanical loading scenarios representative of prosthetic use on skeletal muscles will be evaluated, including static and dynamic loading.
- **Chapter 9:** Potential methods for future work will be highlighted, based on preliminary studies and beyond.
- **Chapter 10:** The thesis will close with a general discussion and a conclusion of the main findings, their implications for prosthetics, and recommendations for future work.

CHAPTER 2

Transtibial prosthetic users as risk group for Deep Tissue Injuries

A scoping review was conducted to map out and critically appraise existing research on Deep Tissue Injuries (DTI) in lower-limb prosthetic users according to (1) the population-specific aetiology, (2) risk factors, and (3) methods to investigate both.

This chapter draws on the author's publication "Exploring the role of transtibial prosthetic use in Deep Tissue Injury Development: A scoping review" in BMC Biomedical Engineering (2020) [39]. It was co-authored by Sarah Day and Dr. Arjan Buis, who permitted reproduction in this thesis.

The idea for this study came from a collaborative effort by the author and her co-authors, Sarah Day and Dr. Arjan Buis. The author's contribution covers the design of the study, including the development of the search protocol, the data collection, the selection of eligible studies, the analysis and interpretation of the data, and the draft of the manuscript.

2.1. Introduction to transtibial prosthetics and Deep Tissue Injury

2.1.1. Transtibial amputation and residual limb pain

Traumatic injuries, tumours, congenital anomalies and severe cases of pathologies like peripheral vascular disease can lead to an amputation of the leg below the knee [40]. During the amputation surgery, foot, ankle joint, and distal tibia and fibula are removed (**Figure 2-1**). Following surgery, amputees often receive a prosthesis to replace the missing limb and restore their mobility. In the UK, over 5000 patients are referred to prosthetic services every year, with 77% of individuals having their limb removed because of dysvascularity, and 42% related to diabetes [41]. The number of diabetic amputees has been increasing significantly over the last decade [41] and issues with dysvascularity are predicted to continue to rise across the western world. In the US for example, the number of amputees due to dysvascularity could increase from less than 1 million in 2005 to 2.3 million in 2050 [40]. This amplifies the need for high-quality prosthetic services and devices.

The main purpose of a transtibial prosthesis is to transfer forces between the ground and the body's support structures during ambulation (**Figure 2-1**). The soft tissues that cover the residual limb become part of this load bearing system, even though they are not physiologically adapted to withstand high external forces. Thus, skin problems, pain, and ulceration may occur, leading to impaired function [42], depressive symptoms [43, 44] and ultimately the rejection of the prosthesis [45–48]. Pain and discomfort are thereby major issues, with up to 76% of amputees reporting on residual limb pain [48]. They describe residual limb pain as an aching, bothersome sensation deep in the residual limb that lasts for several hours or longer [48, 49]. A major problem seems to be the fit of the socket [22, 23, 37, 49–51], which forms the interface between residuum and prosthesis. However, although the link between extensive loading, socket fit and discomfort is clear, the pathophysiological causes for residual limb pain are barely understood.

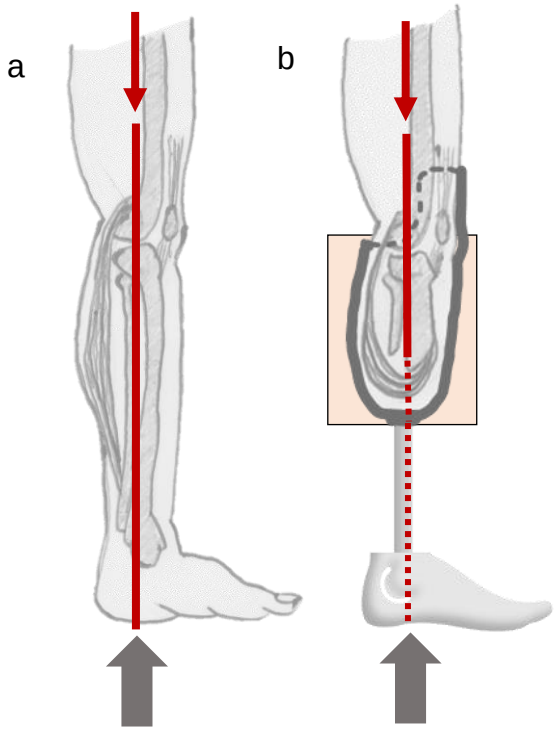

Figure 2-1: Effect of transtibial prosthetic use on weightbearing.

(a) With a sound limb, the bodyweight (red arrow) is transmitted across the skeletal structures to the ground during weightbearing.

(b) In a prosthetic user, the soft tissues of the residuum and the prosthesis become part of this system (dotted line). However, the soft tissues are not adapted to be a weightbearing structure. Accordingly, the residuum becomes a risk area for soft tissue injury (orange box).

2.1.2. Deep Tissue Injuries

One research area which could advance our knowledge towards understanding residual limb pain is pressure injuries. Pressure injuries – also known as pressure ulcers, bedsores or decubitus ulcers – are defined as “localized damage to the skin and underlying soft tissue” and are caused by “intense and/or prolonged pressure or pressure in combination with shear” [24]. The severity of this damage can range from superficial, skin bound deteriorations, to full thickness tissue loss. Whilst severely undermining the well-being of affected patients, pressure injuries also pose a burden on the health care system. In the UK, the estimated cost for pressure ulcer management amounts to £ 507–531 million p.a. [52].

This high number reflects the shortfalls in the prevention, diagnosis, and treatment of pressure injuries, which may be ascribed to ambiguities about their aetiology [53]. An example for ongoing controversies is the recent addition of Deep Tissue Injuries (DTI) to the established pressure injury staging system of the National Pressure Injury Advisory Panel (NPIAP)[1] [24]. It has long been the prevailing opinion that pressure injuries originate at superficial layers and may evolve into deeper tissues [54].

[1] Formerly known as National Pressure Ulcer Advisory Panel (NPUAP)

Accordingly, the NPIAP defined pressure injury stages based on their visual appearance from 1, representing superficial damage, to 4, describing full depth tissue loss [55]. However, an increasing body of literature supports the theory of an opposite route of development [32, 54, 56–58]: Researchers now believe that most pressure-related damage starts in deep tissues at the bone-muscle interface, from where it may progress towards superficial layers in a bottom-up pathogenesis [59, 60]. Based on its origin, this injury is classified as DTI.

The aetiology of DTI involves various biomechanical, physiological, and biochemical processes on cell and tissue level [23, 28]. A detailed description of these processes can be found in Appendix A. The following list gives a summary of the main causes.

Direct deformation can disrupt the integrity of skeletal muscle cells if the applied load is sufficiently high or prolonged.

Ischemia is caused by a collapse of blood vessels, which obstructs the blood flow and therefore the cells' oxygen and nutrient supply.

Ischemia reperfusion describes the phase following load removal, where the reoxygenation of the tissue aggravates ischemic damage, mainly caused by oxidative stress.

Impaired lymphatic drainage from obstructed lymphatic vessels inhibits the removal of potentially damaging substances from the interstitial space and creates a toxic cell environment.

The pathways of tissue damage and cell death are multifactorial and range from external mechanical loading, through the tissue level, down to single cells (**Figure 2-2**) [56, 61, 62]. However, the exact interplay of different damage pathways is still unclear.

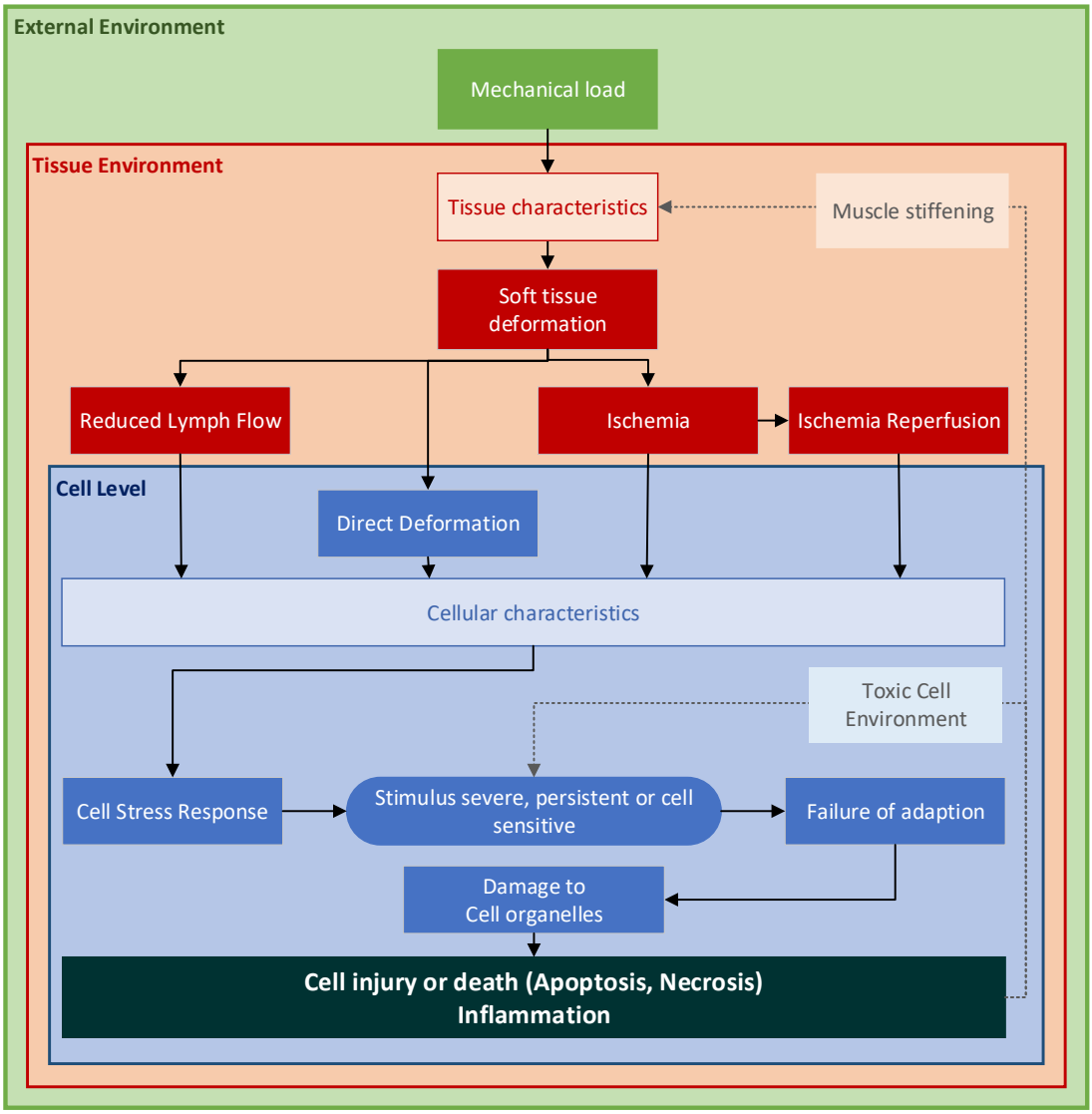

Figure 2-2: Overview over the process of Deep Tissue Injury development across different organisational levels.

2.1.3. Physical Stress Theory

The main cause of DTI is mechanical loading. Mueller and Maluf [63] introduced a fundamental concept on the response of tissues to loading, called the “Physical Stress Theory”. They postulate that all tissues, be it connective, epithelial, nervous, or muscular, display the same five adaptive responses (**Figure 2-3**).

1. **Maintenance:** In the maintenance range, the tissue is in homeostasis, meaning that degeneration and production are balanced.
2. **Decreased stress tolerance:** If the physical stress levels are lower than maintenance, adaptions like atrophy (wasting away of tissue) follow.

3. **Increased stress tolerance:** When the stress level is consistently above the maintenance level, adaptions like hypertrophy (increase and growth of tissue) improve the stress tolerance.
4. **Injury:** Excessive exceedance of the maintenance level can damage tissue without causing any clinically visible dysfunction.
5. **Death:** In extreme cases of overload or, on the contrary, following a severe lack of stress, tissue loses its adaptive capacity, resulting in tissue death either through apoptotic (programmed) or necrotic (accidental) pathways.

Tissue injury and death both cause inflammation, leaving tissue more susceptible to further stress applications.

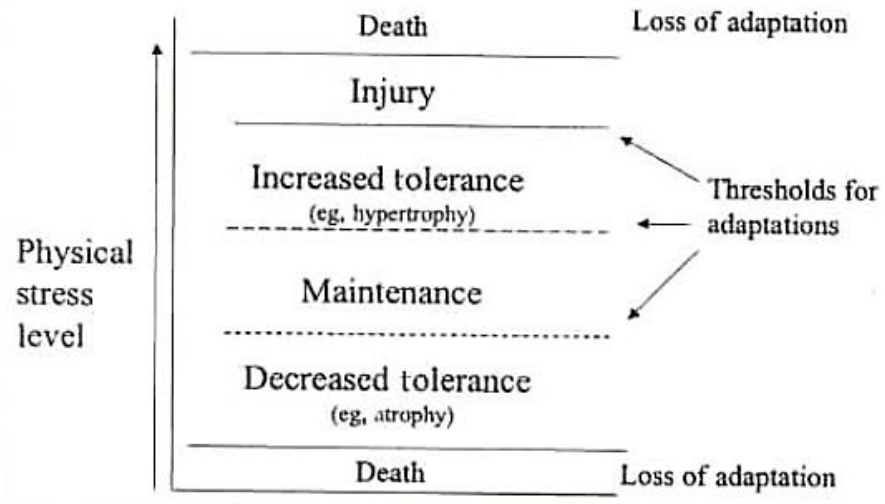

Figure 2-3: Effect of physical stress on tissue adaption. Reproduced from [63] with permission from publisher[2].

Applying this concept to DTI, physical stress beyond the tissue's capacity of adaptation manifests as deep soft tissue damage. The majority of the research on DTI so far focussed on stress overload with either high-magnitude stress for short periods or low-magnitude stress over extended periods of time. Researchers defined internal and external determinants of DTI development for several risk groups. Examples include extended operation duration for surgical patients, sensory impairment in people with spinal cord injury, and limited ability to shift weight in wheelchair users [27, 28, 64–70].

[2] Mueller and Maluf, Tissue Adaption to Physical Stress: A proposed "Physical Stress Theory" to Guide Physical Therapist Practice, Education, and Research, Physical Therapy, 82:4, p. 383-403, by permission of Oxford University Press

Besides overload, Mueller and Maluf [63] stated that insufficient recovery time after injury, followed by further stress can also cause an imbalance between tissue damage and regeneration. However, repetitive stress has gained far less attention in DTI research, policies, clinical guidelines, and clinical practices. Nevertheless, repetitive stress might be the connection between residual limb pain in prosthetic users and DTI.

2.2. Aim of scoping review

The aim of this study was to map out and critically discuss research on DTI in transtibial prosthetic users. The focus was on (1) the population specific aetiology, (2) risk factors, and (3) methods to quantify and measure both. A scoping review was conducted as randomised controlled trials are sparse in rehabilitation science [71]. The nature and extent of various types of research were assessed systematically to identify gaps in the literature. Connecting the multifaceted challenges of the transtibial prosthetic user population with the aetiology of DTI will hopefully precede further research in this area. Additionally, the results of this study could inform policies, guidelines, risk assessment tools, and international classifications for DTI.

2.3. Design and methods of scoping review

The scoping review followed a methodological framework [71, 72] refined by the Joanna Briggs Institute (JBI) [73]. It is also compliant with the PRISMA-ScR checklist 2018 for scoping reviews [74] (Appendix B).

2.3.1. Search Strategy

The database search included Pubmed (Medline), Ovid Excerpta Medica (Embase classic and Embase), and Scopus. It covered the first possible date for each database until June 2019, when the search was conducted. Automatised categorisation of the MeSH term “pressure ulcer” or a database-specific equivalent was utilised. This inclusion of the generic pressure ulcer term ensured full coverage, as DTI was only recently accredited as separate pressure injury category [55]. The full search strategy is displayed in **Table 2-1.**

Reference lists and forward-citation reports of eligible manuscripts were scanned for relevant articles that have not been identified in the automatic search. Additionally, an expert in the field of DTI was contacted for further literature suggestions.

Table 2-1: Search Strategy explained on the example of Ovid Excerpta Medica.

Search #	Search Terms	Key Concepts
1	Deep Tissue Injur*	Deep Tissue Injury (DTI)
2	Deep Tissue Damage	
3	Decubitus/	
4	#1 OR #2 OR #3	
5	Transtibial	Amputation level
6	Trans-tibial	
7	Below knee	
8	#5 OR #6 OR #7	
9	Prosthe*	Transtibial prosthetic users
10	#8 AND #9	
11	#4 AND #10	DTI in transtibial prosthetic users

2.3.2. Study selection and inclusion criteria

Primary and secondary sources were retrieved from the automatic search. Duplicate articles and duplicates published as conference proceedings were filtered out with the aid of a citation software (Zotero 5.0.69).

For further assessment, one reviewer (M.S.) screened the remaining articles. These articles had to be written in English, have an available full text, and have a title and abstract relevant to DTI as a result of prosthetic use. Studies on unrelated conditions and with amputations other than at transtibial level were excluded. Similarly, papers describing superficial, Stage 1, or Stage 2 pressure injuries were disregarded. To ensure a minimum qualitative standard, all papers had to be peer reviewed.

In the following full-text examination, one reviewer (M.S.) evaluated the relevance, study group characteristics, and type of pressure injury. Additionally, transtibial prosthetics and DTI had to be the focus of the article. In case of uncertainty about eligibility of articles, a second reviewer (A.B.) was consulted and possible disagreements discussed until consensus was reached.

Further resources were identified by scanning through reference lists and forward-citations of eligible papers. Their suitability was validated with the previously described process, before including them in the final qualitative synthesis. Recommendations on relevant literature were retrieved from expert contact. All but

one of the suggested sources were already included in the synthesis, with the additional paper being irrelevant for this review.

Data were extracted from the combined search results according to suggestions by the JBI [73] and the PRISMA-ScR checklist [74] with slight adjustments. The variables of interest were author, year, country, type of study, aims and objectives, study population and sample size (if applicable), methodology, outcome measures, and key findings related to DTI in transtibial prosthetic users. The complete range of studies was then grouped thematically for further in-depth analysis, which is presented in tables and supporting narratives.

2.4. Results of scoping review

2.4.1. Search results and grouping of included literature

The automated database search on the 14th of June 2019 resulted in 19 identified sources from Ovid Excerpta Medica, 12 from PubMed, and 68 from Scopus. Removal of duplicates left 72 articles for the screening process. After applying inclusion and exclusion criteria, 24 articles remained for full-text assessment, of which 11 met the eligibility criteria. An additional five articles were identified through references and forward-citation of these sources, amounting to 16 studies in total (**Figure 2-4**).

The 16 identified articles covered various study types. Eleven of them presented primary research, of which seven examined human subjects experimentally [29, 36, 75–79] and one tested *ex vivo* animal tissue (outside of the living body) [80]. Three papers were *in silico* studies (computer simulations) [31, 81, 82]. The other five sources were secondary articles in the form of literature [23, 58, 83, 84] or systematic reviews [38]. They were grouped by research focus into the following categories (**Figure 2-5**):

(1) DTI aetiology in transtibial prosthetic users
(2) Risk factors for transtibial prosthetic users
(3) Methodological approaches to measure aetiological and risk factors in transtibial prosthetic users

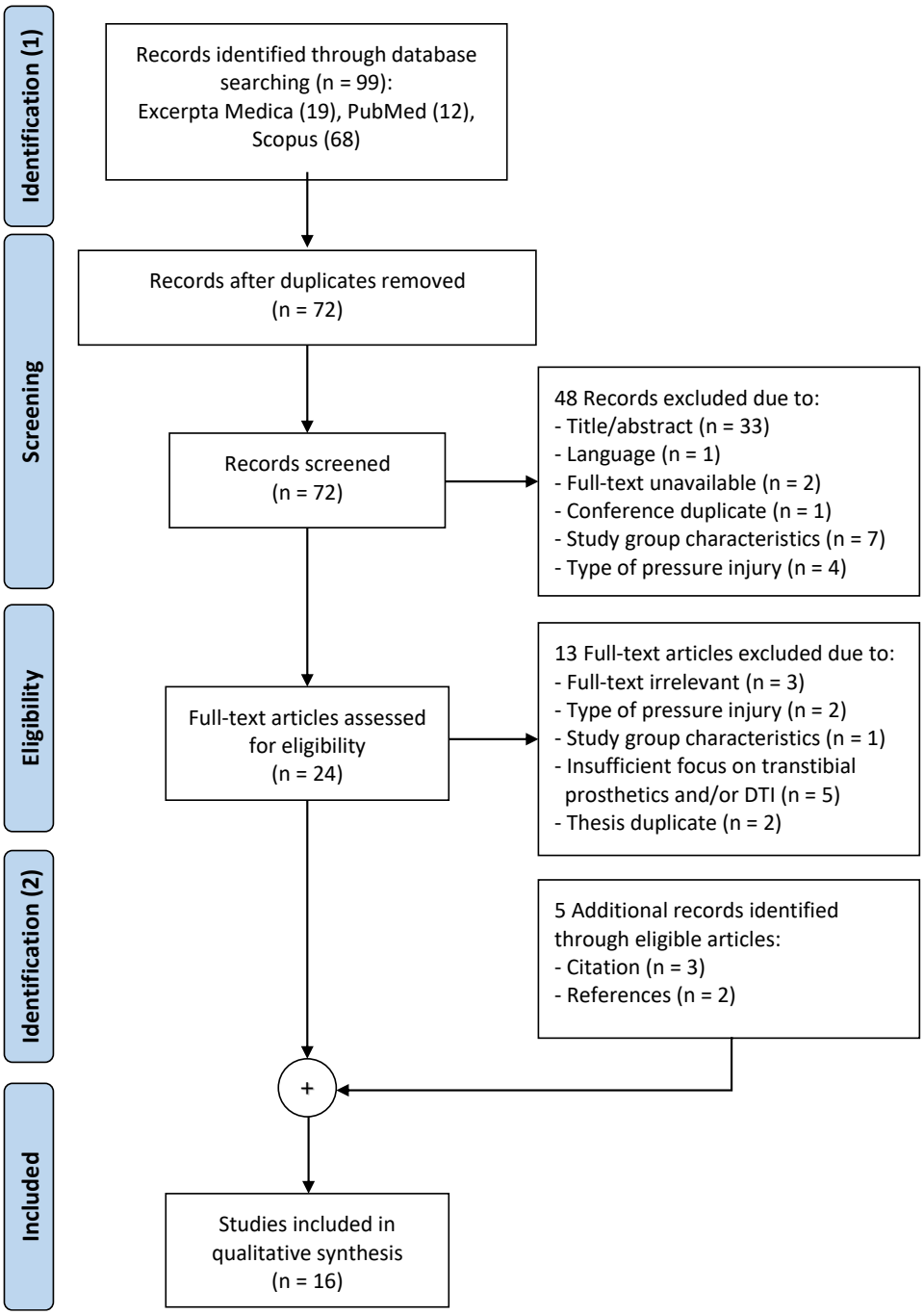

Figure 2-4: PRISMA flow chart for literature search process and results.

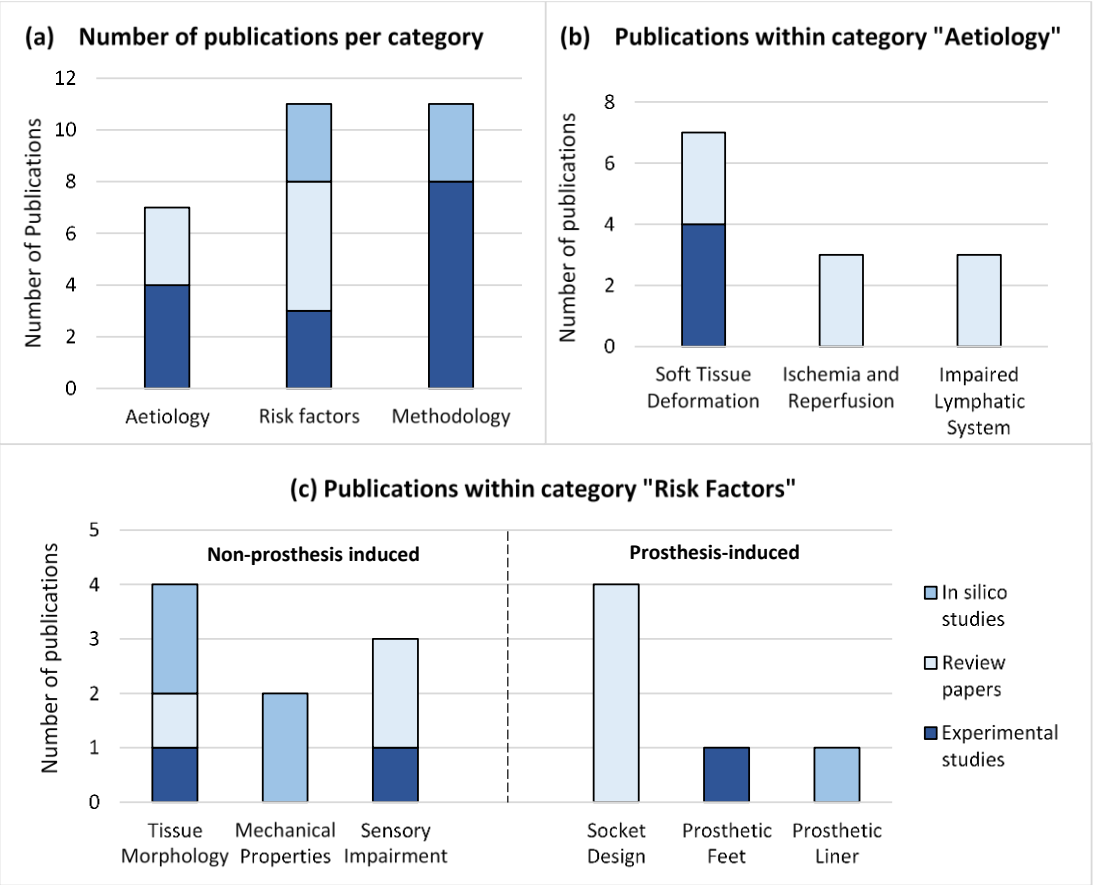

Figure 2-5: Number of publications grouped by topic. (a) Publications per main category. **(b)** Publications within category "Aetiology". **(c)** Publications within category "Risk Factors". The types of papers analysed include reviews (light blue), *in silico* studies (medium blue), and experimental studies (dark blue). Some papers matched multiple groups, thus the total number of publications in this figure exceeds the number of studies analysed.

2.4.2. Aetiology of Deep Tissue Injuries

Of the 16 articles, $n = 7$ (44%) discussed the aetiology of DTI with a focus on residuum biomechanics. Between 2007 and 2011, Portnoy and colleagues conducted four experimental studies [29, 36, 77, 79] on 26 unilateral transtibial amputees (TTA). The participants were typically 44 years old, male (85%), weighted 71.72kg, and presented with trauma as cause of amputation (59%) (**Table 2-2**). The researchers aimed to quantify the internal loading states of deep muscle layers during scenarios encountered by prosthetic users in their daily life: Dynamic walking on various surfaces [36, 77], static weight bearing during standing [29], and prolonged sitting [79].

Across all scenarios, the researchers located peak loads in the tissue encapsulating the distal end of the bones through finite element analysis [29, 36, 77, 79]. During

normal gait, the peak compression and shear stresses were reached between midstance and toe off [36], and the von Mises stress magnitudes were terrain-dependent [77]. When sitting with a donned prosthesis, the load increased simultaneously to the degree of knee flexion [79]. However, high inter-patient variability made it difficult to interpret absolute values [36]. Portnoy et al. therefore compared individual stress and strain values to loading-thresholds for deformation-induced cell death to assess the risk for DTI development [27, 33, 34]. They identified hazardous loading conditions during weight bearing [29], walking over complex terrain [77], and sitting with the knee in 90 degree flexion [34]. Overall, DTI appeared to be a threat for several transtibial prosthetic users in everyday situations.

Cellular deformation is only one of several aetiological factors of DTI. Mak et al. [23, 58] and Bader et al. [83] suspected a link between prosthetic use and disruptions of the lymphatic and microvascular system (**Table 2-3**). When externally applied pressure and shear deform the deep tissues of a residuum [36, 76, 77, 79], the embedded lymphatic and vascular structures will be distorted as well. However, the extent of this deformation and its effect have not been investigated on TTA.

2.4.3. Risk factors for Deep Tissue Injury

A total of *n* = 11 (68.75%) papers examined risk factors of DTI in transtibial prosthetic users. Three experimental and two *in silico* studies investigated a population of *n* = 33, typically male (90.90 %) TTA with traumatic amputation (84.84%), a mean age of 49 years, and an average weight of 81.1kg. These studies, with an additional *in silico* study and five review papers, were divided into two groups: non-prosthesis related (*n* = 7, 63.63%) and prosthesis-related (*n* = 6, 54.54%) risk factors.

Table 2-2: Experimental studies on the deformation as aetiological factor for Deep Tissue Injury in transtibial prosthetic users

Author and year	Objective	Loading scenario	Study Population	Quantitative Results	Qualitative results
Portnoy et al. 2007 [36]	Test of feasibility of real-time FE[1] monitor to estimate internal tissue load	Dynamic load: Treadmill walking	- 5 unilateral TTA[2] - 1 female, 4 male - Mean age 47.2 yrs - Mean weight 68kg	**Max. principal compression stress:** - Fibular axis: 16.38 kPa (3.5 - 31kPa) - Gastrocnemius axis: 8.19 kPa (1.75 - 13kPa)	- Maximum compressive stress between midstance and push-off - High inter-patient variability in stress magnitude
Portnoy et al. 2008 [29]	Estimation of internal tissue load during static load bearing	Static load: Weight bearing	- 1 unilateral TTA - Female - Age 29 - Weight 50kg - Traumatic cause	- Compressive stress 240kPa - Tensile stress 263 kPa - Shear stress 23kPa - Compressive strain 85% - Tensile strain 129% - Shear strain 106% - SED[3] 104 kJ/m^3 - Von Mises stress 215kPa	- Compression slightly above physiological levels in comparison to gluteal tolerance - High tensile and shear strains which may be risk for tissue viability - Stress and strain concentrations in flap under tibial end
Portnoy et al. 2010 [77]	Determination of subject-specific dynamic stresses in soft tissues	Dynamic load: Walking on complex terrain	- 18 unilateral TTA - 1 female, 17 male - Mean age 43 yrs - Mean weight 79kg - 11 traumatic, 7 vascular	**Average peak von Mises stress:** - Plane: 100kPa - Grass: 80kPa - Upstairs: 95.1kPa - Up slope: 83kPa - Downstairs: 115.4kPa - Down slope: 141.9kPa	- High inter-terrain and inter-subject variability - Higher stresses in vascular compared to traumatic patients - No immediate risk of DTI[4] for 10 out of 18 subjects - Elevated peak stress when descending stairs or slope compared to plane gait
Portnoy et al. 2011 [79]	Evaluation of risk of DTI development for during sitting with a donned prosthesis	Static loading: Sitting with 30° and 90° knee flexion	- 1 unilateral TTA - Male - Age 55 - Weight 73kg Traumatic cause	**At tibial end (90° flexion):** - Principal stress: Compression 102.9kPa Tension 66.6kPa - Shear stress 67.2kPa - Von Mises stress 129kPa **Volume of damaged area (after 75min):** - 30°: 13.5mm^3 - 90°: 600mm^3	- Residuum at risk of DTI during sitting with 90° flexion - Risk of DTI posture dependent - Injury rate higher with increased knee flexion - Damage volume may be dependent on muscle thickness

[1] Finite element; [2] Transtibial amputee; [3] Strain Energy Density; [4] Deep Tissue Injury

Table 2-3: Literature reviews on the aetiology of Deep Tissue Injury in transtibial prosthetic users.

Autor and year	Objective	Aetiological factor	Qualitative results
Mak et al. 2001 [23]	Overview over current knowledge about biomechanics in TTA[1]	Deformation, impaired lymphatic system, ischemia	- Skeletal movement and friction lead to soft tissue deformation during gait - Stress and deformation affect cellular and tissue function mechanically and via impairment of ancillary systems - Magnitude, direction, distribution, duration, loading rate are crucial - Possible accumulative effect of repetitive stress
Mak et al. 2010 [58]	Overview over tissue response to loading	Deformation, impaired lymphatic system, ischemia, ischemia-reperfusion	- Immediate muscle damage by direct mechanical insult or over longer period by ischemia - Reperfusion exacerbates damage by oxidative stress and inflammation - Damage may accumulate if insufficient recovery time
Bader et al. 2019 [83]	Analysis of bioengineering tools for device related soft tissue damage	Deformation, lymphatic drainage, ischemia, ischemia reperfusion injury	- Direct deformation, impaired lymphatic drainage, disrupted microvasculature and ischemia reperfusion as aetiological factors - High inter-patient variability

[1] Transtibial amputee

2.4.3.1. Non-prosthesis related risk factors

Non-prosthesis related risk factors originate from intrinsic characteristics of the transtibial residuum. According to the literature body, those factors are tissue morphology, the mechanical properties of the soft tissue, and sensory impairments (**Table 2-4**).

Tissue morphology was studied most frequently. Henrot et al. [84] and Portnoy et al. [31, 76, 81] focussed on surgery-related and pathological changes in tissue morphology. They identified the following risk factors: Thin muscle flaps [31, 81], minimal adipose tissue padding [76], sharp bone edges [31, 76, 84], and osteophytes (bone spurs) [31, 84]. Results on the influence of the bone radius were ambiguous. A numerical *in silico* study indicated that the soft tissue load is reduced with wider bone radii [31], whilst an analytical study found no relationship between the two [81].

The effect of sensory impairment was discussed in three papers. According to reviews [23, 83] the loss of sensation, as it is commonly seen during diabetes, causes a dysfunction of the natural protective pain mechanism to redistribute excessive loads. Kosasih et al. [75] suspected that sensory changes could also result from the amputation process. However, contrary to their expectations, deep pressure sensation of their test subjects seemed to be intact.

The mechanical properties of soft tissue were examined in two *in silico* studies. Both point to a higher susceptibility of stiff muscle to loading damage compared with a flaccid one [31, 81]. This stiffening might be the result of muscle contraction during normal gait [31, 81] or pathological changes like spasticity [31]. Portnoy et al. [31] also suggest that surgical scars change the stress distribution across the residuum. The higher elasticity of fibrous scar tissue may put the surrounding muscle at risk of DTI development.

Table 2-4: Studies on non-prosthesis related risk factors for Deep Tissue Injury

Author and year	Type of study	Objective	Risk factors	Study population	Qualitative results
Henrot et al. 2000 [84]	Literature review	Overview over surgical features of amputation in relation to postoperative stump pain	Tissue Morphology	NA	- Postoperative complications: Heterotopic ossification, aggressive bone edges, pistoning, ulceration - Extrinsic pain: caused by improper fit or alignment - Intrinsic pain: nervous or anatomical cause
Portnoy et al. 2007 [81]	In silico study	Determination of internal stress in muscle flap of TTA[1]; influence of bone sharpness, tissue thickness, mechanical properties	Tissue Morphology, Mechanical Properties	- Use of data from Portnoy et al. 2007 [36]	- Increase in pressure with reduced flap thickness - Increase in pressure with increased muscle stiffness - No clear relationship between bone radius and pressure
Portnoy et al. 2009 [76]	Experimental study	Determination of inter-subject variability in internal tissue loads in TTA with different geometrical features during static loading	Tissue Morphology	- 5 unilateral TTA - Traumatic cause - 1 female, 4 male - Mean age 48.6 yrs - Mean weight 67.8kg	- High inter-subject variability - Risk of DTI[2] for patients with little fat padding - More even pressure distribution with flat compared to sharp tibial ends - Lower strains with longer residua
Portnoy et al. 2009 [31]	In silico study	Identify influence of risk factors on internal loading conditions in TTA	Tissue Morphology, Mechanical Properties	- 1 unilateral TTA - Traumatic cause - Male - Age 44 yrs - Weight 82kg	- Thicker muscle flap and increased bone radius reduce DTI risk - Osteophyte, sharp bevelment and muscle stiffening increase risk - Surgical scars change overall stress distribution
Kosasih et al. 1998 [75]	Experimental study	Identify sensory changes in well healed TTA	Sensory impairment	- 9 unilateral TTA - Traumatic cause - All male - Mean age 55.4 yrs - Weight not specified	- No deep pressure sensory impairment in well healed TTA stumps
Mak et al. 2001 [23]	Literature review	Overview over current knowledge on biomechanics in TTA	Sensory impairment	NA	- Neuropathy leading to usually preventable soft tissue damage
Bader et al. 2019 [83]	Literature review	Analysis of bioengineering tools for device related soft tissue damage	Sensory impairment	NA	- Risk factors: neuromuscular impairments, diabetes

[1] Transtibial amputee, [2] Deep Tissue Injury

2.4.3.2. Prosthesis related risk factors

The prosthesis itself also influences the development of DTI in amputees. Relevant factors are socket design and prosthetic componentry (**Table 2-5**). The most discussed prosthetic element was the socket (n = 4). It distributes pressure and shear forces across the limb during weight-bearing [23, 58, 83]. Based on two fundamentally different socket design philosophies, loads may either be concentrated on proclaimed tolerant areas (Patellar Tendon Bearing, PTB), or spread across the entire residuum as evenly as possible (Total Surface Bearing, TSB) [23, 58]. Whilst differences in interface loads between both design approaches have been discussed in the literature [23, 38], the internal loading conditions have yet to be quantified [23, 38, 83].

Two clinical studies looked at components other than the prosthetic socket [78, 82]. A total of 18 traumatic, mainly male (94%) and unilateral (94%) amputees with an average age of 49.8 years and weight of 85kg participated. Researchers thereby studied the influence of prosthetic foot design [78] as well as gel liners and socks [82] on the internal loading states. Hydraulic and split-toed feet seemed to improve loading conditions in comparison to energy storage and return (ESR) and single-toe feet. Furthermore, using gel liners, especially stiff and thin ones, provided a positive cushioning effect. In contrast, the common practice of adding socks over the liner to counteract volume fluctuations of the stump increased interface shear, which may adversely affect deeper tissues.

Table 2-5: Studies on prosthesis-related risk factors for Deep Tissue Injury

Author and year	Type of study	Objective	Risk factor	Study Population	Qualitative results
Mak et al. 2001 [23]	Literature review	Overview over current knowledge about biomechanics in TTA[1]	Socket design	NA	- Influence of socket shape on pressure distribution - Need to quantify residuum-socket interactions - Need to address controversies in socket design
Mak et al. 2010 [58]	Literature review	Overview over experimental and computational studies on tissue deformation and pressure ulcers	Socket design	NA	- Influence of socket interface on transmission of pressure and shear to residual limb - Pressure profile affected by variations in socket and fitting techniques - Even load distribution as way to reduce DTI[2] risk
Dickinson et al. 2017 [38]	Systematic review	Critical appraisal of state-of-the-art in FE[3] analysis in TTA	Socket design	NA	- Influence of socket design and material properties on loading conditions - Clinical translation of FE models necessary
Bader et al. 2019 [83]	Literature review	Review of Medical Device Related Pressure Ulcers (MDRPUs) and technologies for their detection	Socket design	NA	- Deviations between stiffness of device material and skin/subdermal tissue as major issue - Inadequate guidance for use of devices - Individualisation as key concept
Portnoy et al. 2012 [78]	Experimental Study	Assessment of differences between hydraulic and ESR[4] feet on internal loading conditions when walking over complex terrain	Prosthetic feet	- 9 unilateral TTA - Traumatic cause - All male - Mean age 42.7 yrs - Mean weight 78.2kg	- Significant decrease in internal stress and loading rates with hydraulic vs ESR feet when walking on paved floor or ascending stairs - Tendency towards internal stress reduction when using split-toed ESR compared to single-toe version
Lenz 2017 [82]	In Silico Study (PhD thesis)	Investigation of pressure ulcer formation due to deformation, based on gel liner displacement	Prosthetic liner	NA	- Increased interface shear with addition of socks over liner - Cushioning effect of gel liner - Increase in shear stress at bone-muscle interface with no-slip condition - Increase in shear and von Mises but decrease in compression at bone-muscle interface with decreasing liner thickness - Decreased muscle compressive stress with increased liner stiffness

[1] Transtibial amputee; [2] Deep Tissue Injury, [3] Finite Element, [4] Energy storage and return

2.4.4. Methods in Deep Tissue Injury research

All experimental and *in silico* studies (*n* = 11) were included in a review of methods in DTI research on transtibial prosthetic users. The studies were grouped by finite element analysis (FEA), analytical modelling, acoustic signalling, and sensory analysis.

2.4.4.1. Finite element analysis

FEA is based on computational models of the residuum with defined geometries, material properties, and boundary conditions. Through numerical analysis, visual stress and strain maps are created. With *n* = 6 (54.54%) papers, FEA is the most common method in primary research (**Table 2-6**). The studies were divided into three groups: individualised biomechanical models for aetiological research [29, 76, 79], *in silico* studies for parametric analysis of risk factors [31, 82], and real-time FEA for clinical applications [36].

Researchers collected subject-specific morphological and loading data from Magnetic Resonance Images (MRI) and interface pressure sensors. They also integrated some mechanical properties of soft tissue into the analyses, for example viscoelasticity [29] or hyperelasticity [76, 79]. Others, like heterogeneity and anisotropy were disregarded. The predicted stress and strain levels were then compared to threshold values for deformation-induced cell death to determine the subject-specific DTI risk [76, 79]. One study also considered damage progression through iterative post-processing [79], to incorporate muscle stiffening after the initial damage [85].

For risk factor research, *in silico* modelling was the tool of choice. By changing single input parameters of a Finite element (FE) model, their effect on internal loading conditions can be tested. Portnoy et al. [31] for example altered bone geometry, mechanical properties of the muscle, and tissue homogeneity to assess internal loading states. Lenz [82] simulated the use of different liners and liner-socket interface conditions on a cuboid FE model of soft tissues.

Table 2-6: Studies on Deep Tissue Injury in transtibial prosthetic users using Finite element analysis

Author and year	Type of study	Methodology	Input data	Assumptions	Outcome measures
Portnoy et al. 2008 [29]	Experimental study (aetiological)	- 3D FE[1] model - Donning and static load bearing of one TTA[2] - Analysis of internal loading state	- Interface pressure (pressure sensor) - Tissue morphology and vertical displacement (MRI[3]) - Shear modulus, friction between skin and socket (literature)	- Muscle: isotropic, homogenous, viscoelastic - Skin: isotropic, homogeneous, hyperelastic - No differentiation btw. muscle and fat - No friction between soft tissue layers	- SED[4], principal compressive and tensile stress and strain, max. shear stress and strain, von Mises stress
Portnoy et al. 2009 [76]	Experimental study (aetiological)	- 3D FE model [29] - Static load bearing of five TTA - Analysis of internal loading state and interpatient variability - Evaluation of DTI[5] risk	- See Portnoy et al. 2008 [29]	- Soft tissue: isotropic, homogeneous, hyperelastic - Differentiation btw. muscle and fat - Addition of 2mm skin layer - No friction between soft tissue layers	- Volume of muscle skin with compressive, tensile, shear strains above threshold value [33]
Portnoy et al. 2011 [79]	Experimental Study (aetiological)	- 3D FE model [29] - Sitting with 30° and 90° knee flexion in one TTA - Assessment of internal loading state and estimation of damage area over time	- See Portnoy et al. 2008 [29]	- Soft tissue: isotropic, homogeneous, hyperelastic - Differentiation btw. muscle and fat tissue - Addition of 1mm skin layer - No friction between soft tissue layers	- Principal tensile and compressive stress, max. shear stress, von Mises stress - Time-dependent volume of damaged muscle [33] - Rate of damage progression [85]
Portnoy et al. 2009 [31]	In silico study (risk factors)	- 3D FE model [29] of one TTA - Changes in morphological and mechanical parameters	- See Portnoy et al. 2008 [29]	- See Portnoy et al. 2009 [76]	- SED, principal compressive and tensile stress and strain, max. shear stress and strain, von Mises stress, - Volumes of areas with concentrated elevated stress

Table 2-6 (continued)

Lenz 2017 [82]	In silico study (PhD thesis, risk factors)	- Analysis of internal loading state with simplified cuboid FE model - Simulation of different liners and socks - Differentiation between slip and no-slip condition	- Liner displacement and mechanical properties (motion capturing) - Normal and shear interface forces (two-axis load cell) - Shear modulus, friction between skin and liner, soft tissue and liner thickness (literature)	- Muscle: isotropic, homogeneous, hyperelastic - Differentiation btw muscle, skin, gel liner - No friction between soft tissue layers - Friction between skin and gel liner (slip vs. no-slip)	- Principal compressive stress, max. shear stress, von Mises stress
Portnoy et al. 2007 [36]	Experimental Study (clinical)	- 2D FE model for real time stress analysis - Application on 5 TTA[1] during treadmill walking	- Interface pressure (pressure sensor) - Elastic modulus (Indentation test) - Tissue morphology (X-Ray)	- Soft tissue: isotropic, homogenous, linear elastic - No differentiation btw. muscle, fat, and skin	- Principal compressive stress and strain, shear stress, von Mises stress

[1] Finite Element; [2] Transtibial amputee; [3] Magnetic Resonance Imaging; [4] Strain Energy Density; [5] Deep Tissue Injury

To translate these complex models into clinical use, real-time availability of information is desirable. Thus, Portnoy et al. [36] proposed an X-Ray based 2D FE model of the residual limb, with interface pressure measurements and patient-specific elastic moduli feeding into it. Rendering bones as rectangles and assuming linear elasticity, isotropy, and homogeneity was accepted as trade-off between accuracy and computing time.

Overall, FEA is a common tool in biomechanical research of DTI development. It provides full field information on the internal loading state of soft tissue and allows to assess load distributions and the influence of single risk factors. The model complexity, input, and output data vary widely across the different studies.

2.4.4.2. Analytical methods

For clinical applications, two-dimensional analytical solutions, as used in three primary studies [36, 77, 78], are an alternative to FEA (**Table 2-7**). The models evaluated the internal loading state of the residuum mathematically, based on simplified tissue geometries and mechanical behaviour. The first approach developed by Portnoy et al. [81] calculated the contact pressure between bone and soft tissue based on Hertz contact theory. Despite being validated *in silico*, this model was, to the authors' knowledge, never translated to experimental research.

Instead, Portnoy et al. used a similar model [86] for their experimental studies [77, 78]. The bone was assumed as an axisymmetric, flat indenter, compressing a linear elastic soft tissue layer. Further input was based on individual interface pressure measurements and X-Rays in combination with literature-based values for tissue material properties and boundary conditions. This allowed for a real-time estimation of internal loading states and prediction of risk scenarios.

2.4.4.3. Acoustic signalling

Following the idea of direct deformation as major aetiological factor, Buis et al. [80] attempted to find ways other than imaging to measure tissue distortion (**Table 2-8**). In an *ex vivo* experimental study, they subjected porcine and galline tissue immersed in a saline bath to tensile stress whilst recording acoustic emissions with a hydrophone. However, they were unable to detect sufficient acoustic signals to support the theory that deformation creates detectable acoustic signals.

Table 2-7: Studies on Deep Tissue Injury in transtibial prosthetic users using analytical modelling

Author and year	Type of study	Methodology	Input data	Assumptions	Outcome measures
Portnoy et al. 2007 [81]	In Silico Study	- Application of Hertz contact theory for calculation of contact pressure between bone and soft tissue - Evaluation of sensitivity of pressure calculations to tibial radius, muscle thickness and mechanical properties	- Tissue morphology (X-Ray [36]) - Poisson's ratio (literature)	- Soft tissue: isotropic, homogeneous, linear elastic - No friction between bone and soft tissue - Tibia simplified as flat-ended cylinder - Only vertical bone displacement	Contact pressure between tibia and soft tissue
Portnoy et al. 2010 [77]	Experimental Study	- Development of portable monitor based on an axi-symmetric indentation problem - Use of monitor on 18 TTA[1] to record internal loads during walking on complex terrain - Comparison of internal loads between patient groups and surfaces	- Interface pressure (pressure sensor) - Tissue morphology (X-Rays) - Shear modulus, friction between skin and socket (literature)	- Soft tissue: isotropic, homogeneous, linear elastic - No differentiation between muscle, fat, and skin - Tibia simplified as flat-ended cylinder	Average von Mises stress, loading rate, stress-time integral
Portnoy et al. 2012 [78]	Experimental Study	- Use of portable pressure monitor [77] on 10 TTA - Assessment of internal stress during walking on complex terrain - Comparison of outcomes for ESR[2] foot and hydraulic foot	- See Portnoy et al. 2010 [77]	- See Portnoy et al. 2010 [77]	Average von Mises stress, RMS[3] of von Mises, loading rate, cadence

[1] Transtibial amputee; [2] Energy Storage and Return; [3] Root mean square

Table 2-8: Studies on DTI in transtibial prosthetic users using acoustic emission and sensory tests

Author and year	Type of study	Parameter of interest	Methodology	Input	Outcome measures
Buis et al. 2018 [80]	Ex vivo animal study	Acoustic signalling	- Tensile test setup - Immersion of bovine and galline specimen in saline solution - Recording of acoustic signals during tensile test of specimen with hydrophone	Tensile load and displacement (Instron)	Acoustic emission: amplitude and frequency (No correlation found btw. acoustic emission and deformation)
Kosasih et al. 1998 [75]	Experimental Study	Sensory analysis	- Qualitative sensory assessment of the residuum in 16 TTA[1] - Test sides: pressure tolerant and pressure sensitive areas of residuum - Contralateral limb as control	Physical administration of cotton swab wisp, firm pressure, tuning fork vibration, safety pin prick by physician	Qualitative feedback about sensory response either at detection of stimulus or with description (i.e. sharp or dull pain)

[1] Transtibial amputee

2.4.4.4. Sensory analysis

The only primary study that was not biomechanics related was an experimental study on sensory changes in transtibial prosthetic users [75] (**Table 2-8**). A physician applied light touch, deep pressure, vibration, and pinpricks to the residuum and the sound limb of participants. The resulting sensory perception for each stimulus was evaluated with qualitative feedback. All participants had an intact deep pressure sensation, whilst vibration and pinprick sensation were less detectable with increased age of the participants. Light touch was only minimally impaired.

2.5. Discussion on Deep Tissue Injury in transtibial prosthetic users

In this scoping review, research and literature on DTI as a result of transtibial prosthetic use were identified. Generally speaking, the evidence base was sparse with only eleven primary research studies identified. Overall, three key areas were addressed: First, the aetiology of DTI in prosthetic users is only partially understood. Whilst direct deformation seems to be an important factor, the contribution of ischemia, ischemia reperfusion, and an impaired lymphatic drainage has yet to be evaluated. Second, several risk factors were identified. Intrinsic determinants of DTI are tissue morphology and its mechanical properties, as well as sensory impairment of the residuum. Extrinsic determinants are socket design and prosthetic components. Finally, methodological approaches in both aetiological and risk factor research focussed mainly on biomechanics. The most common research design combined static or dynamic loading with medical imaging and computational analysis. However, the diversity of input data, modelling assumptions, and outcome measures, together with the variability in geometric patient characteristics and prosthetic componentry make a quantitative comparison of results and their clinical translation difficult.

2.5.1. Damage pathways of soft tissue injury

Within the last two decades, major research efforts led to advances in our understanding of DTI. The pathways of tissue damage from external loading were investigated on different organisational levels, from cell cultures over engineered muscle constructs to *in vivo* animal studies (in the living animal) [56, 87]. Results suggest that the relationship between the degree of deformation and time is essential: Whilst high strain can cause immediate direct deformation damage, moderate strain

may injure the tissue by occluding the vascular and lymphatic system over an extended period.

2.5.1.1. Loading biomechanics and direct deformation

The biomechanical profile at the stump-socket interface of lower-limb amputees differs significantly from the frequently studied immobile individuals [27, 28, 30, 66, 88–91]. Prolonged loading only occurs in situations of static weight bearing like standing or sitting with a donned prosthesis. In contrast, with over 8000 steps taken daily by TTA [92], the residuum often experiences dynamic, cyclic loading. During gait, complex internal stresses and strains develop: weight bearing causes pressure at the socket-limb interface [93]; the vertical pistoning movement between the residuum and the socket invokes shear forces [94]; and gait action and bone movement lead to added forces and moments [95, 96]. The combined forces and moments result in internal compressive, tensile, and shear stress [97]. However, it is difficult to quantify the individual contribution of each stress component to DTI development.

So far, DTI research focussed mainly on compressive loading. Researchers have defined threshold levels for direct deformation damage, based on the relationship between pressure or compressive strain and time [33, 34]. They compared these thresholds to computed values of internal compressive stress and strain in prosthetic patients to predict the likelihood of DTI development [76, 77, 79]. However, the results must be interpreted with caution.

First, the threshold levels were derived from experiments on animal tissue and bioartificial muscle constructs, and were not intended to be translated directly to human studies [33, 34]. Second, the experimental design of threshold studies was oriented towards measuring direct deformation damage, whilst the microvascular and lymphatic system were mostly neglected. And last, applying a static, compressive load differs from residuum biomechanics. Researchers found that a cyclic force application may lower static threshold levels [23, 91, 98, 99], implying that the predicted risk of DTI in TTA has been underestimated. Adding a shear component might also increase tissue damage by reducing the capillary closure pressure, which in turn increases the risk for ischemia [100, 101].

To minimise these limitations, new research approaches are needed. The effects of shear and distortion on tissues and cells should be examined with mechanical,

microvascular, and lymphatic damage in mind. Additionally, researchers repeatedly stressed the need for a dynamic threshold level that combines compression, tension, and shear [36, 76, 79].

2.5.1.2. Microvasculature and the lymphatic system

This review revealed a gap in the aetiological research. While the connection between deformation damage and prosthetic use has been established experimentally, the role of microvasculature and the lymphatic system was only discussed in general review papers.

Regarding the vascular system, the effects of a cyclic loading protocol with ischemic and reperfusion phases altering at high frequencies are unknown. The literature on similar loading scenarios is ambiguous: Some experimental results indicate an accumulation of cellular and tissue damage in comparison to continuous loading. However, the studies were either based on animal skin [98, 99, 102] or used prolonged time intervals [90, 91] far below frequencies of about 1 Hz commonly seen during prosthetic gait [77, 103]. Other studies report on the adaptive abilities of soft tissue [20, 104–106], which indicates an increased tissue tolerance towards ischemic and reperfusion damage [107]. Further research into this area is therefore necessary.

The structure and function of the lymphatic system and its response to loading are barely understood. In general, compression in combination with shear stress may affect lymph formation and propulsion [108]. The resulting dysfunction of lymphatic drainage can lead to an accumulation of toxic waste products, which damages cells and tissues [109, 110]. A small number of studies over the last decade supports this theory. Researchers confirmed less lymphatic clearance during compressive loading [111], as well as toxic effects of accumulated bio-wastes like cytokines and reactive oxygen species (ROS) on cell viability [112]. Reperfusion adds further stress on the lymphatic system [113]. These factors might be aggravated in TTA. The initial amputation surgery causes traumatic injury to the lymphatic system [84, 114], followed by a reduced muscle tone post-amputation, which might weaken the propulsive abilities of lymphatic vessels and results in oedema [115].

For a comprehensive understanding of the role of the vascular and lymphatic system in DTI development, high-frequency cyclic loading protocols should be performed on perfused tissue. Besides histological analysis of muscle damage in animal models, arterial spin labelling or dynamic contrast MRI could relate the damage to muscle

perfusion and oxygenation [116]. For clinically oriented studies, the oxidative function of the residual limb could be assessed with near-infrared (NIR) spectroscopy [117, 118]. The lymphatic system could be explored in a similar fashion by visualising lymph flow with NIR fluorescent imaging [111]. With information from direct deformation studies, the results of microvascular and lymphatic experiments can feed into the prevention, diagnosis, and treatment of DTI.

2.5.2. Risk factors in the transtibial prosthesis user population

Identifying population-specific characteristics that may have a negative influence on the soft tissue in amputees is as important as estimating internal loading states. Various risk factors link transtibial prosthetic use to DTI development, as detailed in the following paragraphs.

2.5.2.1. Influence of tissue characteristics

This review revealed a range of tissue-related determinants of DTI risk. First, amputation surgery changes the tissue morphology and geometry in the residual limb. Revisiting established surgical procedures and considering alternatives might reduce some of these risk factors, for example by using of bone bridges [119] instead of bevelled bone edges, or different flap techniques that change the location of surgical scars [120, 121].

On the other hand, naturally occurring risk factors are difficult to eliminate. The residuum commonly undergoes changes of intramuscular fat infiltration and muscular atrophy post-amputation [20, 122], which were both shown to enhance internal tissue deformation in SCI patients [64]. Additionally, amputees often experience complications after surgery like osteophytes or angular deformities [123, 124], which also have adverse effects on tissue loading [31, 84]. Overall, a multitude of amputation-related tissue characteristics aggravate the challenging loading conditions for the residual limb.

2.5.2.2. The role of co-morbidities

The main cause of transtibial amputation in the Global North is dysvascularity. In the UK and the US, most patients suffer from diabetes and other peripheral vascular diseases [40, 41, 125]. This impacts the perfusion of their residua, promotes ischemic damage, and exacerbates inflammation. Neuropathy is another common complication

in diabetic patients. Researchers stressed that as the body's protective pain mechanism is suspended, individuals may not distribute potentially damaging loads anymore [23, 83].

To confirm this link between co-morbidities and DTI development in TTA, epidemiological studies would be valuable. These studies also offer a chance to uncover possible correlations of other factors, such as time since amputation or age. They could also provide insight into the prevalence of DTI in TTA in general. The epidemiology of DTI in the Global South could also be investigated, as their amputation population profiles, surgical procedures, and prosthetic componentry differ significantly from the Global North [125–127].

2.5.2.3. Prosthesis-related risk factors

Prosthetic sockets are in direct contact with the residuum. Hence, they are the component most often associated with DTI development. Researchers highlighted the influence of the socket shape on internal pressure distribution and soft tissue deformation [23, 38, 58]. However, studies that quantify differences in internal loading conditions between the two main socket designs PTB and TSB are missing. To close the gap, mechanical and biological studies could be conducted. This information would help to define "good" prosthetic fit and improve clinical practice.

Other prosthetic componentry like prosthetic feet and liners also influence the internal loading conditions [78, 82]. Before this information can be utilised reliably in clinical practice, more studies with large sample sizes and low variability are needed. This applies not only to studies on prosthesis-related risk factors, but to all experimental DTI studies on human subjects. Thus, consistency in patient groups, socket types, alignment, and componentry are crucial.

2.5.3. Methodological approaches in Deep Tissue Injury research

Tissue loading is a major factor in the development of DTI. Traditionally, the interface pressure between the socket and the residuum was quantified with sensor technologies [23, 128]. With the discovery of deep tissue layers as the potential origin of pressure ulcers [54, 60], the focus shifted towards assessing internal mechanics.

New methods were needed as interface pressure does not reflect the internal loading states [129, 130].

2.5.3.1. Computational and analytical modelling

According to this review, modelling was the measure of choice. Medical images, interface pressure measurements, and data on mechanical properties of soft tissue informed numerical and analytical models. Researchers then used the estimated stress and strain values of those models to find general loading patterns and patient-specific DTI risks during various scenarios.

However, interpreting estimated stress and strain values beyond basic trends is difficult. This comes down to the complexity of soft tissue mechanics. Skeletal muscle exhibits time-dependent behaviour under load, including hysteresis, stress relaxation, and creep [131, 132]. Because of its cellular arrangement in parallel fibrous structures, the direction of load application alters the mechanical properties, known as anisotropy [131]. Additionally, the residuum consists not only of skeletal muscle, but also adipose tissue, connective tissue, and skin, which all have different, patient-specific mechanical properties. Each layer might also be affected by inhomogeneities, like scar tissue or fat infiltration. Taken together, the intricate nature of soft tissues exceeds the modelling capabilities of existing computational approaches [38]. The research on biomechanics of the residual limb is no exception and usually draws on simplified concepts with assumptions of linear elasticity, isotropy, or homogeneity. Even though clinical translatability is a core issue in DTI research, the accuracy of the proposed patient-specific modelling approaches based on these simplifications is questionable.

Nevertheless, methodological developments may increase the accuracy of future research efforts (**Table 2-9**). Another advancement is the integration of model post-processing. Muscle stiffening is a phenomenon observed after the onset of DTI, which redistributes subsequent loads towards adjacent sites and promotes damage progression in a positive feedback loop [85, 133]. Integrating this damage law into FE models for prolonged loading increases the accuracy of DTI prediction [79, 85]. Widening this approach to model pre-processing by incorporating the effects of the donning procedure, as Lacroix and Patino [134] did for transfemoral amputees, would improve modelling even further.

Table 2-9: Potential technologies for advanced FE modelling input

Soft Tissue Property		Technology	Reference
Anisotropy		Diffusion Tensor MRI (DT MRI)	Ramsay et al. 2018 [135]
Inhomogeneity	Different soft tissue layers	MRI, Ultrasound	Bader and Worsley 2018 [136]
	Scar tissue	Elastography	Strijkers et al. 2019 [137]
	Fatty infiltration	Dixon MRI method, Magnetic Resonance Spectroscopy, T2 relaxation time mapping	Strijkers et al. 2019 [137]
Elasticity and stiffness		Elastography	Nelissen et al. 2017 [138] Sigrist et al. 2017 [139]

2.5.3.2. Alternatives to determine internal loading states

Modelling is not the only approach to determine internal loading states. Medical imaging offers ways to visualise soft tissue deformation directly. MRI tagging has been proposed and used to derive strain values of compressed muscle [137, 140]. Another alternative would be to measure physiological features indirectly related to the mechanical state of tissues. DT MRI for example captures changes in diffusivity due to compression [141], making it a potential measure for strain [142]. Given the complexity and limitations that the predictive nature of analytical and computational modelling entails, it seems sensible to integrate technologies that have not yet been used for pressure ulcer research. Nevertheless, even with technological advances, interpreting the produced data remains difficult until we have a more scientific understanding of the influence of loading on soft tissues.

2.5.4. Limitations of the scoping review

Whilst the systematic approach according to the PRISMA-ScR guidelines identified most of the relevant literature, there are various sources of potential bias. First, the lack of registration of the review protocol before performing this scoping review may have introduced reporting bias. Unfortunately, possibilities to report protocols for scoping reviews on common publication platforms like PROSPERO are limited [73]. Bias was therefore minimised by selecting articles according to a pre-defined set of criteria according to the PRISMA-ScR guidelines.

By restricting the search to English language and excluding grey literature, studies might have been missed, introducing selection bias. Further papers might have been overlooked because of the variations in wording and definitions of pressure injuries [57, 143, 144]. Additionally, the review process was mainly conducted by one reviewer. To limit possible selection bias, a combination of common DTI- and prosthesis-related expressions was used in the search strategy. In case of uncertainty during the selection process, a second reviewer was consulted.

Last, the focus of this study was on transtibial prosthetic users. Transfemoral amputees might experience similar conditions and could therefore be included in future endeavours.

2.6. Summary of the scoping review

This scoping review recorded an overwhelming interplay of aetiological and risk factors for DTI in transtibial prosthetic users. It also highlighted the need for fundamental research in this area. Particularly relevant is the unique biomechanical environment created when the residuum and prosthetic socket interact during gait, which is characterised by high shear forces and repetitive loading. Combining the tissue's response to dynamic loading with measurement methods like imaging could provide new insights into the aetiology of DTI. This would build the scientific basis for consensus on much-needed advances in clinical practice: from improved amputation and rehabilitation processes, to updated socket design and fitting procedures, and the optimised use of componentry.

2.7. Research aim

The results of this scoping review revealed that pressure injury and prosthetic research have many similarities regarding aetiology, risk factors, and research methods. Yet, the evidence on the soft tissues' reaction to the biomechanically unique environment within the residuum-prosthesis-complex is limited. Dynamic loading conditions, repetitive soft tissue deformation, and high shear forces are unique to the prosthetic user population. To investigate these conditions, prosthetic research could benefit from applying pressure injury methods and ways of tissue analysis to residual limbs.

Only with a sound understanding of the relationship between the biomechanical environment and the biological soft tissue response, upcoming technologies can be

fully utilised. This applies not only to advanced research methods like image-based FEA, but also developments in clinical digitalisation, like digital shape capturing and additive manufacturing.

Based on this need for further research into the reaction of skeletal muscle to different loading conditions, the key research question for this project forms the following overarching aim for this thesis:

Investigating the influence of prosthesis-related loading on skeletal muscle health

CHAPTER 3

The mechanobiology of Deep Tissue Injury development

This chapter introduces the key concepts around mechanobiological research on skeletal muscle. After an introduction to skeletal muscle, the current knowledge on the reaction of cells and tissues to mechanical loading is discussed with a focus on pressure injuries and prosthetic use. All this information is distilled into the research objectives for this project set out at the end of the chapter.

This chapter is the result of the literature read and reviewed by the author throughout the project. The direction of the research was stimulated by frequent discussions with A. Buis on mechanobiology and prosthetics, as well as A. Wark and M. Sandison on methodological aspects of different muscle-related studies.

3.1. Introduction to mechanobiology in prosthetics

Mechanobiology has emerged as a new field of research over the last decades. It aims to uncover the relationship between biological activities on cell and tissue level and their mechanical environment. Research is thereby mostly centred around the questions of “how” and “what”: How does a cell convert physical cues into a biological response? This is relevant on a microbiological level, i.e. to develop new therapeutic techniques against cancer [145]. The second question is: What does the biological responses of cells and tissues to mechanical stimulation look like? The answers can have a direct impact on prosthetics. Characterising the soft tissue reaction to different mechanical loading scenarios can provide a basis to gauge prosthetic fit, adapt sockets where necessary, and provide recommendations on prosthetic usage.

3.1.1. Scope of mechanobiology in prosthetics

To investigate the influence of prosthesis-related loading on soft tissue health, three main areas need to be addressed: (1) Surgery and clinical rehabilitation, (2) the biomechanics of different loading scenarios, and (3) the cell and tissue response to the physical stress. All three areas stretch across multiple disciplines (**Figure 3-1**), which will be summarised in the following paragraphs.

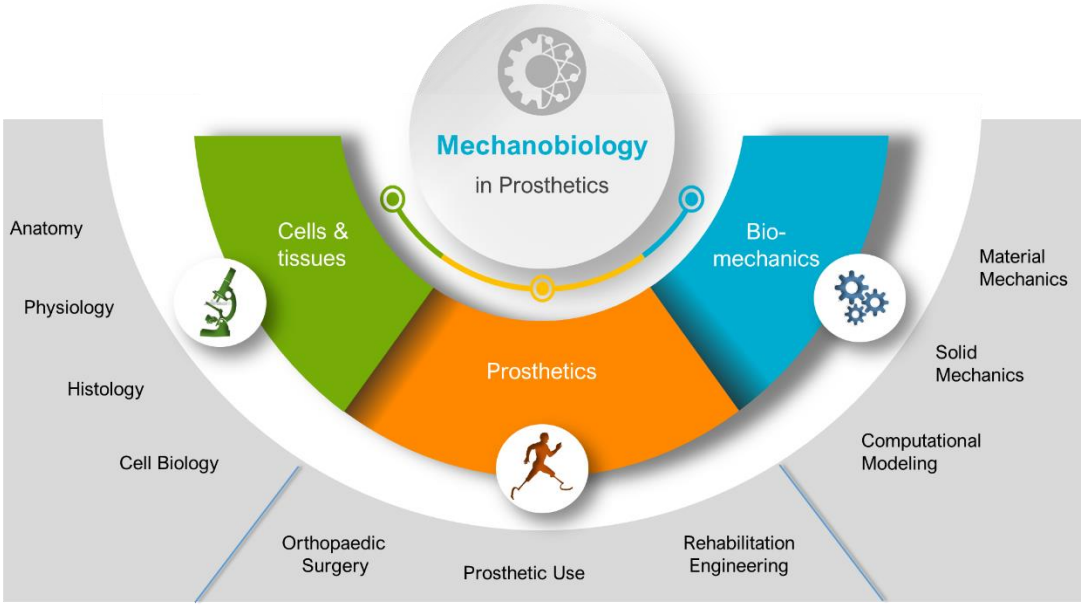

Figure 3-1: Mechanobiology in prosthetics. Mechanobiology is an interdisciplinary field that combines techniques from biological (green) and mechanical research (blue) to understand the influence of physical stress on anatomical structures and physiological processes in living tissue. This approach can be used to characterise the residuum-prosthesis-complex in prosthetic users (orange).

From a clinical perspective, the first decisions that influence the soft tissue and its biomechanical environment are made during orthopaedic surgery, where the shape and general characteristics of the residuum are determined, like the location of scar tissue. The tissue further changes during postoperative care i.e. from wound management and the use of early walking aids. The environment at the residuum is then shaped by socket design and choice of componentry during rehabilitation. Last, the way the prosthesis is used in daily life like walking or running defines the loading conditions.

The combination of clinical aspects produces a certain biomechanical environment at the residual limb, which can be described from two perspectives: solid mechanics characterise forces exerted by the prosthetic system during use; material mechanics define the mechanical properties of the soft tissues that influence load transmission across the residuum. This interdependent system is often analysed with computational modelling as physical measurements are difficult to obtain. To interpret the outcomes of the biomechanical analysis, one needs to understand the general cell and tissue response to mechanical loading. This includes a basic understanding of the anatomy and physiology of cells and tissues within the residual limb. Their micro- and macro-level responses can then be characterised with cell biology and histology techniques.

3.1.2. Fundamentals of mechanical load

A clear definition of terms related to mechanical loading is crucial to avoid misunderstanding when discussing loading, mechanical properties and materials. Within this thesis, a differentiation between external mechanical loading conditions at an interface, i.e. between the socket and residual limb or an indenter and soft tissue, and internal loading conditions like within the muscles of the residual limb was made.

Looking at external loading conditions, perpendicular forces lead to compression or tension of the tissue, and angular forces possess a shear component (

Figure 3-2). Friction also needs to be considered, which is defined as the tangential force acting at the surface of two contacting bodies in opposite direction to their relative motion (**Figure 3-3a**). When the skin of the residual limb is stretched against the support surface due to friction, shear forces start acting upon the superficial layers parallel to the surface and deform it, until slip occurs. These shear forces are

characterised by their equal size, opposing direction, and parallel offset arrangement, as seen in **Figure 3-3b**.

The intensity of a normal force per area is defined by pressure. While pressure is a frequently used term in mechanobiology-related research, its use can be ambiguous. In engineering terms, pressure is a scalar quantity, meaning that it is independent of direction. Stress on the other hand is a tensor that includes both magnitude and direction. In literature, the term pressure is often used interchangeably with direct stress (**Figure 3-3c**). In this thesis, the term pressure will still be used when referring to work by others whilst original work will differentiate between pressure and direct stress.

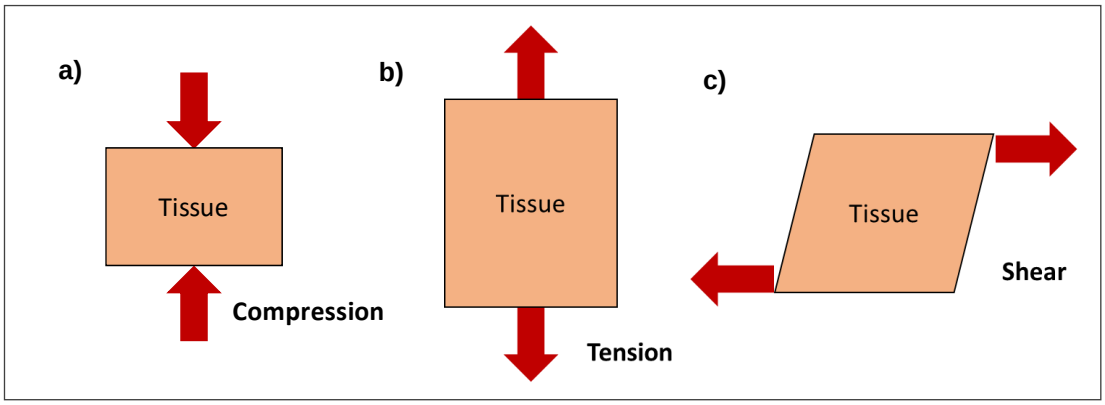

Figure 3-2: Types of mechanical loading of tissue. a) Compression: forces acting towards and perpendicular to surface **b)** Tension: acting away from and perpendicular to surface **c)** Shear: forces acting in parallel to surface in opposite directions.

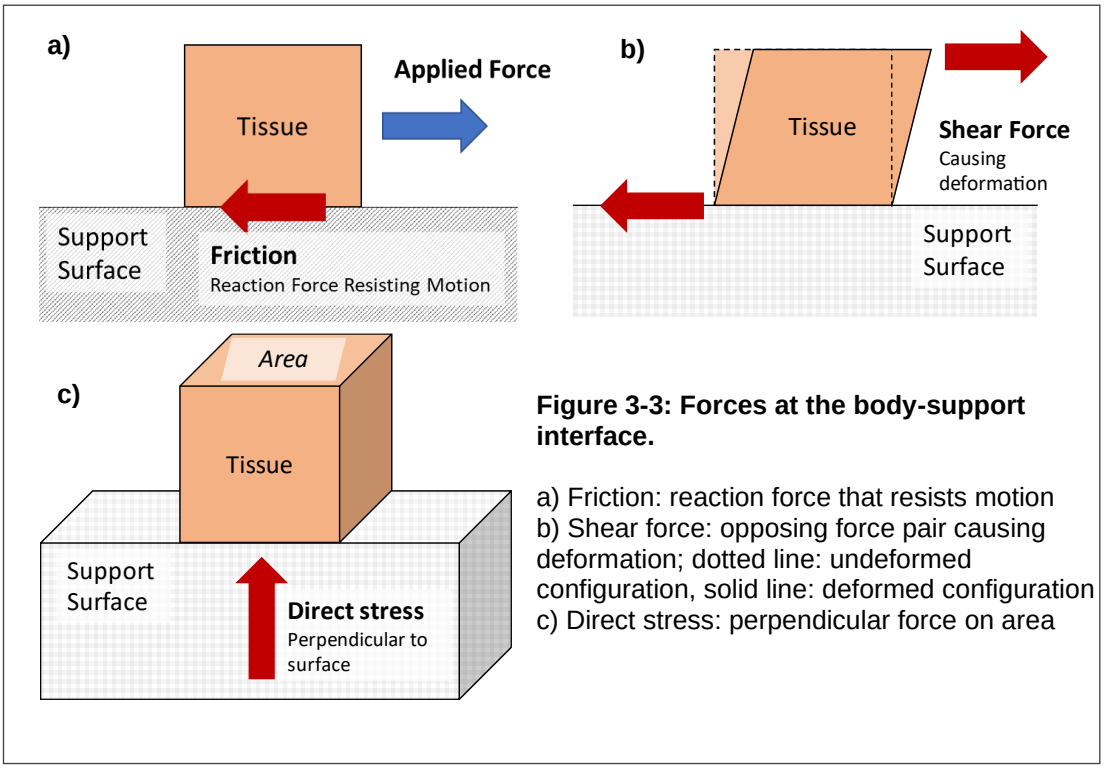

Figure 3-3: Forces at the body-support interface.

a) Friction: reaction force that resists motion
b) Shear force: opposing force pair causing deformation; dotted line: undeformed configuration, solid line: deformed configuration
c) Direct stress: perpendicular force on area

Internal loading conditions on the other hand are characterised with the aid of stress (force per unit area) and strain (deformation). This can be visualised with stress elements, a useful way of representing stresses acting at some point in the body (**Figure 3-4**). A stress element isolates a small element and shows stresses acting on all faces. Dimensions are infinitesimal small but are drawn to a large scale. When a tensile force is acting upon a rectangular object, a stress element in its middle is deformed (stretched) analogously to the object (**Figure 3-5a**). The orientation in which the normal forces that act perpendicular to a plane on the stress element reach their maximum defines the maximum principal stress σ_{max}. The shear stress in this orientation will be equal to zero. If the orientation of the specimen is changed, however, it will be subject to a combination of compression and shear forces (**Figure 3-5b**). The maximum shear stress can be found in a plane at an 45° angle to that of the maximum principal stress orientation, having a magnitude of $\sigma_{max}/2$. Hence, an external tensile or compressive load will always lead to the development of shear stress.

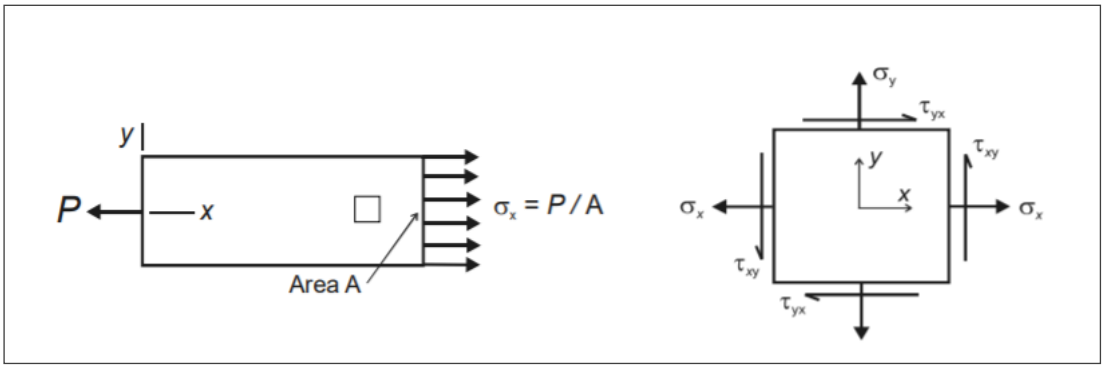

Figure 3-4: Stress elements. A stress element is a way to represent the stresses within a body initiated by external loading, i.e. direct stress/pressure (*P*). It shows normal stresses *σ* acting perpendicular to a plane, as well as shear stresses *τ* acting parallel to a plane.

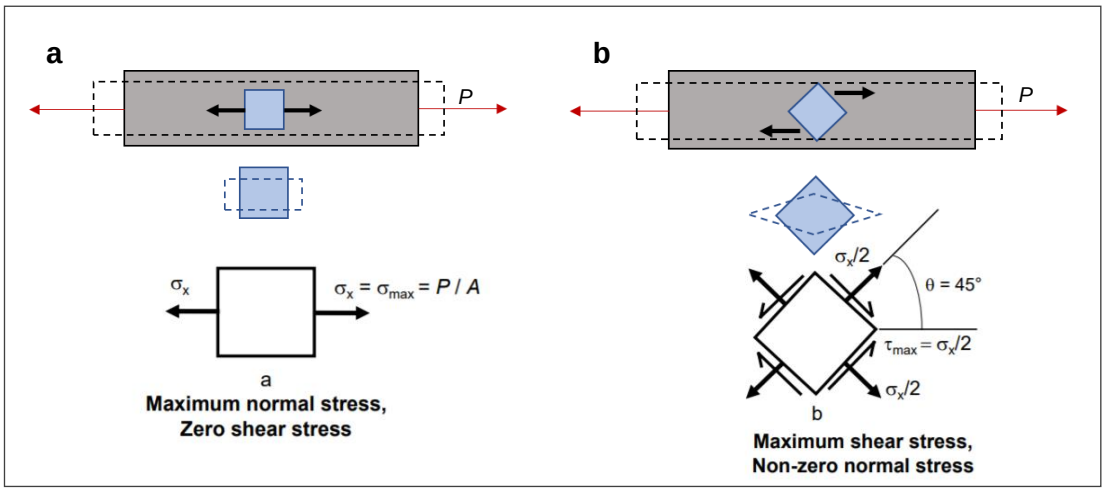

Figure 3-5: Uniaxial tension (a) stress element in orientation that represents the maximum normal stress and zero shear stress **(b)** stress element in orientation that represents the maximum shear stress and a non-zero normal stress; solid lines: undeformed configuration; dotted lines: deformed configuration; red arrows: external tensile load; black arrows: internal load.

3.2. Aim of literature review on mechanobiology of skeletal muscle

The scoping review described in *Chapter 2* highlighted the need for fundamental research into the cell and tissue response to prosthesis-related loading. While two areas of prosthetic mechanobiology, the prosthetic environment and its biomechanics, are comparably well studied, biological research on their influence on cells and tissues of the residual limb is still in its infancy. This chapter will introduce key concepts around mechanobiological research on skeletal muscle. Based on the similarities between prosthetic and pressure injury research, an overview over state-of-the-art research in both areas will be provided to answer the question of how cells and tissues react to mechanical loading. All this information is distilled into the research objectives for this project set out at the end of the chapter.

3.3. Anatomy and physiology of skeletal muscle

3.3.1. Hierarchical structure of skeletal muscle

Skeletal muscle has a complex hierarchical structure and functionality that differs from most other tissues in the human body (**Figure 3-7**). The organisational units of skeletal muscle are separated by various connective tissues (**Figure 3-6**). Surrounding the muscle is the fibrous epimysium. It encloses nerves, blood vessels,

and lymphatic vessels, as well as skeletal muscle cells. Those cells, also known as myofibers, can reach a diameter of 100µm and a length of up to 30cm in human thighs [146, 147]. They are bundled into compartments of fascicles, which are partitioned by the perimysium. Within the fascicles, single myofibers are separated by the endomysium. All the connective tissues come together at the end of a muscle to form tendons (rope-like) or aponeurosis (sheet-like), attaching it to bones.

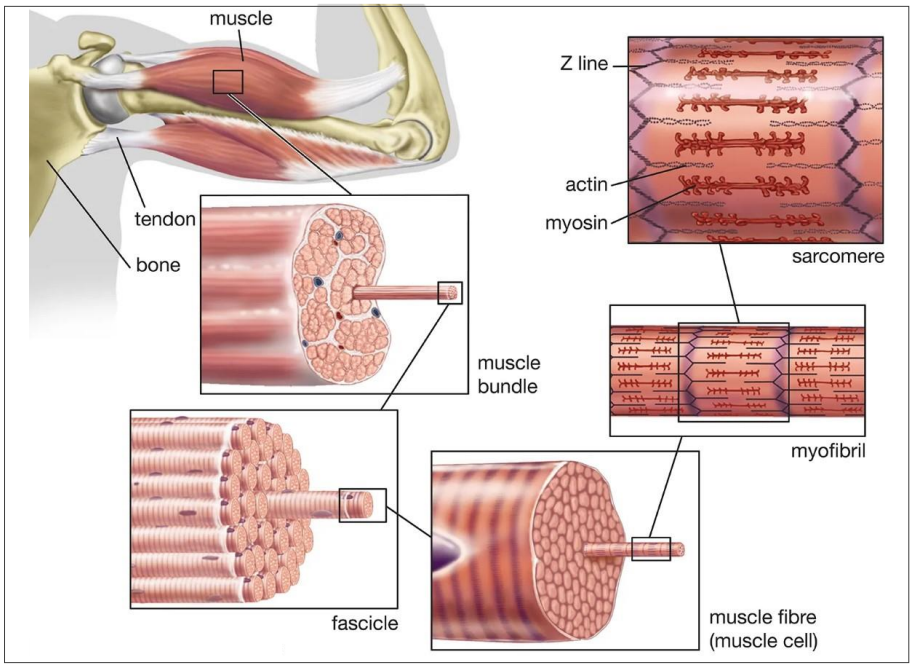

Figure 3-7: Hierarchical structure of skeletal muscle tissue. Image by courtesy of Encyclopaedia Britannica, Inc., copyright 2017 **[148]**; used with permission.

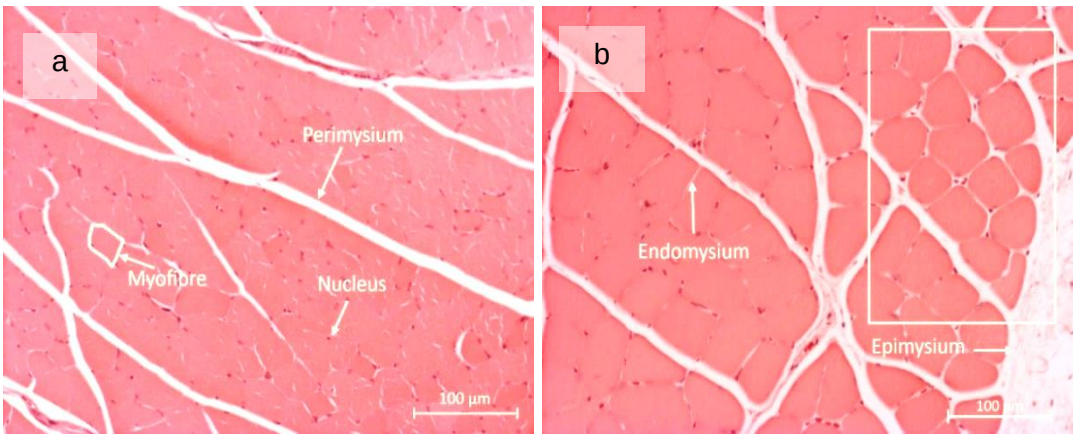

Figure 3-6: Representative control tissue (cross-sectional view). (a) densely packed skeletal muscle tissue with little interstitial spaces between cells and polygonal cell morphology **(b)** minor cell damage in the peripheral area of a sample (white rectangle) with rounded, swollen cells and increased interstitial spaces.

Looking at single myofibers, their structure differs from the typical cell and therefore adopts a specific terminology. Instead of a plasma membrane and cytosol, skeletal muscle cells are surrounded by the sarcolemma, which contains the sarcoplasm. Within the sarcoplasm and adjacent to the sarcolemma are the cell's hundreds of nuclei [146, 149] (**Figure 3-8**). They form through fusion of myoblasts, muscle stem cells, during embryonic development [147, 150].

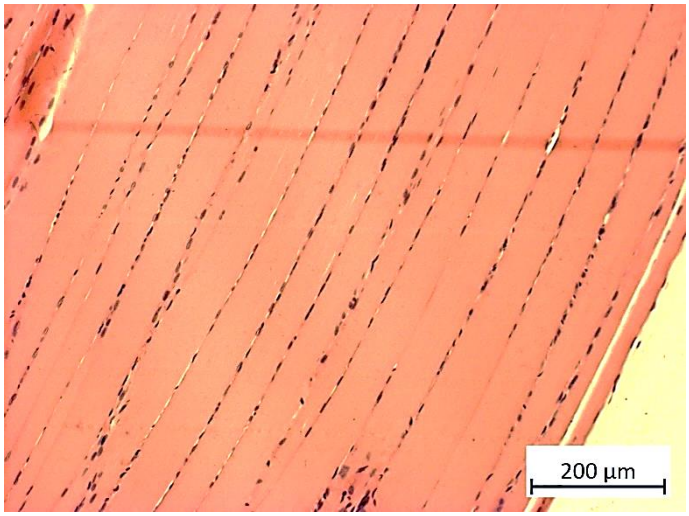

Figure 3-8: Representative control tissue (longitudinal view). Skeletal muscle fibres (pink) in dense, parallel arrangements with only few interstitial spaces; nuclei (blue) are located peripherally.

Skeletal muscle cells have a cross-striated appearance, which stems from the repetitive arrangement of the cytoskeleton. Each myofiber contains multiple rod-like myofibrils which are divided into contractile units known as sarcomeres [151]. Sarcomeres are made of long proteins organised into myofilaments. Thick filaments with a diameter of 15nm are made predominantly of myosin [146]. Thin filaments consist of bundles of actin with a diameter of 5nm [146]. The alignment of both filaments in a regular pattern causes cross-striation [151]: In dark appearing areas, known as A-bands, thin and thick filaments overlap; the lighter appearing I-bands contain only thin but no thick filaments; the Z-bands mark the end of a sarcomere where thin filaments are linked with titin and other structure-providing proteins [146, 151].

3.3.2. Contractile function of skeletal muscle

The cytoskeleton plays a crucial part in muscle function. It provides not only structure and strength to the cell, but also allows for the muscle's unique ability to contract voluntarily. Each contraction is initiated through a change in membrane potential.

When an electrical impulse from the nervous system, also known as action potential, hits the sarcolemma, it is distributed across the whole cell by a network of T-tubules. The transferred action potential triggers the release of calcium ions from the sarcoplasmic reticulum [146, 150]. This in turn activates binding sites on thin filaments, which initiates cross-bridging between the actin and myosin chains. Subsequently, the myosin heads pivot and cause a shortening in the distance between actin and myosin complexes; the muscle contracts. Once the action potential is no longer transmitted, the calcium ions in the sarcoplasm are reabsorbed by the sarcoplasmic reticulum. The active sites that allowed for the formation of actin-myosin cross-bridges are covered up. The muscle will return to its original resting length and relax.

The process of muscle contraction is powered by energy in the form of adenosine triphosphate (ATP). ATP is produced in the mitochondria of a cell, either through glycolysis (breakdown of glucose to generate energy) or oxidative phosphorylation (energy generation through electron exchange in combination with oxygen). Depending on the source of energy used during contraction, different types of muscle fibres can be differentiated [152]. Type I fibres are slow twitching fibres that are used mostly for low power endurance activities like maintaining posture. They have a high mitochondrial density and produce ATP mainly via oxidative metabolism [153]. Type I fibres therefore rely on a rich capillary supply, which together with a high myoglobin content (protein for oxygen transport) makes them appear dark red [152, 153]. Type II fibres are fast twitching fibres that are subdivided into type IIA and IIX. Type IIA fibres are fuelled by both oxidative and glycolytic metabolism, making them ideal for longer lasting, higher energy tasks like walking [153]. Like type I fibres, they have a high mitochondrial density, rich capillary supply and appear dark red [152, 153]. Conversely, type IIX fibres, which are used for explosive movements like running, use glycolysis as their main source of energy and therefore have a low mitochondrial count [153]. They also require less capillary supply and, together with their low myoglobin content, appear pale red [152, 153].

3.3.3. Muscle injury after deformation and repair mechanisms

The fibrous, highly hierarchical structure of skeletal muscle makes it prone to deformation damage like Deep Tissue Injury (DTI) [32, 154]. Globally applied loads deform the tissue, leading to local tensional strains at cell-scale [155]. These tensional

strains cause an increased permeability of the sarcolemma [156]. However, the exact cause for stretch-induced permeability is not fully understood. One possible explanation is structural damage to the cytoskeleton, where the membrane bursts under high load [154, 157, 158]. Another plausible mechanism is the activation of ion channels in the membrane like stretch-activated cation channels, calcium-specific leak channels, or growth factor-regulated channels [158].

Independent of its root, the increased sarcolemmal permeability causes an influx of ions that disturb the cell's homeostasis. To prevent severe damage, the cell has developed several strategies: It can reseal membrane lesions rapidly through intracellular vesicles, which are activated by a calcium overload, through membrane fusion, or by reducing the membrane tension [159–164]. However, if the cell fails to restore its homeostasis promptly, cell death cascades are initiated. The leaky membrane causes a significant rise in calcium ion levels within the cell, which activates cytosolic enzymes like protein kinases, phospholipases, and calpains [150, 165]. Those enzymes attack membrane lipids of cell organelles and dissemble cytoskeletal proteins. Once crucial organelles like the mitochondria are damaged, the cell is depleted of ATP, autolysis is initiated, and reactive oxygen species are released [165]. Ultimately, the cell is irreversibly damaged and inflammatory processes commence.

During inflammation, the small blood vessels supplying the muscle dilate, leading to an accumulation of exudate, known as oedema [107, 166, 167]. The neutrophils, macrophages, and lymphocytes contained in this exudate amplify the inflammatory actions. Damaged cells are broken down, liquefied, and often removed through phagocytosis (elimination by phagocytes that engulf and digest the waste) [146, 165].

Once the tissue is cleared of cellular debris, myosatellite cells are activated to start muscle regeneration. Myosatellite cells are the remnants of embryonic muscle development: While the majority of myoblasts fuse into myofibers, some remain in the periphery of the developing fibres as stem cells [146]. The activated myosatellite cells proliferate and differentiate into myoblasts [149, 150], which in turn fuse with fibres to allow for recovery [146, 150].

In general, muscle is well adapted to respond to low-level damage. The processes of membrane-resealing happen daily as they are commonly induced by exercise for example. However, its structural arrangement makes it prone to injury from severe deformation, which initiates the described three-step cycle of cell death, inflammation,

and regeneration. If the cell death rates exceed the regenerative capacities, severe tissue damage is possible.

3.4. Modelling the biomechanics of skeletal muscle

The scoping review (*Chapter 2*) identified computational modelling as a common tool in DTI and prosthetic research. Finite Element Analysis (FEA) for example is often used to integrate material mechanics into the clinical context. However, considering the complex mechanical properties and the biological adaptability of skeletal muscle, the challenges for developing a realistic computational model are two-fold: Acquiring data input on material properties from mechanical testing; and representing the mechanical behaviour in sufficiently realistic mathematical models.

3.4.1. Mechanical properties of skeletal muscle

Skeletal muscle has various mechanical properties that make its behaviour inherently difficult to predict. The tissue can be considered a composite material of cells, ground substance, and fibres, exhibiting anisotropic and viscoelastic behaviour [131]. Anisotropy means that the direction of the stress application alters the mechanical properties, caused by the arrangement of skeletal muscle tissue in a fibrous structure (**Figure 3-9**). The fibre distribution and their pennation angles (fibre direction relative to the muscle's line of action) play a role as well [168]. Viscoelasticity on the other hand presents as a combination of elastic and fluid-like characteristics. It describes the time-dependency of the mechanical behaviour, meaning that loaded tissue exhibits hysteresis, stress relaxation, and creep (**Figure 3-10**). Consequently, muscle behaviour varies depending not only on the magnitude and direction of load application but also the rate of application, duration, and whether it is of static or dynamic nature.

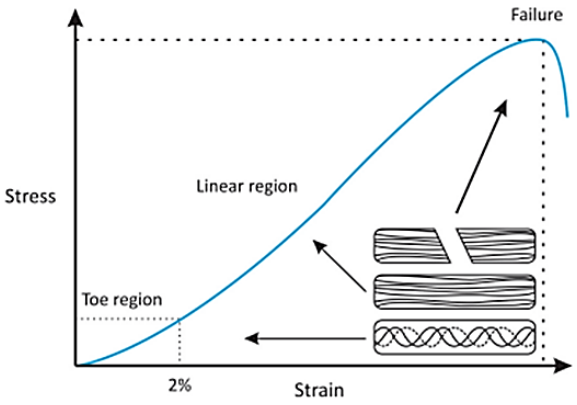

Figure 3-9: Stress-strain curve for tendon. The curve is the result of an unravelling of the fibres, their alignment along the stress direction and final failure. (Image reproduced from **[132]**, published under CC BY 3.0 license)

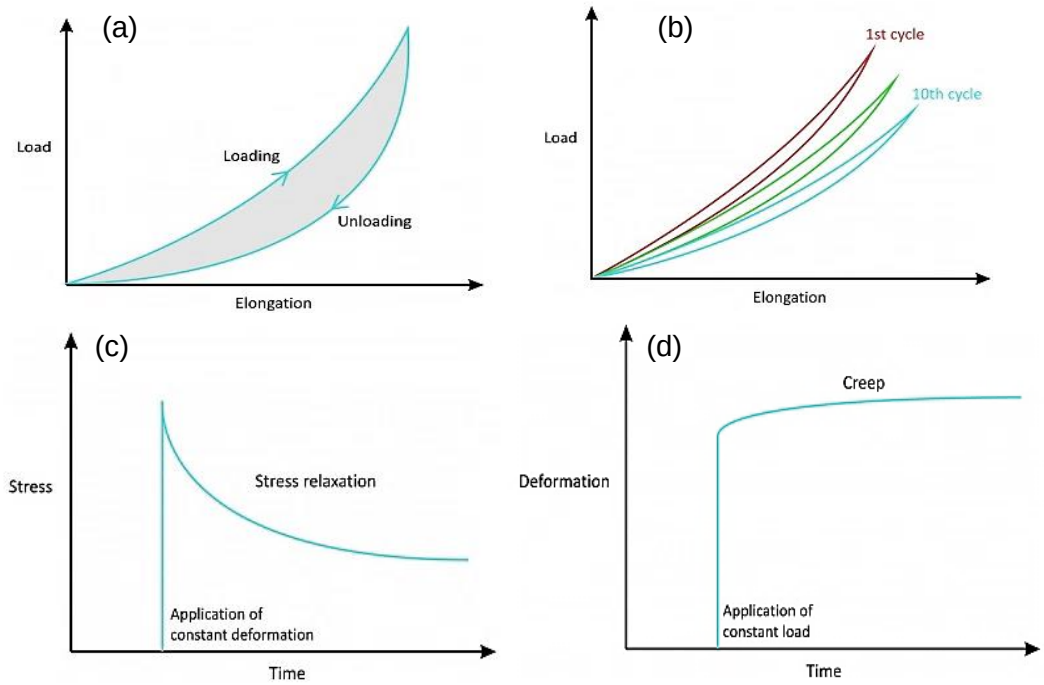

Figure 3-10: Schematic representation of muscle-specific mechanical behaviour. (a), hysteresis describing loss of energy, causing different deformation for the same stress under cyclic load application, **(b)** after several loading cycles, the muscle is "pre-conditioned" and the hysteresis curve becomes reproducible, **(c)** stress relaxation, i.e. reduction in stress, under constant deformation, **(d)** creep describing increasing deformation under constant load (Images reproduced from from **[132]**, published under CC BY 3.0 license)

Complicating computational modelling even further, skeletal muscle is a living material with physiological processes that need to be considered. For example, muscle has shown to stiffen after pressure-related damage [85, 133], which can lead to a redistribution of stress and strain within the undamaged tissue [169]. Additionally, when the tissue is subjected to fluctuating loads, which is often the case in gait-related loading scenarios, its metabolism changes [170]. Consequently, the ATP consumption increases [170], which might induce fatigue at a faster rate than monotonous stress cycles. Another challenge is the contractile ability of skeletal muscle. Besides determining the behaviour of passive muscle, including its active state and electrical stimulation adds yet another dimension [168].

3.4.2. Computational models of skeletal muscle in pressure injury and prosthetic research

Depending on whether a computational model is used for scientific or clinical applications, the accuracy of a complex skeletal muscle model needs to be weighed against computational cost. The most common concepts and parameters used to describe skeletal muscle behaviour are summarised in **Table 3-1**. The complexity of

such models increases drastically the more biophysical phenomena are included. A simple linear elastic model for example only requires two parameters while a highly complex electromechanical model that takes action-potential induced contractions into account can require up to twenty input parameters [168]. The computing power and time needed to solve these models increase accordingly.

Table 3-1: Parameters for computational modelling of skeletal muscle in pressure injury and prosthetic research.

Criterion	Explanation
Linear elasticity:	Linear stress-strain relationship; also known as Hookean model
Nonlinear elasticity:	
- Hyperelasticity	Assumption of large deformation behaviour under loading, i.e. strain-rate independent non-linear behaviour
- Viscoelasticity	Combination of elastic and viscous behaviour, i.e. integration of time-dependency (creep, stress relaxation)
- Poroelasticity	Mechanical behaviour as interaction between fluid and solid, i.e. fluid-filled fascicles surrounded by solid connective tissue
Isotropy:	
- Isotropy	Uniformity, i.e. no fibres
- Anisotropy	Different material behaviour depending on fibre direction
- Orthogonal	Type of anisotropy with three axis of symmetry that describe the fibre orientation
Compressibility:	
- Compressible	Volume change after pressure application
- Incompressible	No change in volume after pressure application
Homogeneity:	
- Homogeneous	Uniform material without irregularities
- Inhomogeneous	Irregularities in material, i.e. scar tissue

In pressure injury research, almost the complete spectrum of theories and combination of criteria can be found. This includes linear elastic [33] as well as a variety of nonlinear elastic [133, 140] and viscoelastic models [27, 171], isotropic behaviour [27, 29], tissue homogeneity [27, 133, 140, 171], and the addition of damage laws [133, 171]. Similarly, Dickinson et al. [38] found a variety of models and parameters in the literature to describe the behaviour of skeletal muscle in residual limbs, including isotropy, linear elasticity, viscoelasticity, and homogeneity. Additionally, Ramasamy et al. [135] recently modelled inhomogeneous fibre alignment and distribution based on Diffusion Tensor MRI images of a residual limb,

which could allow for the integration of inhomogeneous, anisotropic muscle behaviour.

To summarise, computational modelling of skeletal muscle provides a crucial link between experimental and clinical work. The largest obstacle is thereby the vast array of material models, assumptions and parameters used in both pressure injury and prosthetic research, which makes a comparison of outcome measures between studies difficult. While choosing and clearly describing the modelling theories and parameters remains challenging, this flexibility also provides an opportunity to study the influence of single factors independently, which is often difficult in experimental settings. Additionally, the availability of open access Finite Element (FE) software like FEBio [172] can help to increase the comparability of outcome measures.

3.5. Threshold levels in prosthetic and pressure injury research

Although pressure has been identified as the initiating factor for tissue damage like DTI, not every pressure application leads to irreversible damage of soft tissues. According to the physical stress theory, the transfer between different levels of tissue adaption and death is marked by threshold levels [63] (*"2.1.3 Physical Stress Theory"*). Defining these threshold levels is as desirable in pressure injury research as it is in prosthetic practice: If we know under which conditions the cells and tissues cross the threshold between injury and death, we can identify and predict these scenarios before they occur and therefore potentially prevent tissue damage altogether. The following paragraphs will summarise and discuss the most relevant thresholds and techniques currently used in prosthetic and pressure injury research.

3.5.1. Pressure-pain tolerance thresholds

To assess the fit of a prosthetic socket, the pressure level at the residuum is often gauged. For example, a widely used design concept, the Patellar Tendon Bearing (PTB) socket, divides the residuum into pressure tolerant and pressure sensitive areas [173]. While tolerant areas are actively loaded through indentations into the socket wall, pressure is released from sensitive areas by removing material.

The classification into "tolerant" and "sensitive" areas suggests a close relation between pressure and the sensations associated with loading of the soft tissues. Indeed, pain is a natural protective mechanism of the body that activates when

external mechanical loads become a potential risk for tissue health. Hence, a large body of literature has explored the pressure-pain-relationship.

One measure to quantify this relationship is the definition of pressure-pain-thresholds. Through indentation tests on the residuum, an individual's pressure pain threshold (the interface pressure at which a feeling of pain sets in) as well as the pressure pain tolerance (the point at which the pain becomes unbearable) can be determined [174–176]. Alternatively, researchers have used different scales and scoring systems to classify pain, including the Visual Analogue Scale [175, 177], the Socket Comfort Score [178], the Trinity Amputation and Prosthetic Experience Scale [178], or other custom-scales [175]. These assessments revealed that the pain perception differs significantly between individuals [179] as well as between areas of the residuum [174, 177, 180]. The outcomes have been used to quantify socket designs [178, 180], verify computational socket models before fabrication [176, 181], compare different fabrication methods [175], as well as develop adaptive sockets [182].

However, the pressure-pain threshold only provides information for superficial tissue layers at the socket-tissue interface [37, 174, 176, 177, 179–181, 183]. Its relation to deep tissue deformation is missing. In general, deep tissue pain is more diffuse and difficult to localise because of a naturally lower pain function in deep compared with cutaneous tissue [179]. Consequently, the perceived pain might not reflect the severity of tissue damage [179]. This makes pain a less suitable marker to assess deep tissue deformation and potential injury.

Additionally, while tissue damage almost always manifests in pain, the opposite is not necessarily the case [179]. Pain is also a less reliable marker for individuals with sensory impairment like diabetic patients, which form a large group of transtibial amputees. Diabetic patients commonly develop neuropathies, presenting as altered sensation – either an increase or loss – because of nerve damage [184]. Last, as pain is a subjective experience, it remains difficult to define and quantify on a scientific basis, despite the efforts to verbally describe, rate, or scale the sensation. The emotional burden of distress caused by pain and discomfort should still be considered when fitting a prosthesis. However, a physiological approach to define socket fit in relation to pressure or deformation might be more objective and easier to quantify.

3.5.2. Pressure-cell death thresholds

The first physiology-based study documenting the transition between healthy and damaged skeletal muscle caused by pressure application dates back to 1942. Growth [185] observed that the magnitude and duration of pressure application influence the development of muscle damage in rabbits. This was further quantified in animal studies by Husain [186] and Kosiak [187], who proposed an inverse relationship between the magnitude and duration of interface pressure application in relation to muscle damage. With the clinical observations by Roger and Reswick [188] in 1976, the first human-based pressure injury threshold curve was introduced. The researchers proposed an exponential function, also known as Roger-Reswick-Curve (**Figure 3-11**), as measure for a critical pressure-time-threshold. Despite the limited translatability of the absolute values of this pressure-time-threshold, it has since been used as a quantitative benchmark in clinical policies and product development [189].

Over the next decades, research efforts into DTI revealed that tissue deformation as opposed to interface pressure is responsible for damage formation. The relevance of the inverse pressure-time relationship for short time frames (< 3hr) was also debated. To address these developments, the short-term response of skeletal muscle was studied following a hierarchical approach [61]. Researchers used new *in vitro* models, ranging from single cells [157, 190, 191], over cell constructs [154, 192, 193] to bioartificial muscle constructs (BAM) [33, 105, 194]. Additionally, animal models were combined with computational modelling and imaging techniques to relate data on cellular damage to internal deformation [34, 90, 91, 133, 195–198].

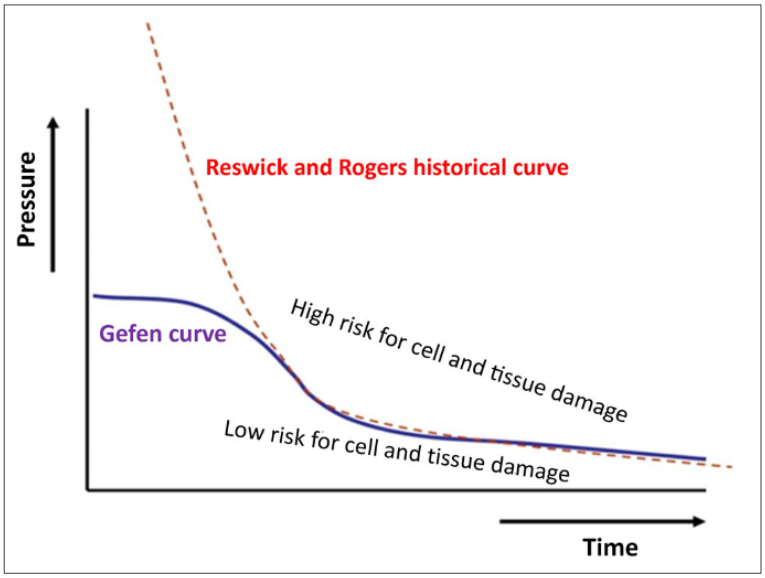

Figure 3-11: Tissue tolerance under mechanical loading. The Roger-Reswick-Curve (dotted line) defines that if the product of an applied interface pressure and the time it is applied for exceeds the critical threshold of 300mmHg x hr, tissue damage will follow. For short term pressure application, the pressure magnitude leading to damage becomes infinitely large. For increasingly longer time frames, the tolerable pressure becomes infinitely small. For these extremes, Linder-Ganz et al. and Gefen et al. proposed a refinement, leading to an adjusted sigmoid injury curve *(solid line, Gefen curve)*. Care needs to be taken when interpreting the graph as it combines three inherently different studies and mechanical loading-related units: Roger and Reswick **[188]** measured interface pressure between the human body and hospital beds; Linder-Ganz et al. **[34]** calculated principal compressive stress within skeletal muscle tissue caused by indentation and used it interchangeably with interface pressure between indenter and muscle; and Gefen et al. **[33]** measured relative deformation in bioartificial muscle constructs following indentation. The notable differences in subjects, methodology, and measurement make a direct overlap of threshold curves as presented in this image difficult. Nevertheless, the focus is on the sigmoid shape of the newly developed threshold curve in comparison to the Roger-Reswick graph. (Image reproduced from **[26]** published under CC BY-NC 4.0 license)

3.5.2.1. Compressive pressure and strain thresholds for static loading scenarios

Most notable are studies by Linder-Ganz et al. [34] and Gefen et al. [33] who both proposed a sigmoid threshold curve rather than a hyperbolic function (**Figure 3-11**). Linder-Ganz et al. [34] found that pressures of >32kPa cause structural damage of skeletal muscle in rat hindlimbs in less than an hour; for extended periods of >2h this pressure tolerance level declines to 9kPa. Similarly, Gefen et al. [33] discovered that BAM can withstand compressive strains of up to 65% for 1h and 40% for up to 4.75h. While limitations in the methodology restrict the direct applicability of these quantitative values to clinical settings, the studies mark a significant step towards the predictability of DTI and provided the basis for a variety of patient-centred studies [30, 76, 89].

3.5.2.2. Shear strain thresholds for static loading scenarios

The described research on cell-death thresholds levels focused on sustained compression. However, shear strain also needs to be considered as external pressure application causes distortion of deeper tissues ("*3.1.2 Fundamentals of mechanical load"*), particularly if the pressure distribution is non uniform. Ceelen et al. [198] and Loerakker et al. [91] addressed this topic in their combined MRI and computational modelling-based animal studies. They demonstrated that shear strain and shear strain energy have a linear relationship to deep tissue damage and observed that damage only arises after a threshold level is reached. These damage thresholds were identified as a maximum shear strain of 0.75 [mm/mm], a strain energy of 0.45 [J/mm], a strain energy density of 6-7kPa [91, 198]. However, these values are not universal but vary between individuals. Additionally, a recent MRI study by Traa et al. [199] challenged the existence of a clear threshold level but proposed a transition zone between low and high risk for damage instead. Further research using shear forces instead of compressive forces could help to elucidate the contribution of each component to skeletal muscle injury.

3.5.2.3. Thresholds for dynamic loading scenarios

While static loading scenarios are relevant for many pressure injury cases, the biomechanical environment at the residual limb is dominated by cyclic, repetitive loading. This is similar to the field of diabetic foot ulcers, where the repeated application of moderate pressure during gait promotes tissue injury [200, 201]. The soft tissues at the diabetic heel however differ fundamentally from the muscles found at the residual limb regarding their mechanical properties, vascular supply, and their neuropathic status [202, 203]. Nevertheless, researchers hypothesised a negative effect of dynamic loading on bone and muscle precursor cells when the load is sufficiently high or applied for a long time [204, 205]. Low level cyclic stress on the other hand appears to strengthen cells against compressive damage as the cytoskeleton remodels [205].

Despite these increased research efforts on the mechanobiology of pressure-related soft tissue injury, the effect of dynamic loading, particularly in the context of prosthetic use, is still largely unknown. This is surprising, considering that as far back as 1972, an initiative by the Committee on Prosthetic Research and Development pointed at the need for a more comprehensive understanding of the influence of dynamic loading

scenarios on soft tissue [35]. However, to the author's knowledge, no threshold studies on the relationship between skeletal muscle damage and repetitive deformation exist.

3.5.3. Closing pressures for the vascular and lymphatic system

Besides direct deformation damage to cells, other determinants relating to the vascular and lymphatic system have been proposed to identify threshold levels. A variable often quoted in ischaemia research is the critical capillary closing pressure. It is the pressure needed to cause a collapse of capillaries, and traditionally equivalent to an interface pressure of 32mmHg or 4.3kPa [206, 207]. While this value is still commonly promoted [208], its applicability in a clinical context has been challenged. The critical pressure is dependent on local pressure gradients. As the traditional value was established at the epidermis of the fingers, an interface pressure of 4.3kPa is unrepresentative of internal loading conditions. Moreover, the closing pressure varies significantly between subjects [209] and is based on healthy individuals, therefore ignoring the effects of pathophysiological changes [58] i.e. caused by diabetes. Researchers also found that adding a shear component to the compressive load reduces the critical closing pressure significantly, making even physiological strain levels potentially dangerous [100, 101, 210]. The clinical relevance of the established capillary closure pressure is therefore debatable.

Like the vasculature, the lymphatic system is also susceptible to pressure damage. Gray et al. [111] found that an interface pressure of 8kPa can occlude lymphatic flow in the human forearm. This threshold might be lowered with impaired vascularisation and subsequent reperfusion [113]. Additionally, toxic biowastes might build up, which can render muscle cells more susceptible to deformation damage [112]. However, the shortage in information on the role of the lymphatic system in DTI development requires further research.

3.5.4. Threshold levels as the "holy grail"

So far, this chapter has demonstrated that several studies have attempted to define threshold levels that quantify the transition from healthy to damaged tissue with varying degrees of success and clinical relevance. But is this quest for threshold levels, potentially even finding "the" threshold level, the right way to predict DTI?

The idea of a “holy grail” of threshold levels might be misleading. First, externally applied pressure triggers many processes on the macro-, meso-, and microscale. This explains the variety of thresholds proposed in the literature ranging from clinically oriented pressure-pain thresholds to the physiology-based relationship of pressure and cell death. Naturally, the units and magnitudes of these proposed thresholds are all different. Choosing a single, most relevant threshold is therefore almost impossible.

When looking at the methodologies of threshold studies, the way that tissue damage is measured also varies significantly, even within the same threshold category. Direct damage to cells for example has been defined as a loss of cross-striation in skeletal muscle [34, 195, 211], a change in cell morphology [154], a change in metabolic activity [105], as well as through the uptake of different membrane-impermeable fluorescent dyes [33, 156, 193, 194, 212]. Consequently, comparing outcomes even between experiments that measure the same parameter is difficult.

Pressure-related damage is also not necessarily harmful. Our bodies have the inherent ability to repair cellular damage, and obvious injury only occurs when the damage rate exceeds the repair capabilities. Thus, factors that impair an individual’s ability to restore homeostasis like co-morbidities and medication also influence the individual threshold levels for DTI development.

Even though defining “the” pressure threshold is a mere idealistic vision, the strive to define damage thresholds is nonetheless important. By searching for threshold values and trying to quantify the biological response of tissue to mechanical loading, our understanding of the aetiology of DTI has improved greatly over the last two decades. It not only helped to determine direct deformation, ischaemia, reperfusion, and an impaired lymphatic system as the main drivers of DTI, but also to differentiate the order and time course over which these processes orchestrate cell death (**Figure 3-12**).

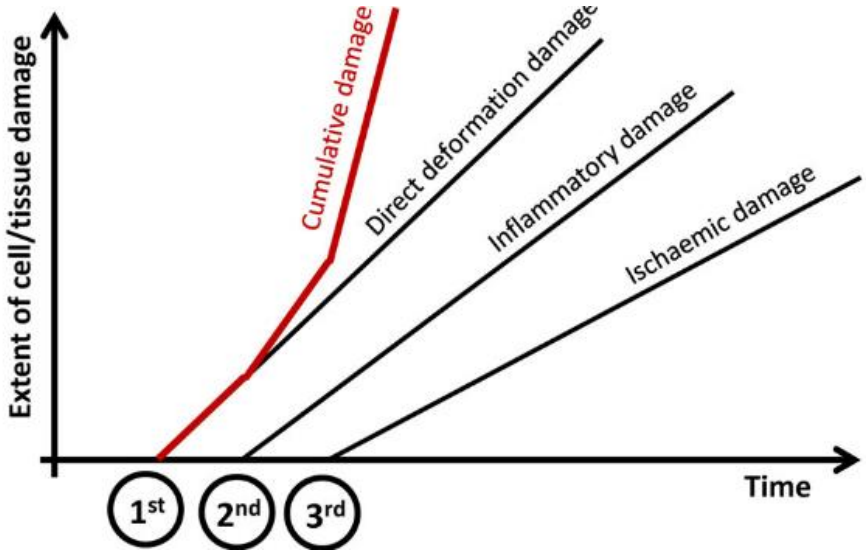

Figure 3-12: Time course of the three major contributors to mechanically induced tissue damage. Deformation, inflammation, and ischemia (Image reproduced from [26], published under CC BY-NC 4.0 license)

Threshold-based research also allows to compare the influence of single parameters, like the effect of time, magnitude, or direction of pressure application on cellular integrity. Consequently, high-risk situations can be identified more easily in clinical and every-day settings. With this improved understanding of individual aetiological factors, recent research endeavours worked on combining respective markers to predict, define, and monitor the status of soft tissues more accurately [199, 213–216]. In the future, these multifactorial marker arrays could be tailored towards risk groups and enhance the measurement accuracy even further. This is an exciting move towards scientifically based clinical practice and translating theoretical, experimental research from the bench to the bedside.

3.6. Skeletal muscle models for mechanical stress studies

The cell death cascade following excessive, sustained mechanical loading is triggered by direct deformation. It therefore seems logical to focus on this damage pathway first when trying to understand how prosthesis-related loading damages skeletal muscle. However, singling out this factor in human studies is almost impossible because every pressure application will also affect the vascular and lymphatic system. Instead, model systems are need.

Similar to the hierarchical development of DTI [56, 217], muscle damage mechanisms can be investigated on different levels (**Figure 3-13**). Starting with the micro-scale, the response of single cells and monolayers to mechanical loading has been explored

[112, 157, 190, 191, 212, 218]. By increasing the model complexity to basic cell constructs [154, 193] and BAM [33, 105, 219], the meso-scale response has been documented as well. On the macro-scale, researchers induced DTI on murine models before recording cellular damage [34, 194, 195].

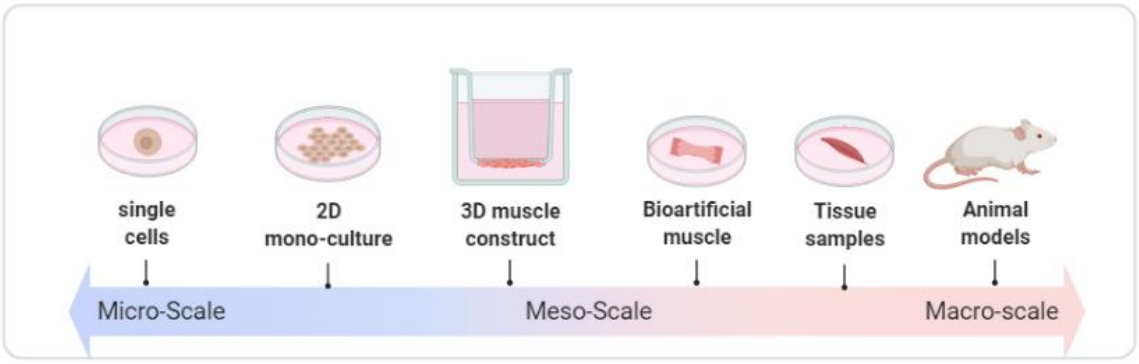

Figure 3-13: Complexity of experimental studies on Deep Tissue Injury from micro- to macro-scale.

3.6.1. *In vitro* studies on deep tissue injuries

Two of the perhaps most influential studies on DTI aetiology were conducted by Linder-Ganz et al. [34] and Gefen et al. [33]. As described in *"3.3.2 Pressure-cell death thresholds"*, they identified a sigmoid pressure and strain-cell death threshold curve for static loading in rat hindlimbs and BAM. From a methodological point of view, both studies have their advantages and disadvantages.

In vitro studies like by Gefen et al. provide a highly controllable environment that allows to investigate the influence of mechanical deformation as an isolated factor. Additionally, the variability between different muscle constructs is low [33], as are ethical hurdles for experiments with cell lines. However, premature cell development and a limited hierarchical structures lead to morphological and functional deficiencies [220–222], which can impact on the mechanical loading response [212]. The dense superficial layers of BAM also limit the transport of oxygen and nutrients, often causing a hypoxic core [194]. These hypoxic areas are not only unsuitable for analysis, but they can affect the surrounding cellular community through apoptosis-related communication [223]. BAM are also sensitive to distortion, exhibiting damage from impact shocks like transferring samples [194]. This could be a major drawback for experimental setups that require frequent handling. Regarding the setup, the way

BAM are grown in a Petri dish also lends itself to compression and shear loading experiments, whereas tensile arrangements are difficult to realise.

3.6.2. *In vivo* animal models for deep tissue injury

In vivo animal models on the other hand provide a fully developed muscle structure with a variety of cell types. Rodents in particular have a similar wound development as humans [224], making them ideal candidates for pressure injury modelling. An intact vascular and lymphatic supply and drainage allow long-term experiments in a live environment. However, this complex system makes it difficult to observe deformation as an individual damage mechanism. An external load application will not only influence the muscle cells, but all organisational levels in its vicinity [225], potentially causing ischaemic, reperfusion, and inflammatory damage. Additionally, anaesthetics delivered before experimental procedures can influence physiological processes [226, 227]. The generated results are often difficult to interpret because of the natural biological variability between animals [211]. Ethical hurdles for research on live animals are also high with Home Office licences required in the UK. The attachment of the muscle to the body also restricts the loading conditions that can be tested.

3.6.3. *Ex vivo* animal models for mechanically induced skeletal muscle damage

To minimise the drawbacks of *in vivo* animal studies, fields outside of pressure injury research like myopathic [228–231] and exercise-related research [232–235] commonly resort to *ex vivo* animal models. Isolated muscle tissue has a fully developed hierarchical structure and can be mechanically loaded without other structures being involved. Ethical approval for working with *ex vivo* tissue is also comparably easy to obtain. Nevertheless, high biological variability remains problematic. Additionally, the time frame for experimental work is defined by the tissue's limited lifespan once removed from the body, as oxygen and nutrient supplies as well as waste transport systems are no longer functioning. While the body fluids surrounding native muscle tissue can be mimicked to some extent, keeping the maximum duration of experiments to 3-4h is advisable to avoid irreversible ischemic damage and rigor mortis [236–239].

Taken together, the pros and cons of different skeletal muscle models need to be considered when setting up an experiment on the influence of prosthesis-related loading on skeletal muscle. While *in vitro* models allow for parametric studies, *in vivo* models provide the natural physiological environment that allows to observe the response across all organisational levels. *Ex vivo* studies balance some advantages and disadvantages of both other approaches, despite not being used for pressure injury research yet. Nevertheless, independent of the choice of model, it is important to keep model-related shortcomings in mind when interpreting data and building bridges to clinical situations.

3.7. Ways of detecting cell damage

Just like the choice of a model system, there are numerous ways to assess skeletal muscle damage, as mentioned in "*3.5.4 Threshold levels as the "holy grail"*. The basics of the most common methodological approaches will be discussed in the following paragraphs.

3.7.1. Histological staining in pressure injury research

Sarcolemmal damage is often assessed through optical imaging. With the aid of stains or dyes, one can visualise structures and physiological processes indicative of the cell's stress response to mechanical loading or highlight dead cells (**Table 3-2**).

The most widely used approach to gain information on the microanatomy of tissue is through histological stains. These bind selectively to the structure of interest in a cell and change its light absorption properties [240], making it visible for microscopic imaging. For histology, tissue processing is necessary. Samples need to be preserved (fixed) to halt the degradation process and cut into thin sections. The muscle is typically either snap-frozen for cryosectioning or formalin-fixed and paraffin embedded (FFPE) before being cut on a microtome.

A routine staining combination is haematoxylin and eosin (H&E) (**Table 3-2**). The oxidation product of haematoxylin, named haematin, stains nuclei blue, whereas eosin makes the cytoplasm appear red (**Figure 3-6, Figure 3-8**). Transverse tissue slices can therefore be assessed for their staining intensity, cellular and nuclear distribution, and cell shape and arrangement. Alternatively, damaged cells might exhibit a loss of cross-striation in longitudinal view when stained with Toluidine Blue,

Phosphotungstic acid haematoxylin (PTAH), or Gomorri's trichrome. These results are often described qualitatively, but semi-quantitative assessments are also possible, where the severity of the damage is rated subjectively, based on selected criteria [241, 242].

Table 3-2: Overview of optical imaging studies in pressure injury research.

	Reference	Histology and fluorescent staining			Definition of cellular damage
		Sample	**Fixation**	**Stain**	
Colourimetric assays (microscopy)	[90, 133, 154, 186, 187, 192]	Single cells, Skeletal muscle tissue	Formalin, Bouin's, Paraform-aldehyde, Cryo-sectioning	Haematoxylin and Eosin	nuclear pyknosis (increased density of nuclei), infiltration of inflammatory cells, centralised nuclei, fragmentation, increased interstitial spaces, hypertrophy, irregular cell shape, intense staining of damaged cells
	[133, 195, 197]	Skeletal muscle tissue	Bodian's fluid, Formalin	Toluidine Blue	loss of cross-striation, infiltration of inflammatory cells, centralised nuclei, increased interstitial spaces, irregular cell shape, disorganised internal structure
	[34, 133]	Skeletal muscle tissue	Formalin	PTAH	Loss of cross-striation
	[187, 196]	Skeletal muscle tissue	Bouin's solution, Formalin	Gomorri's Trichrome	Loss of cross-striation, infiltration of inflammatory cells, reduced staining of dead cells
	[192]	Single cells	NA	Trypan blue	Staining of membrane impaired cells
Spectrofluorometric assays and pH	[105]	BAM	NA	MTT assay	Indirect measurement: Strong colour indicates high metabolic activity
	[105]	BAM	NA	LDH assay	Indirect measurement: Strong colour indicates active transport capabilities of cells
	[105]	Medium around BAM	NA	Metabolic activity (glucose, lactate, pH)	Indirect measurements: high absorbance of reagents indicative of high metabolic activity
Fluorescence assays	[33, 112, 157, 192–194, 212]	Single cells, BAM	NA, Paraform-aldehyde	Propidium Iodide	Staining of membrane impaired, apoptotic cells (live cell staining); nuclear pyknosis (fixed cell staining)
	[194]	BAM	NA	YO-PRO-1	Staining of membrane impaired, necrotic cells
	[192]	Single cells	NA	Ethidium homodimer-1	Staining of membrane impaired cells

3.7.2. Metabolic assays in pressure injury research

Another option is to test the extent of healthy cellular function as an indirect measure for cellular damage. Gawlitta et al. [105] used an MTT assay that measures the reduction of tetrazolium salt by active cells, in combination with the release of lactate

dehydrogenase (LDH) by damaged cells to evaluate cell viability. This was supported by assays measuring physiological activity like glucose, lactate, and pH levels in the culture medium. A multifactorial setup of this kind that combines different assays can help to single out the effect of individual factors of pressure injury development on cells.

3.7.3. Fluorescence imaging of skeletal muscle damage

Fluorescence imaging is another powerful tool for the optical assessment of biological processes within cells and tissues that would otherwise be inaccessible. Researchers used fluorescent staining to investigate the effect of physical stress on the permeability of the cellular membrane [156], on intracellular calcium changes [243], on the diffusion of macromolecules [141], and on cell death development [33].

In general, the potential for microscopic imaging to provide high quality data for biological and physiological research is growing constantly. The two major drivers are advances of imaging equipment, be it fluorescence-based or complementary techniques, and the increased availability of (open-source) analysis software, like ImageJ [244] and CellProfiler [245].

3.7.3.1. Basic principles of fluorescence imaging

For successful fluorescent staining and imaging, it is helpful to understand the underlying principles. Light is characterised by its wavelength: short wavelengths (ultraviolet or blue) have higher energy compared with longer wavelengths (red). During fluorescence imaging, the sample is excited with a wavelength characteristic for the fluorescence marker of interest. The incoming light energy (a photon) is absorbed by the substrate. This excitation energy causes a short-term transition of the molecules to a higher electronic state [246]. Upon return to the ground state, the energy is released as an emission photon. Between the excitation and emission process, energy is partly lost through vibration or heat so the emission wavelength is lower than the excitation wavelength (**Figure 3-14**) [247]. The wavelength of the emitted photon can then be detected by the microscope with appropriate filters.

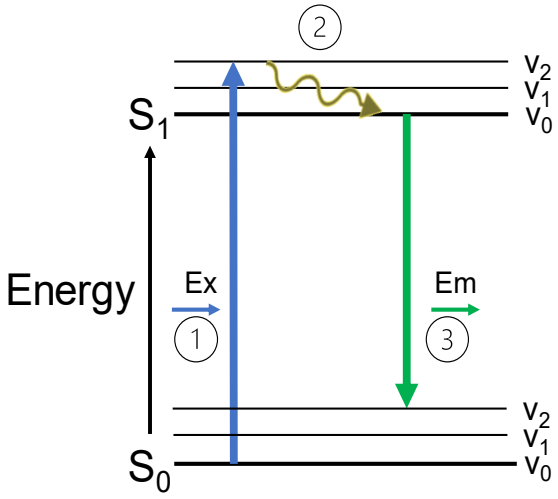

Figure 3-14: Perrin-Jablonski Diagram of fluorescence. Jablonski diagram illustrates excited states of a molecule and transitions between them (1) Light excitation with short wavelength (blue) delivers high-energy photon. This causes an electron in the target molecule to move from its ground electronic state S0 to a higher electronic state S1, often with increased vibrational energy v2. (2) Vibrational relaxation reduces the energy to S1, v = 0. (3) The remaining energy additional energy is emitted as the electron moves back to ground state S0, often with increased vibrational energy v2. The resulting wavelength is lower than that of the incoming light.

3.7.3.2. Equipment for fluorescence microscopy

The standard equipment for fluorescence imaging is an epifluorescence microscope, which can be found in most commercial laboratories and imaging facilities. This microscope illuminates the full thickness of a sample. However, light from a fluorescence probe might be reflected, diffracted (spread around an object), or refracted (redirected caused by a change in medium) as it passes through the sample, making a clear identification of the signal's origin difficult [248]. With this out-of-focus light potentially obstructing the real fluorescence signal [247, 248], epifluorescence microscopy is most useful for imaging single cell layers. To gain information on thicker samples, additional processing is often necessary to prepare thin tissue slices.

An alternative is confocal imaging. Confocal microscopes create three-dimensional maps of the stain's distribution within a sample. After scanning the specimen at specified intervals, the created 2D images are combined to a 3D stack. The specimen is thereby imaged at a specific depth rather than the whole sample at once, keeping background scattering and out-of-focus signal to a minimum. Nevertheless, the capabilities of confocal microscopy are still restricted. The scanning speed is often slow, leading to a low temporal resolution; reflection, diffraction, and refraction reduce the signal-to-noise ratio; and the spatial resolution is often limited [249].

Beyond the standard equipment, other advanced microscopes have been developed [246, 250] that address some drawbacks of confocal microscopy. Multiphoton fluorescence imaging uses two (or more) rather than one photon in the Near Infrared

(NIR) spectrum to excite fluorescence molecules. Both photons thereby arrive simultaneously, and their sum energy is equal to the energy needed for the transmission from the ground to the excited state (**Figure 3-15**) [246, 247]. By using a lower wavelength light source, scattering effects are lessened, which in turn allows for a deeper light penetration [251].

A similar approach yet without the need for fluorescence probes is second-harmonic imaging (**Figure 3-15**). This label-free technique can visualise non-centrosymmetric structures (no point of symmetry through which the structure could be "inverted") such as collagen and myosin. On interaction with light, these structures return a signal that is exactly half the wavelength of the entering light [252]. Researchers used this phenomenon to visualise structural features of different tissues, for example muscle cross-striation [253] or fibrosis following myocardial infarction [254]. The advantage is hereby that photobleaching and phototoxicity effects are avoided.

Besides the two alternative techniques explained here, numerous other microscopy techniques have been developed and applied to biological research over the last decades, like super-resolution microscopes [247]. However, their use is often restricted to advanced imaging and research facilities [246]. The focus of this thesis is therefore on the more commonly available equipment and techniques.

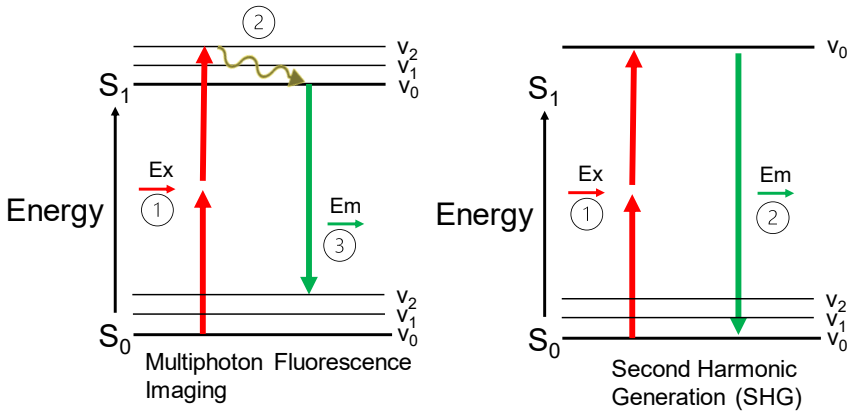

Figure 3-15: Perrin-Jablonski Diagram of multiphoton imaging. Multiphoton fluorescence imaging relies on two simultaneously delivered NIR signals (1) that excite the fluorescence probe to the transition stage. After vibrational relaxation (2) a longer wavelength photon is emitted (3). Second harmonic generation visualises non-centrosymmetric structures like collagen without fluorescence labelling. These structures return the incoming light (1) at exactly half the incoming wavelength (2).

3.7.3.3. Introduction to fluorescent stains and autofluorescence

To introduce fluorescence to a sample, it is stained with naturally fluorescence proteins or synthetic dyes that attach to a molecule of interest. By targeting combinations of excitation and emission wavelengths specific to the dye of choice, structures and biological processes within the sample can be visualised.

However, samples also commonly display natural fluorescence behaviour, also known as autofluorescence. These signals can arise from endogenous or exogenous sources, like red blood cells, collagen in the extracellular matrix, or formaldehyde fixation. The majority of samples respond to short wavelength stimulation, leading to blue or green emissions [255]. Indeed, skeletal muscle tissue reportedly fluoresces strongly in the green spectrum [256]. The resulting non-specific background might interfere with the fluorescence signal of interest, making analysis difficult.

Unfortunately, autofluorescence is difficult to prevent. Potential options include chemical quenching, i.e. with Sudan Black B staining [257–259], and photobleaching [258], where the sample is exposed to high irradiation to degrade the fluorescence structures. However, ideally, spectral overlaps between the fluorescent stain and autofluorescence of the sample should be avoided by careful choice of the fluorescent stain.

3.7.3.4. Fluorescent staining in pressure injury research

In pressure injury research, fluorescent staining has so far been used mainly for live-cell imaging (**Table 3-2**). Propidium iodide (PI) is thereby a popular stain. It penetrates cells with increased membrane permeability and binds to the DNA, making it a useful marker for necrosis. With increased cellular permeability being a major injury mechanism in DTI development [154, 156], membrane impermeable dyes in general are the most relevant type of live/dead stain for pressure injury research. The staining process is performed on live cells or BAM and can be viewed under a confocal microscope without further processing.

3.7.3.5. Fluorescence imaging for skeletal muscle damage

Outside of the field of pressure injury research, fixable viability stains have been used. During the fixation process, common fluorescent stains might be quenched by the chemicals in use. Fixation also makes cell membranes permeable, potentially causing

cross-over of dyes to previously intact cells. Fixable stains have been developed to avoid those issues. They bind covalently to the structures of interest, which allows them to be preserved beyond fixation.

A common family of fixable stains used in skeletal muscle research is Procion dyes. Originally a fabric dye, Procion orange is the most popular one. It has a low molecular weight and accumulates in the cytosol of structurally compromised cells. Hence, Procion orange has been used to visualise sarcolemmal damage following exercise or myopathic disease [229, 230, 260–265]. The stain can either be administered intravenously to an *in vivo* animal model [266], or the muscle sample is submerged in it before fixation [263, 264, 267]. Tissue slices can then be assessed under an epifluorescence microscope.

Another type of fixable stain are amine-reactive dyes. Intracellular proteins have free amines that these membrane impermeable stains bond to in damaged cells. The stains are available from a range of suppliers, including Alexa Fluor Dyes (ThermoFisher), Live-or-Dye (Biotium), and Zombie Dyes (BioLegend). Zombie for example has been used to detect dead cells from skeletal muscle cell suspensions and in myotubes [268–270].

Besides fixable stains, Evans blue is commonly used in skeletal muscle research. This membrane impermeable stain is not chemically fixable but compatible with cryofixation [271]. Like Procion dyes, it can either be injected [271–273] or samples submerged in Evans blue solution to label injured myofibers [271]. The stain thereby binds to albumin and can enter membrane-impaired cells [274]. Once stained, the tissue can either be homogenised (mechanical and/or chemical separation of tissue into cells in solution) and analysed on a microplate reader [271, 272], or cryosectioned to image with an epifluorescence microscope [271–273].

Overall, many live/dead stains are available. The choice of a suitable one depends on the working principle, the available equipment, and favoured administration and processing techniques. The resulting quantitative cell death measurements are particularly valuable in comparative studies.

3.8. Chapter summary

This chapter covered the basic anatomy, physiology, and biomechanics of skeletal muscle. On this foundation, the most common techniques to define threshold levels

in prosthetic and pressure injury research were discussed, ranging from clinical over physiological to imaging-based and functional studies. A few difficulties with research on mechanical loading of soft tissues emerged in the process: quantifying processes in the largely inaccessible deep muscle tissue; clearly distinguishing overlapping physiological processes; drawing generally valid conclusions from parametric studies; and relating laboratory results to the clinical environment, to name a few. Nevertheless, each study contributed to improve our understanding of DTI development.

Another point deserving attention is that the majority of the literature came from a pressure injury context. Mechanobiological research in general seems to be a largely unknown approach in prosthetics and orthotics, which is surprising, considering the unavoidable impact of mechanical loads on soft tissues during gait. As established over the last two chapters, current techniques to assess prosthetic fit seem insufficient; be it pressure-pain thresholds, which are subjective and mechanically and biologically inconclusive, or interface pressure measurements that overlook the effect of deep tissue deformation. This might be one reason neither technique is routinely used in a clinical environment. Instead, clinical expertise and experience are still the major drivers in socket design. However, by applying pressure injury methods and ways of tissue analysis to the prosthetic context, a deeper understanding and therefore a more scientific way to assess socket fit could be created that can complement current clinical practice.

3.9. Research hypothesis and objectives

The work described in this thesis focuses on investigating and comparing the tissue response of skeletal muscle to static and cyclic loading related to transtibial prosthetic use. The following hypothesis was thereby proposed:

Cyclic loading scenarios are more damaging to skeletal muscle tissue than static loading

Considering the large impact of direct deformation on muscle health, the assessment of the structural integrity of myofibers was at the forefront of this project. By starting from the cell and tissue level, fundamental research questions on the behaviour of skeletal muscle on the micro-scale can be answered before being up-scaled to the meso- and macro-scale. The newly gained insights might make it worth revisiting

existing studies, some of which have been described in *Chapter 2*. Additionally, the results can inform future clinical studies and hopefully be ultimately translated into the clinical context and the ongoing process of digitalisation to improve prosthetic socket design.

Based on the research hypothesis, a number of objectives were identified to achieve the aim of investigating the influence of prosthesis-related loading on skeletal muscle health, which are discussed over the next chapters.

Objective 1: Designing an experimental setup with the potential to quantify cellular damage to skeletal muscle following mechanical loading representative of prosthetic use. (Chapter 4)

To test the influence of prosthesis-related loading on skeletal muscle, experimental work was needed. With direct deformation as main cause for mechanically induced soft tissue damage [25, 56], the experimental setup should replicate typical loading scenarios and allow to measure deformation-induced cell and tissue damage. Several model systems have been proposed in the past [33, 198, 228, 233]. By reviewing the benefits and limitations of each approach, a suitable model will be found and adapted to allow for a flexible loading setup, including static as well as dynamic scenarios. Subsequently, different processing, staining, and imaging methods will be tested to quantify sarcolemmal damage.

Objective 2: Developing a robust microscopic setup and image analysis workflow to quantify sarcolemmal damage within the skeletal muscle model. (Chapter 5)

With the experimental setup in place, important questions about sample size and data management will be answered. Additionally, image acquisition parameters for the microscope will be optimised for the samples and stain in use. Once these settings are in place, a robust analysis workflow will be developed and validated.

Objective 3: Replicating the experimental setup in computational models to estimate the loading conditions throughout the samples. (Chapter 6)

While the mechanical loads at the sample interface are easy to determine and control, internal loading conditions might differ and are difficult to detect. With computational modelling, stresses and strains can be predicted more easily. Hence, FE models will

be developed to analyse the mechanical environment within the samples during static and dynamic mechanical testing.

Objective 4: Validating the experimental setup and analysis process for a static loading scenario. (Chapter 7)

To validate the experimental setup and analysis workflow, a static compressive stress-cell death threshold will be established. The direct stress and duration times will be based on a similar study by Linder-Ganz et al. [34], who applied load to murine skeletal muscle *in vivo* with a different staining and image analysis protocol. The study will be supported by computational modelling with the previously developed FE model to estimate the internal loading conditions in relation to the direct stress application. The resulting stress-cell death threshold curve will be compared to Linder-Ganz et al.'s and other studies for validation.

Objective 5: Quantifying sarcolemmal damage in skeletal muscle in response to static and dynamic loading. (Chapter 8)

Currently, there is a gap in information on the skeletal muscle response to prosthesis-specific loading conditions [39]. The developed experimental setup will be used to quantify and compare cellular damage across three loading scenarios mimicking daily activities in the life of a prosthetic user:

(1) standing or sitting, i.e. static loading

(2) walking, i.e. low frequency dynamic loading, and

(3) running, i.e. high frequency dynamic loading.

The mechanical integrity of skeletal muscle cells following each loading protocol will be evaluated with the developed imaging analysis workflow and compared between each group. This will help to determine in how far each scenario might contribute to muscular damage development in prosthetic users.

Following the experimental studies, **Chapter 9** will explore potential alternative methodologies for future work. An overall summary, discussion, and conclusion of this project can be found in **Chapter 10**.

CHAPTER 4

Development of a method to measure cell death in skeletal muscle tissue following transverse mechanical loading

This chapter summarises the preliminary experiments for designing an experimental setup with the potential to quantify cellular damage in skeletal muscle following transverse mechanical loading representative of prosthetic use (**Objective 1**).

The ideas for the study were conceived by the author and Dr. Arjan Buis. Tissue collection and preparation were conducted by the author with initial advice and support from Dr. Mairi Sandison. Tissue staining, processing, and standard light microscopy were also performed by the author. Spectral analyses of the tissue and dyes was completed by Dr. Alastair Wark who also introduced the author to mapped epifluorescence imaging. For mechanically induced damage, the author designed static loading rigs which were 3D printed by Dr. Buis.

4.1. Introduction to biological analysis of pressure injury

4.1.1. Model system for the analysis of cell death after prosthesis-related loading

Human studies are often a crucial part of (bio)medical research. Similarly, the effect of prosthesis-loading on the soft tissues of the residuum would ideally be assessed with human participants. However, ethical hurdles for human studies are high and a well-established scientific basis is necessary to earn approval. Researchers therefore often use model systems in a first instance, which can provide the basis for further clinical investigations.

In the past, numerous model systems have been proposed for pressure injury research. They can be divided into *in vitro* and *in vivo* models, as discussed in *"3.6 Skeletal muscle models for mechanical stress studies". In vitro* models range from single cell studies to bioartificial constructs, which are characterised by a great controllability of the test environment but at the cost of a less realistic representation of real-life conditions. *In vivo* models are the opposite; experimenting with living organisms replicates the real-life scenario but at the expense of a variable environment. *Ex vivo* models lie in between, allowing both a lifelike environment and controllability up to a degree. While these types of models cannot be found in pressure injury research, they are commonly used in mechanobiological research on skeletal muscle in other areas like myopathic research.

To decide on the most suitable approach for this project, a multi-criteria decision analysis was performed (**Table 4-1**). Single cells, bioartificial muscles (BAM), *ex vivo* tissue, and *in vivo* experiments were rated based on six weighted criteria. These are, from most to least important:

(1) The representation of the morphology and physiology of skeletal muscle, i.e. its hierarchical structure, functionality, and connection to supply systems; this is important for a realistic response to deformation.

(2) The controllability of the damage mechanism, i.e. the ease to separate the cell response to direct deformation from other factors like ischemia; this is important for drawing conclusions on structural damage as an individual aetiological parameter for soft tissue damage.

(3) **The feasibility of sample preparation and testing,** i.e. the availability of equipment and expertise, as well as the effort needed to prepare the experimental setup; this is important to ensure the chosen experimental model and method are viable.

(4) **Fulfilment of 3Rs and ease of ethical procedures,** i.e. consideration of replacement, reduction, refinement as well as the potential need for ethics applications; this is important to ensure a balance between ethical approval and the resources needed for potential applications.

(5) **Low cost,** i.e. expenses for specimen, equipment, and consumables; this is important as the budget for this project was limited.

(6) **Low variability,** i.e. introduced by environmental factors or from natural biological variability; this is important to obtain meaningful, significant results.

Based on these six criteria, an *ex vivo* approach appeared to be most suitable for this project when weighted against the characteristics of *in vitro, ex vivo,* and *in vivo* models (**Table 4-1,** Appendix C). In addition to the explained criteria, an *ex vivo* setup allows for static and dynamic testing as well as different combinations of compression, tension, and shear. An *ex vivo* model is therefore easily adaptable not only for this study but also future research. A wide range of processing and imaging techniques are also available that can provide information from the sub-cellular to the tissue scale.

Table 4-1: Multi-criteria decision analysis of possible pressure injury models. Criteria selection and weighting (out of 100%) was adjusted to the proposed research question and anticipated experimental procedure; key for the scoring system of 1 - 4 for each criterion was chosen as follows: 1 = insufficient realisation of criterion, 2 = sufficient realisation of criterion, 3 = strong realisation of criterion, 4 = optimal realisation of criterion; the total for each criterion and model system was obtained through multiplication of the weight of the criterion with the value assigned to the model system; the model with the highest overall score is deemed most suitable for this study. A detailed description of how the scores were assigned can be found in Appendix C**.**

			Single Cells		**BAM**		***Ex vivo* studies**		***In vivo* studies**	
Criteria	**Example**	**Weight**	Value	Total	Value	Total	Value	Total	Value	Total
Representation of true morphology and physiology	*Hierarchical structure, functionality, blood and lymphatic support of skeletal muscle*	0,30	1	0,30	2	0,60	3	0,90	4	1,20
Controllability of damage mechanisms	*Separation of deformation-related damage from other factors*	0,20	3	0,60	3	0,60	2	0,40	1	0,20
Feasibility of preparation and testing	*Availability of equipment, training, and expertise*	0,20	3	0,60	2	0,40	3	0,60	3	0,60
Fulfilment of 3Rs and ease of ethical procedures	*3Rs: Replacement, Reduction, Refinement; Ethics application and home office licensing*	0,15	4	0,60	4	0,60	3	0,45	1	0,15
Low cost	*Expenses for specimen, equipment, consumables*	0,10	3	0,30	2	0,20	3	0,30	2	0,20
Low variability	*Environment and inter-subject variability*	0,05	4	0,20	4	0,20	2	0,10	1	0,05
Total		100%		2,6		2,6		**2,75**		2,4

4.1.2. Preliminary studies to visualise cell damage: live-cell imaging, histology, and fluorescence imaging

From the literature discussed in *"3.7 Ways of detecting cell damage"*, optical imaging appeared to be the method of choice to identify sarcolemmal damage in model systems. Based on existing mechanobiological research on skeletal muscle health, three different imaging streams were explored (**Figure 4-1**). Live-cell imaging, basic histology, and fluorescence-based histology. For successful quantification of sarcolemmal damage, the sample type, the working principle of the stains, the processing steps, and the microscopic visualisation need to be considered. Accordingly, a series of preliminary studies was proposed:

(1) Live-cell imaging with Propidium Iodide
(2) Histology with Haematoxylin and Eosin
(3) Spectral analysis of fluorescent stains and autofluorescence signal
(4) Fixed-cell imaging with membrane impermeable dyes as indication for sarcolemmal damage and therefore cell death

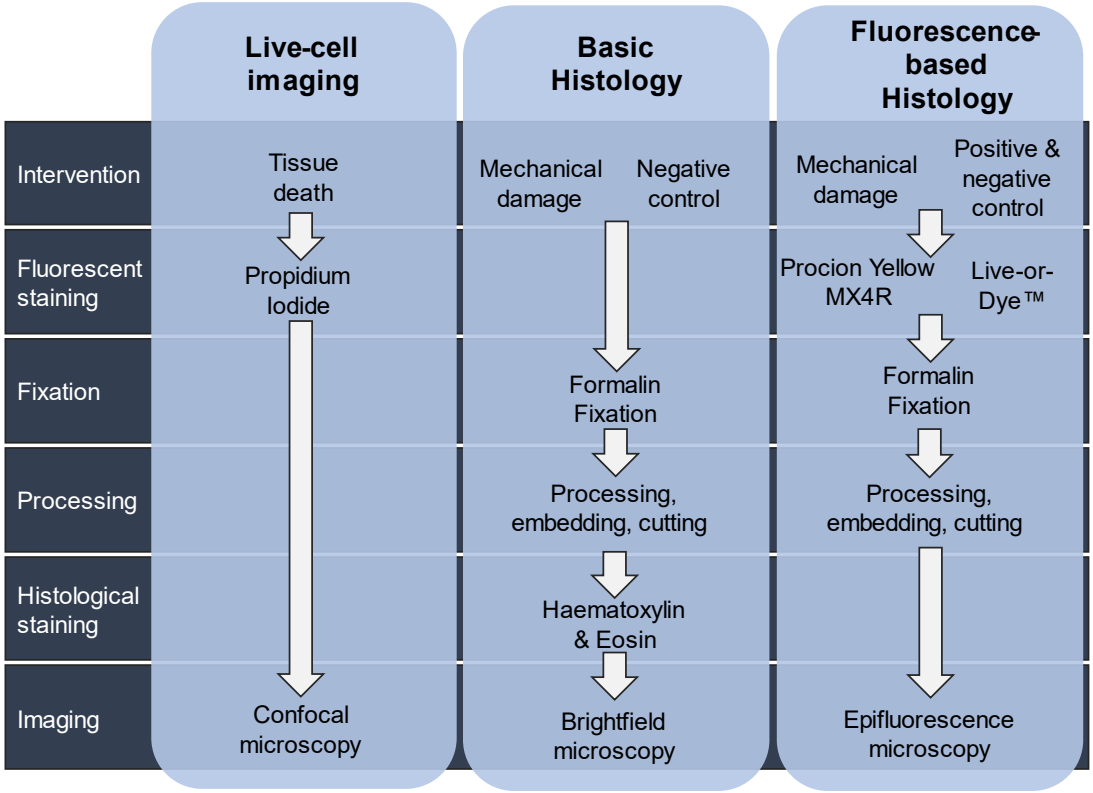

Figure 4-1: Methodological streams explored in preliminary studies.

4.2. Aims and objectives of *ex vivo* model development

Based on the decision on an *ex vivo* model system, several preliminary studies were conducted to define a method to detect and quantify cell damage from transverse mechanical loading. The focus was on an optical imaging-based method, which is widely used in pressure injury and skeletal muscle research. The objectives of these studies were to:

(1) assess suitable environmental conditions for *ex vivo* skeletal muscle experiments
(2) test appropriate tissue processing protocols
(3) identify a stain or dye to visualise cellular damage
(4) define suitable optical imaging techniques

The materials and protocols that apply to most of the *ex vivo* experiments are described first before the specifics of each preliminary experiment (**Figure 4-1**) and the results are discussed. By the end, a procedure for a new *ex vivo* pressure injury model was established to study soft tissue damage in skeletal muscle. The full description can be found in Appendix D.

4.3. General materials and methods for *ex vivo* experiments

4.3.1. Materials and solutions for *ex vivo* experiments

All experiments were performed on *ex vivo* tissue. The muscles were submerged in physiological buffer to keep them alive during the experiments. A MOPS-based buffer solution was prepared from 145 mM sodium chloride, 2mM MOPS, 4.7mM potassium chloride, 1.2mM monosodium phosphate, 1.2mM magnesium chloride, 5mM glucose, 0.2mM EDTA, 2mM sodium pyruvate, and 2mM calcium chloride, all acquired from Sigma Aldrich, St. Louis, and adjusted to pH 7.4 (Appendix D-2).

For basic as well as fluorescence-based histology, tissues were fixed in 10% neutral buffered formalin (NBF, Sigma Aldrich). For additional storage as well as further processing, Ethanol (EtOH, Fisher Scientific) was purchased, together with Histoclear (National Diagnostics), Paraffin (Raymond Fisher Scientific), and wax for embedding (BDH Laboratory Supplies Paramat). Other materials needed for processing and mounting included histology cassettes (Simport Scientific), microscope slides and

coverslips (Thermo Scientific), and DPX mountant (Sigma Aldrich). For staining, the following materials were purchased: Propidium Iodide (PI, Thermofisher) for live-cell staining; Harris' Haematoxylin, Acid Alcohol, and Eosin Y (Sigma Aldrich, St. Louis) for basic histology; and Live-or-Dye™ (Biotium) and Procion Yellow MX4R (Sigma Aldrich, St. Louis) for fluorescence-based histology.

4.3.2. Collection and preparation of murine skeletal muscle tissue

The soleus (SOL) and extensor digitorum longus (EDL) muscles were isolated from the hindlimbs of 6 – 7 weeks old male Sprague-Dawley rats (Appendix D-4) within an hour of euthanisation with an intraperitoneal overdose of sodium pentobarbital (200mg/kg). Both muscles are easy to access and dissect, have a similar size, and a low pennation angle [275]. With a low pennation angle, it is easy to achieve a consistent direction of mechanical loading in relation to the fibre orientation and to produce cross-sectional muscle slices for microscopy.

The muscles had an average mass of 0.11g (SOL) and 0.12g (EDL). Their cross-sectional diameter was approximately 2mm. According to Barclay et al. [276], oxygen diffusion in resting isolated skeletal muscle in rats can reach a radius of 1.5mm at ambient temperature. Both SOL and EDL would be small enough for sufficient oxygen supply across the full muscle when superfused with an oxygenated bathing solution, which minimises the risk of anoxia.

Following dissection, the muscles were pinned out in Petri dishes covered with medical grade silicon. This prevented fibre distortion from involuntary contractions that was otherwise observed. To enhance the viability of excised muscle tissue during the experiment, it was submerged in MOPS-based buffer solution and kept at ambient temperature (22°C). Researchers found that at this temperature, the metabolic demand of skeletal muscle is lower, functionality is preserved, and the risk of hypoxic damage in the central areas is minimised compared to physiological temperatures (37°C) [276, 277]. Nevertheless, experimental procedures should not exceed four hours to avoid ischaemic damage and rigor mortis [236–239].

All experiments were in line with the ethical guidelines of the Biological Procedures Unit at the University of Strathclyde. The 3R principles of replacement, reduction, and refinement [278] were followed wherever possible. Partial replacement was ensured

by using tissues taken from animals without conducting previous scientific experiments that could cause suffering. Reduction was also achieved by taking tissue from rats that have been assigned for other non-muscle-based research and by using four muscles per animal to minimise the number of animals. Additionally, for all indentation experiments, each muscle was divided into indentation and control areas (outside of indentation zone), which were analysed separately.

4.3.3. Mechanical loading setup

To inflict mechanical damage to skeletal muscle, an indenter was lowered onto the pinned-out samples with a custom rig. The first rig was constructed from components sourced in-house (as described in **Figure 4-2**). To increase the throughput of samples, a second design was developed with CAD software (Solidworks 2019) for 3D printing (**Figure 4-3**). Unlike the first prototype, this design was reproducible and easily customisable. The steel indenter attached to it had a flat shape with a diameter of 2mm and mass of 11g to deliver a compressive stress of at least 30kPa to the muscle. This is equal to the direct stress resulting in cellular damage after static compression for 30min [34]. Added load up to 60g was applied by adding mass on top of the indenter.

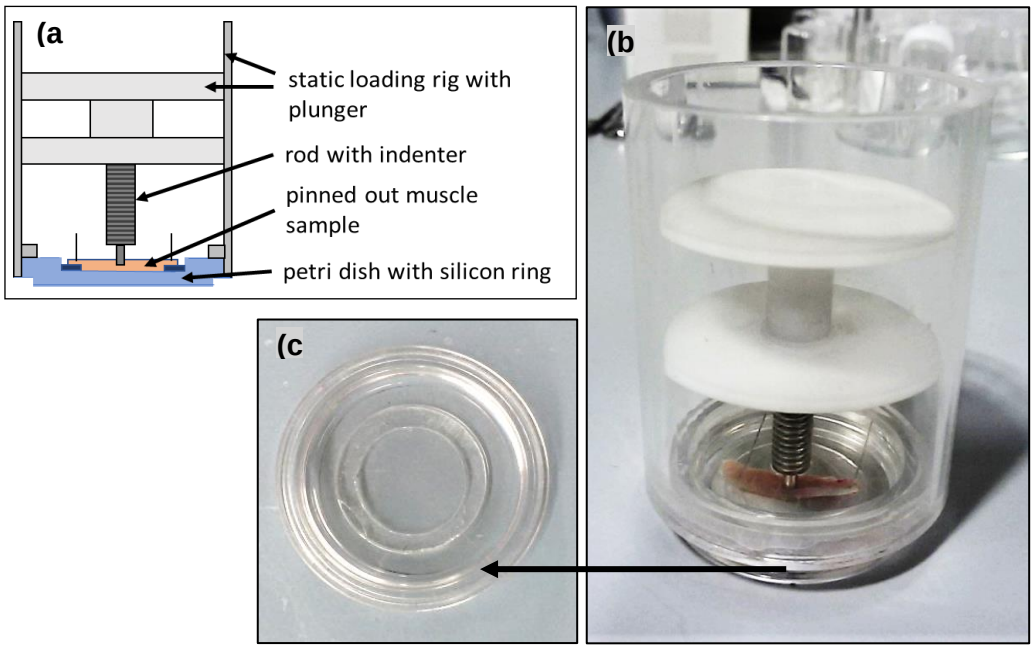

Figure 4-2: Pre-fabricated experimental setup. (a) Schematic drawing of static loading device, consisting of plastic tubing (grey), plastic plunger (white), and flat-ended round indenter (r = 1mm, black) fabricated from standard rod. The construction fits onto a standard 35mm cell culture dish (light blue) that had a thin silicone ring (dark blue) glued to the bottom to facilitate pinning of the muscle sample. **(b)** static loading device indenting isolated skeletal muscle. **(c)** Petri dish with silicon ring for fixation of specimen.

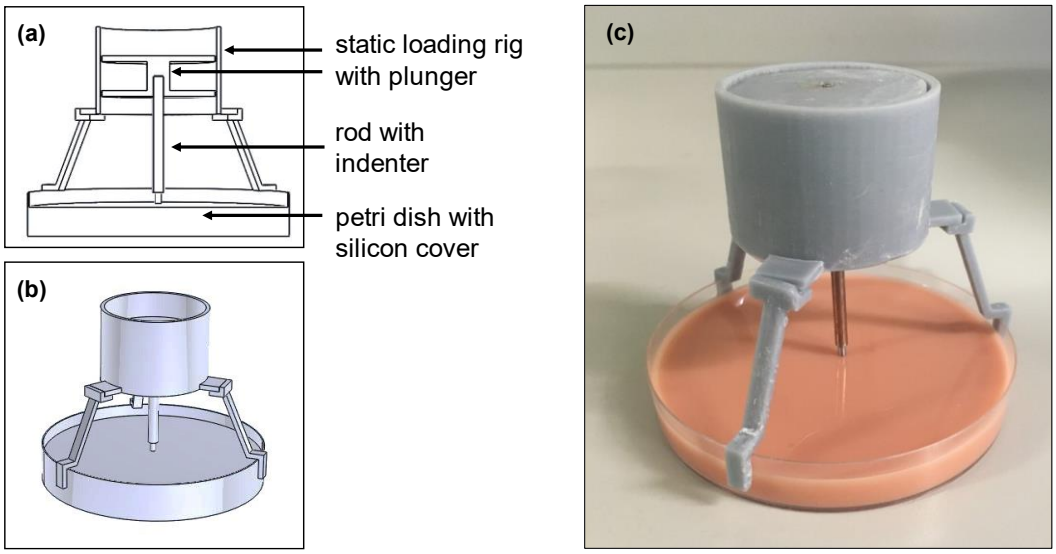

Figure 4-3: 3D-printed experimental setup. **(a)** CAD model of static loading device that allows for reproducible 3D printing and customisation. Consists of 3D-printed loading rig with plunger that has steel rod with flat-ended round indenter attached to it (r = 1mm). The construct fits on top of a standard 100mm Petri dish that was filled with medical-grade silicone to facilitate pinning of muscle specimen and prevent slipping of the sample. **(b)** Rendering of static loading device. **(c)** 3D-printed static loading setup.

Initial experiments highlighted the need to demark the indentation site; otherwise, a clear identification of the mechanically loaded area and therefore its analysis were nearly impossible, especially when only minor damage was inflicted. In literature, different ways have been described to mark histological samples. Unlike Patil et al. [279], we found that applying acrylic colour to the outside of the muscle in the indentation area led to smudging when submerged in solutions for further processing. India ink (Farber Castel) was used instead to demark the indentation site [280], making it clearly distinguishable after fixation.

4.3.4. Tissue processing through formalin fixation and paraffin embedding

Basic as well as fluorescence-based histology require further tissue processing in preparation for microscopy. Generally, histology is more compatible with formalin fixation and paraffin embedding (FFPE) than cryosectioning (cutting of frozen tissue). Cryosectioning can lead to freezing artefacts that distort the morphological structure of the tissue and therefore skew histological results. Equipment for cryosectioning was also not readily available at the University. Hence, the following paragraphs describe the FFPE process established for this project (**Figure 4-4**).

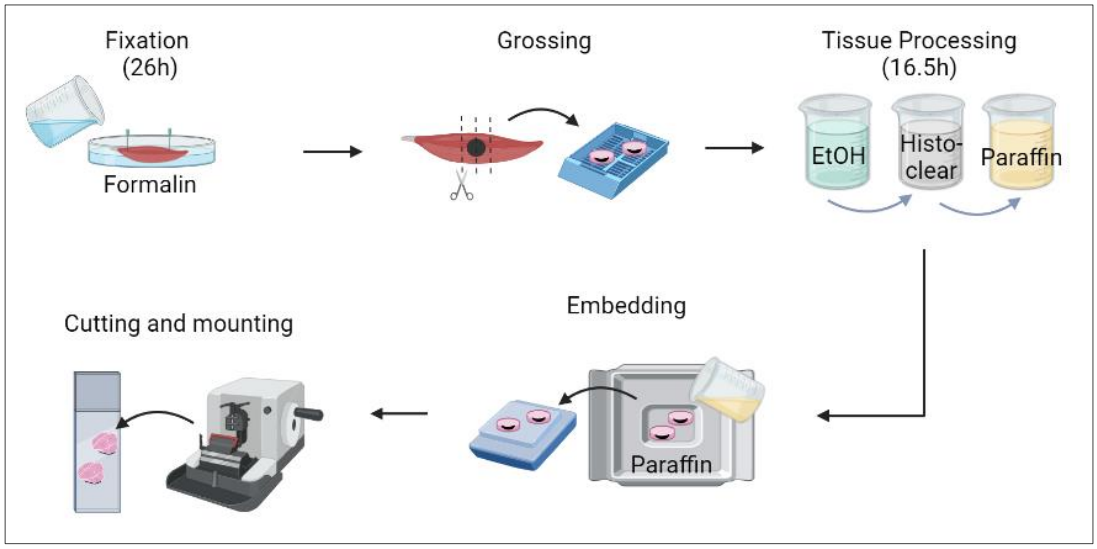

Figure 4-4: Formalin fixation and paraffin embedding of isolated murine skeletal muscles. This process followed a transverse mechanical indentation experiment. The protocol of fixation, grossing, processing, embedding, cutting, and mounting was followed for both mechanically damaged samples (as illustrated, indicated by the black marked indentation area) as well as control samples from the periphery of the same muscle.

For FFPE, tissues were fixed in 10% NBF for 28h and stored in 70% EtOH if immediate processing was not possible, before being grossed. To section transverse slices, the mechanically damaged area was cut with a scalpel into two halves of approximately 3mm width. The samples were processed overnight (Thermo Shandon Citadel 1000) in graded alcohol, Histoclear and Paraffin. A detailed processing scheme has been provided in Appendix D-5.

The tissues were then embedded in wax and cut into 3-4µm thick cross-sectional slices on a microtome (Leica RM2125RTF). Three slices were preserved at approximately every 120µm. This process was repeated six times for each block to ensure that for mechanically damaged samples, the majority of the 2mm indentation area was recorded (**Figure 4-5**). In addition to the preparation of cross-sectional slices, several muscles were processed as a whole and embedded for longitudinal cutting with identical parameters.

Following cutting, the slices were added to a water bath (Electrothermal, Essex) at 35°C to flatten before being picked up on glass slides, dried overnight at ambient temperature and for up to 1h at 60°C (drying oven, Scientific Laboratory Supplies Ltd.). Samples were then either stained or directly mounted with DPX.

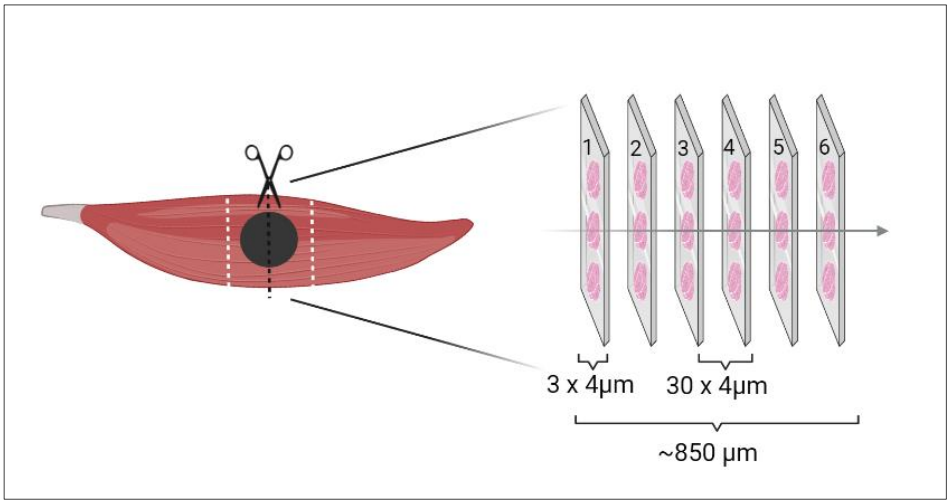

Figure 4-5: Schematic of cross-sectional cutting of mechanically damaged skeletal muscle. The indentation site is marked with India ink and grossed into two parts. Each was cut into 4µm slices with a microtome. Every 30th as well as the two following slices were mounted for microscopy.

4.3.5. Microscopic imaging

Fluorescently stained samples were imaged on a Leica SP8 system. The system consisted of a Leica DMi8 inverted microscope with 10x objective as well as a Leica DFC7000T DDC camera (4.54 µm pixels). Mounted tissue sections were imaged in widefield mode with the LASX software (Leica Application Suite X V.3.1.5.16308) to enable mapping of the full cross-section. A detailed description of the microscopic equipment is provided in "*5.3.1 Imaging equipment and technique in* use".

Basic histology samples were imaged either with a Carl Zeiss microscope (Axioimager Z1) at 10x and 20x magnification or a Motic BA210 (with Moticam 10+ Camera and Motic images plus 3.0 software) at 10x, 40x, and 100x magnification. All images were analysed qualitatively with Zen 3.1 (Carl Zeiss) and FIJI/ImageJ (Vers. 1.53s, NIH).

4.4. Live-cell imaging to detect cell death in *ex vivo* skeletal muscle samples

Depth limitations of standard confocal microscopy can be a hinderance for imaging thick samples like whole skeletal muscle tissue (s. *"3.7.3.2 Equipment for fluorescence microscopy"*). Nevertheless, this setup, similar to Gefen et al.'s study on BAM [33], was tested to get an indication for the penetration depth of the confocal microscope and its ability to identify Propidium Iodide (PI)-positive cells in mature

skeletal muscle tissue. PI penetrates cells with increased membrane permeability and binds to the DNA, making it a marker for necrosis.

4.4.1. Method for live-cell imaging with Propidium Iodide

To investigate the feasibility of confocal live-cell imaging, *n* = 1 SOL and *n* = 1 EDL muscle were isolated and stored in MOPS-based buffer for 21h at 5°C. Next, the samples were submerged in PI (1mg/mL) for 10min before being washed 3 x 5min in phosphate buffered saline (PBS) prior to imaging. No further processing like FFPE was needed for live-cell imaging. The Leica SP8 system was used in confocal imaging mode (*"4.3.5 Microscopic imaging"*) with excitation and emission wavelengths set to 535/617nm respectively. The 10x objective scanned each sample with a step size of 5µm until no signal was detected.

4.4.2. Suitability of Propidium Iodide to detect cell death *ex vivo*

Skeletal muscle tissue has a high metabolic demand that is heavily reliant on the availability of oxygen and nutrients. When storing the muscle samples for 21h without this supply, high cell death rates can be expected. Accordingly, PI-positive cells were visible in the outer layers of the muscle tissue (**Figure 4-6**). However, the stain could only be detected to a maximum depth of 100µm in this inverse confocal microscopic setup, which is equivalent to 5% of the overall muscle thickness, making it insufficient for full muscle analysis.

The limited detection depth can be explained by the high scattering effects of native tissue, which in turn reduces the penetration depth of light [281]. To overcome this issue, advanced microscopes like a Mesolens [282], or techniques such as optical tissue clearing [281] could be employed. Both concepts were trialled in additional preliminary studies, which are discussed in *Chapter 9*. However, these approaches have only limited compatibility with PI staining.

Based on the results of this preliminary study, PI was unsuitable to quantify cell death in mature skeletal muscle tissue. Its detection was restricted to superficial layers, making it impossible to assess the full extent of the damage. PI staining also requires timely imaging of samples, which presents additional logistical restrictions in terms of equipment location. An alternative staining procedure was therefore needed.

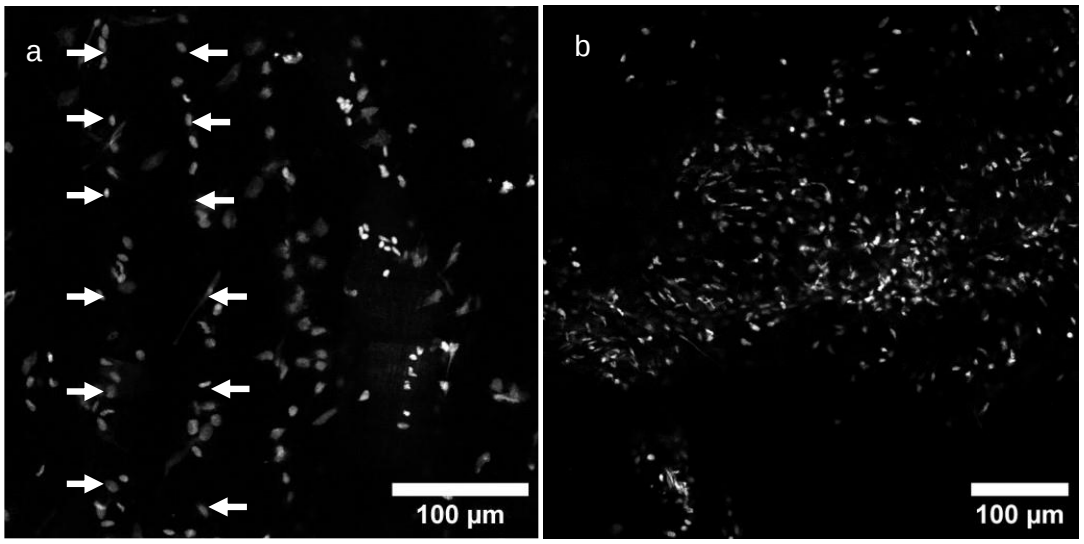

Figure 4-6: Propidium Iodide staining of skeletal muscle tissue. EDL and SOL muscles of Sprague Dawley rats were isolated and stored in MOPS buffer at 5°C for 21h without oxygenation to induce cell death. Nuclear damage was visualised through confocal imaging of PI staining, represented by light spots. **a)** Some nuclei appear in parallel longitudinal alignment indicated by alignment of white arrows. This is typical for skeletal muscle where nuclei are usually located in the periphery of muscle fibres. **b)** In most areas no clear pattern in nuclei distribution was visible as nuclei become centrally located within damaged fibres**.** Both images were taken at a depth of 40µm, representative of *n* = 2 samples.

4.5. Assessment of the *ex vivo* experimental setup with basic histology

Histology is the gold standard for tissue imaging in many laboratories. It was the method of choice to examine the experimental setup, including the dissection process and storage of tissues in buffer solution. Samples were processed with FFPE and stained with Haematoxylin and Eosin (H&E). Qualitative analysis of mechanically damaged tissue was also performed as a first indication for successful mechanical indentation.

4.5.1. Method for Haematoxylin and Eosin staining

First, the suitability of MOPS buffer for skeletal muscle storage was tested. Skeletal muscle samples were isolated from Sprague-Dawley rats and either directly fixed and processed via FFPE (*n* = 6) or stored in MOPS for 3h at 22°C prior to processing (*n* = 5) for comparison.

Additionally, *n* = 9 muscles (*n* = 5 EDL, *n* = 4 SOL) were mechanically damaged through transverse indentation (s. "*4.3.3 Mechanical loading "*) with a force of 11 –

60N. Muscles from the contralateral limb served as negative controls (*n* = 9). They were held in the same conditions for the same time but without any load application.

All samples were processed according to the general FFPE protocol (s. *"4.3.4 Tissue processing through formalin fixation and paraffin embedding"*). Once the tissue slices were dried onto microscope slides, a standard H&E protocol was followed to visualise the microanatomy of the tissues (Appendix D-6). The samples were submerged in a series of Histoclear, graded EtOH, Harris' Haematoxylin, tab water, Acid Alcohol, and Eosin Y. Once stained, the samples were mounted with DPX. The prepared slides were then imaged with the Axioimager Z1 and a Motic BA210 as described in *"4.3.5 Microscopic imaging"*.

4.5.2. Suitability of skeletal muscle storage in MOPS-based buffer solution

The cross-sectional view of both control group and directly processed muscles displayed the typical polygonal appearance of skeletal muscle cells for most samples (**Figure 4-8a**). Only few interstitial spaces were present, and nuclei were placed peripherally. Staining intensity was uniform across the samples. In some samples, peripheral cells displayed signs of damage, including increased interstitial spaces and rounded morphologies (**Figure 4-8b**). This damage might be the result of chemical fixation [283], or was introduced during the dissection process. While minor fixation damage is unavoidable, great care should be taken during sample collection and handling. If samples are obviously damaged during any stage of handling, they should be excluded from analysis to avoid bias. Nevertheless, it is expected that damage introduced by the experimenter would reduce with increasing experience.

Compared with control samples, small areas with minor cell damage were visible in the samples stored in MOPS solution for 3h. The damage was marked by increased interstitial spaces, varying cell size and staining intensity, rounded morphologies, and centralised nuclei (**Figure 4-7**).

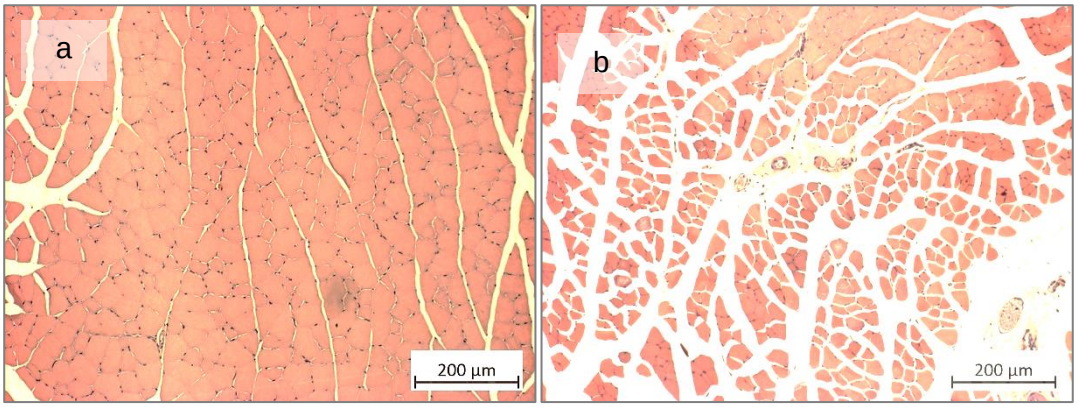

Figure 4-8: Representative cross-sectional view of negative control samples of skeletal muscle tissue. Samples were taken from Sprague-Dawley rats, directly fixed, processed, and stained with H&E. **(a)** cross-sectional view of healthy, densely packed muscle fibres with polygonal shape. **(b)** outer edges of control tissue with damaged, swollen fibres, irregular cell shapes, higher staining intensity, and increased interstitial

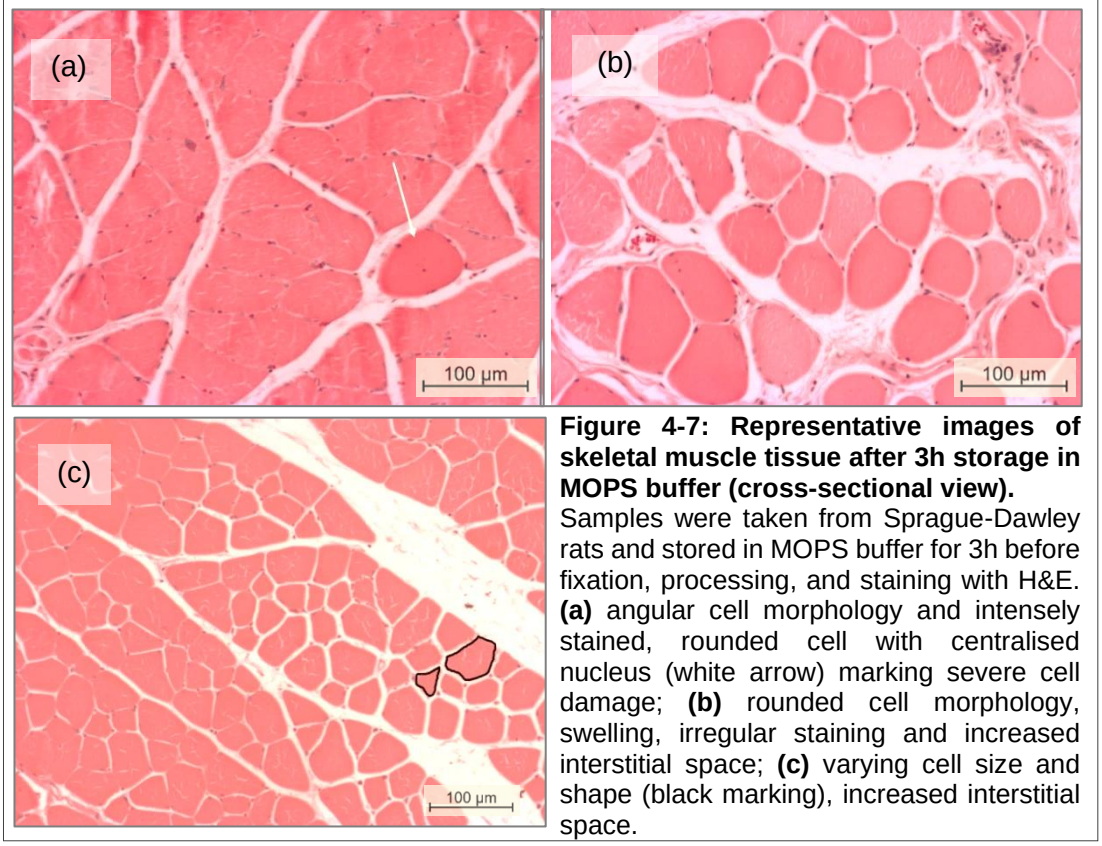

Figure 4-7: Representative images of skeletal muscle tissue after 3h storage in MOPS buffer (cross-sectional view). Samples were taken from Sprague-Dawley rats and stored in MOPS buffer for 3h before fixation, processing, and staining with H&E. **(a)** angular cell morphology and intensely stained, rounded cell with centralised nucleus (white arrow) marking severe cell damage; **(b)** rounded cell morphology, swelling, irregular staining and increased interstitial space; **(c)** varying cell size and shape (black marking), increased interstitial space.

Looking at control samples in a longitudinal view, cross-striation was visible as well as the structural arrangement of cells in long fibres with peripheral nuclei (**Figure 4-10**). These arrangements were sometimes disorganised in MOPS-stored samples (**Figure 4-9**), especially when the samples were not pinned out to prevent involuntary contractions. Additionally, striation was partially lost and structural damage apparent. Some fibres also showed signs of swelling and multiple internal nuclei.

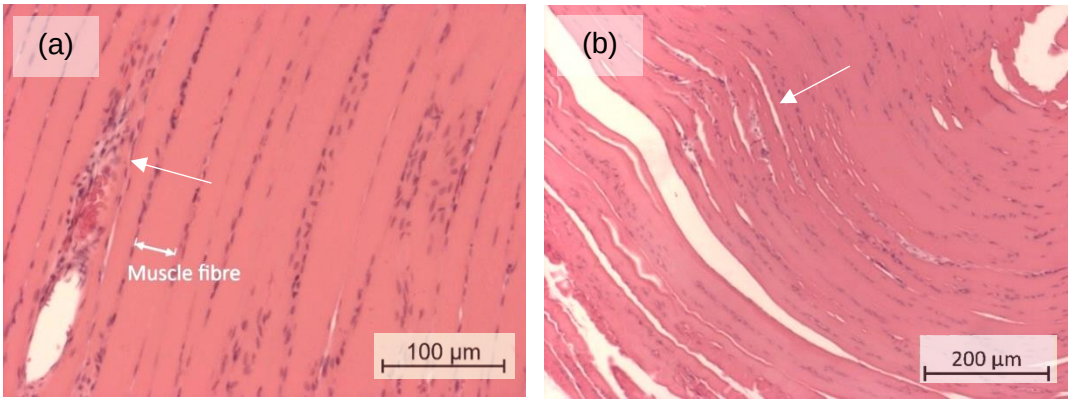

Figure 4-10: Representative longitudinal view of control tissue. Samples were taken from Sprague-Dawley rats, directly fixed, processed, and stained with H&E. **(a)** Skeletal muscle fibres in dense, parallel arrangements with only few interstitial spaces; arrow indicates area of fibre damage with increased number of nuclei in centralised location. **(b)** Skeletal muscle fibres with most nuclei located peripherally; arrow indicates areas with increased interstitial spaces.

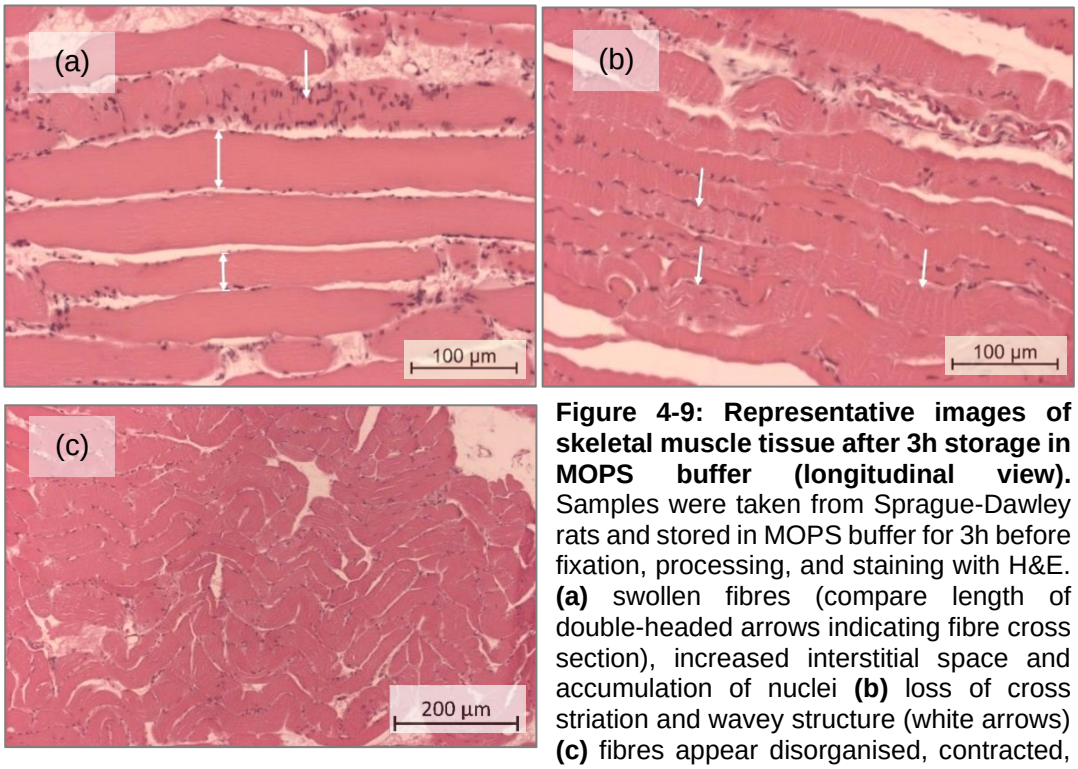

Figure 4-9: Representative images of skeletal muscle tissue after 3h storage in MOPS buffer (longitudinal view). Samples were taken from Sprague-Dawley rats and stored in MOPS buffer for 3h before fixation, processing, and staining with H&E. **(a)** swollen fibres (compare length of double-headed arrows indicating fibre cross section), increased interstitial space and accumulation of nuclei **(b)** loss of cross striation and wavey structure (white arrows) **(c)** fibres appear disorganised, contracted, and disrupted, with increased interstitial spaces.

In both cross-sections and longitudinal sections of the 3h MOPS group, minor damage was observed compared to the freshly fixed samples. A possible explanation is the missing oxygenation of the buffer solution. While it is common practice for *ex vivo* experiments to integrate oxygenation into the setup, limited equipment availability and added cost made it unachievable for this project. To minimise the potential influence of storage-related cell death on the mechanical cell death measurements, comparison of each intervention group with a control that was kept in identical environmental conditions was paramount. In the following experiments, each sample was physically divided after the intervention: areas at the indentation site were allocated to the "intervention" group; untouched areas in the periphery served as control. This way, not only environmental influences on each sample were captured but it also reduced the number of samples needed.

4.5.3. Basic histological assessment of cellular damage in mechanically indented skeletal muscle tissue

In mechanically damaged samples, the indentation site was clearly distinguishable (**Figure 4-11**). In longitudinal slides, uneven staining, inflammatory cell infiltration and swelling of damaged fibres was visible. For cross-sections, tissue damage could be identified through uneven staining, increased interstitial spaces, and varying cell sizes and shapes. Notably, the majority of the tissue damage was located close to and opposite to the indentation site whilst the middle regions of the muscle seemed intact. This is congruent with other studies that reported a damage propagation away from the loaded region [198, 199].

Some cross-sectional slices also had a concavity formed at the surface. The permanent deformation coincided with visible India ink marking, indicating the indentation site. This concavity might interfere with longitudinal cutting of the surface area of muscle samples, leading to holes. Cross-sectional rather than longitudinal sectioning might therefore be more suitable to capture the full extent of cellular damage within a sample.

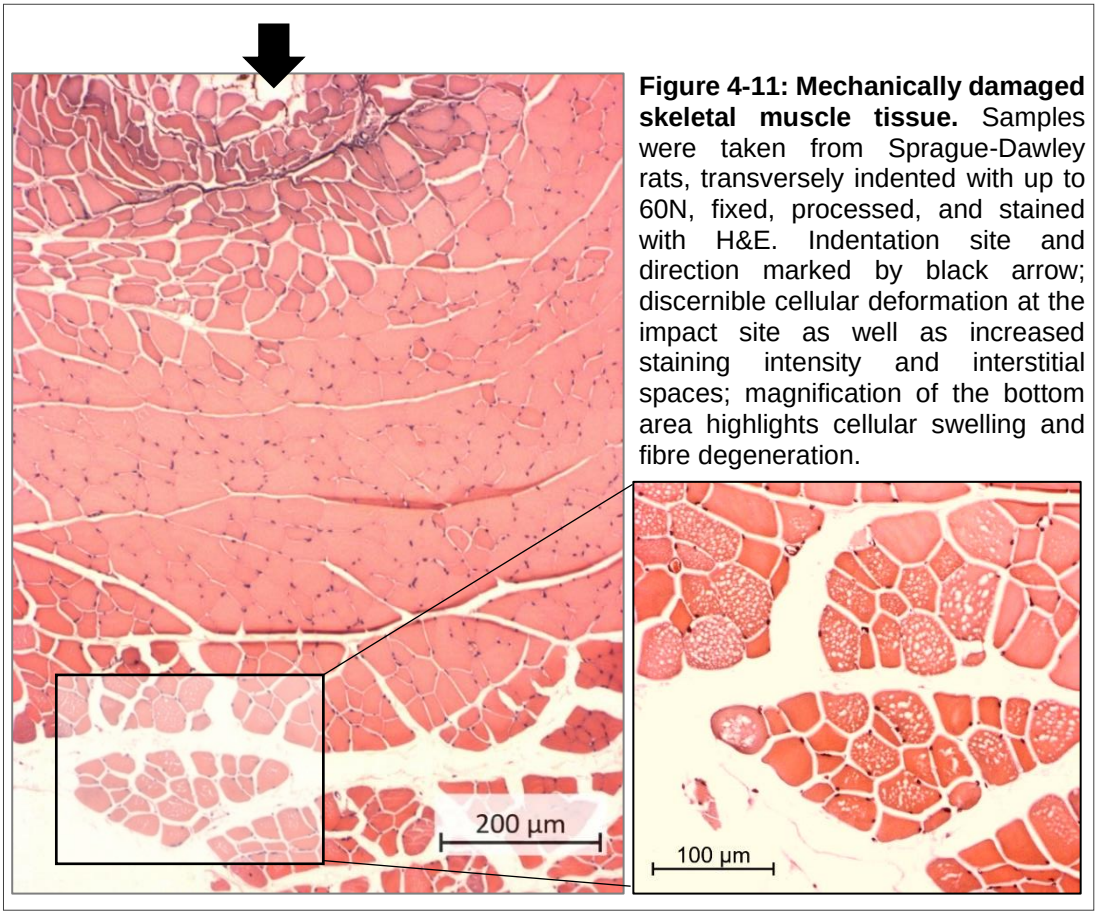

Figure 4-11: Mechanically damaged skeletal muscle tissue. Samples were taken from Sprague-Dawley rats, transversely indented with up to 60N, fixed, processed, and stained with H&E. Indentation site and direction marked by black arrow; discernible cellular deformation at the impact site as well as increased staining intensity and interstitial spaces; magnification of the bottom area highlights cellular swelling and fibre degeneration.

4.5.4. Artefacts from histological procedures

Not all sections were suitable for analysis. Artefacts from microtoming included knife marks and scores (**Figure 4-12**). Incorrect mounting resulted in folds, air bubbles and air-drying of some samples. Great care must therefore be taken during the cutting and mounting steps to produce high-quality slices, i.e. by ensuring correct fixation of the microtome blade, frequent changing of the blade to retain sharp edges, and careful handling and mounting of cut slices [284, 285].

Trimming artefacts were also observed, most often in longitudinally mounted samples. Pre-processing might not be optimised for the slightly larger sample size compared with the small tissue pieces for cross-sectional cutting. Insufficient dehydration, clearing, or infiltration with wax can all influence the integrity of the tissue. Additionally, the effect of uneven sample embedding is more pronounced in longitudinal than transverse slices. Together with difficulties in visualising the spatial damage distribution in longitudinal sections (s. *"4.5.3 Basic histological assessment of cellular*

damage in mechanically indented skeletal muscle tissue"), cross-sectional slicing was favoured in future experiments.

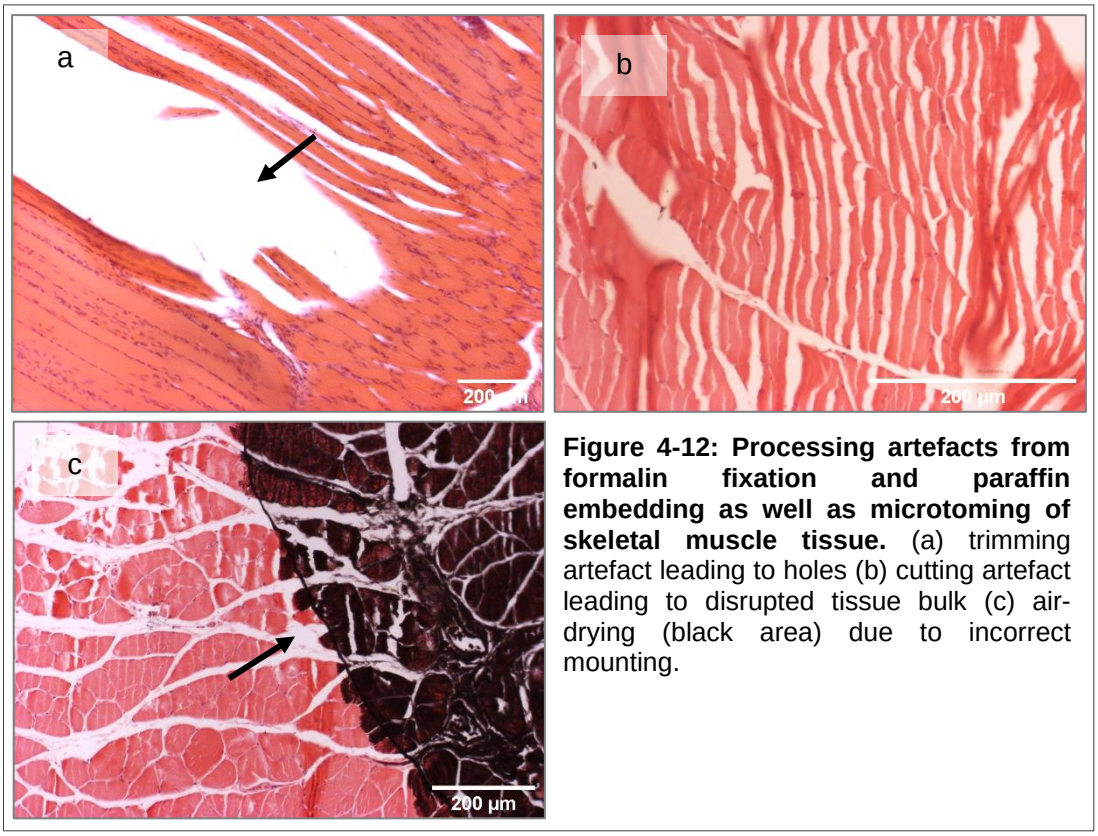

Figure 4-12: Processing artefacts from formalin fixation and paraffin embedding as well as microtoming of skeletal muscle tissue. (a) trimming artefact leading to holes (b) cutting artefact leading to disrupted tissue bulk (c) air-drying (black area) due to incorrect mounting.

4.5.5. Summary of preliminary study on basic histology

Histology is a gold standard method to analyse skeletal muscle samples and has been essential for establishing a robust experimental process. First, sample distortion from involuntary contractions could and should be avoided by pinning out the tissue samples once extracted [286]. Second, cross-sectional slicing made it easier to visualise the extent of cellular damage compared to longitudinal cutting. Although cross-sectional slicing largely avoids processing artefacts, great care must be taken when microtoming and mounting slices to prevent other artefacts. Last, sample storage in MOPS buffer seemed to keep skeletal muscle reasonably stable during experiments when the time frame was kept to 3h. However, the lack of oxygenation may introduce minor cell damage, which needs to be considered when analysing cell death rates after mechanical insult. To overcome this issue, areas outside of the indentation zone could be used as negative control group. Relative cell death measurements (i.e. difference between indentation zone and periphery) can then be

examined for standardisation when comparing samples across different loading durations.

The presented lessons-learned were the result of qualitative analysis of histologically stained muscle samples. However, comparing the extent of cellular damage after different mechanical loading scenarios might be more difficult and at a higher risk of bias with a qualitative approach. Semi-quantitative analysis can reduce the risk for bias slightly by using scoring systems to classify samples according to the degree of damage [287]. Alternatively, automated algorithms can be deployed, which often rely on extensive machine learning [288]. To ensure the risk for bias is minimal without increasing the need for time and resource consuming machine learning, an alternative staining procedure was sought for this project.

4.6. Spectral analysis of fluorescence signal of stains and skeletal muscle tissue

For a more quantitative approach to assess cellular damage, two FFPE fixable, membrane impermeable, fluorescent stains were identified: Live-or-Dye™ and Procion Yellow MX4R. Live-or-Dye™ (LoD) is an amine-reactive dye that crosses the membrane of impaired cells and reacts with free amines in the cytoplasm. Procion Yellow MX4R, or ProY, is part of the family of Procion stains and binds irreversible to cytoplasmic components containing amines and hydroxyl in structurally compromised cells.

Other labelling methods like immunohistochemistry (fluorescent or chromogenic labelling of antibodies) were omitted as they are generally more complex, expensive, and time consuming. They are also less compatible with FFPE processed tissue as antigens might be masked by protein cross-linking, requiring added processing steps.

Sourcing the Procion stain proved to be difficult. In the majority of papers on skeletal muscle tissue, the procion stain in use is simply referred to as Procion Orange. However, multiple names exist that describe the same or similar stains, including Reactive Orange 14, Procion Yellow M4RS, Procion Yellow MX4R, Procion Orange MX2R, and Procion Red. This may be attributed to differences between suppliers [289], as well as changes in nomenclature [290]. According to Rost et al. [290], the first three on the list (Reactive Orange 14, Procion Yellow M4RS/MX4R) describe the same stain. On the contrary, the molecular structure of Procion Yellow MX4R

(C20H19ClN4Na2O11S3, MW 669.018) and Reactive Orange 14 (C19H12Cl2N8O9S2, MW 631.4) appear to be different [291, 292]. Despite these ambiguities, the final decision was made to use Procion Yellow MX4R, which was readily available and has also been used to visualise sarcolemmal damage in the past [229, 230, 260–262].

For the successful analysis of fluorescently stained tissue, the fluorescence properties of the samples as well as stains need to be known. Spectral information on LoD was readily available from the manufacturer but unavailable for ProY. The ambiguities around the ProY stain made spectral analysis of this stain necessary. The autofluorescence behaviour of skeletal muscle was characterised and discussed in relation to both fluorescent stains.

4.6.1. Method for Spectrofluorometry

To identify suitable filter settings for epifluorescence microscopy, spectrofluorometry of ProY was performed on a Cary Eclipse System (Agilent Technologies). The absorbance of the stain dissolved in water (0.2% wt) was measured as ratio of incident light intensity over emitted light intensity. Emission intensity was recorded in the range of 500-800nm for excitation wavelengths of 430nm, 480nm, 515nm, and 580nm.

Autofluorescence signal was also quantified. Unstained EDL samples (n = 2 for repeated measure) were imaged with 10x magnification on the Leica SP8 system (s. *“4.3.5 Microscopic imaging”*). The microscope allows for slit-based emission wavelength detection. Images were recorded with 488nm excitation over an emission range of 500nm – 735nm with 15nm increments. The images were imported to FIJI/ImageJ and randomly selected regions of interest (ROI) analysed to obtain the emission intensity.

4.6.2. Spectral characteristics of skeletal muscle tissue and fluorescent stains

To identify suitable microscopy settings for fluorescently stained samples, spectral analysis was performed. ProY solution had its absorption maximum at around 435nm. The strongest emission intensity was achieved with 480nm excitation and reached its maximum around 605nm (**Figure 4-13a**). From the filters available on the microscopic

system, the FITC filter was chosen for further imaging of ProY-stained slides, which has an excitation and emission bandwidth of 482/35nm ex and 536/40nm em.

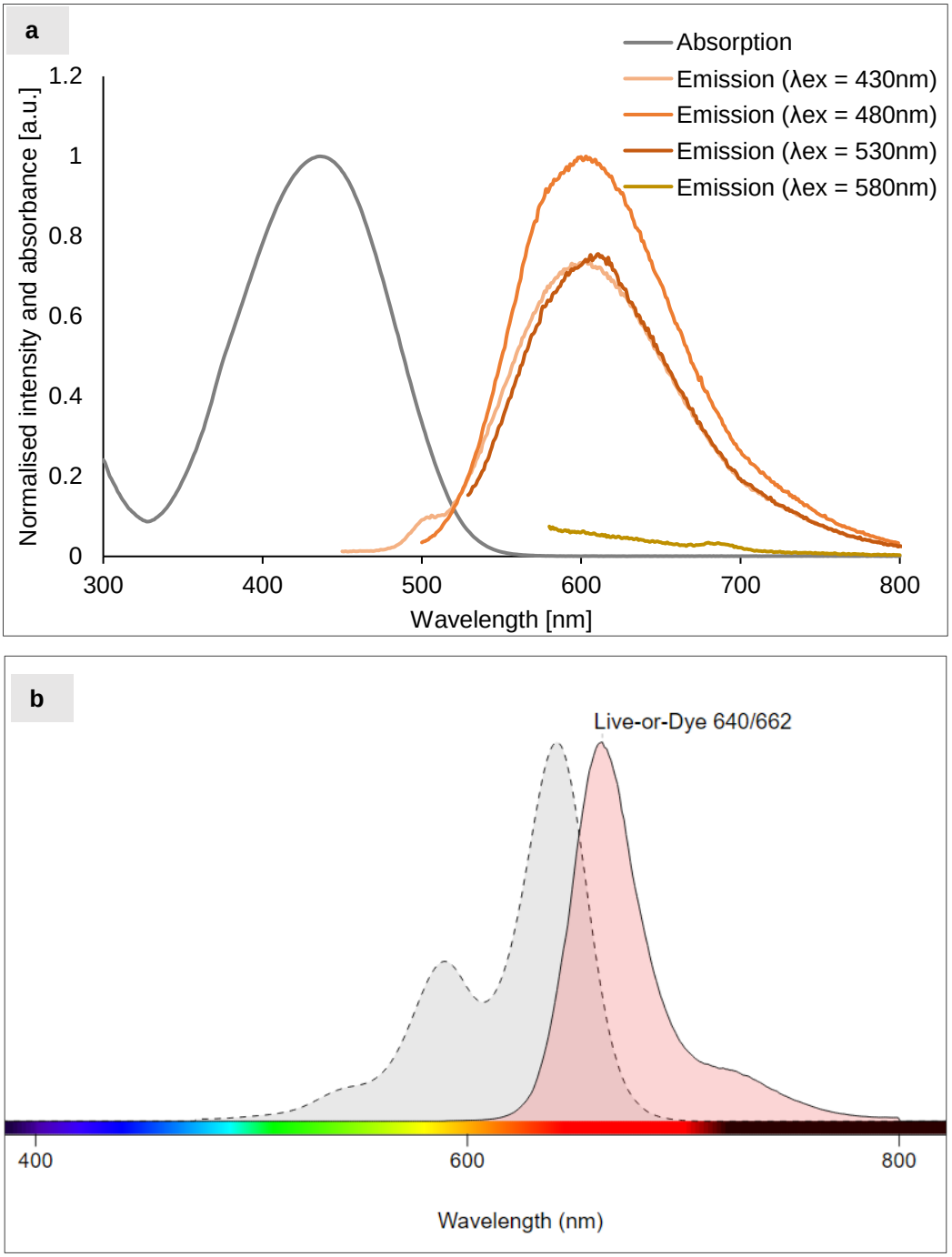

Figure 4-13: Absorbance and fluorescence emission spectrum of ProY and LoD. a) Absorption spectrum (grey) of ProY had its peak at 436nm. Spectrum is normalised to the maximum absorbance. The fluorescence emissions (orange) were recorded over different excitation wavelengths λ_{ex} with the highest emission signal at λ_{ex} = 480nm. The peak emission intensity was recorded at around 605nm. Spectra are normalised to the maximum emission intensity. **b)** Spectral information for LoD was obtained from **[293]**. Peak absorption (grey) and emission (red) are at 594nm and 614nm.

The results of the spectral analysis indicate that the autofluorescence signal (**Figure 4-14**) and fluorescence of ProY might be interfering, potentially causing problems with identifying ProY-positive cells. LoD was identified as an alternative stain. It is available for a range of excitation/emission wavelengths. For this project, the stain with excitation/emission wavelengths of 594/614nm was chosen (**Figure 4-13b**), which has been validated for microscopical use. It was captured with a Y5 filter (Ex /60, DC 660, Em 700/75).

According to the spectral analysis, the Leica SP8 system used for this experiment had suitable filters available for both ProY- and LoD-stained samples. While the Y5 filter chosen for the LoD samples excluded the majority of the autofluorescence signal inherent to skeletal muscle tissue, the FITC filter was within the natural fluorescence range of the samples. Detection of mechanically damaged cells with ProY might therefore be difficult, yet not impossible.

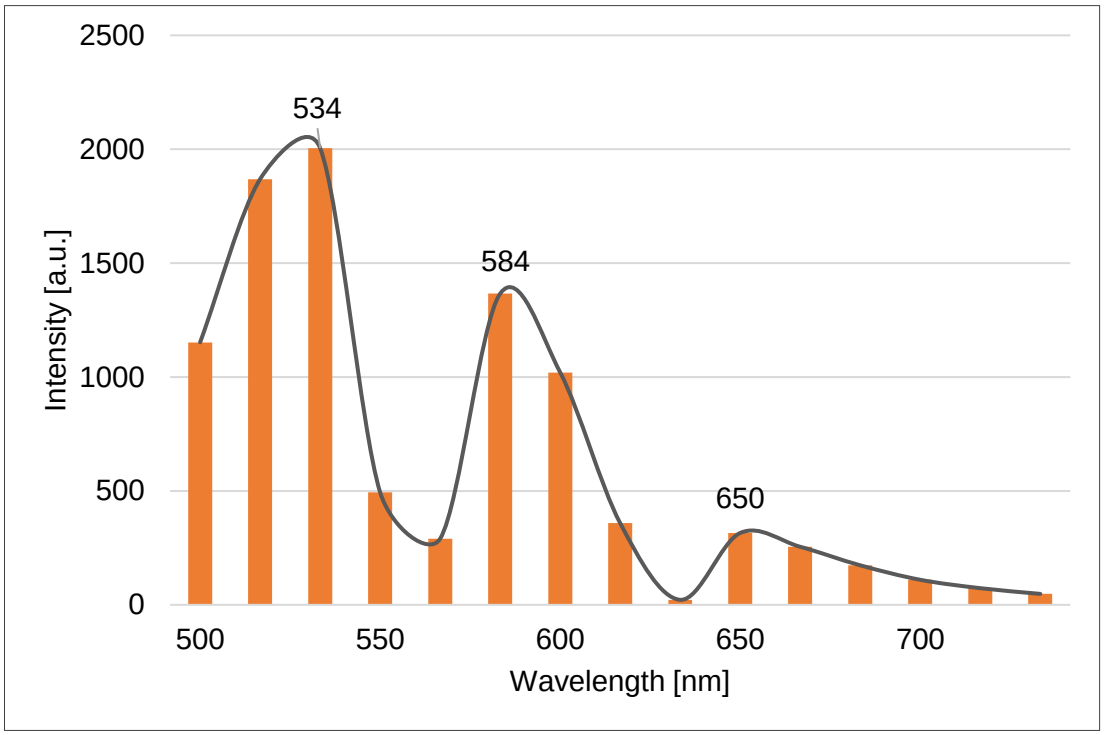

Figure 4-14: Average emission intensity spectrum of unstained skeletal muscle cross-sections. Peak emission intensity values were observed at 534nm, 584nm and 650nm with an excitation of 488nm. Data is average of multiple ROI from two different samples.

4.6.3. Approaches to avoid autofluorescence

During the imaging process, strong autofluorescence signal was detected, which could overlap potential signal from the ProY stain. The signal appeared mainly as green fluorescence and has been reported in other studies on skeletal muscle [256, 294, 295]. It originates either from endogenous fluorophores like lipofuscin [66, 67], NADPH [255, 296, 297], NADH [256], myoglobin [298], and flavin [256, 297], or is related to the tissue fixation process [299]. Researchers have suggested numerous ways to reduce autofluorescence, including chemical quenching, photobleaching, and technology-based separation like spectral unmixing.

Photobleaching was considered unsuitable for this project, seeing as fluorescent staining is performed prior to any further tissue processing. Subsequent photobleaching would therefore not only reduce autofluorescence signal but also compromise the stain of interest.

Chemical quenching is another option to reduce the fluorescence of a specific fluorophore by adding another substance. One example is staining with Sudan Black B (SBB) to reduce lipofuscin-induced autofluorescence. The main source for lipfuscin fluorescence are lipid structures, which are abundant in nerve cells, making brain a common application area for SBB staining [258, 259]. Myocardiocytes and aged skeletal muscle tissue might also display lipofuscin-related fluorescence induced by the breakdown of old red blood cells and damaged cell components. It often presents as fluorescence granules that could be misinterpreted as positive fluorescent staining [257, 300]. However, in healthy skeletal muscle of laboratory animals as used in this project, age-related damage and therefore the relevance of SBB staining is limited.

The fixative used during tissue processing may also induce fluorescence as it reacts with amines and proteins to create fluorescent products [299]. Glutaraldehyde is thereby most prone to fluorescence interference, which is often counteracted by sodium borohydride ($NaBH_4$) quenching [299, 301, 302]. With formalin-based fixation being less responsive to sodium borohydride [295], it is expected that this quenching method is less relevant for this project.

Instead, other sources for autofluorescence signal are highly prevalent, including elastin and collagen [255, 303]. Both are found in the extracellular matrix (ECM) of skeletal muscle tissue [304] with elastin as the stronger fluorophore. Its spectrum of

488/515nm [303] coincides with the autofluorescence spectrum obtained from muscle samples (s. **Figure 4-14**). Different protocols are available to chemically reduce elastin fluorescence [299]. Similarly, researchers have developed chemical-based methods to minimise other sources of endogenous autofluorescence like FCCP staining to reduce NAD(P)H signal [305]. However, these treatments come with a risk of simultaneously reducing the signal of interest [306] and the level of reduction of autofluorescence signal is often unclear [305], making it less appropriate for quantitative fluorescence analysis.

Instead of chemical quenching, the overlapping fluorescence signals of the skeletal muscle samples could be separated through filtering or digital processing, like spectral unmixing. Fluorescence signal from flavin for example, which is considered a main source for green fluorescence in skeletal muscle tissue [256], has been successfully separated in cardiomyocytes through spectral unmixing [307]. This relatively complex process requires the definition of a full spectral profile of a specimen in addition to microscopic imaging, making it time and resource consuming [306]. Spectral unmixing is also limited when background signal, noise, or a large signal overlap are present [308], as well as when dealing with high biological variability [306]. Technology-based separation of autofluorescence signal was therefore not pursued.

Overall, different procedures to reduce autofluorescence are available, yet many of them either have a limited applicability and prospects of success for this project or are time and labour consuming to develop. Consequently, preliminary experiments on the suitability of the selected dyes ProY and LoD were performed without any means of reducing autofluorescence.

4.7. Fixed-cell fluorescent staining to assess sarcolemmal damage

Once spectral characteristics of the stains and samples were identified, loading experiments were performed. Both stains were tested for their suitability to detect mechanically-induced sarcolemmal damage in *ex vivo* skeletal muscle tissue. The results were compared with positive controls (stained, chemically permeabilised samples) as well as negative controls (stained tissues without any loading).

4.7.1. Method for Live-or-Dye and Procion Yellow MX4R staining

Preliminary studies on the suitability of MOPS buffer for *ex vivo* storage of skeletal muscle revealed minor cell damage after 3-4 hours, which was used as guidance for the maximum duration of each experiment. A total of *n* = 21 skeletal muscles were isolated from Sprague Dawley rats (s. *"4.3.2 Collection and preparation of murine skeletal muscle tissue"*) and assigned to one of three groups: (1) mechanical damage, (2) negative control, (3) positive control.

4.7.1.1. Experimental protocols for different groups

A total of *n* = 13 skeletal muscles (*n* = 7 SOL and *n* = 6 EDL) were assigned to the mechanical damage group. Samples were pinned out and indented transversely with the setup described in *"4.3.3 Mechanical loading "*. A range of loads were applied for 60min, 90min, 120min, or 150min. The different loads were achieved by placing a small container with water on top of the indenter to generate a combined weight of 11g, 33g, or 60g. The aim was to successfully induce and detect sarcolemmal damage.

The allocation of samples to experimental conditions is listed in **Table 4-2**. Initially, different time frames were tested across the 11g loading condition with the LoD stain only. As damage was only identifiable at the longer durations, further testing of both stains at higher loads (33g and 60g) was performed for a duration of 90min and 120min to ensure sarcolemmal damage.

Table 4-2: Sample allocation for mechanical damage group. Samples were indented with the loads and durations marked in bold prior to staining with ProY or LoD.

	11g		**33g**		**60g**	
	ProY	*LoD*	*ProY*	*LoD*	*ProY*	*LoD*
60min	-	*n* = 2	-	-	-	-
90min	-	*n* = 1	-	*n* = 1	-	*n* = 2
120min	-	*n* = 1	*n* = 2	-	*n* = 2	-
150min	-	*n* = 1	-	-	-	-

Three negative control samples were taken from the periphery of each mechanically damaged sample (*n* = 13) in 3mm thick sections and processed according to the FFPE

protocol (s. *“4.3.4 Tissue processing through formalin fixation and paraffin embedding”*).

To validate the fluorescent staining protocol, *n* = 8 samples (*n* = 6 SOL and *n* = 2 EDL) were treated with Triton-X for positive control [309] (**Table 4-3**). Triton-X induces cell lysis, meaning it permeabilises the membrane of living cells chemically [310]. Samples were submerged in 0.1% Triton-X 100 (Sigma Aldrich, St. Louis) for 10min to 2h at ambient temperature before being fluorescently stained. Results were compared with negative controls and mechanically damaged samples.

Table 4-3: Sample allocation for positive control. Samples were treated with Triton-X for time frames indicated in left column prior to staining with ProY or LoD.

Triton-X	ProY	Live-or-Dye
10min	*n* = 2	-
20min	*n* = 1	*n* = 1
120min	*n* = 2	*n* = 1

4.7.1.2. Fluorescent staining protocols

Following the mechanical and chemical damage protocols, samples were submerged either in ProY or LoD. Varying suggestions for the amount and duration for Procion staining of skeletal muscle can be found in the literature. Concentrations range from 0.1% to 1%, durations from 5min to 180min [229, 230, 262–265, 267, 311–318]. For this experiment, the ProY solution was prepared with a concentration of 0.1% of Procion Yellow MX4R in PBS (Appendix D-2), which is equivalent to other methods [229, 230]. The duration was set to 1h, similar to what other researchers used for EDL and SOL muscles [263, 265, i.e. 311–313].

For the Live-or-Dye™ stain, a concentration of 1:1000 of the provided stock solution and a staining duration of 30min were chosen, according to the supplier’s recommendations. After being stained, all samples were washed in PBS to remove excess stain (3 x 5min) before being fixed and embedded (s. *“4.3.4 Tissue processing through formalin fixation and paraffin embedding”*).

4.7.1.3. Epifluorescence microscopy of fluorescently stained samples

Imaging was performed on the Leica SP8 system. This inverted microscope has a motorised stage to acquire images in a series of x-y tiles that can be stitched with an automatic software (Leica LAS-X) to assemble final images of full muscle cross-sections. Two acquisition options were tested: mapped confocal imaging, and widefield imaging with automatised stitching.

For LoD samples, a Y5 filter (Ex 620/60, DC 660, Em 700/75) was applied with a 10x magnification. ProY-stained samples were imaged with an FITC filter (Ex 482/35, Em 536/40) as identified earlier through spectral analysis. Illumination intensity and integration time were kept the same across samples for comparability. Each cross-section was scanned, and the tiled images merged for analysis. All images were imported to FIJI/ImageJ and visually inspected for their suitability to distinguish damaged from control areas.

4.7.2. Suitability of Live-or-Dye stain to detect cell damage

The flexibility of the LoD stain in terms of available spectral profiles is a benefit when dealing with highly autofluorescence samples. By choosing a configuration in the far-red spectrum, a high signal-to-noise ratio can be achieved for clear visualisation of damaged cells. This was successfully demonstrated with two of the eight tested samples: After a loading duration of 120min and 150min with a weight of 11g, damaged cells were visible in the indentation zone (**Figure 4-15a**). The damage was mostly localised to the area around the indenter. In the remaining six samples, no localised cell death could be observed. However, these samples had shorter loading times albeit with higher mass in some cases. Another possibility is that control rather than indentation areas were imaged because India Ink demarcation of the indentation site was only introduced part way through the preliminary studies (s. "*4.3.3 Mechanical loading* ").

For validation, negative and positive controls were also analysed. While samples without any intervention had no damaged cells, chemically damaged samples had a clear ring of LoD-positive cells at the outer layer (**Figure 4-15b**). The thickness of this layer increased when increasing the submersion time in Triton X from 20min to 120min, indicating higher damage rates.

However, despite these promising first results, the fluorescence tagging mechanism might present a problem when dealing with densely packed tissue. According to personal communication with the manufacturer [319], the majority of the staining would be restricted to outer cell layers. Circumventing this problem by increasing the incubation time is not an option, considering the short-lived labelling reaction (15-30min). With literature on similar methodological setups missing, further experiments would be necessary to either confirm the suitability of LoD for skeletal muscle tissue samples or adjust the experimental setup. With time restrictions in mind, efforts were focused on an alternative route, using the ProY stain instead.

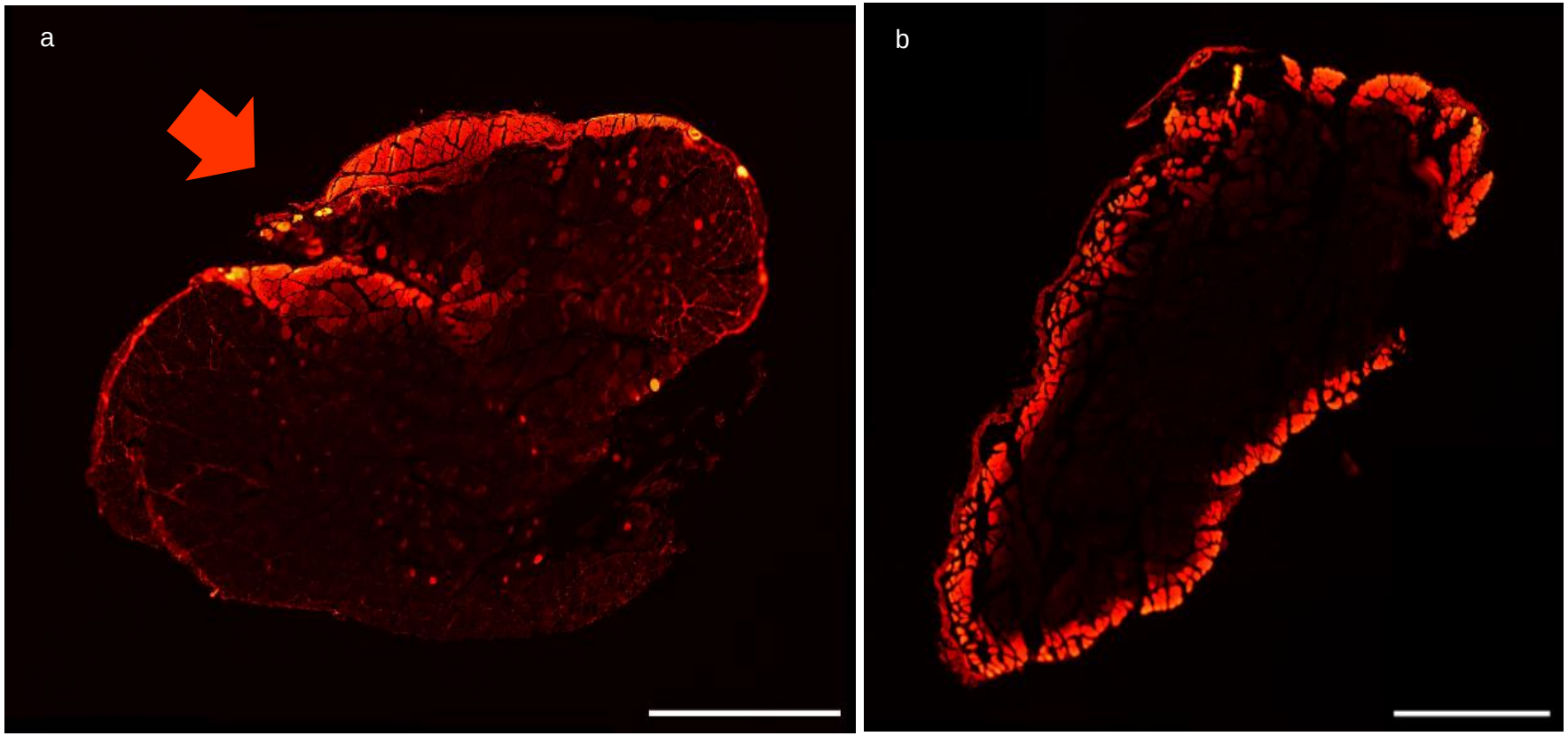

Figure 4-15: Fluorescent labelling of skeletal muscle tissue with Live-or-Dye. a) mechanical indentation (orange arrow) for 120min with a weight of 11g induced cell death, marked by red staining. **b)** Positive control tissue submerged in Triton X for 120min exhibits LoD-positive cells at the outer layers, indicating chemically-induced cellular damage. Images were obtained with a Y5 filter (Ex 620/20, DC660, Em 700/750). Scale bar 1000µm.

4.7.3. Suitability of Procion Yellow to detect cell damage

Compared to LoD, ProY had a weaker fluorescence signal during absorbance and fluorescence tests. Additionally, the signal overlapped with the autofluorescence background, making it potentially more difficult to differentiate dead from live cells.

The two samples that were mechanically indented with a mass of 60g for 120min showed no sign of cell damage after ProY staining. However, the experimental procedure was still at an early stage. Demarcation of the indentation site was missing, and staining was performed during indentation rather than afterwards. This could have hindered full penetration of the stain at the indentation site. The procedure was adjusted accordingly to stain after indentation and was implemented for the 33g loading condition. As a result, cell death could be visually detected in two samples that were mechanically indented with a load of 33g for 120min (**Figure 4-16a**).

To verify the stains specificity, positive and negative controls were also analysed. Samples treated with Triton X displayed ring-shaped layers of dead cells in the periphery (**Figure 4-16b**), similar to the positive controls for LoD. In negative control samples without intervention, no cell death was apparent.

The absence of excessive cell death in the negative control samples should also be interpreted in the context of their long-term storage in MOPS buffer. The results confirm that despite the cellular re-organisation documented in the basic histology study (s. *"4.5.2 Suitability of skeletal muscle storage in MOPS-based buffer* solution*"*) cells remained viable throughout the course of the experiment.

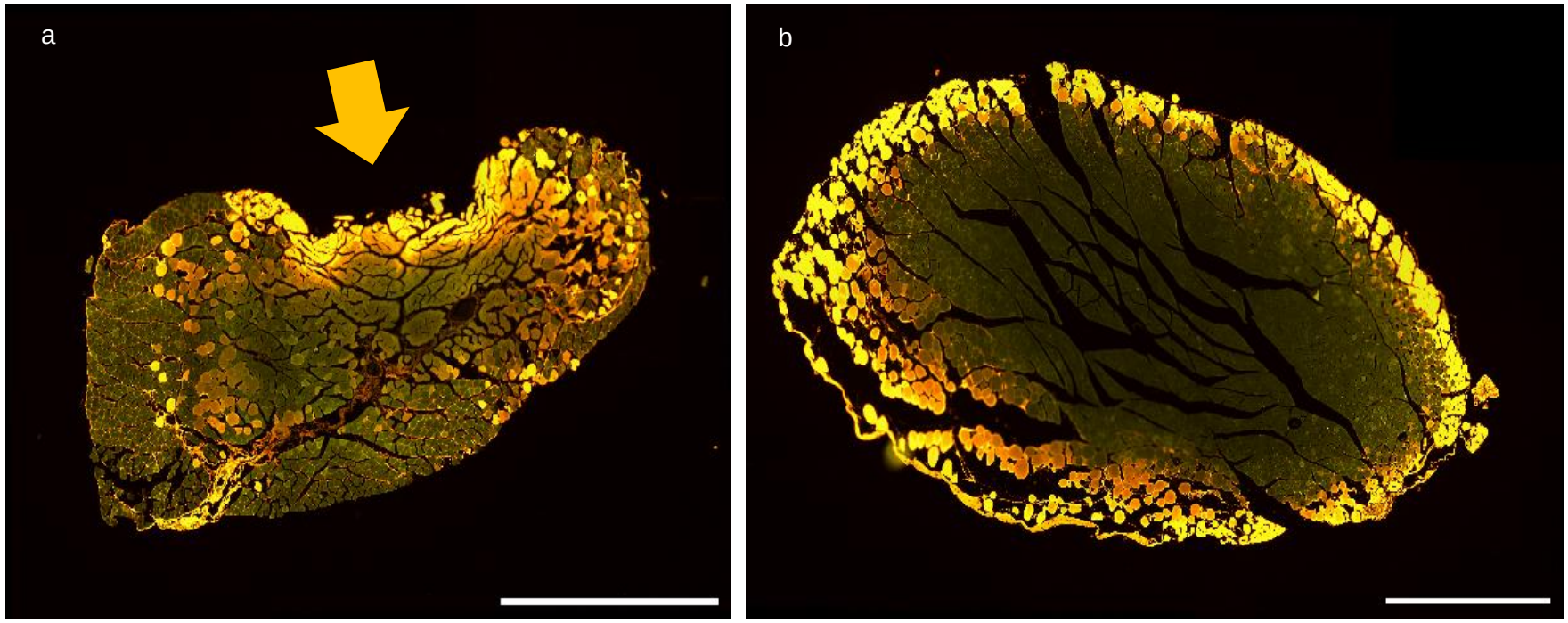

Figure 4-16: Fluorescent labelling of skeletal muscle tissue with Procion Yellow MX4R. a) mechanical indentation (yellow arrow) for 120min with a mass of 33g induced cell death, marked by yellow staining. **b)** Positive control tissue submerged in Triton X for 120min features ProY-positive cells at the outer layers, indicating chemically-induced cellular damage. Green autofluorescence of muscle cells is also visible. Images were obtained with a FITC filter (Ex 482/35, Em 536/40). Scale bar 1000µm.

4.7.4. Choice of fluorescent stain

Both LoD and ProY staining could detect sarcolemmal damage in skeletal muscle samples following mechanical indentation. This was underpinned by positive and negative control samples. While the spectral properties of LoD were more compatible with the natural fluorescence response of the samples, penetration depth is a potential limitation. Instead, ProY was favoured, which is a well-established dead-cell stain for skeletal muscle that has been used on SOL muscles of Sprague-Dawley rats in the past [320]. Unlike LoD, ProY also penetrates the full tissue, facilitated by the dye's low molecular weight and different staining mechanism. ProY was therefore the stain of choice for this project.

4.8. Complete experimental procedure

This chapter described several preliminary experiments to measure cell death after transverse mechanical loading. Three streams were explored: live-cell staining, basic histology, and fluorescent staining. The limited penetration depth of confocal microscopy on *ex vivo* samples made live-cell imaging unsuitable. The main drawback of the histological approach was the difficulty to objectively obtain quantitative data on the extent of cell death. This limitation can be overcome with fluorescent staining, which allowed for clear demarcation of dead cells.

Combining the results of the preliminary experiments, a robust methodological procedure can be described. The foundation is *ex vivo* murine tissue that is subjected to transverse mechanical loading before being stained and processed for imaging with an epifluorescence microscope. **Figure 4-17** provides an overview over the main steps. A detailed summary of the materials, methods, and processes can be found in Appendix D.

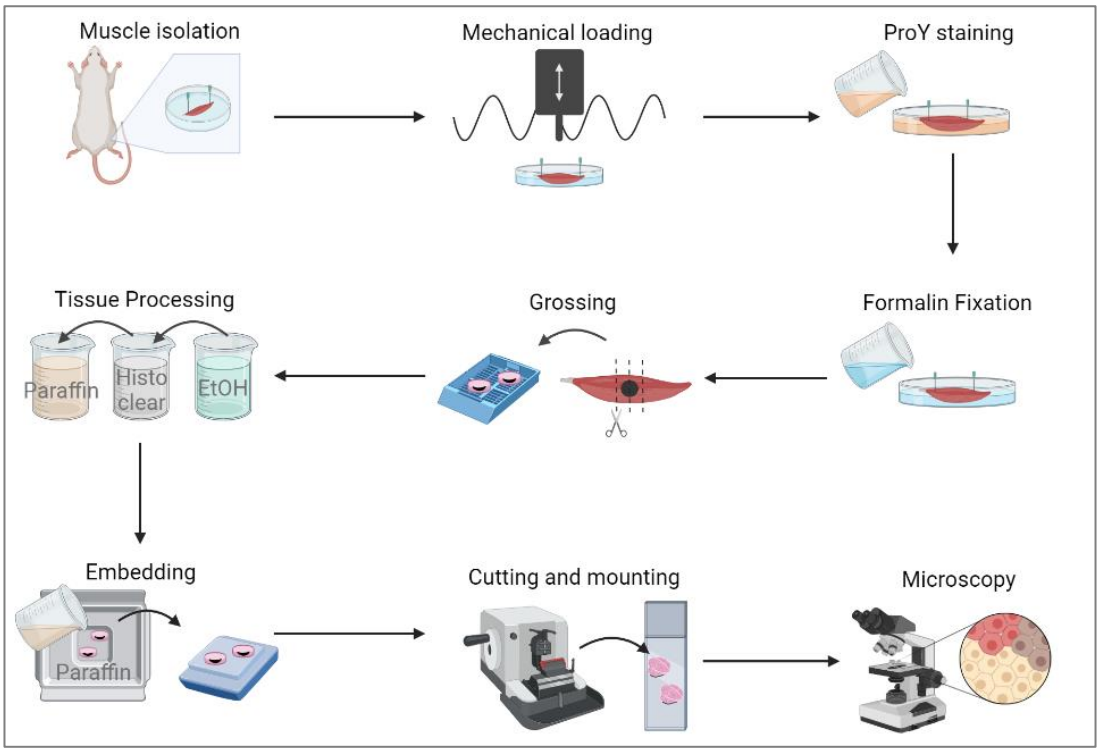

Figure 4-17: Complete experimental procedure.

The *ex vivo* model combines benefits of *in vivo* and *in vitro* experiments, like the hierarchical structure, intact function, and a controllable environment. The samples are also well-suited for transverse mechanical loading studies, yet not restricted to this form of setup. The compatibility with most mechanical testing equipment means that further conditions such as shear stresses could be applied in the future.

With ProY, a well-established marker for skeletal muscle damage has been identified and verified for its capability to highlight sarcolemmal damage in mechanically stressed tissue. It is compatible with standard FFPE processing as well as with cryosectioning, as other studies demonstrated [263, 264, 311]. The staining procedure is rather simple, compared with immunofluorescence protocols for example, and yet specific enough to indicate membrane damage for quantitative analysis. ProY is also more compatible with *ex vivo* samples than LoD and was therefore chosen for this project.

Apart from the general procedure, the preliminary experiments highlighted best practices: Pinning of the muscles at approximately resting length until fixed avoids involuntary contractions; keeping the temperature below physiological levels and restricting the maximum duration of the experiments to 4h ensures viability of the samples; demarcation of the indentation site ensures easy differentiation between

mechanically damaged and control groups; and careful microtoming and extensive practice make for high-quality tissue slices, to name a few. Taking these points into consideration, one should be able to produce high quality samples on a reliable basis.

4.9. Limitations of the experimental methods and materials

Like any study, the proposed method comes with limitations. First, animal models have only a limited translatability to the clinical case of prosthetic use. However, they allow to approach the clinical problem of socket fit from a basic scientific angle in a highly controlled environment. Individual parameters like the influence of different loading conditions can therefore be tested. Nevertheless, the clinical relevance of results needs to be discussed with care and further experiments will be necessary to relate the basic scientific knowledge to socket design and fit.

Regarding the experimental design, keeping animal tissue *ex vivo* for the duration of the experiment comes at the risk of introducing hypoxic conditions. The slight damage seen after 3h MOPS storage might be a result of this. As a preventative measure, the physiological solution around the tissue would ideally be perfused with oxygen. This was unfortunately not possible for this study because of lack of equipment, added cost, and logistics. However, ischaemia should only have a minor effect on cell death rates for the comparably short experimental duration [91, 105]. Additionally, the functionality of the muscle can be mostly preserved by the addition of nutrients like glucose to the buffer solution [321]. Data gathered from these *ex vivo* experiments should therefore still be largely related to deformation-induced rather than ischaemic damage.

Prolonged loading not only increases the risk for ischaemic damage but also leads to an accumulation of biowastes. Indeed, Yao et al. [112] found that 2h of compressive loading can create a toxic cell environment for myoblasts that might lower the cells' resistance to mechanical stress. In how far this time frame applies to *ex vivo* tissue is unknown. The possibility of toxic effects on cell damage rates therefore needs to be considered when comparing data from short and long-term loading conditions. To avoid this problem, the bathing solution could be refreshed regularly in future experiments.

Beside the experimental design, the staining procedure has a few shortcomings. The fluorescence signal of ProY is in the same spectral region as the autofluorescence of the skeletal muscle, which could influence the sensitivity of the analysis.

Nevertheless, signal from mechanically damaged cells could still be clearly distinguished from live ones after careful determination of the microscopic settings (**Figure 4-16a**). The potentially reduced sensitivity with ProY staining is also less important for the planned experimental studies; the idea is to contrast the extent of cellular damage in skeletal muscle under different loading conditions rather than reporting absolute cell death values. ProY-staining is hence still suitable for this project.

Another shortcoming is that ProY has not been tested for its penetration depth. Potential differences in fluorescence signals between central and peripheral regions of the samples might therefore not be considered. However, others have used ProY on EDL muscles in mice, and a similar Procion stain (Reactive Orange 14) on SOL muscles in Sprague-Dawley rats without any reports on penetration limitations [262, 320]. The risk for insufficient penetration was therefore viewed as a minor one.

Last, the tissue processing procedure is laborious and might introduce artefacts through chemical treatment and microtoming. This could be partially avoided by working with frozen instead of FFPE tissue. Optical clearing methods could be explored to avoid the need to slice the samples. Nevertheless, the results indicate that even with the combination of FFPE and microtoming, high-quality samples can be produced repeatedly.

4.10. Chapter summary

With the described set of preliminary experiments, the following general methodological procedure was established: isolation of murine skeletal muscle; transverse mechanical loading; fluorescent staining with ProY; FFPE processing; microtoming; and epifluorescence imaging. Next, a robust image analysis protocol needs to be developed to ensure that the produced images are translated into quantifiable data on cell death.

Overall, the developed method provides the basis for standardised research while being easily adaptable. The influence of other mechanical loading scenarios like tension and shear on skeletal muscle health could be investigated as well as the different environmental conditions mimicking ischemia or reperfusion [33, 212]. Different staining or microscopy techniques can also be integrated. By adjusting the loading setup, not only murine muscle but fresh human biopsies could be tested. This

could give an indication for the translatability of murine test results to human studies and bridge the gap from the lab to the clinical environment.

CHAPTER 5

Development of a fluorescence microscopy and image analysis workflow for the quantification of sarcolemmal damage in *ex vivo* skeletal muscle tissue

Achieving the best results from experiments involving fluorescent staining relies heavily on an optimised microscopic setup and a reliable and unbiased analysis protocol. This chapter therefore describes an optimised workflow to quantify ProY-positive cells in skeletal muscle tissue (**Objective 2**).

Experimental planning was performed by the author. The microscopic setup was optimised by Dr. Alastair Wark with support from the author. The corresponding analyses were performed by the author.

5.1. Introduction to fluorescence image analysis

Converting fluorescently stained tissue slices into quantifiable data requires an optimised microscopic setup and a robust analysis workflow. For this project, damaged myocytes are fluorescently labelled with ProY (s. *Chapter 4*). Image analysis procedures for Procion dyes have changed over the last decades as supporting software became widely available. Originally, image analysis relied on manual procedures of scoring and counting ProY-positive cells [229, 267, 314]. More recently, analysis software like MATLAB and ImageJ have been integrated [313, 316, 318] to simplify the process and reduce bias. Thus, not only the percentage of damaged fibres [316] but also the area of damage [262, 263, 313, 318] became easier to measure.

To review common practices in microscopic setups and image analysis methods, 15 studies that used Procion staining on skeletal muscle were identified and analysed [229, 230, 262–265, 267, 311–318]. Unfortunately, the literature provided only limited detail on image acquisition and analysis tools. Three studies specified the excitation and emission settings of the epifluorescence microscope [230, 262, 314]; a further two gave a general indication of using a filter but without exact excitation and emission bands [317, 318]. Additionally, the way that cells were identified as ProY-positive was often unclear. Some researchers used thresholding methods [262, 264, 313, 316], in which the autofluorescence signal of a control sample was used as cut-off value above which cells were classified as damaged. All other papers did not specify what distinguished “stained” and “unstained” cells. Additional processing steps that are common practice in quantitative fluorescence image analysis like background subtraction or a conversion of images to greyscale before analysis were also rarely mentioned [313, 315]. Overall, the available information was insufficient to replicate methods for fluorescence image acquisition and analysis.

General literature on how to conduct a fluorescence imaging study [i.e. 322–325] highlighted common themes: reproducibility, repeatability, and the minimisation of bias. These principles guided the development and description of the microscopy and image analysis process for this study. Specifically, the proposed workflow was oriented towards a comprehensive checklist provided by Lee and Kitaoka [322] for an effective and rigorous fluorescence imaging experiment (**Figure 5-1**).

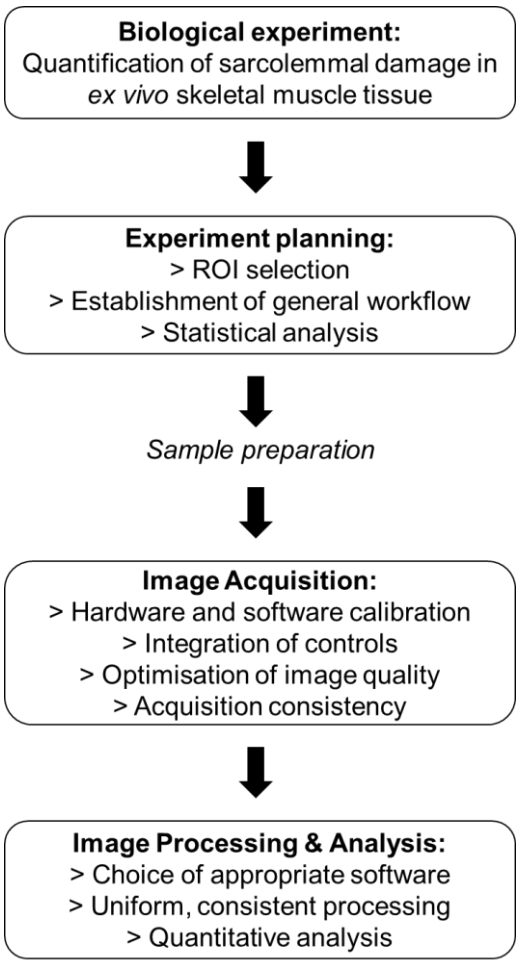

Figure 5-1: Imaging workflow. Based on workflow suggested by Lee and Kitaoka **[322]**. For details on sample preparation, see *Chapter 4*.

5.2. Aims of image acquisition and analysis development

The aim of this chapter is to describe a rigorous process for fluorescence image acquisition and analysis of ProY-stained samples from the *ex vivo* pressure injury model (described in *Chapter 4*). The desired output was quantitative cell death counts. By following guidelines framed by Lee and Kitaoka [322] and adhering to the principles of repeatability, reproducibility, and the reduction of bias, an effective fluorescence imaging and analysis workflow was developed. When combined with the *ex vivo* pressure injury model, reliable data on the influence of mechanical loading on skeletal muscle tissue health can be retrieved.

5.3. Planning of *ex vivo* loading experiment and imaging procedure

5.3.1. Imaging equipment and technique in use

5.3.1.1. Microscope and software specifications

All imaging was conducted on a Leica Microsystems TCS SP8 system with a Leica DMi8 inverted microscope. The added DFC7000T camera produces 12-bit images. The long working-distance objective with low 10x magnification (HC PL APO CS2, NA 0.4) provided a large field of view. This kept image acquisition times comparably low while still providing sufficient detail to distinguish single cells (**Figure 5-2b**). To capture the fluorescence of the samples and ProY stain, two long pass filters were fitted on the system: a FITC filter (ex 482/35, em 536/40) and a Y5 filter (ex 620/60nm, em 700/75nm).

The motorised stage of the microscope allowed to acquire series of images of a user-defined region of interest (ROI). The Leica LAS X software platform (Leica Application Suite X V.3.1.5.16308) then automatically divided the ROI into squares with an overlap of 10%. Each square was imaged in a bidirectional raster sequence and stitched together to create a large map of the ROI (**Figure 5-2a**). The resulting images were saved as .tiff files.

Images saved as .tiff files open as 32-bit RGBs in FIJI/ImageJ (ImageJ 1.53s, Java 1.8.0_172, 64-bit) [244]. The files were converted into 8-bit greyscale images using the following formula:

$$grey = (red + green + blue) / 3$$

This down sampling meant that 24-bit of information were compressed into 8-bit, losing part of the fine detail of the images. However, this reduction was necessary as the majority of operations in FIJI/ImageJ are based on 8-bit images. The thresholding feature for example, which other researchers used to analyse ProY-stained images [262, 264, 313, 316], only works on 8-bit greyscale images. After converting the images, further analysis could be performed.

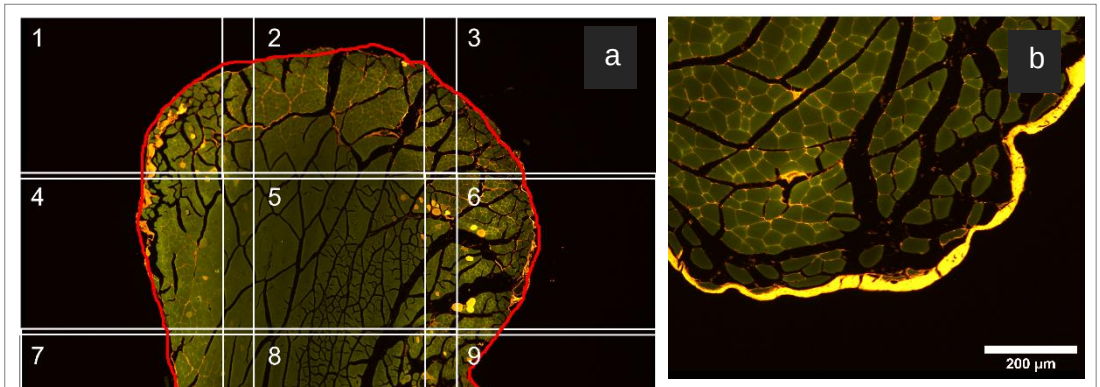

Figure 5-2: ROI and resolution of cross-sectional muscle sample. a) Red line indicates hand-drawn ROI surrounding full cross-section of muscle. White lines indicate borders of individual images that were stitched into larger map with 10% overlap. Numbers represent scanning order of the images. **b)** Magnification of square 14 with high resolution to distinguish single cell features. All images were taken with 10x objective.

5.3.1.2. Choice of ROI and definition of data output for analysis

Before image analysis, the ROI needed to be defined. Damage inflicted by transverse indentation of the muscle propagates away from the indentation site [198, 199]. To assess the extent of cell death, the full depth of the muscle should be investigated. The full cross-section of the skeletal muscle samples was therefore defined as ROI.

Within each cross section, the absolute number of damaged cells should be obtained and compared between experimental groups. Relative numbers, i.e. number of damaged cells divided by the total number of cells per cross-section, would be less meaningful, seeing as the indentation area was constant, irrespective of the muscle size. To verify the use of absolute cell death numbers, cell density was measured within the same sized ROI across five randomly selected samples. Single cells within each cross-section were segmented through Cellpose (s. "*5.5.3 Segmentation of individual cells from cross-sectional images of skeletal muscle tissue*") and automatically counted in ImageJ. The average number of particles/cells within the ROI was 364.4 ± 31.0. The coefficient of variation of $CV = 0.085$ was deemed sufficiently low to assume equal cell density across samples.

5.3.1.3. Choice of imaging technique

The last setting to decide as part of the experimental planning was the means of imaging. ProY-stained slides prepared for the preliminary experiments (s.*"4.7.1 Method for Live-or-Dye and Procion Yellow MX4R staining"*) were imaged in confocal as well as wide-field mode with identical settings.

A confocal approach was thereby less suitable for imaging fluorescently stained cross-sections of skeletal muscle tissue. The main reason was severe photobleaching of samples, most likely caused by high illumination. Although confocal imaging rejects out-of-focus light, areas above and below the focal plane are still illuminated [326]. Together with the longer scan times compared to widefield imaging, samples might be overexposed.

The usual benefits of additional depth information from confocal imaging are also less relevant for the analysed tissue samples. Samples consisted of thin transverse sections of 4µm width, which is far less than the average muscle fibre length of over a centimetre [275]. Even if sarcolemmal damage is restricted to only part of the fibre, it should be visible throughout the whole depth of each cross-sectional slice. Imaging in widefield mode should therefore be sufficient to obtain information on cell death.

Unlike in confocal mode, widefield imaging generated reproducible images of ProY-stained samples. Bleaching was only observed when samples were left in the microscope for extended periods (>30min) with open shutters (**Figure 5-3**). However,

Figure 5-3: Local photobleaching. Cross-sectional slice of skeletal muscle displaying photobleaching from extensively long illumination, demarcated by white semicircle. Yellow staining on top of muscle represents tendon attachment, as collagen is prone to ProY staining. Scale bar 1000µm.

this was a result of careless practice, not of the imaging mode. In the following experiments, shutters were therefore closed whenever possible, and samples removed from the microscope stage during breaks.

5.3.2. Power analysis and sampling

A suitable sample size was determined before conducting imaging experiments. The sample size should be sufficiently large to allow for reliable interpretation of the data but small enough to avoid unnecessary use of animals, resources, and time [327]. For this project, a “sample”, also known as experimental unit [327, 328], was equivalent to one isolated muscle.

To determine how many experimental units to include for every indentation condition to achieve statistically meaningful results, sample size calculations were needed. Differences in cell death counts between the indentation conditions were calculated through one-way ANOVA (analysis of variances) in Minitab (Vers. Version 19.2020.1). Accordingly, sample size calculations with the “Power and Sample Size” tool in Minitab were based on one-way ANOVA. Required input parameters were as follows: expected variability in the number of dead cells (standard deviation); maximum difference between mean dead cell counts; number of levels (how many categories are being compared); power (probability that a difference between groups is detected when this difference actually exists); and the significance level (probability that a difference is detected when this difference does not exist) [329].

Information on standard deviation and maximum difference between means is commonly derived either from preliminary experiments or relevant literature. Without any preliminary results available, three papers were identified that are similar to the proposed experiment; researchers compared the number of ProY-positive cells in murine extensor digitorum longus (EDL) muscles following eccentric contractions to undamaged control samples [267, 311, 330]. From these papers, standard deviations of the average number of ProY-positive cells and maximum differences between mean values were extracted for mechanically damaged and control samples (**Table 5-1**). The number of levels was set to three, as a maximum of three different indentation settings were planned to be compared in the experiments (static, low frequency dynamic, high frequency dynamic). The occurrence level for a type I error was set to $\alpha = 0.05$, allowing a 5% chance of false-positive results. The power was

defined as 80%, meaning that there is a 20% chance (β = 0.2) for false-negative results.

Table 5-1: Parameters for sample size calculations. The mean percentage of ProY-positive cells and variability for the mechanical damage and control group were taken from literature. Values in the control group that are marked with (*) were missing in the literature and assumed to be equal to zero. The maximum difference between means was calculated as difference in ProY$^+$ cells between group 1 and group 2.

	Group 1 (mech. damage)		Group 2 (control)		Max. difference between means
Source	Mean of ProY$^+$ cells [%]	Variability (SD) [%]	Mean of ProY$^+$ cells [%]	Variability (SD) [%]	
Petrof et al. [267]	4	0.5	1	0.25	3
Lou et al. [311]	3	0.8	0*	0*	3
Deconinck et al. [330]	1.8	0.15	0*	0*	1.8

With all required parameters defined, sample size calculations were performed for each dataset. The exact formulas and methods are detailed in [331]. The null hypothesis “no difference between group means” (H_0: $\mu_1 - \mu_2 = 0$) was tested against the alternative hypothesis “difference in means between the mechanically stressed and control group” (H_a: $\mu_1 - \mu_2 \neq 0$). The resulting estimated sample sizes are summarised in **Table 5-2**.

A maximum calculated sample size was $n = 3$. However, the software presents the calculated sample size as integers [332], meaning that the true value could be slightly above $n = 3$. Several other variables should also be considered. The mechanical loading protocols of the proposed transverse compression study differs from the referenced eccentric contraction experiments. Additionally, processing errors could make samples unusable for analysis, which would reduce the sample size dramatically. The sample size was therefore increased to $n = 5$, which is similar to sample sizes used in comparable research [33, 34, 212, 267, 311, 330].

Table 5-2: Estimated sample sizes for indentation studies on skeletal muscle tissue. Variability and minimal relevant difference values were taken from the sources indicated in column one. Sample sizes were calculated with one-way ANOVA with α = 0.05 and β = 0.2. The following hypotheses were tested: H_0: $\mu_1 = \mu_2$, H_a: $\mu_1 \neq \mu_2$)

Source	Variability	Minimal relevant difference	Calculated sample size
Petrof et al. [267]	0.005	0.03	2
Lou et al. [311]	0.008	0.03	3
Deconinck et al. [330]	0.0015	0.018	2

5.3.3. Data management

To ensure adequate documentation of the images and analysis steps, a data management plan was developed (s. Appendix E). A manual lab book was kept to capture metadata. The acquired images were saved on a computer hard drive as well as in a cloud storage and on an external hard drive for backup. All relevant data will also be made available on the pure network (https://pureportal.strath.ac.uk/) for future access.

Additionally, a consistent labelling system was adapted from the initial sample preparation through to the final images to ensure traceability. Samples were labelled systematically with:

(1) an abbreviation for the muscle (EDL or SOL)

(2) a consecutive number for the dissection

(3) either 1 or 2 to distinguish between the same muscle type from two different hindlimbs

(4) the letters “CTRL” (control) or “i" (indentation) to mark the intervention group.

An example is the label SOL14-1-CTRL for soleus muscle, dissection number 14, muscle 1, control. When mounting samples, an additional consecutive number was added, representing the microscope slide, to facilitate further differentiation when imaging cross-sections from the same sample.

5.4. Optimisation of the image acquisition procedure

With the experimental method and the general parameters of the experiment and analysis in place, suitable image acquisition settings were determined. Keeping acquisition parameters consistent between all specimen is key for comparability and to avoid bias [322, 323].

Alongside other parameters like filters and acquisition mode, three microscope parameters were optimised to generate high-quality images: intensity of the light source, integration/exposure time, and gain (signal amplification of the camera). The goal was to reach sufficient brightness and a high signal-to-noise ratio (SNR) without inducing phototoxic effects on the sample or over- or undersaturating the images [324]. Integration time and gain should also be adjusted to use the entire dynamic

range of the detector and avoid data clipping [323]. Performing this optimisation process on various samples, including mechanically loaded as well as control ones, ensures the suitability of the chosen settings for the full data set.

The effect of out-of-focus imaging on intensity measurements was also tested. This was necessary because variations in sample thickness and imperfect mounting lead to fluctuations in the optimal location of the in-focus plane when working with automated scanning of large samples.

5.4.1. Method to optimise image acquisition procedure

To assess microscopic settings, *n* = 5 different cross-sectional sample slices were randomly selected from preliminary experiments. They were taken from two EDL and three SOL muscles from different Sprague-Dawley rats. A further *n* = 5 cross-sectional slices from SOL muscles were used to assess the relevance of in-focus imaging on emission intensity measurements. Of those, *n* = 3 were from a mechanically loaded area, *n* = 2 were from control sections. For details on sample preparation, refer to "*4.3 General materials and methods for ex vivo experiments*". All slides were ProY-stained and imaged through an FITC filter on the Leica TCS SP8 system (s. *"5.3.1 Imaging equipment and technique in* use*"*).

One centrally located rectangular area per section was brought into focus. An exposure time of 2s, illumination intensity level of 3, and gain of 6 were set as starting values through trail-and-error. To establish image acquisition parameters, these settings were kept constant while adjusting one of the following: Illumination intensity level from 2-4; integration time from 1s to 2s to 4s; and gain level from 3 to 6 to 9.

To assess imaging across different focus planes, the in-focus depth of the allocated samples was established and an image taken. Next, the focus was changed by ±1µm and ±2µm, covering the full thickness of the approximately 4 µm thick sample slices. Exposure time, illumination intensity, and gain were kept constant.

All images were imported into FIJI/ImageJ for analysis. One sample was excluded from the image acquisition parameter group because of unclear metadata. For the remaining samples, mean greyvalue emission intensities were measured and documented. Additionally, histograms were viewed to detect potential saturation and assess contrast.

5.4.2. Results of image acquisition optimisation study

5.4.2.1. Effect of illumination light intensity level on image intensity measurements

A scatterplot was composed to visualise the measured mean intensity of cross-sectional skeletal muscle tissue when increasing the illumination light intensity across three levels (**Figure 5-4**). A positive relationship between illumination light intensity level and emission intensity was observed for all samples. This response can be described by a third-degree polynomial (R^2 = 98.41%). With rising illumination light intensity level, the between-sample variation in emission intensity increased as well (level 2: SD_2 = ± 1.92, level 4: SD_4 = ± 8.31).

The images recorded with the microscope increased in brightness when rising the intensity level of the illumination source (**Figure 5-5**). Looking at the corresponding histograms, two peaks are visible across all of them. The highest contrast marked by the widest range of emission intensity values is found at level 3, the smallest at level 2 with 170 and 105 greylevels respectively. At level 4, a sharp cliff is visible at a greylevel of 180, indicating signal saturation.

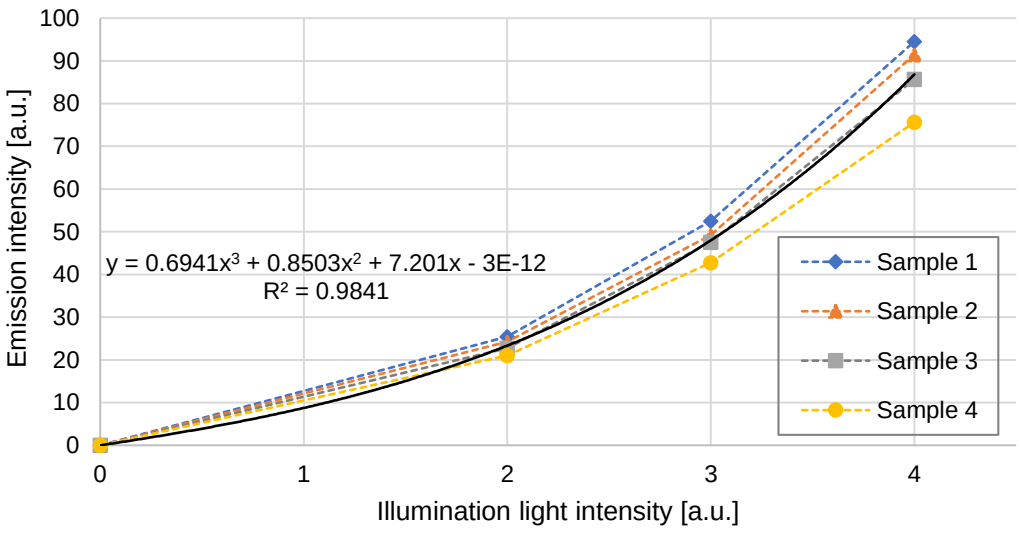

Figure 5-4: Comparison of illumination and emission light intensity. Four cross-sectional slices were prepared from ProY-stained murine EDL (*n* = 2) and SOL (*n* = 2) muscles. A centrally located ROI was imaged for each and emission intensity measured at increasing illumination light intensity. Integration time and gain level were kept constant. Illumination and emission light intensity were positively correlated for all four samples, following a polynomial function (bold black line) $y = 0.6941x^3 + 0.8503x^2 + 7.201x - 3E\text{-}12$ with $R^2 = 0.9841$. Standard deviations also increased from SD_2 = ± 1.92 at level 2 to SD_4 = ± 8.31 at level 4.

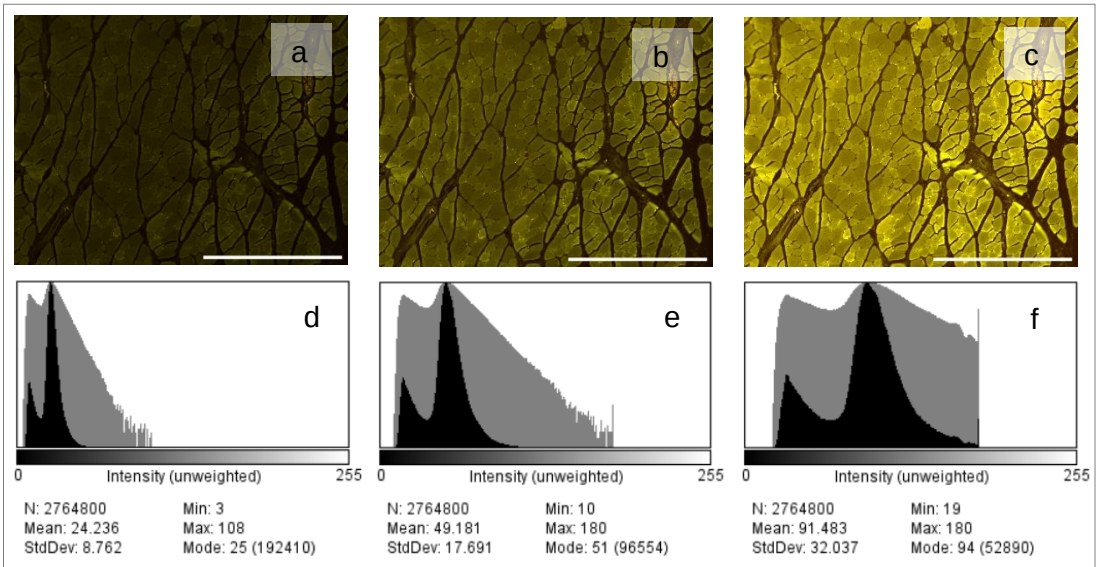

Figure 5-5: Effect of illumination intensity on emission intensity measurements. Images of representative ROI of skeletal muscle cross-section with the intensity of the illumination source increasing from 2 (a) to 3 (b) to 4 (c) leading to increasing brightness. The sample was prepared from ProY-stained murine EDL muscle and imaged at constant integration time and gain level. Scale bar: 500 µm. Corresponding histograms d, e, f depict emission intensities on standard (black) and log scale (grey).

5.4.2.2. Effect of integration time on image intensity measurements

To identify a potential relationship between integration time and emission intensity of the same four samples, a second scatterplot was created (**Figure 5-6**). Here, a linear dependence of the emission intensity on the integration time was observed, which could explain R^2 = 99.02% of the variance in the data. As before, the variability in measured intensities between samples increased with longer integration times (2s: $SD_2 = \pm 1.97$, 4s: $SD_4 = \pm 6.35$).

By increasing the exposure time, the brightness of the recorded images increased drastically (**Figure 5-7**). The histograms reflect this observation, with the highest mean emission intensity of 88.4 [a.u.] after 4s of exposure. The widest range of emission intensities was recorded after 2s of exposure with 168 greylevels. After 4s integration time, the greyvalues appeared truncated at 180 [a.u.].

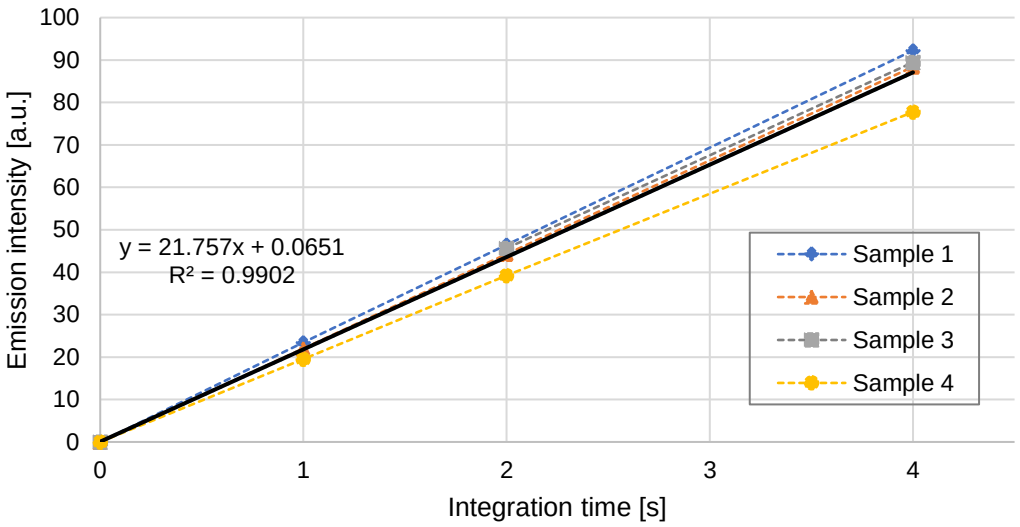

Figure 5-6: Comparison of integration time and emission intensity. Four cross-sectional slices were prepared from ProY-stained murine EDL (n = 2) and SOL (n = 2) muscles. A centrally located ROI was imaged for each and emission intensity measured at increasing integration time. Light source intensity level and gain level were kept constant. A direct, positive linear relationship (bold black line, y = 21.757x + 0.0651) was found between integration time and measured intensity across all four samples (R^2 = 0.9902). Standard deviations increased from SD_2 = ± 1.97 at 2s to SD_4 = ± 6.35 at 4s.

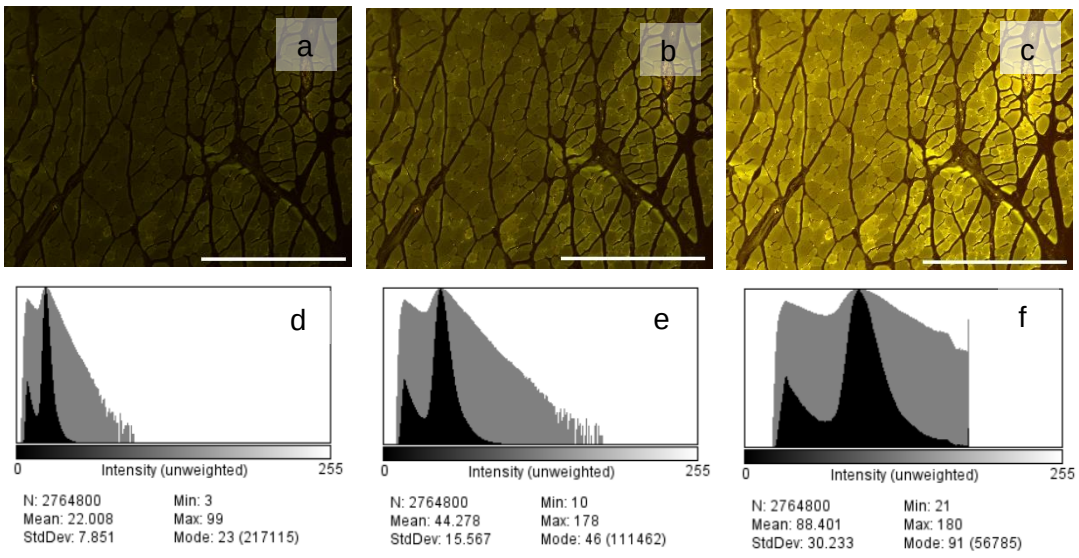

Figure 5-7: Effect of integration time on emission intensity measurements. Images of representative ROI of skeletal muscle cross-section with the integration time increasing from 1s (a) to 2s (b) to 4s (c) leading to higher brightness. The sample was prepared from ProY-stained murine EDL muscle and imaged at constant illumination light intensity and gain level. Scale bar: 500 µm. Corresponding histograms d, e, f depict emission intensities on standard (black) and log scale (grey).

5.4.2.3. Effect of gain adjustment on image intensity measurements

Similar to the effect of illumination light intensity on mean emission intensity measurements, the relationship between gain and emission intensity was positive and linear for all four samples (R^2 = 98.55%, **Figure 5-8**). The inter-sample variability increased with higher gain levels (gain 3: SD_3 = 1.58, gain 9: SD_4 = 5.75). The mean emission intensity of sample 1 at gain 9 deviated from the expected value. Instead of the calculated emission intensity of 65.02 [a.u.], a mean intensity of 42.65 [a.u.] was recorded. This data point was classified as outlier and excluded from analysis.

The brightness of the recorded images increased with higher gain levels (**Figure 5-9**). The corresponding histograms displayed the highest mean emission intensity of 59.34 [a.u.] and the widest range of greyvalues (167) at a gain level of 9. Additionally, the greylevel of 180 appeared to be a cut-off value.

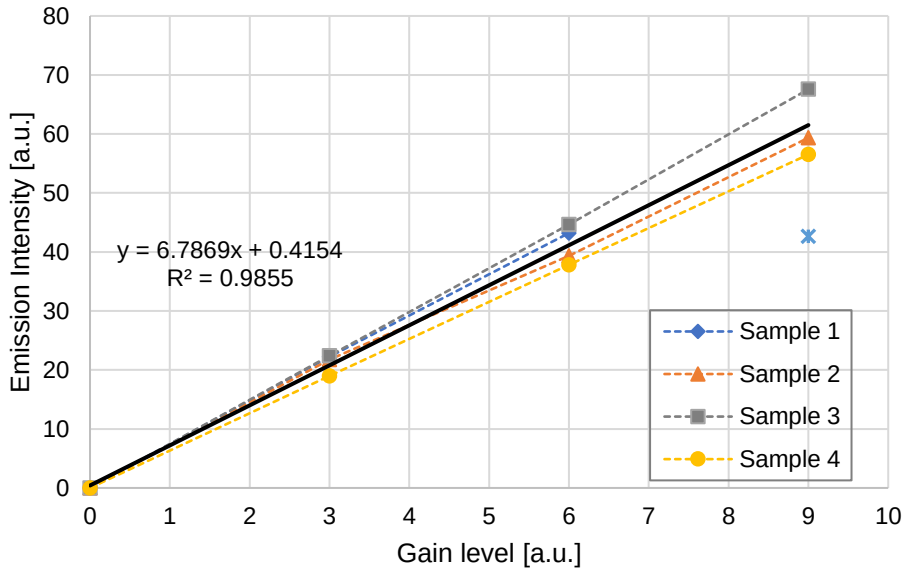

Figure 5-8: Comparison of gain level and emission intensity. Four cross-sectional slices were prepared from ProY-stained murine EDL (*n* = 2) and SOL (*n* = 2) muscles. A centrally located ROI was imaged for each and emission intensities measured at increasing gain level. Light source intensity level and integration time were kept constant. A direct linear relationship (bold black line, y = 6.7869x + 0.4154) was found between gain level and emission intensity (R^2 = 0.99). One outlier from sample 1 (gain level 9, intensity 42.65), which is marked with a blue cross, was removed from the analysis.

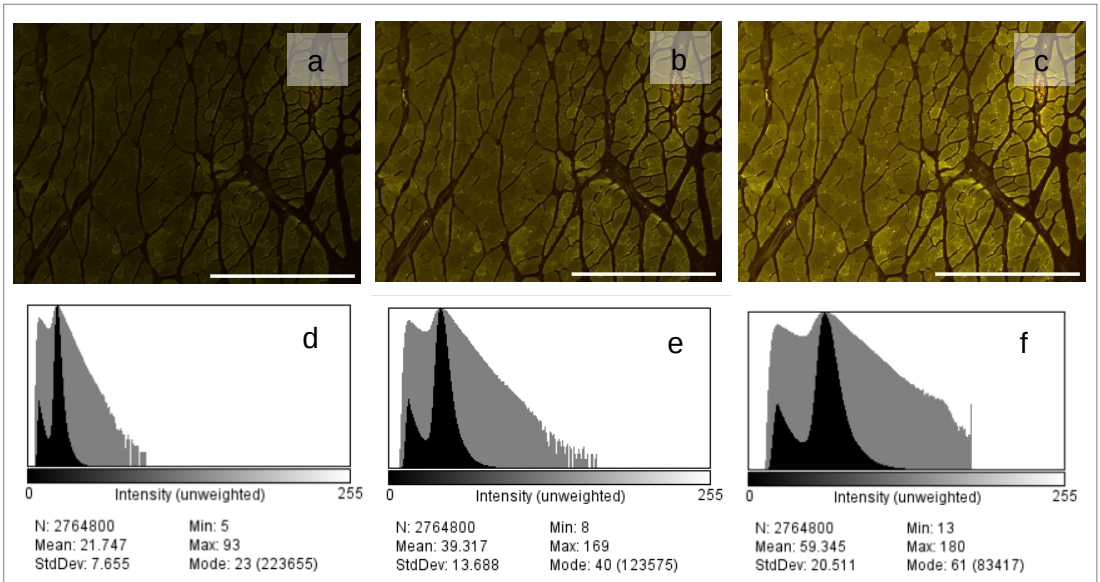

Figure 5-9: Effect of gain level on emission intensity measurements. Images of representative ROI of skeletal muscle cross-section with the gain level increasing from 3 (a) to 6 (b) to 9 (c) leading to higher brightness. The sample was prepared from ProY-stained murine EDL muscle and imaged at constant illumination light intensity and integration time. Scale bar: 500 µm. Corresponding histograms d, e, f depcit emission intensities on standard (black) and log scale (grey).

5.4.2.4. Effect of changes in focus on image intensity measurements

The average emission intensity of five samples was measured across different focus planes from “in focus” (0µm) to ±1µm and ±2µm, covering the full thickness of a sample slice. Emission intensity measurements peaked at the in-focus plane for all five samples (**Figure 5-10**) Outside of the in-focus plane, emission intensity remained relatively steady for each sample, the average standard deviation being SD = ± 2.63 [a.u.]. The highest between-sample variation was recorded for the in-focus plane (SD = ± 20.34 [a.u.]). When looking at types of samples, the mean emission intensity of the mechanically damaged samples 1–3 (avg. intensity = 69.47 ± 10.68 [a.u.]) was generally higher than for control sections 4 and 5 (avg. intensity = 39.62 ± 3.96 [a.u.]).

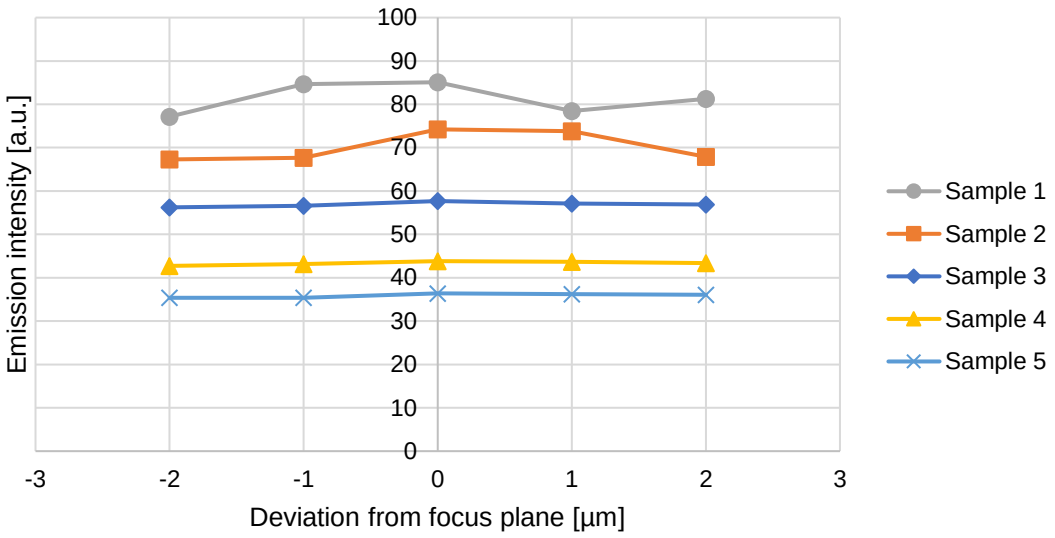

Figure 5-10: Effect of out-of-focus imaging on emission intensity measurements. Five cross-sectional slices were prepared from ProY-stained murine SOL muscles. Samples 1-3 represent ROIs from mechanically loaded areas, samples 4 and 5 from control sections of skeletal muscle. A centrally located ROI was brought into focus before being imaged and the focus moved ±1µm and ±2µm. Emission intensity was measured at constant illumination time, illumination intensity level, and gain level. The emission intensity values were relatively constant with a standard deviation of SD = ± 2.63 [a.u.].

5.4.3. Discussion on the microscopic settings for quantitative fluorescence imaging

Before performing any fluorescence image analysis, the microscopic setup needs to be tested. This includes finding a filter combination suitable for the fluorescent stain of choice; understanding the influence of microscopic imaging settings on intensity measurements; and validating the stability of the microscope.

The effect of illumination light intensity levels, integration time, and gain on mean emission intensities was tested as indication for the reliability of the system for the following quantitative cell analysis. Overall, the microscope produced stable output data. As expected, rises in integration time and gain were directly proportional to the measured intensity for all samples. The intensity also increased when intensifying the light emitted by the illumination source, although in a non-linear way, which is common for lasers [325]. All three parameters displayed the respective behaviour strongly across all samples ($R^2 \geq 98.41$), which indicates a high system stability.

The data had one outlier in the gain adjustment group at gain level 9. The most likely explanation for this is human error in the microscopic setup. This stresses the

importance of consistency and careful control of the acquisition parameters before taking each image.

5.4.3.1. Establishing optimal image acquisition parameters

The suitability of acquisition parameters can also be assessed based on the distribution of greyvalues within an image. The histograms for changes in light source intensity, integration time, and gain level (**Figure 5-5, Figure 5-7, Figure 5-9**) revealed similar trends as the emission intensity measurements. At the lowest chosen levels, i.e. light source intensity 2, integration time 1s, gain level 3, histograms were positively skewed with a low signal range. This indicates that settings need to be optimised by increasing the respective parameters for an effective use of the intensity range and improved contrast [333]. At the highest chosen levels on the other hand (light source intensity 4, integration time 4s, gain level 9), data appeared truncated. This cut off is attributable to software offset settings which provide a pre-defined correction for noise. Parts of the images were oversaturated and intensity and spatial resolution information was lost [324]. This oversaturation was also apparent when imaging highly damaged areas with an integration time of 2s (data not shown). The optimised imaging parameters were therefore chosen as follows: Light source intensity 2, integration time 1s, gain level 3.

5.4.3.2. Influence of focus on image intensity measurements

Reducing the impact of out-of-focus imaging on emission intensity measurements is crucial for quantitative analyses, especially when producing large-scale tiled images. One factor is inconsistencies in sample thickness and mounting, which might be minimised by rigorous preparation practices but are still unavoidable.

As expected, the highest emission intensity values and the highest between-sample variability were apparent at the chosen “in-focus” plane. Nevertheless, the Leica LAS X software’s auto-focus function can help to maintain that the focus throughout the imaging process of a full cross-section. It is based on intensity measurements as well as sharpness and spatial distribution. Small deviations caused by differences in sample thickness and uneven mounting can therefore be counteracted.

The results also indicate that operating “in focus” provides the optimal environment to detect differences between samples. More importantly, however, moving out of focus

only seemed to have a minor effect on overall emission intensity measurements (standard deviations <10% of maximum emission intensity).

5.4.4. Limitations of the preliminary studies to find optimal image acquisition parameters

The preliminary studies to find optimal image acquisition parameters come with a few limitations. First, limited human capacity made blinding between the imaging and analysis impossible. Potential bias was nevertheless reduced by following a predefined acquisition and analysis protocol.

Montero-Llopis et al. [325] also suggest to measure irradiance (power density) to identify potential light source instabilities between the beginning and end of an imaging session as well as between imaging sessions [325]. Unfortunately, suitable tools were unavailable. However, the system, including the light source, is serviced regularly to identify and correct potential instabilities. Additionally, other sources of variability were minimised. Dedicated cooling systems for the hardware and temperature- and moisture-control systems for the whole room were in place to allow for consistent imaging conditions and reduced dark noise effects. Samples were also stored in adequate slide boxes, handled at dimmed room light, and imaged inside a shielded chamber to minimise environmental light impact and minimise variability.

5.4.5. Summary of optimised image acquisition parameters for quantitative fluorescence imaging

In summary, working with the described image acquisition parameters (light source intensity 2, integration time 1s, gain level 3) in the in-focus plane is advisable for optimal results. Small deviations in focus seem negligible as they had no major influence on emission intensity measurements and could be controlled with the autofocus function of the microscopic system. To minimise other sources of variability, controlling environmental settings and taking care with sample handling should be paramount when collecting quantitative data.

5.5. Development of a workflow for fluorescence image processing and analysis

To ensure reliable, high-quality results, analysis protocols for fluorescence images should be unbiased and repeatable. However, natural and artificially introduced variability in fluorescence signals complicates the compilation of multiple biological samples into comparable data. The challenge lies in identifying a suitable combination of potential analysis steps and tools to filter out the information of interest. For this project, the goal was to quantify cellular damage in ProY-stained samples from the *ex vivo* animal model. The premise was therefore to develop a sensitive workflow that works on samples with strong, minor, or no mechanical damage. Consistency across all intervention groups was key to ensure comparability [322, 334].

In the past, researchers have published studies using ProY on skeletal muscle tissue [263, 265, 267, 311–313, 315, 330, 335, 336]. A common feature in their image analysis protocols was the use of thresholding and segmentation. Based on the working principles of fluorescent dyes, ProY-positive fibres differ from negative ones by an increase in fluorescence emission intensity. To distinguish between high and low intensity areas, one usually needs to establish a baseline signal (= no damage). This baseline signal can function as threshold, above which fibres are classified as ProY-positive and therefore injured.

Manual operations like tracing and counting (i.e. [267, 314, 337]) were avoided because of the vast number of images to be processed for this study and the risk for bias. Instead, the following semi-quantitative procedure was adapted:

1. Pre-processing: improves image quality
2. Segmentation: partitions images into objects of interest, i.e. myocytes
3. Thresholding: divides images based on pixel values into foreground and background, i.e. ProY-positive and ProY-negative myocytes
4. Particle analysis: automatically counts segmented objects in the foreground

While the majority of papers on ProY imaging shared these procedural steps (i.e. [262, 264, 313, 316, 318]), detailed descriptions were sparse. Hence, the following paragraphs will refine the general image analysis workflow.

Identifying suitable procedures for each of the four steps of pre-processing, segmentation, thresholding, and particle analysis was not a linear process but needed multiple iterations. However, to aid understanding, the linear structure will be followed when detailing each step in the next paragraphs. For clarification, unstained samples that only emit autofluorescence signal will be referred to as “autofluorescence” and ProY-stained control samples from outside the indentation zone of a muscle as “CTRL”. “Intensity” means emission intensity unless specified otherwise.

5.5.1. Background subtraction for fluorescence imaging

Background signal was determined for every image to account for potential variation in microscopic hardware, i.e. differences in illumination by the light source between sessions. As other researchers suggested [i.e. 315, 338, 339], n = 5 areas on a microscope slide without any tissue were selected, mean intensities recorded, and the average values subtracted from every pixel in the image. This was favoured over the “rolling ball” algorithm[3] [i.e. 340], as later processing corrects potential spatial variations in illumination.

5.5.2. Image normalisation for ProY-staining

The next pre-processing step was image normalisation. In this project, different mechanical insults can lead to an increased intracellular fluorescence induced by ProY staining. However, differences in hardware performance between imaging sessions, amongst others, can introduce unwanted technical variability to intensity measurements. Despite the benefits and importance of image normalisation, protocols for ProY-stained samples were unavailable from literature (s. “*5.1 Introduction to fluorescence image analysis*”).

5.5.2.1. Approaches for image normalisation

One common approach for normalisation in image analysis, including MRI and histological images, is quantile normalisation [341–343]. In this technique, the samples signal distributions are aligned with each other to correct for intra-sample variations. However, having only few positively stained cells - as it is expected in

[3] The “rolling ball” algorithm uses a circular area around a pixel to determine an average background intensity value that is then subtracted from the original image.

mildly damaged samples – might change the overall intensity profiles [344] and skew the results.

Another possibility is using an additional image feature as reference. This feature should exert constant intensity, irrespective of the intervention [345]. One option is using reference standards [346] like fluorescence probes or beads that are introduced to each sample. Needing additional processing steps and potentially adding another source of variability, this option was disregarded. Instead, the use of an internal standard was explored.

5.5.2.2. Proposal for normalisation procedure for ProY-stained images

The previous spectral analysis of ProY determined the stain's excitation and emission characteristics ("*4.6 Spectral analysis of fluorescence signal of stains and skeletal muscle tissue*"), which were imaged through an FITC filter. A reference image taken at a ProY-insensitive wavelength could then be used as an internal standard for normalisation. This removes intensity variations stemming from different section thicknesses and non-uniform illumination.

ProY has its peak excitation and emission around 480nm and 534nm respectively. However, the fluorescence emission tends to zero in the longer wavelength regions (≥ 650nm). The ProY signal recorded with a Y5 filter, which was used previously for LoD stained samples, would therefore be minimal, as its excitation and emission bandwidths are ex 620/60nm and em 700/75nm. (*"4.6.2 Spectral characteristics of skeletal muscle tissue and fluorescent stains"*).

From a technical point of view, the microscope can change the filter set and repeatedly image the same cross-section. It is therefore possible to take consecutive images of the same ROI with both the FITC and Y5 filter. Through arithmetic operations in FIJI/ImageJ, a ratio of the FITC signal divided by the Y5 image can be obtained to normalise each image. By working with "floating point", a non-byte format in which images are not quantised until after the division process, potential loss of information is minimised.

5.5.2.3. Suitability of Y5 as internal standard

Before applying the proposed Y5 normalisation procedure, the general suitability of Y5 images as internal standard was tested on five mechanically damaged samples.

For each sample, a representative cross-section was chosen for which three ROI were selected from damaged areas and three from unloaded areas in the periphery. Images were taken under identical settings as described previously (s. *"4.3.5. Discussion on the microscopic settings for quantitative fluorescence imaging"),* with an integration time of 4s for the Y5 filter to obtain sufficient signal. After recording the mean intensity of each ROI with FIJI/ImageJ, Mann-Whitney tests were performed in Minitab because of non-normal data distribution. FITC and ProY intensities were compared for the "indented" and "control" condition ($p \leq 0.05$).

Analysis of the FITC-filtered images revealed a statistically significant difference in intensity between indented and control areas of the muscle ($p = 0.000$) with the median intensity more than doubling (2.75-fold increase) (**Figure 5-11**). Y5-filtered images on the contrary had a similar level of intensity for both groups ($p = 0.309$). Y5-filtered images therefore seemed to provide a constant intensity value irrespective of the loading condition. This makes them a potential candidate as internal standard for image normalisation.

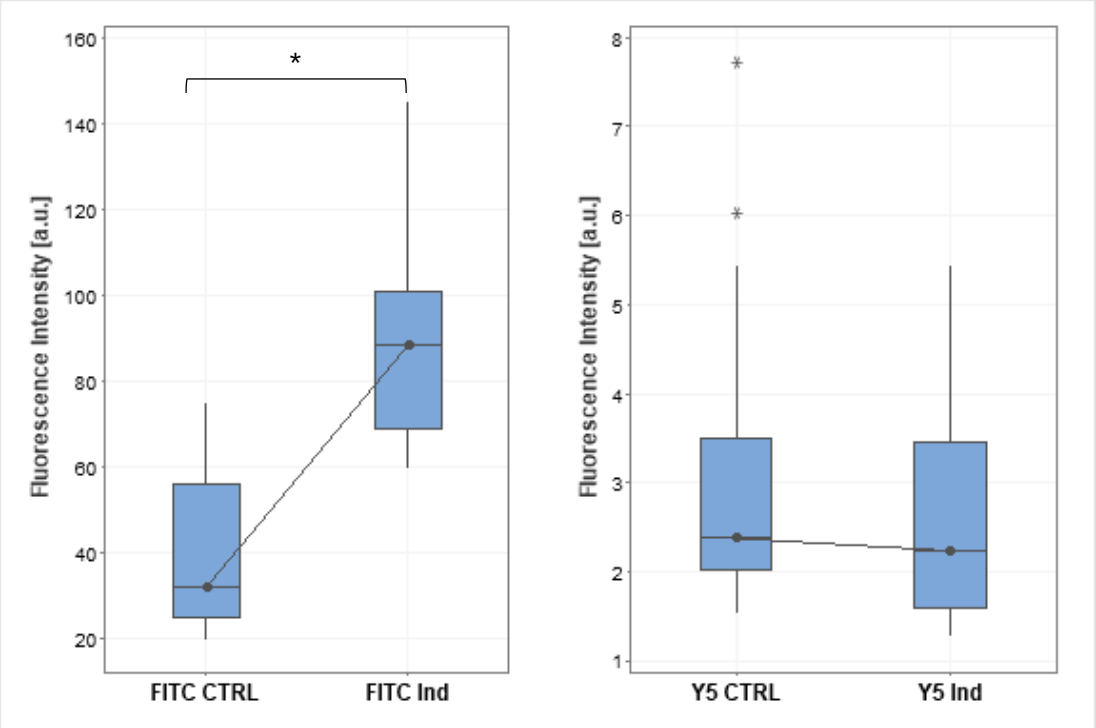

Figure 5-11: Suitability of imaging with Y5 filter as internal standard for ProY-stained samples. Median intensities from $n = 5$ fluorescently stained cross-sections of murine skeletal muscle were compared with Mann-Whitney tests ($p \leq 0.05$). Three ROI each were selected from a mechanically damaged area of the cross-sections ("Ind") and its undamaged periphery ("CTRL"). Each ROI was imaged with an FITC filter to capture ProY and a Y5 filter outside of the ProY stain's spectral response. While the median fluorescence intensity captured with the FITC filter increased significantly between control and indented areas ($p = 0.000$, "+"), no such change was observed with the Y5 filter ($p = 0.309$).

5.5.2.4. Benefit of Y5 normalisation for image analysis

Next, the potential benefit of adding a Y5-based normalisation protocol was investigate on two successive cross-sections. Although they were taken from the same mechanically damaged sample, their overall intensity varied significantly. To get an indication for the suitability of the normalisation protocol, both cross-sections were analysed with and without normalisation.

In brief, background was subtracted for each image before an identical segmentation process was applied (s. "*5.5.3 Segmentation of individual cells from cross-sectional images of skeletal muscle tissue*"). Next, two different thresholds were obtained, one from normalised and one from non-normalised control images (s. *"5.5.4 Thresholding to identify ProY-positive cells"*). These thresholds were applied to the segmented images prior to visual assessment and automated dead cell counting. Without normalisation, the cells identified as damaged in the first cross-section were almost identical with the ProY-positive cells in the raw image (**Figure 5-12 a, b**). In the second cross-section, however, almost the whole area was classified as damaged (**Figure 5-12 d, e**). This discrepancy between the two cross-sections could be attributed to the higher overall brightness of the second cross-section. Despite the use of image-specific background subtraction, this difference was not accounted for before applying the global threshold. Accordingly, the analysis workflow without normalisation seems unsuitable for universal analysis.

Adding a normalisation protocol improved the accuracy of the analysis workflow. The location of dead cells correlated well with the raw images for both cross-sections (**Figure 5-12 c, f**). This is underpinned by the quantitative dead cell count for each scenario (s. "*5.5.5 Particle Analysis to quantify ProY-positive cells*"): The number of dead cells for the non-normalised image differed by n = 1681 (n = 345 in the first cross-section, n = 2062 in the second). After normalisation, n = 204 and n = 278 dead cells were counted respectively. This proves the improved accuracy when quantifying cell damage with the normalisation protocol. The combination of normalisation, segmentation, and global thresholding therefore seems suitable to reliably detect dead cells from ProY-stained muscle cross-sections.

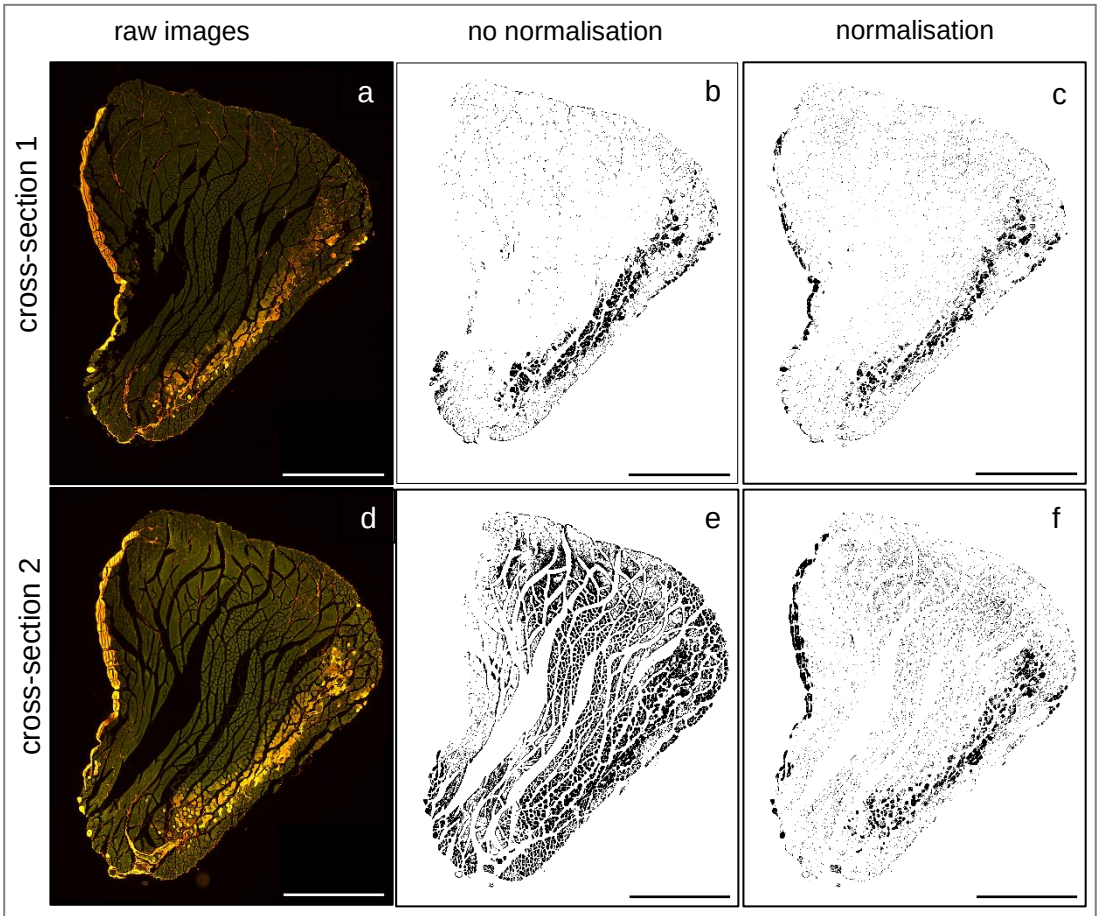

Figure 5-12: Comparison of thresholding with and without normalisation. The first column (a, d) displays raw images of two cross-sections from the same mechanically damaged muscle taken with a few hundreds of microns distance between each other. Yellow staining indicates ProY-positive (= dead) cells. The second column (b, e) displays the images following the segmentation process without normalisation to identify damaged cells (black colour) via thresholding. The majority of the second cross-section is classified as damaged when applying the threshold (e). The last column (c, f) displays the same images but with normalisation, showing similar amounts of damage across both cross-sections. Scale bar = 1000µm.

5.5.2.5. Validation of Y5 normalisation for the image analysis of ProY-stained muscle samples

An internal standard should be applicable to all experimental conditions [347]. The validity of Y5 normalisation was therefore tested on three representative samples: a heavily damaged muscle (2h static loading with 2.88g), one with minor damage (1h static loading with 33g), and one without damage (2h static loading with 1.6g). A total of n = 12 cross-sections were analysed for each muscle. Six of them were control samples from the periphery, the other six from the indentation area. Two images were taken for each cross-section, one with the FITC filter, one with the Y5 filter.

For analysis with FIJI/ImageJ, background signal was subtracted from each image. Next, FITC images were normalised by division with Y5 images of the same cross-section. Images from the control area were then segmented and the mean intensity measured. The mean intensity across the six control samples was averaged and set as threshold for the indented samples (s. "*5.5.4 Thresholding to identify ProY-positive cells*"). Following thresholding, the indented cross-sections were also segmented (for details s. "*5.5.3 Segmentation of individual cells from cross-sectional images of skeletal muscle tissue*") and the remaining dead cells counted (s. "*5.5.5 Particle Analysis to quantify ProY-positive cells*").

The image analysis workflow, including the normalisation protocol, seemed to identify cell death correctly across all three categories of damage. The sample appearing most heavily damaged (i.e. major ProY-positive staining) had an average dead cell count of $n = 296 \pm 67$ dead cells. In the medium damage sample (i.e. minor ProY-staining), $n = 162 \pm 50$ dead cells were counted. The least damaged sample (i.e. very few ProY-positive cells) had an average of $n = 49 \pm 21$ dead cells. Comparing the produced damage masks with raw ProY-stained images, areas of cell damage and intense ProY-staining appeared to overlap (**Figure 5-13**).

One limitation of Y5 normalisation was the possibility of a slight shift of the microscope slide when changing between FITC and Y5 filters, potentially caused by the mechanical impact from the filter movement. Without precise overlap of both images, normalisation is impossible. However, this scenario was a rare exception as the microscope and its moving parts are well dampened to avoid any uncontrolled movement.

With the normalisation process in place, the workflow seemed to be sensitive enough to identify dead cells across the full damage range expected from the experimental *ex vivo* setup. Normalisation of FITC-filtered images with Y5-filtered images was therefore added to the standard imaging workflow.

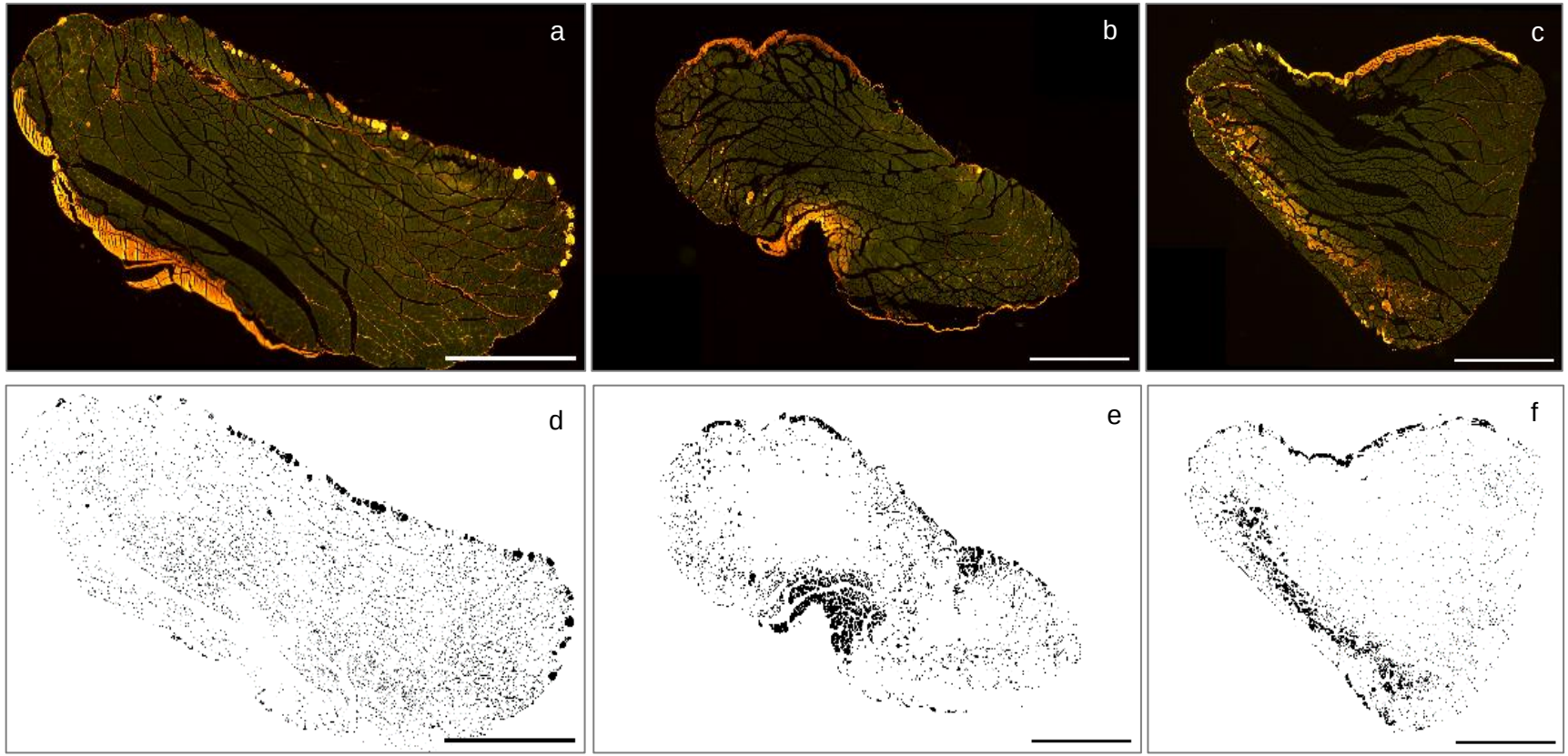

Figure 5-13: Representative images of the image analysis workflow including normalisation. In the top row are raw images of minimally (a), moderately (b), and heavily damaged (c) skeletal muscle cross-sections. The bottom row (d, e, f) displays the corresponding background subtracted, normalised, segmented, and thresholded images that enable dead cell counting. Good agreement between the ProY-positive cells in the raw (orange) and processed images (black) can be seen across all three damage levels. Scale bar = 1000µm

5.5.3. Segmentation of individual cells from cross-sectional images of skeletal muscle tissue

Skeletal muscle contains not only myocytes but also small blood vessels, the endo-, peri-, and epimysium, fascia, and tendons among others. When the muscle is submerged in ProY, the stain highlights not only membrane impaired cells but also connective tissue structures. Hence, images should be segmented to enable exclusive analysis of myocyte-related ProY signal.

5.5.3.1. Automatic thresholding with ImageJ

First, segmentation operations available in FIJI/ImageJ were tested. Automatic thresholding is commonly used in cell counting protocols [338, 339, 348]. Compared to manual methods, it increases reproducibility, reduces the risk for bias and variability, and enables automatisation. Several methods are readily available in the "Auto Threshold" plugin in FIJI/ImageJ, for example the Isodata and Otsu algorithm.

All automatic thresholds in FIJI/ImageJ were tested on a representative image of a control sample. Several algorithms produced images with lacking contrast or wrongly assigned parts of the muscle to the background; others correctly displayed the overall shape of the cross-section but were unable to identify single cell structures (**Figure 5-14a**). Attempts to segment these images further into single cells through various combinations of filters and operations like "watershed" and "find edges" failed to achieve the intended segmentation. This may be ascribed to the tight structure of skeletal muscle with touching fibres as well as weak contrast of the borders between cells. While the achieved detail may be sufficient to obtain a general threshold value from control samples, it is unsuitable for cell counting. Having the consistency across the analysis process in mind, the use of automated thresholds was therefore disregarded.

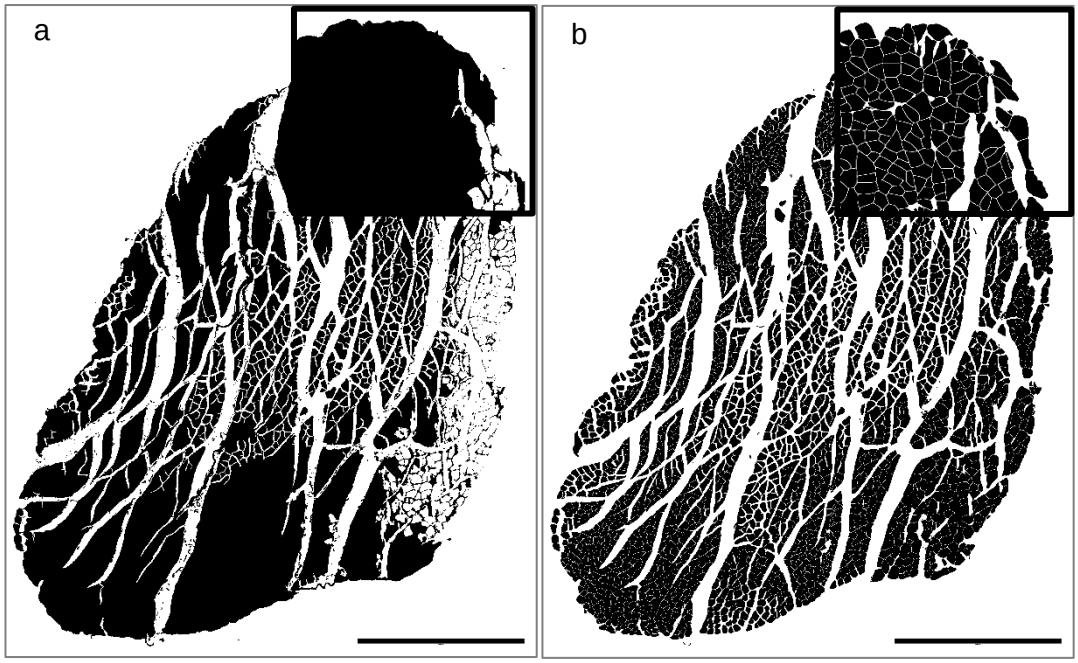

Figure 5-14: Segmentation of skeletal muscle cross-section. (a) Densely packed top and bottom areas of the cross-section are not separated into individual cells (all black) with the Otsu algorithm. On the right side of the cross-section, cells are falsely assigned to the background (white). **(b)** Segmentation with Cellpose algorithm successfully distinguishes single cells (black) throughout. Scale bar = 1000µm. Insets on top right corner display magnification of upper edge of samples for more detailed view.

5.5.3.2. Segmentation algorithms

Possible alternatives for segmentation are algorithms with a specific focus on segmentation of skeletal muscle tissue. Over the last decade, several approaches for the segmentation process of histologically and fluorescently stained muscle have been published [349–358]. The majority is compatible with FIJI/ImageJ and freely available. However, upon testing, many programs were difficult to install, required extensive training of the underlying model, or needed specific staining combinations for successful segmentation. One algorithm that seemed promising was Cellpose [358], which has been trained and tested on various cell types and shapes.

The suitability of Cellpose (v0.7) for image segmentation was tested on fluorescently stained skeletal muscle cross-sections (**Figure 5-14b**). The program was run through Google Colab to avoid issues with run speed caused by the large size of imaging files [359]. The GUI (graphical user interface) version was also downloaded to convert the files created in Colab into .png format for further processing in FIJI/ImageJ.

5.5.3.3. Running Cellpose

Cellpose requires the input of an average cell diameter. This value is either estimated by the program on a per image basis or added by the user. As providing an average value speeded up the processing times considerably, cross-sections of n = 2 mechanically damaged and n = 2 control samples were used to estimate an average cell diameter by Cellpose. The cell diameters averaged to 55.8 pixels (px), which was thereafter used as input for the program.

For segmentation, the background-subtracted and normalised images were imported to Colab via Google Drive. The code was adjusted to run the 'cyto' model to segment the cytoplasm from greyscale images with the previously defined average cell diameter. The script was run in batches of three images at a time to avoid disconnection caused by limited RAM capacities. The runtime for each batch was approximately 4-6min, excluding installation, import, and export times. Once the process was completed, the resulting files were saved in .npy format and downloaded. Each file was opened in the GUI before being saved as .png.

5.5.3.4. Validation of Cellpose

The segmentation process was validated on the same three samples as the normalisation procedure, representing no damage, minor damage, and heavy damage. For each sample, both indented and control areas with n = 6 cross-sections each were segmented, following the process described above.

The segmentation algorithm seemed to work well across the cross-sectional area of both damaged and control samples (**Figure 5-14b**). Neither odd cell shapes in heavily indented areas nor strong ProY-staining impaired the quality of the segmentation.

Minor problems arose in blurry areas, where cells were either segmented in larger groups or divided incorrectly. This can be avoided by visual assessment of out-of-focus areas during imaging. Alternatively, additional membrane stains like laminin could be used in the future to visualise cell borders more clearly instead of relying solely on autofluorescence signal. Nevertheless, potential small deviations from the true segmentation were considered a minor drawback seeing as the cell-death count for each sample was averaged across six individual cross-sections.

Another source of error in the segmentation process was the tendon visible in several images (**Figure 5-15**). Whilst the algorithm could distinguish small ProY-stained

connective tissue structures and vessels from myofibers, the size and shape of tendons was seemingly more difficult to differentiate. With the strong ProY-signal transmitted by tendons, considering them as myofibers could skew the cell death count. It was therefore necessary to manually remove large tendons from cross-sectional images before the segmentation in Cellpose.

Overall, the Cellpose algorithm segmented individual cells in both control and indented samples successfully. It was integrated into the standard image analysis procedure.

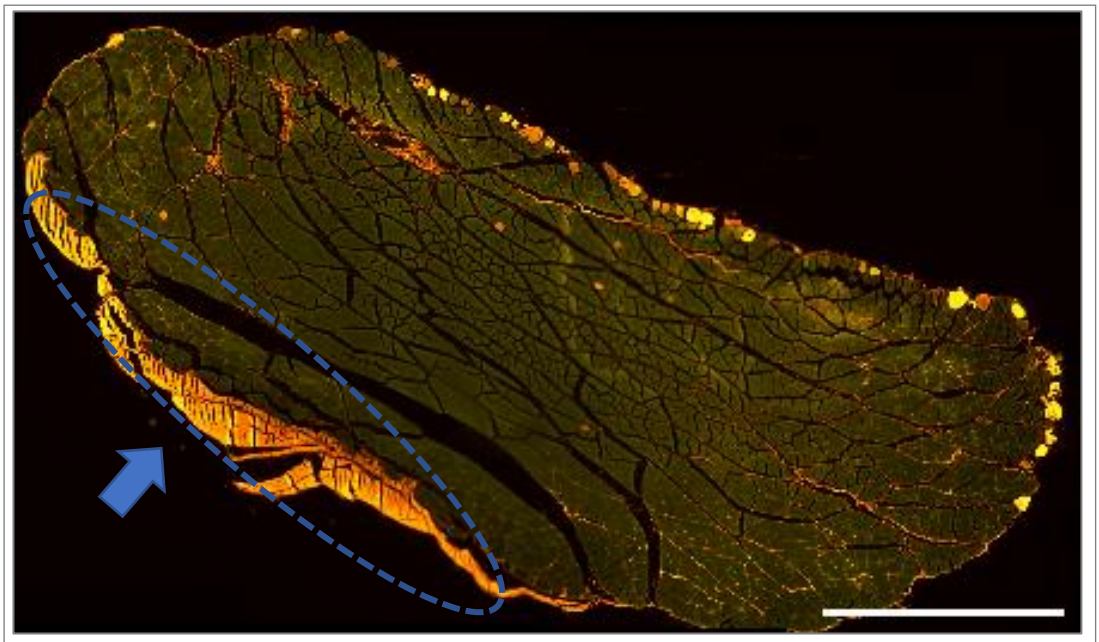

Figure 5-15: ProY-stained tendon structure (blue arrow). High collagen content makes tendon structure strongly fluorescent after ProY-staining. Segmentation with Cellpose might not be able to distinguish it from skeletal muscle cells, leading to potential errors when counting the number of dead cells. Tendon structures were therefore manually removed from images prior to segmentation. Scale bar 1000µm.

5.5.4. Thresholding to identify ProY-positive cells

Thresholding describes the process of dividing the pixels of an image into foreground and background, creating a binary image. In this project, greyscale values above a certain threshold represent ProY-positive cells and would therefore be considered foreground, while everything below turns into background.

Setting the threshold value for each image manually has several limitations. The reproducibility of this process is very low. It also has a high risk for bias, high intra-

and inter-user variability, and is incompatible with (semi-)automatic processing [344, 360]. Instead, an objective process was needed to obtain suitable threshold values.

5.5.4.1. Thresholding with autofluorescence controls

In the past, researchers used unstained muscle samples to determine the autofluorescence signal of skeletal muscle tissue [264, 316]. This then served as threshold to single out Procion-positive cells in the intervention group. A similar attempt was made in this project to define the autofluorescence intensity of muscle samples which could serve as ProY threshold.

After isolating *n* = 2 SOL muscles from a Sprague-Dawley rat, each sample was processed into six cross-sections (s."*4.3.4 Tissue processing through formalin fixation and paraffin embedding*"). Each section was imaged with an FITC and a Y5 filter on a Leica SP8 system, as described under "*5.5.2 Image normalisation for ProY-staining*". Next, background subtraction, normalisation, and segmentation were performed before measuring the average intensity of the segmented images. Their mean value was used as threshold level on a representative set of mechanically damaged cross-sections (s. **Figure 5-12**) and their controls to gauge the effectiveness of the threshold.

The average intensity of the unstained samples measured with the FITC filter was 9.5 ± 1.19 [a.u.]. When applying this threshold to the representative dataset, the majority of the muscle cross-sections lay above the threshold, although damage was visibly restricted to a small area (**Figure 5-16b**). The same was true for the respective control samples which originally displayed no obvious ProY-staining but had vast areas classified as above the threshold.

These results indicate that the intensity threshold obtained from unstained samples was not universally applicable to either mechanically damaged muscle or control samples. Overall, intensity measurements of unstained samples were unable to differentiate between ProY and autofluorescence signal.

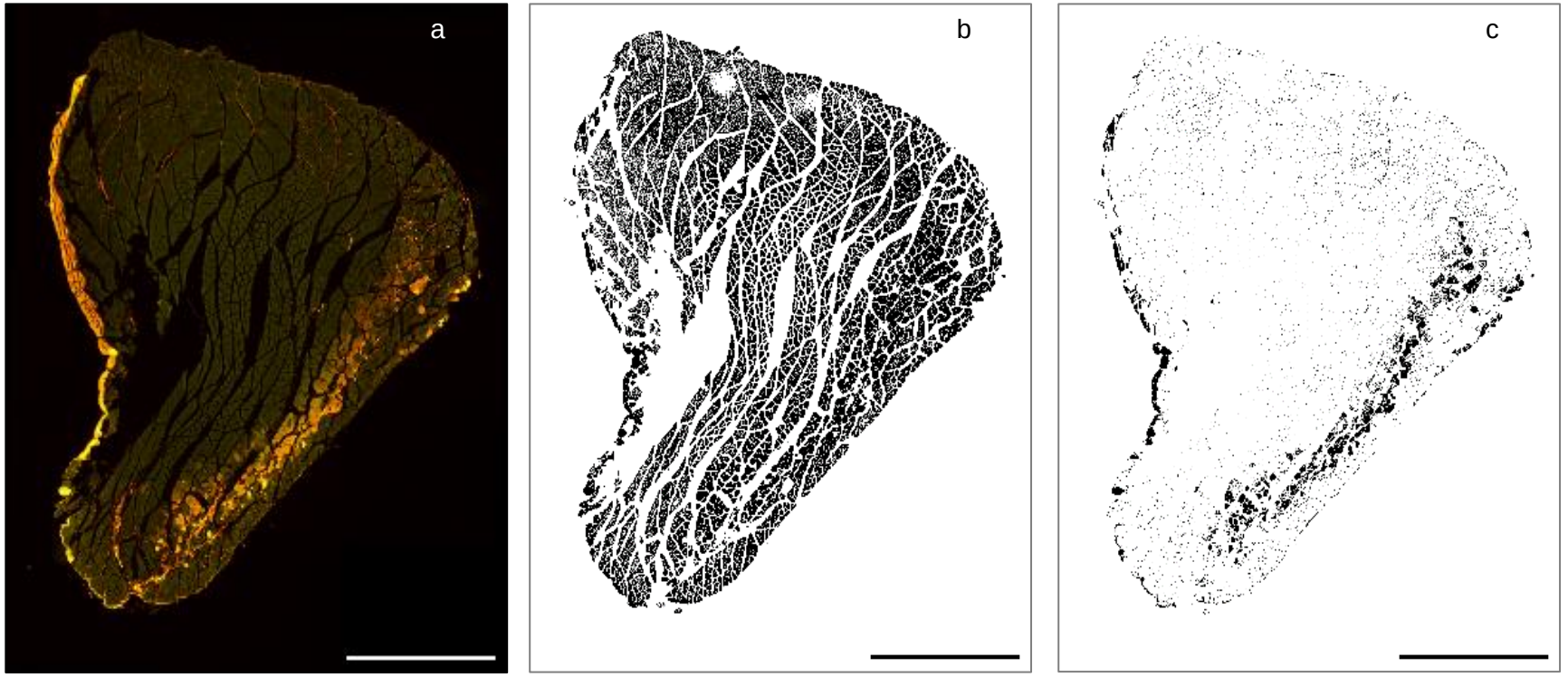

Figure 5-16: Thresholding of skeletal muscle cross-sections. (a) raw image with ProY-positive cells in orange. (b) unsuccessful thresholding with value obtained from unstained, autofluorescence samples, classifying the full muscle as ProY-positive (black). (c) successful thresholding with value obtained from stained control samples. Only cells indicating orange staining in raw image classified as damaged (black). Scale bar = 1000µm.

5.5.4.2. Comparison of intensity measurements from unstained and stained samples

To get a better understanding of the cause for the failed intensity thresholding with unstained samples, the images of the preliminary thresholding study were analysed further. Average intensities of FITC-filtered images were compared for each group (unstained control, stained control, stained damage). Further spectral analysis was performed to compare an additional set of unstained (n = 2) and stained (n = 2) muscles. The samples were processed into cross-sections and ROI were imaged on the Leica SP8 system with 10x magnification and an excitation wavelength of 488nm. The spectral response was recorded from 500nm – 735nm em in 15nm intervals and compared between the stained and unstained group.

Quantitatively, stained control tissue appeared 1.4-fold brighter than the unstained autofluorescence samples. The spectral analysis of the added samples showed a similar trend: stained controls produced a higher fluorescence response across the full emission spectrum compared to the unstained group (**Figure 5-17**).

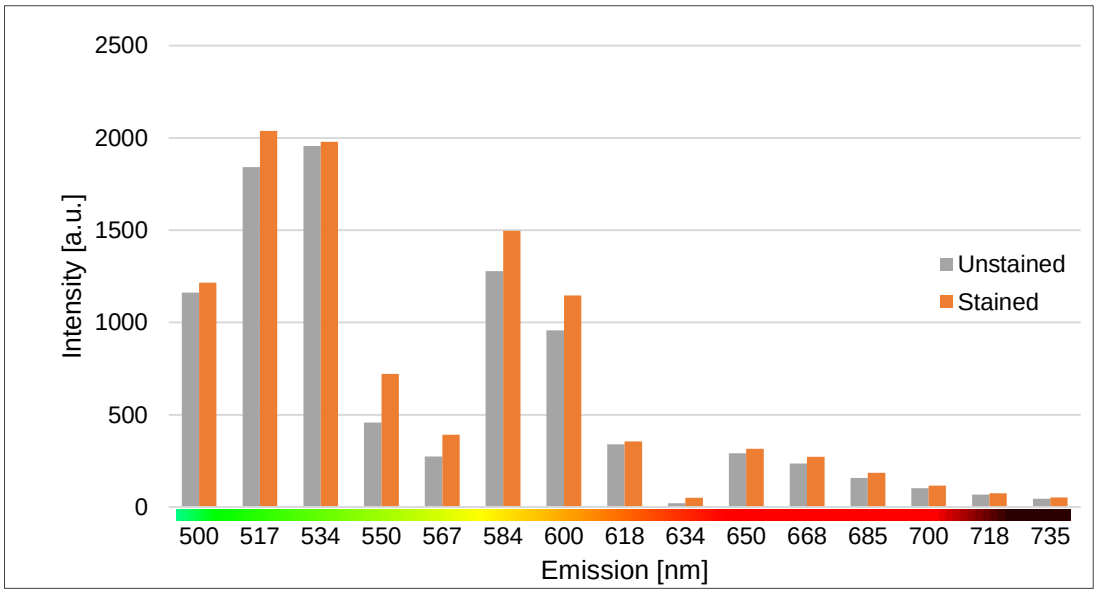

Figure 5-17: Emission spectrum of unstained and ProY-stained skeletal muscle cross-sections. Data was compiled from n = 2 unstained and n = 2 stained muscles from Sprague-Dawley rats. Multiple ROI on each cross-section were imaged at 488nm ex. Intensity measurements were taken at wavelengths of 500–735nm in 15nm intervals. Average intensity levels of the stained samples (orange) were always above those of the unstained samples' autofluorescence (grey).

One possible explanation for the difference between stained and unstained controls is nonspecific ProY-staining. While the stain fully penetrates cells with membrane damage, it might still attach to undamaged structures or cause partial staining through electrostatic absorbance or hydrophilic and hydrophobic interactions. For successful thresholding, this problem of intensity differences between the autofluorescence of unstained samples and the higher signal of ProY-stained controls needs to be addressed.

Nguyen et al. [315] observed a similar phenomenon in their experiments with Procion staining. They circumvented this issue by adding a fibre specific fluorescence measurement assay on top of the standard counting procedure. However, this means that additional resources, time, and staining procedures would be needed. Alternatively, the higher signal from ProY-stained samples could be compensated by offsetting the threshold value of the autofluorescence samples. However, tissue samples have a high inherent biological variability. Defining a universal offset value might therefore be difficult. Other researchers have reported similar issues with high tissue-to-tissue variation of autofluorescence levels, making global thresholding approaches nearly impossible [344]. A different approach that allowed for more targeted thresholding without the bias of manual operations was therefore needed.

5.5.4.3. Thresholding with stained control samples

Instead of determining the autofluorescence signal, the control slides of each sample could be used for thresholding. Samples were taken from the periphery of the muscle, outside the mechanical loading zone. As samples were only separated after the intervention, each control was treated identically to the intervention group. Using control slides for thresholding would therefore reduce biological and technical variability and take potential other sample-specific damage into account, i.e. from an extended experimental duration or the staining procedure.

The non-damaged, medium damaged, and highly damaged samples described in "*5.5.2.5 Validation of Y5 normalisation for the image analysis of ProY-stained muscle samples*" were used to test the suitability of stained controls for thresholding. Each control image was background subtracted, normalised, and segmented. The mean intensity of the segmented area was then obtained with FIJI/ImageJ. A total of $n = 6$ control sections were analysed to determine the average intensity level. The defined value was then used as threshold for the corresponding indented samples.

For all three samples, thresholding with control samples seemed to be successful. The thresholded images were in good agreement with the raw images regarding both the amount and location of cells identified as ProY-positive (**Figure 5-16c**). Hence, the thresholding procedure for this imaging protocol was based on sample-specific control samples.

5.5.5. Particle Analysis to quantify ProY-positive cells

The last step in the image analysis workflow was to determine a quantitative number of ProY-positive cells per cross-section. For this, all previously described processes for background subtraction, normalisation, segmentation, and thresholding were combined to create two types of images: The first was an image clearly distinguishing all cells within the cross-section; the second was an image representing all areas with ProY-positive staining. By overlaying both images, individual cells with ProY-positive staining can be identified.

5.5.5.1. Preparation of an image of individual ProY-positive cells

To obtain an image representing a segmentation of the individual cells within a cross-section, the .png files created in the segmentation process with Cellpose (s. *"4.4.3. Segmentation of individual cells from cross-sectional images of skeletal muscle tissue"*) were converted into FIJI/ImageJ masks with the LabelsToROIs plugin [361]. Images were imported as ImageJ ROI and the area of each ROI reduced by 2px around its outline to ensure full separation of individual cells. The resulting ROI were added to a blank image with the same dimensions as the thresholded image to be segmented. Next, the ROI image was flattened, made binary, and holes filled to create a mask with black cells on white background (**Figure 5-18b**). This image was then combined with the thresholded image **(Figure 5-18c)** through the MIN operator to create the clear cell segmentation of damaged cells needed for further processing **(Figure 5-18d)**.

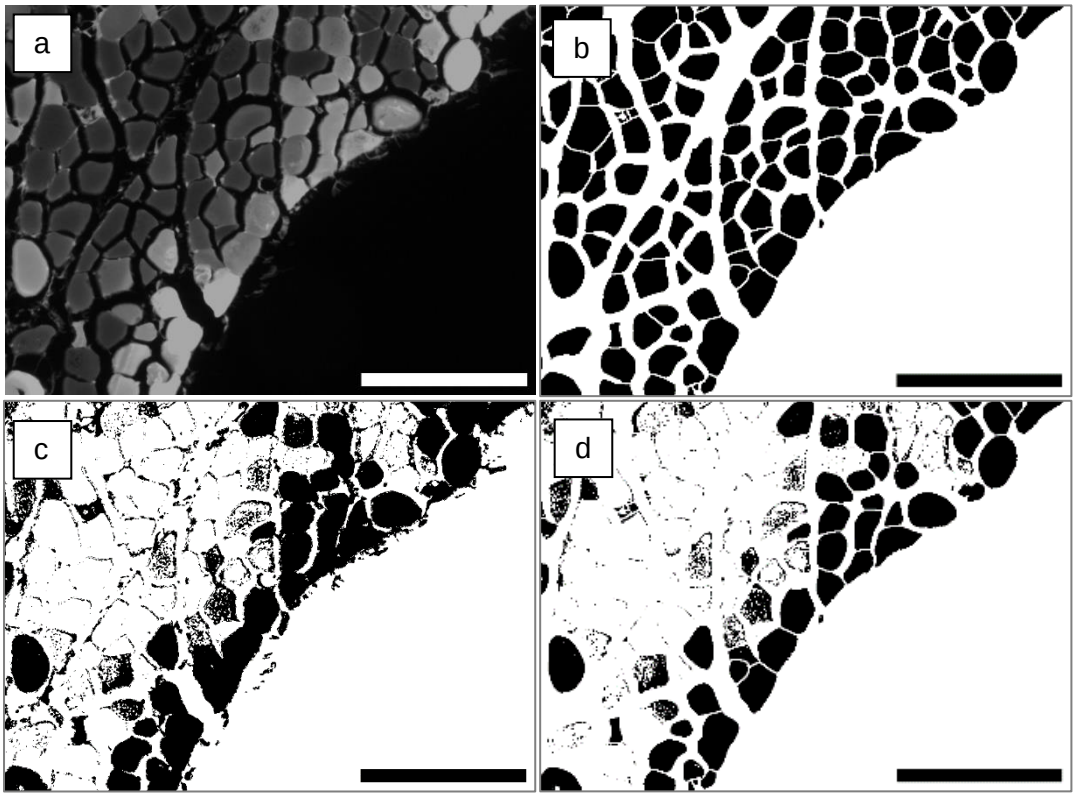

Figure 5-18: Preparation of fluorescently stained muscle cross-section for particle analysis. a) Original image after background subtraction and conversion to greyscale. Light grey areas indicate ProY-positive staining for dead cells. **b)** Segmentation of cells from image A after use of Cellpose algorithm and LabelsToRoI plugin in FIJI/ImageJ. **c)** Thresholding of image A with threshold value obtained from corresponding control tissues. Remaining structures (black) indicate ProY-positive staining. **d)** Combination of images B and C with MIN operator in FIJI/ImageJ. ProY-positive cells (black) are clearly distinguishable. Scale bar 200µm.

5.5.5.2. Automated particle analysis

Particles within the fully thresholded and segmented image were counted automatically with the “particle analysis” function in FIJI/ImageJ. A suitable minimum size and roundness had to be defined to exclude unwanted objects like stained debris from the analysis without disregarding small and odd shaped cells. For this, the relationship between both parameters and the number of particles identified was determined for three mechanically indented cross-sections. First, the minimum size (area) was increased from 200 px^2 to 500 px^2 in 50px^2 increments at a constant circularity of 0.25. Then the size remained constant at 250px^2 and the circularity was increased from 0.1 to 0.7 in 0.1 steps.

When increasing the size, the number of particles detected decreased proportionally (**Figure 5-19**). This strong relationship was observed across all samples (R_1 = 99.15, R_2 = 99.58, R_3 = 98.91). Similarly, the number of particles reduced linearly with increasing circularity (R_1 = 96.26, R_2 = 93.87, R_3 = 97.60) (**Figure 5-19**).

For this project, the difference in cell death counts between samples is important, whereas the absolute numbers are less relevant. Considering that both circularity and particle size were proportional to the number of particles identified, the choice of the value for each parameter is secondary, if it is kept constant across samples.

The following parameters were chosen: A size of 250px^2 correlated almost exactly with the predicted linear regression lines for all samples and visibly removed debris while keeping smaller cells; A circularity of 0.3 – 1.0 correlated well with the linear regression model of each sample. It also preserved deformed cells at the indentation site while removing smaller debris and superficial staining of tendons and fascia.

Despite the careful choice of parameters for the particle analysis process, a chance for error remained. Some cells might be smaller than the defined size; and cells that are only partly above the threshold might be excluded from analysis or counted twice. This is attribute to the semi-automated nature of the process, which was prioritised over potential small errors in the analysis. Additionally, the effect of such errors will be minimised by obtaining average cell death counts from six cross-sections for each sample rather than just one.

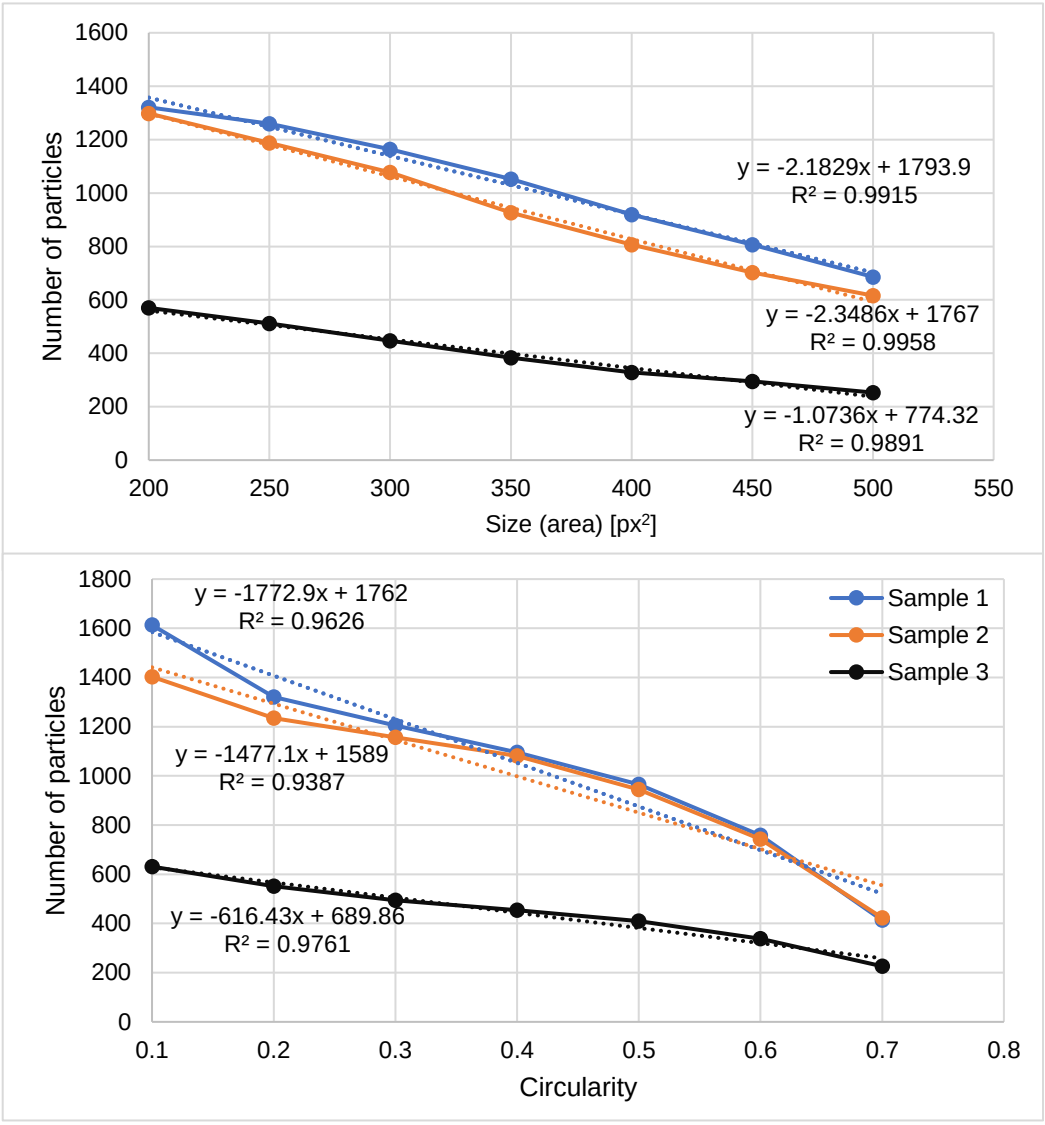

Figure 5-19: Dependence of particle analysis algorithm on input parameters. Automated particle analysis was performed with FIJI/ImageJ on three ROI of mechanically damaged skeletal muscle cross-sections. The first figure shows the number of particles identified when increasing the minimum size (area). All samples display a strong, negative linear relationship. The second figure displays the number of particles identified across the same three samples when increasing the circularity measure (circularity = 4π (area/perimeter^2). All samples show a strong, negative linear relationship.

5.5.6. Overview over the image analysis workflow

A robust analysis workflow was developed to quantify fluorescently stained skeletal muscle cells from full tissue cross-sections (**Figure 5-20**). A thorough description of each step with corresponding validation was deemed necessary considering the sparse information on image analysis of ProY-stained skeletal muscle tissue in the

literature. By developing a set workflow that applies to all samples across the different experimental conditions, bias was reduced. The automatisation of each step further improved the objectivity of the analysis.

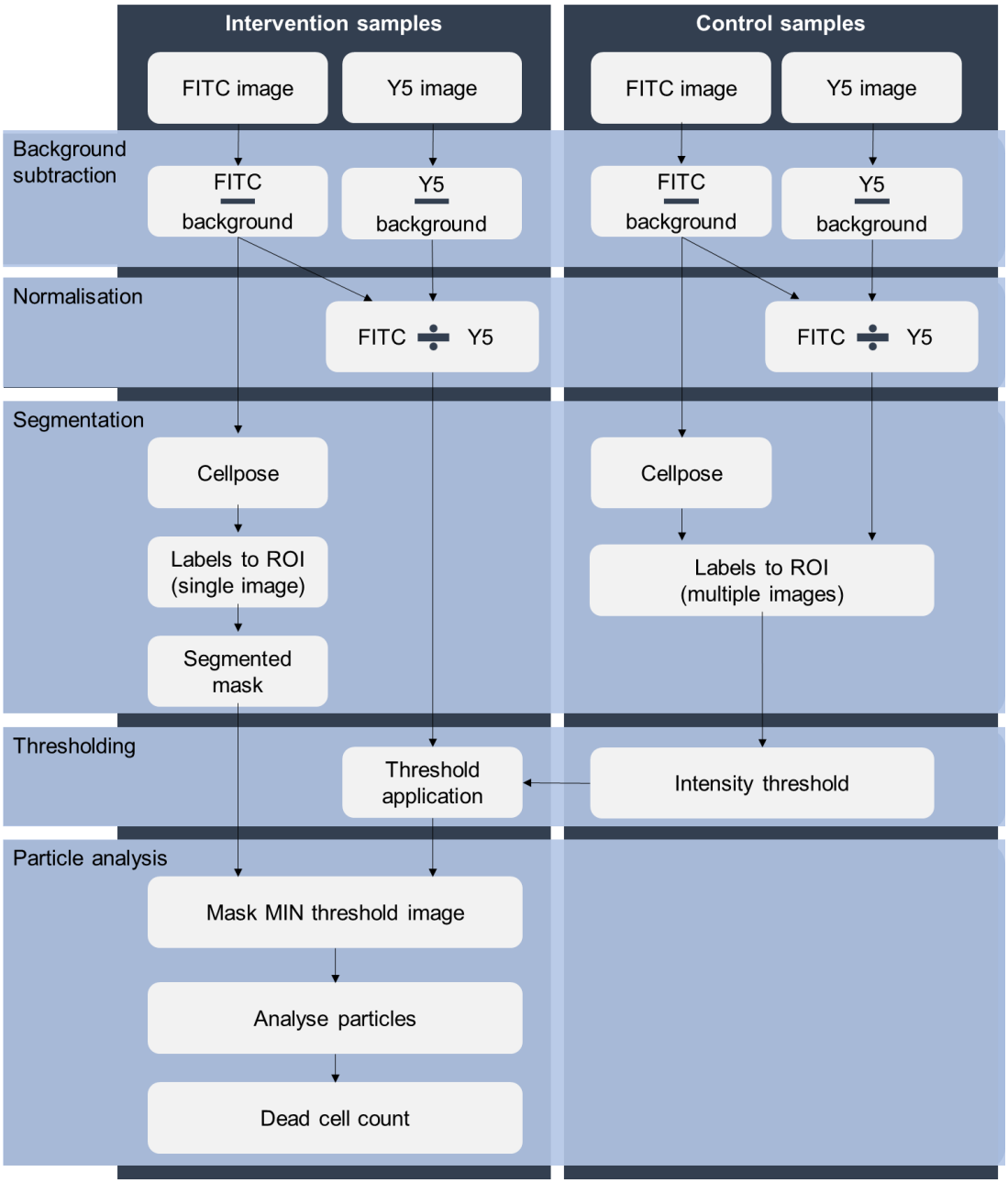

Figure 5-20: Image analysis workflow to quantify sarcolemmal damage in ProY-stained skeletal muscle cross-sections.

The main analysis steps are background subtraction, normalisation, segmentation, thresholding, and particle analysis. All processes were adjusted to ProY-stained images and validated on images from samples representing the full spectrum of the planned experiments, including controls, as well as undamaged, mildly damaged, and

heavily damaged mechanically loaded samples. A detailed description of each step is provided in Appendix F.

5.6. Limitations of the image analysis workflow

Despite setting up a robust image analysis workflow with little potential for bias, several limitations remain. The first step in the workflow requires the images to be compressed from 24-bit to 8-bit. Thus, a part of the information and image detail will be lost. While this process would ideally be avoided, it is necessary for further analysis with certain operational functions in FIJI/ImageJ like thresholding. One advantage is that 8-bit files have a reduced size, making the analysis process less computationally expensive.

Another drawback is the semi-automated nature of the analysis process. While operations are applied in an automated fashion, i.e. through Cellpose or FIJI/ImageJ, many steps still require manual input, which is a source for human error. This also means that the image analysis is time consuming. On top of that, frequent storage of images and other files is needed at different stages, making high computing power and storage capacities essential. Nevertheless, a semi-automated process with thorough validation is still preferred over a subjective process without background corrections, normalisation, and automated cell counting.

5.7. Chapter summary

This chapter described the development of a robust workflow to quantify sarcolemmal damage in fluorescently stained skeletal muscle cross-sections. First, image acquisition parameters were optimised for a Leica SP8 system with a DMI8 microscope. Suitable settings to image ProY-stained slides were identified, including a light source intensity of 2, gain level 3, and integration time 1s (for FITC filter) and 4s (for Y5 filter). Further best-practice guidelines were defined, like in-focus imaging and minimising photobleaching. With the right settings in place, full cross-sections were scanned consecutively with an FITC and Y5 filter. Once the resulting TIFF-files were exported to FIJI/ImageJ, further analysis could be performed.

The developed analysis workflow is based on recommendations for good practice in quantitative fluorescence imaging [322, 325, 334, 362], like reducing bias, validating processes, and providing thorough descriptions of the equipment and methods. Compared to existing methodological approaches for analysis of ProY-stained

samples, additional steps were considered and validated for their suitability; for example, a normalisation protocol was included as well as cell segmentation with Cellpose. This allows for a semi-automated quantification of fluorescently labelled cells. It also reduces the risk for bias introduced in commonly used ProY analysis protocols and produces robust outcomes, independent from the intervention. By using open-source software, the workflow is easy to replicate and adjust for other applications beyond the quantification of dead cells in transversely loaded skeletal muscle tissue.

CHAPTER 6

Development of a Finite Element model to study transverse compression of *ex vivo* skeletal muscle tissue

This chapter replicates the transverse compression of *ex vivo* skeletal muscle tissue with Finite Element Analysis (FEA) to estimate the mechanical environment within isolated muscles during indentation experiments (**Objective 3**). A parametric study was also performed to assess the influence of muscle geometry on the mechanical environment within the samples.

The FEA was performed by the author with support from Prof. Erkan Oterkus and Prof. Selda Oterkus on the general use FEA.

6.1. Introduction to contact mechanics

The role of computational modelling in health-related research is becoming increasingly important. Traditional structure and fluid mechanics methods like Finite Element Analysis (FEA) and computational fluid dynamics (CFD) are now applied to the human body to simulate mechanical and (patho-)physiological processes like the development of Deep Tissue Injuries (DTI).

The majority of pressure injury research is laboratory work and clinical studies. Different sensory systems and imaging modalities like pressure sensors [363, 364] or MRI [27, 140] provide macro-scale information on the biomechanical environment. However, DTI forms in deep tissue structures, starting with micro-scale damage [61]. When looking at biological samples *in vivo*, deep tissue imaging and sensing with high resolution present a major challenge. Biological variability, ethical restrictions, cost, and limited resources also restrain the extent and reproducibility of these experiments.

Researchers therefore commonly rely on computational modelling to link physiological and mechanical data from micro-scale *in vitro* studies to a clinical context. In the past, Finite Element (FE) modelling has been used to estimate loading conditions and damage thresholds in cell and animal experiments [34, 212]. The results were translated to human subjects i.e. to estimate the DTI risk for transtibial prosthetic users [31, 36, 77, 79].

To investigate potential soft tissue damage from prosthesis-related loading further, an *ex vivo* pressure injury model was developed (*Chapter 4*). Like other studies in this field [33, 81], the proposed model represents a classic indentation problem. The setup consists of an indenter being lowered onto a substrate, applying a defined force. Most often, indentation experiments record the material response to the mechanical loads, helping to characterise material properties [365–367]. For this project, the indentation setup was used to apply transverse compression to isolated hindlimb muscles of Sprague-Dawley rats to mimic prosthetic use.

In engineering, such experiments fall under the category of contact mechanics. The focus of contact mechanics is to evaluate the deformation of solid bodies touching each other. Hertz [368] and Boussinesq [369] were among the first to solve contact problems analytically. They assumed that a rigid indenter with radius *a* is lowered onto

an elastic half space with a thickness of $z \geq 0$. The indenter was commonly either flat-ended or spherical.

6.1.1. Spherical indentation of a semi-infinite half space

Hertz' contact mechanics give an analytical solution for the deformation, stresses, and strains within a half space under spherical indentation (**Figure 6-1**) [368, 370].

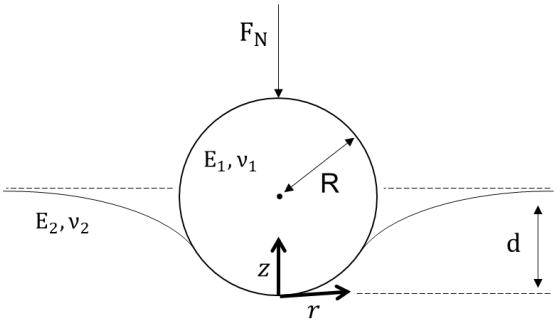

Figure 6-1: Normal indentation of an elastic half-space by a rigid spherical indenter. $\boldsymbol{F_N}$: applied normal force; R: radius of indenter; E: elastic modulus; $\boldsymbol{\nu}$: Poisson's ratio; d: indentation depth; z, r: coordinates.

According to Hertz, the maximum pressure p_0 in the half space can be calculated as

$$\boldsymbol{p_0 = \left(\frac{6F_N E^{*2}}{\pi^3 R^2}\right)^{\frac{1}{3}}} \qquad \textbf{(6-1)}$$

with F_N as the applied normal force, R as the radius of the indenter and E^*as the effective elasticity modulus, which is given as:

$$\boldsymbol{\frac{1}{E^*} = \frac{1-\nu_1^2}{E_1} + \frac{1-\nu_2^2}{E_2}} \qquad \textbf{(6-2)}$$

E_1 and E_2 are the Young's moduli of the two bodies, ν_1 and ν_2 their Poisson's ratios.

Since its publication in 1882, Hertz' contact theory has been refined to accommodate deviations from the original assumptions. Ning et al. [371] for example adjusted the analytical solution to apply to thin layers rather than a semi-infinite half space. Gefen et al. [33] used this adaptation to estimate the strain field in skeletal muscle under transverse mechanical loading with a round indenter. When applying a round indenter to a substrate, the deformation and therefore the strain field throughout the sample is non-uniform. Gefen et al. utilised this effect to observe the circular development of

cellular damage in their muscle samples over time and related it to the calculated deformation ratios.

However, round indenters are less favourable for the experiments proposed in this project. With the whole indentation area being used for analysis, it would be difficult to assign cross-sections to specific deformation ratios. In the dynamic loading scenario, the change in contact radius would also lead to different loading frequencies on cells throughout the indentation area. A round indenter therefore seemed unsuitable for the proposed experiments.

6.1.2. Flat indentation of a semi-infinite half space

Compared with a round indenter, a flat shape (**Figure 6-2**) produces a uniform displacement of a substrate. The contact area thereby remains constant. Indentation problems with a flat rigid indenter of radius a on an elastic half-space $z \geq 0$ has been described in Boussinesq's theory [369]. It reduces the contact force to a concentrated normal force F_N in the middle of the indenter. Sneddon [372] and Popov [373] proposed two popular analytical approaches to solve the Boussinesq problem.

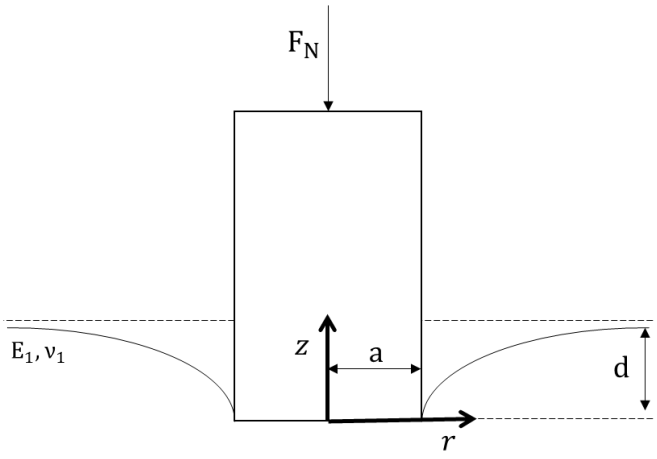

Figure 6-2: Normal indentation of an elastic half-space by a rigid flat indenter. $\boldsymbol{F_N}$: applied normal force; a: radius of indenter; d: indentation depth; E: elastic modulus; $\boldsymbol{\nu}$: Poisson's ratio, z, r: coordinates.

According to Sneddon [372], the deformation d caused by F_N is given by

$$\boldsymbol{d = \frac{F_N \times (1-\nu)}{4\mu a}} \qquad \textbf{(6-3)}$$

with the shear modulus μ as a function of the elastic modulus E.

$$\mu = \frac{E}{2(1+\nu)} \qquad (6\text{-}4)$$

The pressure distribution under the indenter can then be calculated as:

$$\sigma_{zz}(r,0) = -\frac{2\mu d}{\pi(1-\nu)}\left(a^2 - r^2\right)^{-\frac{1}{2}}, \quad 0 \le r \le a \qquad (6\text{-}5)$$

An alternative method to solve the Boussinesq problem is the method of dimensionality reduction (MDR) by Popov [373]. The deformation can be calculated as:

$$d = \frac{F_N}{2E^* a} \qquad (6\text{-}6)$$

The stress distribution in the contact area is given by:

$$\sigma_{zz}(r,d) = -\frac{E^* d}{\pi\sqrt{a^2 - r^2}}, \quad r \le a \qquad (6\text{-}7)$$

However, the assumption of a semi-infinite half space does not represent the proposed experiments; the isolated skeletal muscle tissue has a finite thickness of approximately 2mm, equal to the diameter of the indenter.

Alternatively, researchers adjusted the existing analytical solutions to represent the indentation of a thin film or layer fixed to a rigid boundary [374, 375]. They defined a factor κ that can be added to the existing analytical solutions to account for geometric and material effects, as well as large deformation and friction. Since then, the κ-factor has been used to describe the indentation behaviour of cartilage [376, 377], tendon [378], and foot plantar tissue [379].

The κ-factor has also been integrated in prosthetic research. Portnoy et al. [81] applied an analytical approach to assess the influence of different tissue parameters on soft tissue deformation. The tibia was thereby assumed as the indenter that compresses the soft tissue envelop onto the rigid socket. Using an analytical approximation rather than a more complex FE model simplified the integration into clinical monitoring systems to generate real-time data.

Despite adding the κ-factor for the indentation of thin layers, it remains difficult to describe the proposed experiments of this project with an analytical solution. Instead of a rigid surface, the muscle is compressed onto a deformable silicone layer, which

may alter the deformation of the muscle substrate. Additionally, muscle exhibits viscoelastic material properties, which are not considered in the simplified analytical solutions. It was therefore necessary to develop an FE model to investigate the loading conditions within the skeletal muscle samples during the proposed indentation experiments.

6.2. Aims of finite element analysis

To tap into the full potential of the proposed experimental work, the link between the mechanical loading conditions and the cellular damage observed within the *ex vivo* pressure injury model needs to be established. The aim was therefore to develop an FE model of the transverse mechanical loading experiment.

The multi-layered FE model incorporated the indenter, skeletal muscle, and silicone layer that covered the bottom of the Petri dish during the experiments. Furthermore, the effect of changes in the muscle geometry was assessed as an indication for the influence of biological variability on numerical results.

Beyond the specific project application, the proposed FE model can be the basis for any future research that relies on information on stresses and strains within transversely compressed biological material.

6.3. Development of a finite element model of transverse mechanical indentation of skeletal muscle

6.3.1. Definition of material properties for muscle, indenter, and silicone

6.3.1.1. Material properties of the flat punch indenter

All FE simulations were performed in Ansys (Ansys Workbench 2021 R2). The indenter was modelled as rigid body by assigning linear elastic properties with a high Young's modulus ($E_i = 200GPa$) and Poisson's ratio equivalent to steel ($\upsilon_i = 0.3$).

6.3.1.2. Material properties of the muscle layer

The muscle was considered as nearly incompressible ($\upsilon_m = 0.495$). Its mechanical properties were taken from Bosboom et al.'s study [171] passive, transversely

compressed tibialis anterior muscle of rats. They fitted a first-order Ogden model, which can be described as

$$\boldsymbol{W = \frac{\mu}{\alpha}(\lambda_1^{\alpha} + \lambda_2^{\alpha} + \lambda_3^{\alpha} - 3)} \qquad \textbf{(6-8)}$$

with W as the strain energy function, μ and α as material parameters, and λ_i as principal stretch ratios (ratio of the length of deformed element to corresponding undeformed element along principal axes). The elastic parameters were defined as $\mu = 15.6kPa$ and $\alpha = 21.4$. A Prony series expansion was added to describe the viscoelastic behaviour of muscle under compression, according to the following formula:

$$\boldsymbol{S = (1 - \delta)\frac{\partial W}{\partial E} + \int_0^t \delta \frac{\partial W}{\partial E} e^{-(t-\xi)/\tau}\, d\xi} \qquad \textbf{(6-9)}$$

where S is the second Piola Kirchhoff stress, E is the Green Lagrange strain, and δ and τ are viscoelastic parameters. The viscoelastic parameters assigned by Bosboom et al. [171] were $\delta = 0.549$ and $\tau = 6.01s$.

6.3.1.3. Material properties of the silicone layer

To obtain the material properties of the silicone, indentation tests were performed. The Petri dishes used in the experiments were covered with a silicone layer of 8mm thickness. Each petri dish (*n* = 3) was inserted into the bottom of a material test instrument (Bose Electroforce 3100, TA Instruments). A 22N load cell was fitted to the top of the Bose with the same flat punch steel indenter (*r* = 1mm) used for the *ex vivo* experiments attached to it (s. "*4.3.3 Mechanical loading* "). The system was allowed to stabilise for 30min before the indenter was lowered onto the silicone layer until a contact force of -0.01N was established. Next, compression with a maximum force of 0.324N and loading rate of 0.01mm/s was applied whilst recording the displacement. The force was chosen according to the maximum load applied during muscle indentation experiments (s."*7.3.2 Experimental setup for static loading experiments*"). In addition to the static testing, viscoelastic behaviour was assessed in a dynamic setup with the same overall maximum force and a sinusoidal load of either 1.42Hz or 4Hz frequency (s. "*8.3.2 Static and dynamic loading experiments*") for 300 cycles. The tests were repeated three times for each Petri dish.

The slow ramp compression revealed a strong linear relationship between load and deformation (R^2 = 99.97% overall), suggesting linear elastic material behaviour.

Accordingly, stress (σ) and strain (ε) values were computed (**Figure 6-3**) to obtain an average Young's modulus of $E_S = 3.42 \pm 0.22MPa$ (s. Appendix G) based on the formula:

$$\boldsymbol{E = \frac{\sigma}{\varepsilon}} \qquad \textbf{(6-10)}$$

The dynamic data supported the findings of the static analysis with no phase-lag between load application and deformation for both tested frequencies, which would indicate viscoelasticity (**Figure 6-4**). The silicone layer was therefore modelled as linear elastic material with a Young's modulus of $E_S = 3.42MPa$ and Poisson's ratio of $\upsilon_S = 0.495$ to mimic incompressibility.

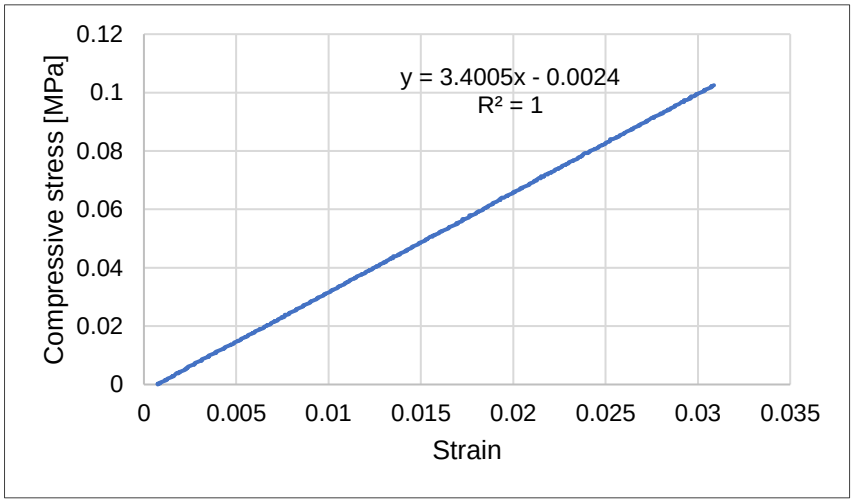

Figure 6-3: Representative results static testing silicone. Linear stress-strain relationship (R^2 = 100%) recorded from indentation of 8mm thick silicone layer with flat punch. Loading rate was 0.01mm/s up to a maximum compressive force of 0.324N.

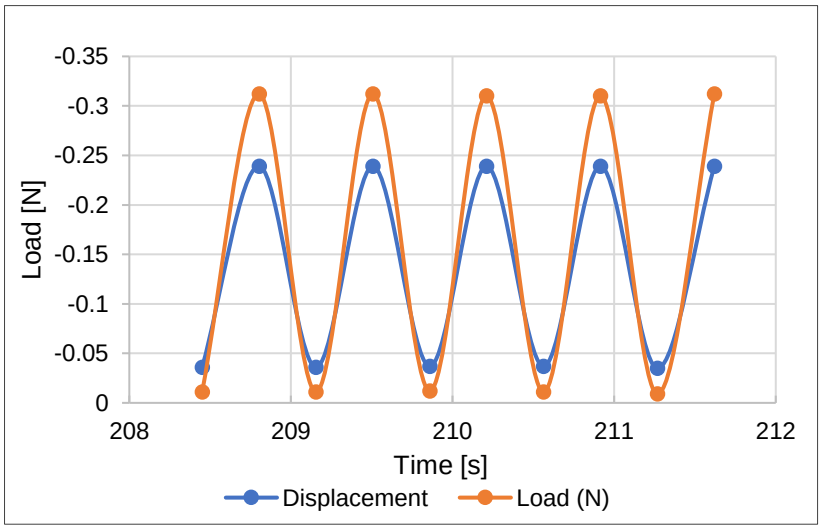

Figure 6-4: Representative results dynamic testing silicone. Sinusoidal indentation of silicone layer with flat punch with max. force of 0.324N and frequency of 1.42Hz.

6.3.2. Definition of geometry of the finite element model

The indentation experiment has a 3D geometry with a flat indenter tip being lowered onto the muscle substrate. Running such a 3D analysis comes at high computational cost, making simplifications necessary. The 2mm diameter of the indenter and its radius of influence were significantly smaller than the 1.5-2cm length of the muscle. The length of the muscle specimen was therefore reduced to 8mm to replicate only the region beneath and immediately around the indenter. The thickness was set to 2mm as measured during *ex vivo* experiments. The silicone layer had a thickness of 8mm and was extended to a length of 20mm. To reduce computational cost even further, the setup was simplified to a 2D axisymmetric model that included only half the indenter, muscle, and silicone layer (**Figure 6-5**). A small radius (0.1mm) was added to the corner of the indenter. Removing the sharp edge improved the convergence of the contact between the indenter and muscle and avoids stress concentrations. It also kept the applied compressive stress from converging to infinity.

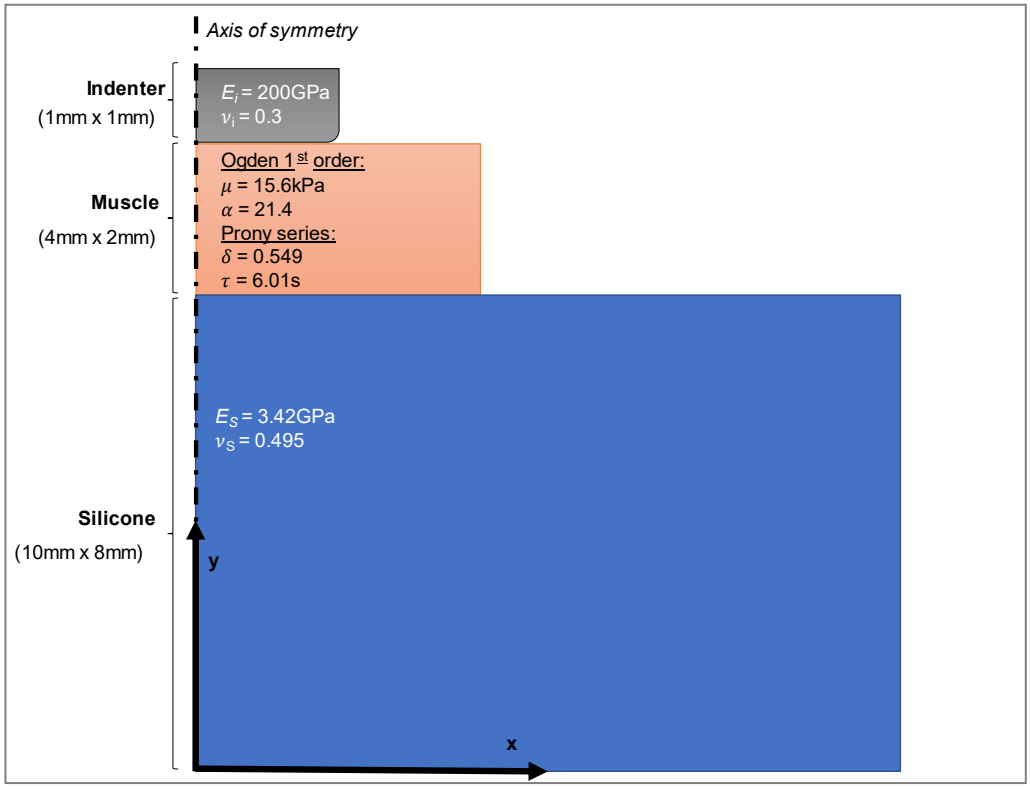

Figure 6-5: Geometry and material properties of the axisymmetric 2D model for flat punch indentation.

The model was set up to confirm with the standard coordinate system, with the bottom left corner of the silicone layer at its origin (**Figure 6-5**). Accordingly, the movement of the indenter as well as the deformation of the substrates were in negative y-direction. Resulting values like the directional deformation or normal stress would therefore be represented by a negative number with their true maximum regarded as minimum values by Ansys. To avoid confusion, these negative "minimum" values will be considered as positive "maximum" in all following results and discussion sections.

6.3.3. Creation of meshing for the finite element model

For FEA, the geometry of a body is divided into smaller elements, defined by a finite number of nodes, for which partial differential equations are solved individually. Often, a mesh convergence study is performed to determine an element size that provides sufficiently accurate results while keeping computational expenses to a minimum. Typically, a finer mesh results in a more accurate result but also increases the computer power needed for solving.

To create the mesh for the model, four-node quadrilateral elements with two degrees of freedom (DOF) were used under axisymmetric conditions. The elements of the indenter were created through face meshing with a refinement level of 3. With the elastic modulus of steel being over 4000 times larger than that of muscle ($E_{steel} = 3.42MPa, E_{muscle} = 47kPa$ [171]), the indenter was regarded as a rigid body. Thus, the effect of further mesh refinement on numerical results was deemed minimal, making a mesh convergence study of the indenter obsolete.

For the muscle and silicone layers, a mesh convergence study was performed. Through h-refinement with a factor of $\lambda = 2$ (splits each side of the element into two, creating four elements out of one), the element size of the mesh on the muscle and indenter was systematically reduced from 4.0×10^{-8}m² to 6.25×10^{-10}m² across four iterations. A compressive stress of 103kPa was then applied to the top line of the indenter (s. "*6.3.6 Force application"*) and the FE model solved. The following data was recorded for each iteration of mesh refinement: the number of elements for the muscle and silicone layer, the computing time for each solution run, and the y-displacement of the indenter. The directional deformation calculated by Ansys was then mapped against the computational time of each iteration to find the optimal mesh size.

The results showed that, as expected, the y-displacement converged towards its true value with each iteration while the computational time increased (**Figure 6-6**). The difference between the displacement values of each iteration thereby decreased; the difference in displacement was 0.1052mm between the first and second iteration, 0.0246mm between the second and third, and 0.0121mm between the third and fourth iteration. On the contrary, the computing time increased almost linearly (R^2 = 99.78%) with the computing time of the fourth iteration (1543.94s) being over four times as long as that of the third iteration (364.22s).

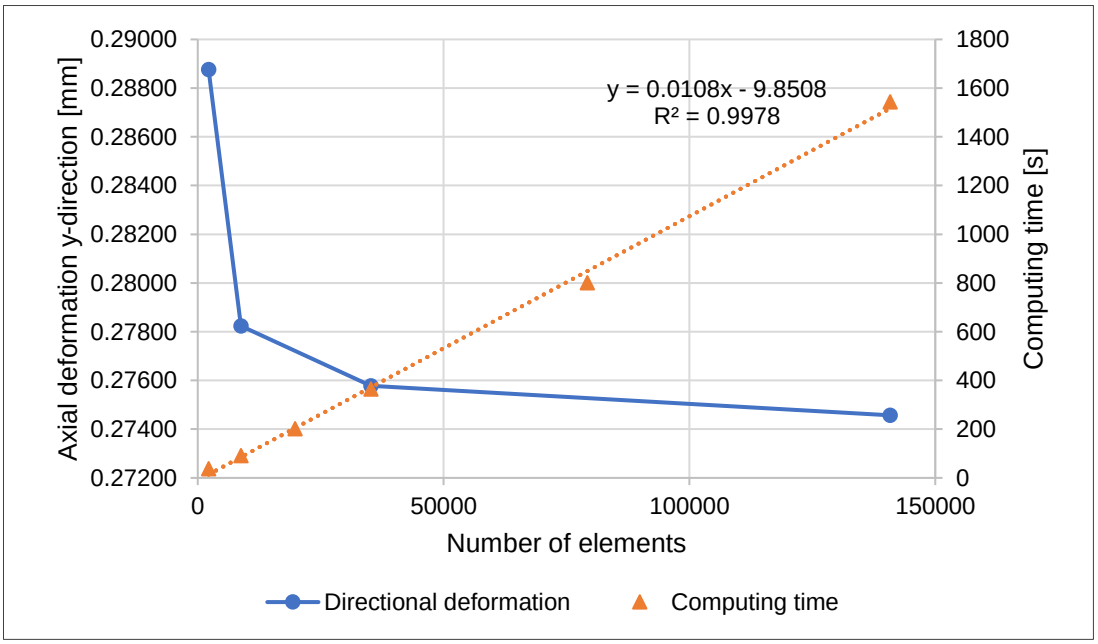

Figure 6-6: Mesh convergence study. The FEA model of a flat indenter compressing a muscle and silicone layer was solved with increasingly finer mesh size. The element size of the muscle and silicone layer was reduced from $\mathbf{4.0 \times 10^{-8}}$m² to $\mathbf{6.25 \times 10^{-10}}$m² in four iterations. Directional deformation in y-direction and computational time were recorded and plotted against the number of elements in the two layers. Computing time increased almost linearly (R^2 = 99.78%), whereas the directional deformation converged towards its true value.

Taking the results for both the y-displacement and computing time together, the model was regarded as sufficiently converged after the third iteration, after which no significant improvement in accuracy was observed whilst the computational time increased drastically. The element size at the third iteration was 2.5 x 10^{-9}m², creating 35,200 elements across the muscle and silicone layer. The element size of 2.5 x 10^{-9}m² was therefore adapted for the muscle and silicone layer of the FE model, achieving a balance between computational expense and numerical accuracy (**Figure 6-7**).

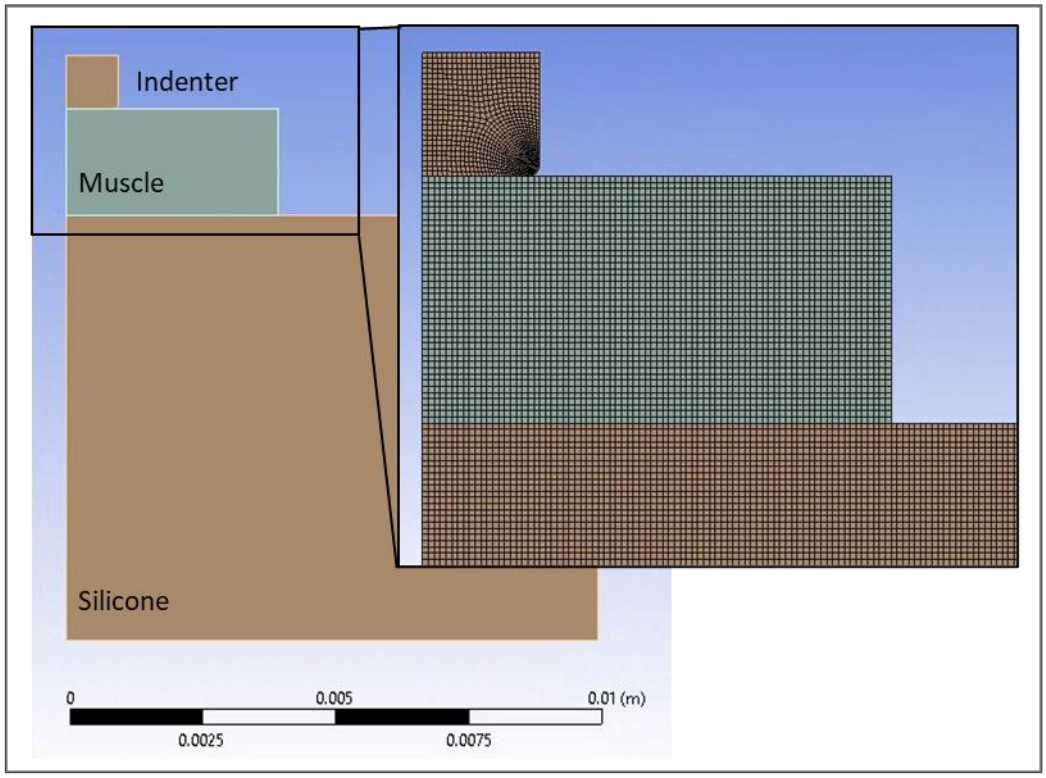

Figure 6-7: Meshing of the FE model. Overall geometry of the created three-component model with a close-up of the indenter, muscle, and upper corner of the silicone layer to show shape and size of quadrilateral elements. Face meshing was created on the indenter with level 3 refinement; muscle and silicone layers have an element size of 2.5 x $10^{-9}m^2$.

6.3.4. Contact definition between indenter, muscle, and silicone layer

To characterise the interaction of two bodies, contact parameters need to be defined. A frictionless, asymmetric surface-to-surface contact pair was defined between the bottom line of the indenter and the top line of the muscle. In line with similar indentation experiments [33, 212], frictionless contact was assumed with the physiological solution lubricating the muscle samples. The augmented Lagrange method was chosen as contact algorithm (**Figure 6-8**). Standard values for penalty tolerance and stiffness were adopted as given by Ansys with an update at each iteration.

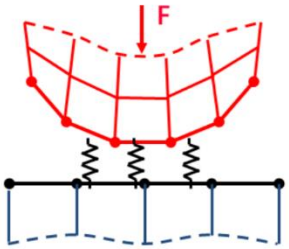

Figure 6-8: Augmented Lagrange contact method. Iterative series of penalties where a contact "spring" characterises the relationship between the target (red) and the contact (blue) when a force F is applied [380].

The contact between the bottom line of the muscle (target element) and the top line of the silicone layer (contact element) was modelled as "no separation" condition. The nodes of the contact are bonded to the target surface in normal direction while allowing for sliding in tangential direction. The no-separation condition was introduced to simulate the fixation of the muscle to the silicone layer with pins as well as the extended muscle length that was not included in this axisymmetric model.

6.3.5. Boundary conditions

To ensure that the FE model can be solved numerically, boundary conditions needed to be defined. The model was constrained in x-direction at the axis of symmetry (**Figure 6-5**) to account for the axisymmetry of the components. Additionally, a fixed support was added to the bottom of the silicone layer. It represents the attachment of the silicone to the Petri dish and prevents movement in x- and y-direction. The edges of the muscle were not restricted as parts of the muscle were freely deformable in the experimental setup. Although the muscles were pinned out in the periphery, this fixation was localised and distant from the modelled indentation area. Nevertheless, the restriction of muscle edges in x-direction was tested and had only minimal influence on numerical results of the standard FE model.

6.3.6. Force application

Beside static boundary conditions, ANSYS allows for external load application in form of force, displacement, or pressure (i.e. direct stress) to the top line of the indenter to represent the indentation process. For the static loading scenario for example, a constant compressive stress can be added, while the dynamic scenario can be replicated with a mathematical function or tabular data. The exact values depend on the test scenario. For the studies performed as part of the FE model development, a static direct stress of 103kPa was applied to the top line of the indenter in negative y-

direction. This value is at the top end of the range that would be tested in the experimental settings (s."*7.3.2 Experimental setup for static loading experiments*").

6.3.7. Analysis settings

The final step of setting up an FE model is to define analysis settings. For the FE model development, the static direct stress was applied in one step over 1s. The number of initial substeps was defined as 100, with a minimum of 50 and a maximum of 1000 to reach convergence. A direct solver was chosen over an iterative approach, and the large deflection feature was activated to account for changes in stiffness caused by changes in shape.

6.3.8. Summary of setup for finite element analysis

The transverse mechanical loading experiment of *ex vivo* skeletal muscle tissue (s. "*4.8 Complete experimental procedure*") was translated into an FE model. It was simplified to an axisymmetric problem with a flat steel punch indenting a rectangular layer of skeletal muscle resting on a thick layer of silicone. The material model for the muscle was taken from literature [171] and considered non-linearity as described by a first order Ogden model ($\mu = 15.6kPa$, $\alpha = 21.4$). It was extended with a Prony-series to account for viscoelasticity ($\delta = 0.549$, $\tau = 6.01s$). The material behaviour of the incompressible silicone layer was determined in indentation tests under static and dynamic conditions to characterise its linear elastic behaviour ($E_S = 3.42MPa$). A mesh-convergence study was also performed, determining an element size of 2.5 x $10^{-9}m^2$ as a balanced choice between accuracy and computational expense of the analysis.

6.4. Finite element analysis of transverse mechanical loading of skeletal muscle tissue

6.4.1. Method for finite element analysis and parametric study on the influence of muscle geometry

With the FE model for the indentation of a skeletal muscle layer in place, FEA was performed, representing a static compression of 103kPa. Deformation, maximum principal compressive stress, and maximum shear stress were recorded to get an

indication for the general mechanical environment from a transverse mechanical loading experiment.

Biological variability is a major concern for *ex vivo* experiments. One aspect is the muscle geometry. Hence, the influence of changes in muscle length and thickness on numerical results was assessed. First, the y-dimension of the muscle was adjusted from 4mm to 3mm to 2mm (overall change in width from 8mm to 6mm to 4mm). Second, the thickness of the muscle was reduced from 2mm to 1mm. The magnitude and distribution of axial deformation, maximum principal compression stress, and maximum shear stress were recorded. Graphical representations were normalised to the same scale for comparison.

6.4.1. Results of the finite element analysis and parametric study

6.4.1.1. Assessment of mechanical environment within transversely loaded skeletal muscle tissue

Solving the FE model revealed that, in the muscle layer, the magnitude of deformation in y-direction decreases successively towards the silicone layer from >0.244mm in the superficial region to <0.041mm in the bottom layer (**Figure 6-9a**). The isolines of the different deformation values had a flat U-shape with almost horizontal direction underneath the indenter, turning into a nearly vertical pathway just outside its impact area. The maximum axial displacement of 0.276mm was predicted at the interface between indenter and muscle.

Beside displacement, stress distributions and magnitudes were analysed. As described in *"3.1.2 Fundamentals of mechanical load"* both maximum principal stress and maximum shear stress describe the same stress through a different coordinate system. The maximum principal stress is acting perpendicular to a sectional plane with zero shear stress. For this project, the maximum principal compression stress is of interest, which is the principal stress component representing the minimum value as compression is indicated by a negative sign. The maximum value of the maximum principal compression stress (248.72kPa) was observed around the edge of the indenter (**Figure 6-9b,c**). Underneath the indenter, the maximum principal compression stress was mostly uniform throughout the depth of the muscle with an average of 69.09kPa (range of 55.27 – 82.91kPa) (**Figure 6-9b**).

The maximum shear stress (124.36kPa) was also observed at the edge of the indenter. Its maximum value as well as the maximum shear stress underneath the indenter was approximately half the principal compression stress with 34.55kPa on average (range of 27.64 – 41.45kPa) (**Figure 6-9c**). This reflects the "ideal" scenario of a uniaxial loading condition (*"3.1.2 Fundamentals of mechanical load"),* indicating that the compressive load applied by the indenter produces a compressive stress field throughout the sample with minimal stresses in x-direction. The shear stress magnitude increased around the bottom half of the muscle midline to an average of 48.41 (range of 41.54 – 55.27kPa).

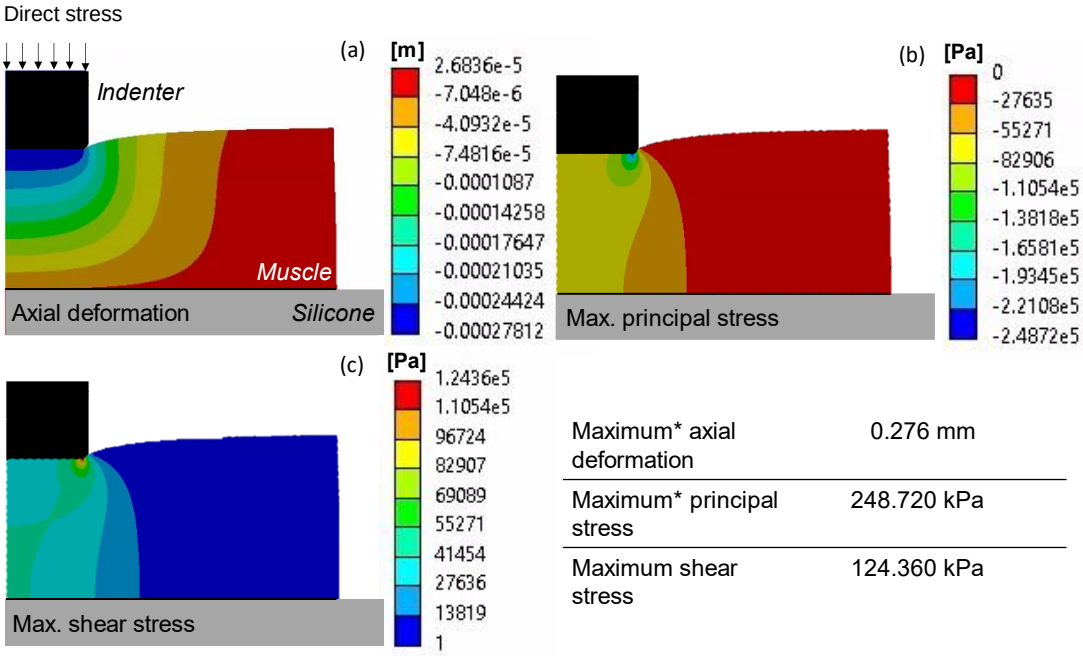

Figure 6-9: Representative FE calculation of axial deformation, maximum compression stress, and maximum shear stress in rat skeletal muscle. Axisymmetric model showing a flat indenter compressing a muscle onto a silicone layer with a direct stress of 103kPa. The dimensions of the silicone layer exceed those shown in the images. Maximum axial deformation and principal stress values marked with * are technically minimum values as the deformation of the muscle specimen took place in negative y-direction. (a) axial deformation in Y-direction with a maximum displacement of 0.276mm; (b) principal stress with a maximum of 248.72kPa; (c) shear stress with a maximum of 124.36kPa.

6.4.1.2. Influence of change in muscle width on numerical results

When changing the width of the muscle from 8mm to 6mm to 4mm at a constant thickness of 2mm, axial deformation, maximum principal compression stress, and maximum shear stress remained almost constant (**Table 6-1**). The difference in the maximum axial deformation was marginal with the change between the 8mm and 4mm width being less than 1% (2.34 x 10^{-3}mm). Similarly, the deformation field underneath the indenter was almost identical for all muscle widths with a successive

decrease in deformation values towards the silicone layer from >0.244mm to <0.041mm (**Figure 6-10a-c**). The isolines of the different deformation values also all displayed a flat U-shape with almost horizontal direction underneath the indenter.

The maximum principal compression and shear stress values were only minimally affected by the change in muscle width. The maximum principal compression and shear stress both reduced by 1.56% (3.88kPa and 1.94kPa) between the 8mm and the 4mm width (**Table 6-1**). These values were observed around the edge of the indenter (**Figure 6-10d-i**). The principal compression stress fields underneath the indenter remained mostly homogeneous with the same average of 69.09kPa for all shapes (**Figure 6-10d-f**). The shear stress also showed a similar distribution across all samples with magnitudes of 34.55kPa towards the edges of the indentation field and 48.41kPa towards the centreline (**Figure 6-10g-i**).

Table 6-1: Change in stress and deformation calculated by FE model with different muscle widths. A muscle specimen was modelled to be compressed between a flat ended indenter and a silicone layer. When decreasing the width from 8mm to 6mm to 4mm at a constant thickness of 2mm, maximum axial deformation, principal stress, and shear stress all remained almost constant (approx.1% change in magnitude). Maxima marked with * are minimum values as the deformation of the muscle specimen took place in negative y-direction.

Muscle width	Maximum* axial deformation [mm]	Maximum* principal stress [kPa]	Maximum shear stress [kPa]
8mm	0.27578	248.72	124.36
6mm	0.27722	247.23	123.62
4mm	0.27812	244.84	122.42

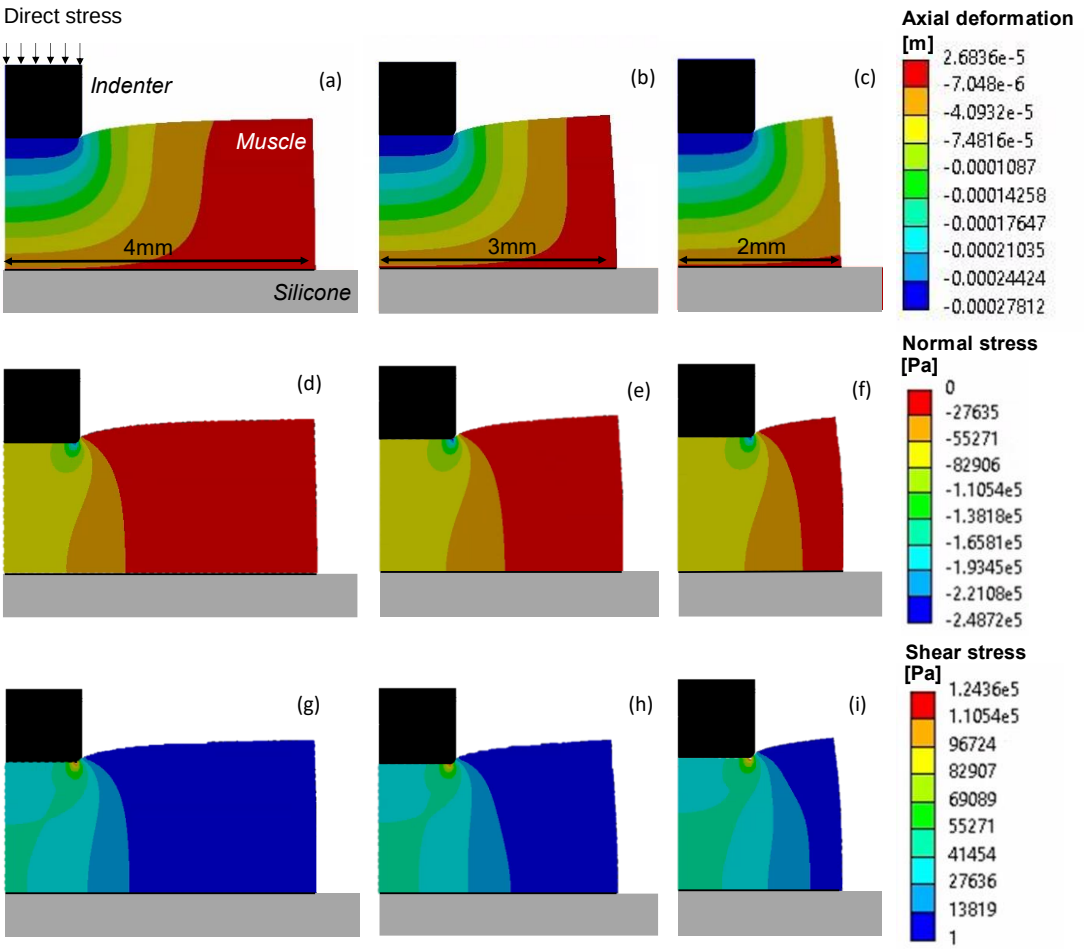

Figure 6-10: Representative FE calculation of axial deformation, normal stress, and shear in compressed rat skeletal muscle with different widths. Model showing a flat indenter compressing a muscle onto a silicone layer with a direct stress of 103kPa. Because of the axisymmetry of the model, the overall widths were 8mm (a, d, g), 6mm (b, e, h), and 4mm (c, f, i). The images show only a section of the full model for better visibility, the dimensions of the silicone layer exceed those shown in the images.

6.4.1.3. Influence of change in muscle thickness numerical results

Reducing the thickness of the muscle sample from 2mm to 1mm at a constant width of 8mm almost halved the maximum axial deformation from 0.276mm to 0.153mm (**Table 6-2**). The overall distribution of the isolines for axial deformation was taking a flat U-shape (**Figure 6-11a, b)**, as described in "*6.4.1.2 Influence of change in muscle width on numerical results"*. Like the thicker muscle, the magnitude of the deformation in the thinner muscle decreased towards the silicone layer from >0.142mm to <0.041mm.

Table 6-2: Change in stress and deformation predicted by FE model with different muscle thicknesses. A muscle specimen was modelled to be compressed between a flat ended indenter and a silicone layer. By decreasing the thickness from 2mm to 1mm at a constant width of 8mm, the maximum axial deformation as well as the maximum principal and shear stress decreased. Maximum values marked with * are technically minimum values as the deformation of the muscle specimen took place in negative y-direction.

Muscle thickness	Maximum* axial deformation [mm]	Maximum* principal stress [kPa]	Maximum shear stress [kPa]
2mm	0.27578	248.72	124.36
1mm	0.15346	201.29	100.64

The maximum principal compression stress and shear stress both decreased by 19.07% (47.43kPa and 23.72kPa respectively) when reducing the thickness from 2mm to 1mm (**Table 6-2**). These maximum values were found near the edge of the indenter (**Figure 6-11c-f**). Reducing the thickness also introduced some inhomogeneities into the stress fields with additional areas of higher principal compression stress towards the midline of the muscle. The average stress thereby increased by 27.63kPa from 69.09kPa to 96.73kPa (range of 82.91 – 110.54kPa) from the thicker to the thinner muscle (**Figure 6-11c, d**). The shear stress field on the other hand was more homogenous at a thickness of 1mm. Its magnitude averaged to 48.36kPa (range of 41.45 – 55.27kPa) for the majority of the muscle area underneath the indenter (**Figure 6-11e, f**) compared to 34.54kPa at a thickness of 2mm.

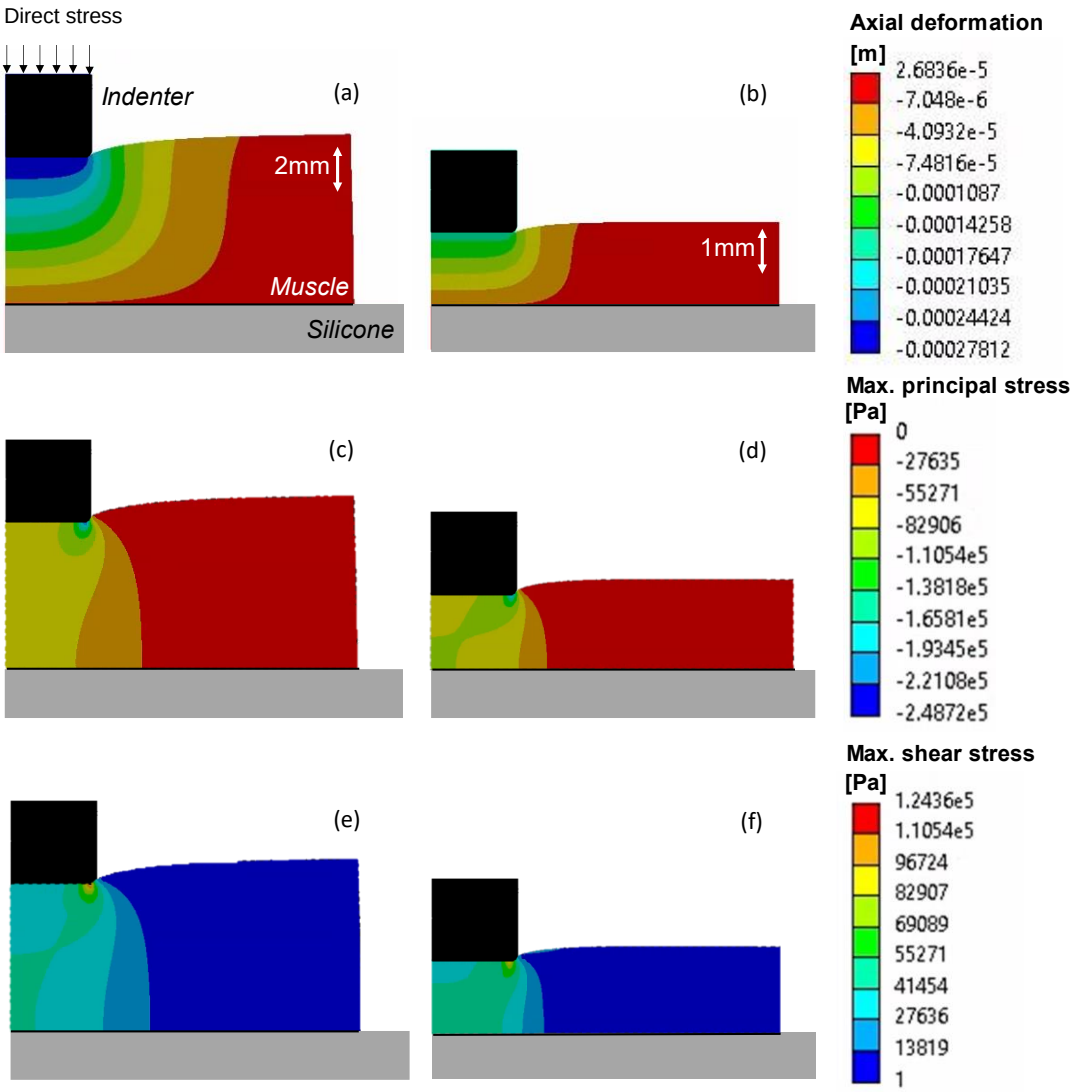

Figure 6-11: Representative FE prediction of axial deformation, maximum principal compression stress, and maximum shear stress in rat skeletal muscle with different thicknesses. Axisymmetric model showing a flat indenter compressing a muscle with an overall thickness of 2mm (a, c, d) and 1mm (b, d, f) onto a silicone layer with a direct stress of 103kPa. The images show only a section of the full model for better visibility, the dimensions of the silicone layer exceed those shown in the images.

6.4.2. Discussion on finite element analysis of a transverse indentation experiment

6.4.2.1. Mechanical environment within transversely compressed skeletal muscle tissue

Based on the determined model parameters, FEA of a static indentation scenario with a direct compressive stress of 103kPa was performed. The results revealed a gradually degrading axial deformation of the skeletal muscle in y-direction with almost

horizontal isolines underneath the indenter (**Figure 6-9a**)**.** The magnitude of maximum shear and principal compression stresses were thereby mostly uniform across the whole thickness of the muscle with changes only seen towards the edge of the indenter (**Figure 6-9b, c**). This indicates that transverse compression creates an almost homogeneous mechanical environment in the muscle layer underneath the indenter. It therefore seems appropriate to take cross-sections from the whole indentation area to determine a collective cell death number, as described in ”*4.3.4 Tissue processing through formalin fixation and paraffin embedding*”.

The stress and deformation graphs (**Figure 6-9**) also showed that the indentation had almost no influence on the mechanical environment in the periphery of the muscle layer. Areas outside the direct impact zone should therefore not experience any mechanical effects of the indentation. From an engineering point of view, it is hence acceptable to use areas peripheral to the indentation site as control samples, as suggested in “*4.7.1 Method for Live-or-Dye and Procion Yellow MX4R staining*”.

When comparing shear to principal compression stress magnitudes, the estimated maximum of the compressive stress was twice as high as that of the shear component (**Figure 6-9**). The general principal compression and shear stresses in the muscle layer underneath the indenter showed a similar tendency: the compressive stress was at least 1.5-times, if not two-times higher than that of the shear component. It therefore seems likely that compression rather than shear would be the main cause of cellular damage in the indentation area.

The FE model also illustrated that the average magnitude of principal compression stress in the muscle below the indenter was only approximately two-thirds that of the direct stress (69kPa vs 103kPa) (**Figure 6-9**). Thus, the applied load does not represent the mechanical environment within the muscle layer. Instead, the developed FE model could be used to predict the average compressive stress within the muscle model when interpreting future experimental results.

6.4.2.2. Influence of geometric variability on results of finite element modelling

The influence of biological variability on the FE results was tested with a focus on potential differences in geometry of the skeletal muscle layer. The effect of a reduced muscle width on the stress field underneath the indenter was thereby minimal. Stress distribution patterns for both compression and shear stresses were almost identical

(**Figure 6-10**) and their maximum values differed by less than 2% (**Table 6-1**). The influence of muscle width on computational results can therefore be regarded as insignificant when the muscle width exceeds the diameter of the indenter.

Reducing the muscle thickness, on the other hand, had a greater impact on the mechanical environment. Maximum stress values decreased by 19% (**Table 6-2**) in a thinner muscle. However, these maximum values were confined to the edges of the indented area. On the other hand, both compression and shear stress displayed an increasing area of higher stress levels (38% increase in stress levels) in the muscle layer underneath the indenter (**Figure 6-11**). It should be noted that this effect was achieved by reducing the muscle thickness by half, representing a case of significant biological variability. Variability of this scale should be avoidable through careful experimental design, i.e. by using the same age and sex of animals that have been kept under almost identical conditions. Deviations of the predicted mechanical environment from the real values can therefore hopefully be kept to a minimum.

6.4.3. Limitations of the finite element model and preliminary studies

One limitation of FEA for biological applications is the need to express material behaviour through mathematical models. While linear elastic material responses like for steel are easy to predict, the complex behaviour of soft tissue is difficult to reproduce. The skeletal muscle tissue was modelled according to the results of a static compression study on rat muscle by Bosboom et al. [171]. They tested the tibialis anterior of Brown Norway rats under *in vivo* conditions rather than soleus and extensor digitorum longus muscles of Sprague-Dawley rats as in the proposed *ex vivo* experiment. Nevertheless, the material model by Bosboom et al. is a good estimate for the viscoelastic behaviour and was therefore considered sufficiently similar to the proposed setup of transverse static compression.

It should also be noted that the FE model presented in this chapter is a macro-model without consideration of anisotropy and heterogeneity. Over the last decades, researchers started to divide skeletal muscle models into five hierarchical levels [381]: entire muscle (as done in this study), fascicles, muscle fibres, myofibrils, and sarcomeres (s. "*3.3.1 Hierarchical structure of skeletal muscle*"). By combining them into multiscale models [381–385], researchers showed that the highest hierarchical level does not necessarily represent the mechanical environment within the other

levels. For example, tension on tissue level leads to shear stress at cell level from connections to neighbouring cells [381]. Tissue compression leads to tensile stress in the cell membrane as the cells flatten perpendicular to compressive loading direction [155, 386] and fibres might slight across one another, introducing shear stress into the sample [387]. Additionally, low-level tissue bulk deformation can induce large cell-level deformations [388]. The collagen network of the extracellular matrix (ECM) also has its own mechanical properties and structural orientations, which influence cellular stress [382, 389]. These factors need to be taken into consideration when interpreting experimental studies based on a macro-level FE model. Nevertheless, a low-level model was accepted in return for a simpler material model without the need for further, complex material testing and extensive mathematical modelling.

Another shortcoming in the FE model setup was the geometry. In the model, the sharp edge of the indenter was softened with a rounded corner to improve convergence. Accordingly, the shear stress in the area around the edges in the actual muscle sample is presumably higher than estimated. Potential misalignment between indenter and muscle could lead to further stress concentrations. However, the effect of these stress peaks on the overall mechanical environment of the muscle should be negligible.

The most significant geometric simplification was presenting the muscle as a cuboid. Irregularities in muscle shape that deviate from this ideal could influence the stress and strain distribution within the samples. The performed parametric studies indicated that potential deviations in muscle length and thickness should only have a minor effect on the results. Further shape changes could be assessed in future parametric studies.

6.5. Chapter Summary

FE modelling is a popular tool to determine and visualise mechanical effects within materials that would otherwise be largely unattainable. Accordingly, an FE model was developed to assess the mechanical environment in skeletal muscle tissue on a layer of silicone under transverse compression with a flat-ended, circular indenter. Contact mechanics were applied to produce a simplified, axisymmetric model of the experimental setup while integrating complex viscoelastic behaviour of soft tissue.

Compressive stress dominated the mechanical environment in the muscle. The muscle geometry thereby only seemed to change the mechanical environment when

the thickness of the muscle layer was reduced significantly. Otherwise, a mostly homogeneous stress field was predicted, making the experimental setup suitable for cell death analysis across multiple cross-sections of the indented muscle area. Areas outside of the indentation field can be used as controls as they remained largely unaffected by direct stress application.

The results also indicated that the general stress magnitude within the muscle layer was lower than the direct stress applied by the indenter. Hence, future experimental studies should include computational modelling to predict the mechanical environment within the muscle layer. The model could also be adapted to dynamic loading scenarios. Further validation of the muscle material model might be necessary, for example by comparing displacement data from the dynamic indentation with numerical predictions by the FE model. Lastly, a multi-scale model could be developed in the future to assess the mechanical loading environment across the different hierarchical levels of skeletal muscle tissue.

CHAPTER 7

Validation of the *ex vivo* animal model by development and comparison of a static stress-cell death threshold

A static loading protocol was tested on the newly developed *ex vivo* animal model with the image analysis workflow to obtain a stress-cell death threshold. The results were compared to existing *in vivo* and *in vitro* studies for validation (**Objective 4**).

The study was conceptualised by the author and Dr. Arjan Buis. The experiments were setup and conducted by the author. Imaging and analysis were also performed by the author, with support from Dr. Alastair Wark.

7.1. Introduction: Validity, verification, and validation of the *ex vivo* model and image analysis workflow

Over the last few chapters, an *ex vivo* model system and image analysis workflow have been developed to determine sarcolemmal damage after mechanical loading. When developing a new methodological approach, validation is crucial to ensure the reliability of results. However, the term validation is often used interchangeably with verification and validity. Their meanings are similar and therefore subject to ongoing debates across different disciplines [390, 391]. In the context of this project, terms are defined as follows:

Validity – Does it make sense what I am doing?

Proving validity involves giving a rational for a decision. Theoretical background and assumptions are presented and discussed to create an argument for a justifiable representation of a problem. In this thesis, the reasoning for choosing an *ex vivo* approach as opposed to *in vivo* or *in vitro* models was discussed in "*4.1.1 Model system for the analysis of cell death after prosthesis-related loading*", making a point of the model's validity.

Verification – Am I doing the thing right?

Verification is mostly concerned with whether a model or product meets the technical requirements. In relation to this project, a few verification processes have been included into the experimental design and image analysis procedures. Capabilities to detect sarcolemmal damage with ProY-staining, for example, were verified by including positive and negative controls (s."*4.7.1 Method for Live-or-Dye and Procion Yellow MX4R staining*"). This ensures that the developed method measures outcomes correctly.

Validation – Am I doing the right thing?

Validation is needed to confirm that a model actually achieves its intended purpose. Although preliminary studies showed that the *ex vivo* setup developed in this project can measure sarcolemmal damage, the link between the mechanical loading environment and cell death needs to be confirmed. A first indication for this link were visual differences between undamaged and damaged samples (i.e."*4.7.3 Suitability of Procion Yellow to detect cell damage*"). However, for good practice, these qualitative observations should be backed up with quantitative results.

A good way to validate the *ex vivo* model is to perform a study that allows to compare outcomes to an already established, independent dataset on stress-related cell death. From a methodological point of view, the *in vivo* study performed by Linder-Ganz et al. [34] is closely related to the proposed *ex vivo* approach. The researchers applied static direct stress to the hindlimb of male Sprague-Dawley rats with a flat indenter, either directly to the gracilis muscle or superficially through the skin. Samples of the muscles were fixed with formalin and processed for histopathological analysis. Following staining with PTAH, muscles were observed for a loss of cross-striation to classify them as “no damage” or “cell death”.

The mechanical loading protocol tested different combinations of stress magnitude and duration, from 15min up to 360min and from 11.5kPa to 77kPa. Linder Ganz et al. then combined their data with results from previous animal studies to develop a sigmoid pressure-time cell death threshold curve (**Figure 7-1**).[4]

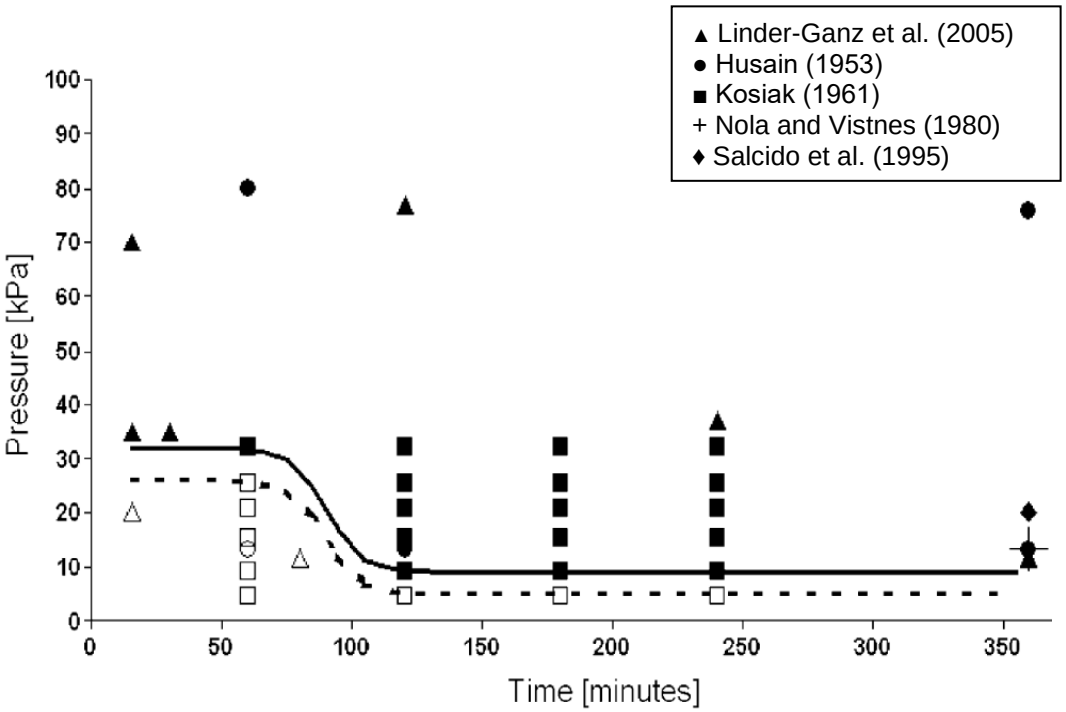

Figure 7-1: Pressure-time cell death threshold (Reproduced from [2] with permission from publisher [4]). Presented data is collated from different studies [2, 5–8] and depicts the cellular response of skeletal muscle to static mechanical loading. Above the solid line, pressure-time combinations led to cell death (solid markers), below the dashed line no damage was detected (hollow markers). In between is a transition zone of uncertainty.

[4] Reprinted from Journal of Biomechanics, 39:14, Linder-Ganz E. et al., Pressure–time cell death threshold for albino rat skeletal muscles as related to pressure sore biomechanics, p.2725-2732, Copyright (2006), with permission from Elsevier.

7.2. Aims of static threshold study

The aim of this chapter is to validate the combination of the proposed experimental design (*Chapter 4*), image acquisition, and analysis workflow (*Chapter 5*). Static mechanical compression was applied to *ex vivo* muscle tissue and the resulting cell death measured through fluorescent ProY-staining. The loading protocol was based on an *in vivo* study by Linder-Ganz et al. [34] to allow for comparison of the results. This will form the next step towards quantifying the physiological response of skeletal muscle to prosthesis-related mechanical loading.

The results of the direct comparison between the *in vivo* and *ex vivo* study will also be discussed in the context of other threshold studies performed in an *in vitro* environment [33, 212]. This will aid the interpretation of outcomes from existing and future studies to create a clearer picture of the effect of direct stress on skeletal muscle.

7.3. Design and methods for static threshold experiment

7.3.1. Collection and preparation of murine skeletal muscle tissue

Tissue samples were collected from male Sprague Dawley rats (n = 12) and prepared as described in *"4.3.2 Collection and preparation of murine skeletal muscle tissue"*. In brief, soleus (SOL, n = 5*)* and extensor digitorum longus (EDL, n = 7) muscles were isolated from both hindlimbs, pinned out in silicone-covered Petri dishes, and submerged in MOPS-based buffer solution at ambient temperature (22°C).

7.3.2. Experimental setup for static loading experiments

Transverse compression was applied by lowering a flat, round indenter (r = 1mm) onto the samples. The indenter was either part of a customised loading rig (s. "*4.3.3 Mechanical loading* ") or attached to a Bose Electroforce 3100 (TA Instruments) to allow for parallel processing of four muscle samples at once. Customised rigs were used for loads ≥0.11N, which is equal to the dead weight of the indenters. For loads >11N, weight was added to the top of the indenter.

The Bose Electroforce was used for loads <11N. It was fitted with a load cell (22N) connected to a flat steel indenter (**Figure 7-2**). The system was allowed to stabilise

for 30min prior to usage. The Petri dishes with samples were inserted on the bottom plate and raised towards the indenter. To initiate contact, the top mover was activated to bridge the remaining distance until a contact force of -0.01N was established.

The static direct stress ranged from 5 – 103kPa and was applied for 30min – 120min (**Table 7-1**). For each duration, three stress values were chosen that represented the "cell death" (= above threshold), "threshold" (= transition zone), or "no cell death" (= below threshold) region defined by Linder-Ganz et al. [34]. Each stress-duration-combination was tested on one sample and the maximum experimental duration was restricted to 3.5h to ensure tissue viability.

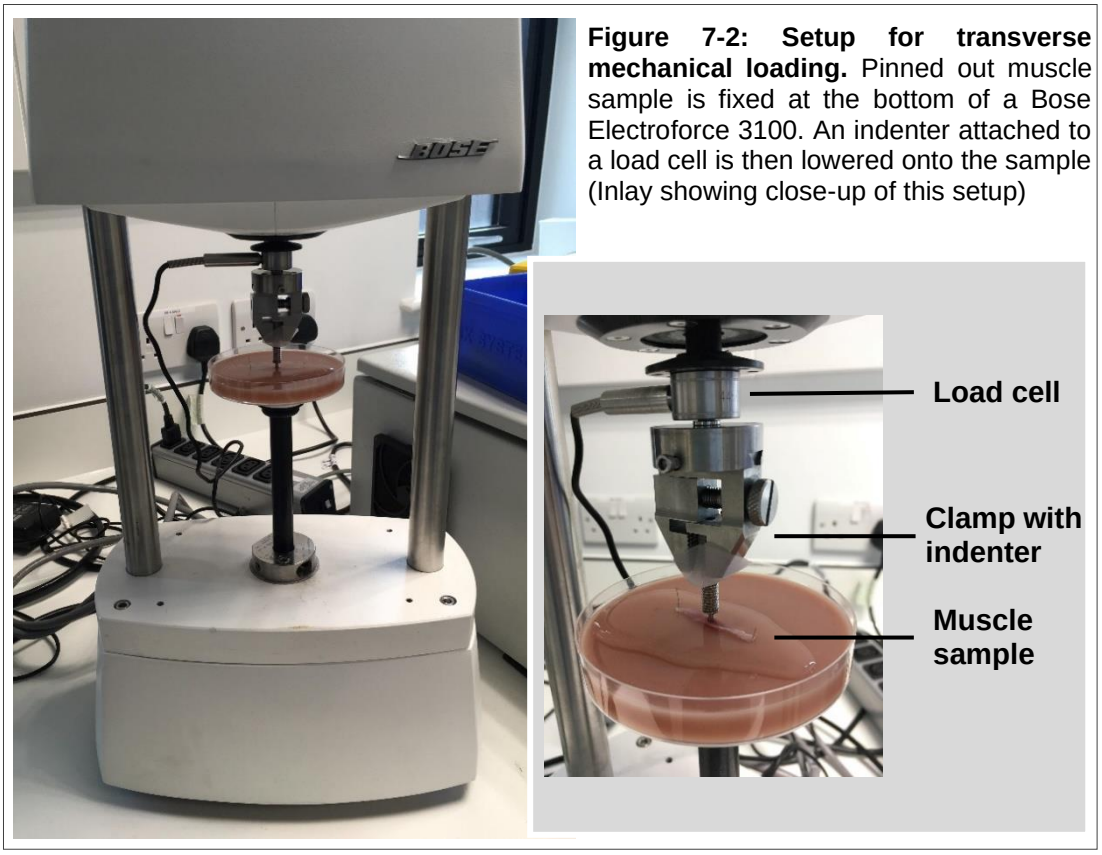

Figure 7-2: Setup for transverse mechanical loading. Pinned out muscle sample is fixed at the bottom of a Bose Electroforce 3100. An indenter attached to a load cell is then lowered onto the sample (Inlay showing close-up of this setup)

Table 7-1: Overview static compressive loading protocol. Compressive loads ranging from 0.02 – 0.32N (direct stress 5 – 103 kPa) were applied to skeletal muscle samples for durations between 30 – 120min. Each stress-duration-combination represents one sample and was chosen based on the pressure-cell death threshold defined by Linder-Ganz et al. [34].

	30min	**60min**	**90min**	**120min**
Above threshold	0.32N / 103kPa	0.32N / 103kPa	0.10N / 32kPa	0.10N / 32kPa
Close to threshold	0.11N / 34kPa	0.11N / 34kPa	0.06N / 20kPa	0.03N / 9kPa
Below threshold	0.08N / 25kPa	0.08N / 25kPa	0.03N / 9kPa	0.02N / 5kPa

7.3.3. Fluorescent staining of muscle tissue with ProY and tissue processing

Following dissection and mechanical loading, the tissues were stained with 0.1% Procion Yellow MX4R for 1h before being fixed in 10% neutral buffered formalin for 28h. For each experimental group, the indented muscle area as well as peripheral control samples were processed and embedded separately into paraffin before being cut into 4µm cross-sections as described in "*4.3.4 Tissue processing through formalin fixation and paraffin embedding*".

7.3.4. Image acquisition and analysis

Fluorescently stained slides were imaged on a Leica SP8 system in widefield-mode. For each mechanically damaged and control sample, n = 6 cross-sections were imaged with x10 magnification through an FITC filter (Ex 482/35, Em 536/40), followed by a Y5 filter (Ex 620/60nm, Em 700/75nm). Full cross-sectional images were composed through automated tiling with the Leica LAS X software (V.3.1.5.16308). A detailed description can be found in "*5.3.1.1 Microscope and software specifications*".

All images were imported into FIJI/ImageJ and converted to 8-bit greyscale images before an established analysis workflow was performed (s."*5.5.6 Overview over the image analysis* workflow"). In short, all images were background subtracted and normalised before further processing. For control sections, the combined average intensity was determined for each sample. This value was set as threshold to mask unlabelled fibres in sections from the indented areas. Following segmentation with Cellpose [358] to separate individual myofibers, the number of dye-positive cells in the indented area was counted for each cross-section and averaged across each sample.

7.3.5. Definition of damaged and undamaged samples

Unlike in Linder-Ganz et al.'s setup [34], samples could not simply be classified as damaged when ProY-positive cells were detected, as all cross-sections had cell death counts of ≥ 53. However, those dead cells were not necessarily associated with mechanical loading. Possible other sources are naturally occurring cell death, damage from sample handling, or storage without oxygenation. A baseline-level above which a cross-section is classified as damaged therefore had to be defined.

The differentiation between “cell death” and “no damage” was based around damage distribution. In samples with high cell death counts, damaged cells were arranged in a centralised pattern (**Figure 7-3b**), which was also observed by other researchers in similar experiments [195, 198, 199]. In comparison, samples with low dead cell counts were missing a distinctive pattern with dead cells scattered throughout the samples (**Figure 7-3a**). It is therefore likely that a centralised damage distribution is related to mechanical damage from the indentation.

Based on this observation, all processed images were viewed to determine whether a distinctive damage pattern was visible. If one or more of the sections belonging to the same sample displayed a localised damage distribution, the whole sample was categorised as “cell death”. From this, the lowest average number of dead cells in damaged samples could be defined as baseline threshold, above which samples were categorised as “cell death”, and below as “no damage”.

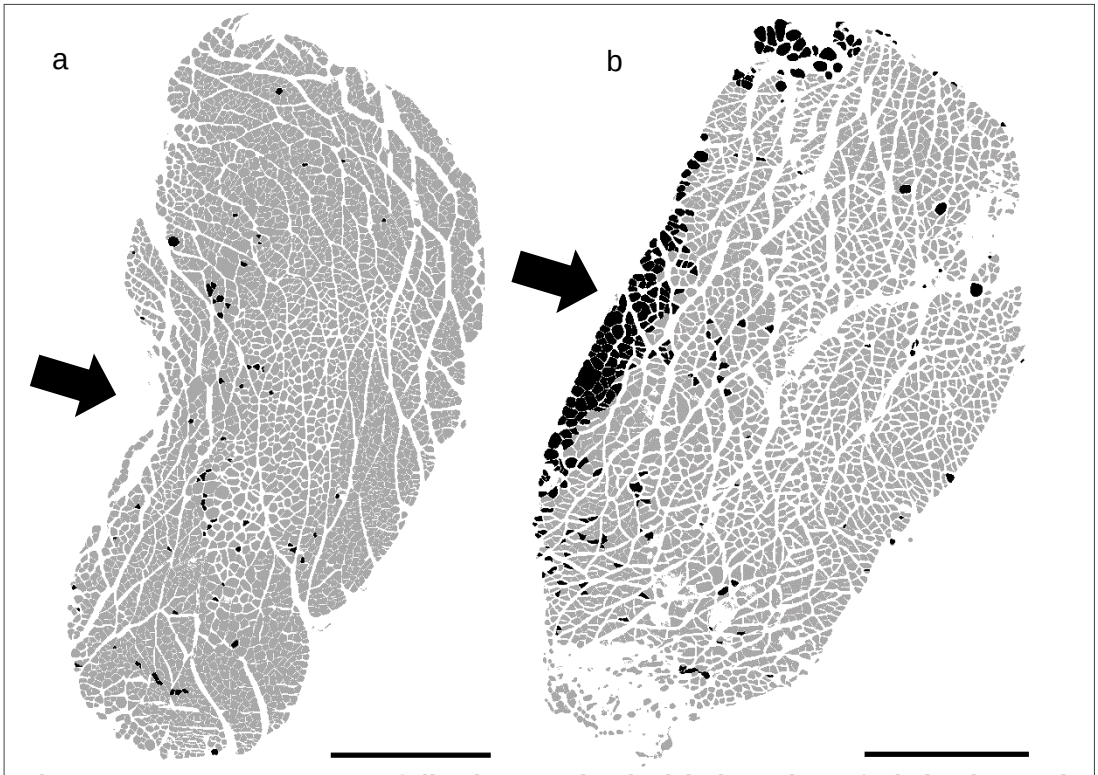

Figure 7-3: Damage pattern following mechanical indentation of skeletal muscle tissue. Healthy cells are grey in colour, dead cells are marked in black. Black arrows indicate location and direction of indentation. **a)** Cross-section of skeletal muscle tissue indented with a flat indenter (r = 1mm) for 30min with 25kPa. No clear pattern on dead cell distribution discernible. **b)** Skeletal muscle cross-section after 30min of indentation with 103kPa. Clear accumulation of dead cells on the left-hand edge where the sample was indented. Scale bar 1000µm.

7.3.6. Finite element analysis of static transverse mechanical loading setup

As discussed in "*6.4 Finite element analysis of transverse mechanical loading of skeletal muscle tissue*", the direct stress externally applied by the indenter might not match the compressive stress within the sample. Accordingly, Finite Element Analysis (FEA) was performed in Ansys (Workbench 2021 R2) to determine the mechanical conditions within the muscle samples for each stress application. The detailed model setup is described in"*6.3 Development of a finite element model of transverse mechanical indentation of skeletal muscle*". In brief, an axisymmetric model of the indentation setup was designed with rectangles representing each body – indenter, muscle, silicone – according to real-life measurements (**Figure 7-4**). The indenter and silicone were both assigned linear elastic material properties whereas the muscle was described by a first-order Ogden model with Prony series expansion. The indenter was meshed through general face meshing with quadrilateral elements, the mesh for the muscle and silicone had a defined element size of $2.5 \times 10^{-9} m^2$. The contact between the indenter and muscle was assumed to be frictionless; the contact between the muscle and silicone layer allowed sliding but prohibited separation. Displacement restrictions in X-direction were placed on the axis of symmetry, and the bottom of the silicone layer was treated like a fixed support.

A direct stress was then applied to the top line of the indenter, according to the loading scheme described in **Table 7-1**. The resulting normal stress in y-direction was computed to assess the overall distribution as well as the average compressive stress in the muscle layer in the indentation zone. Potential differences between the direct stress and average compression stress were also plotted.

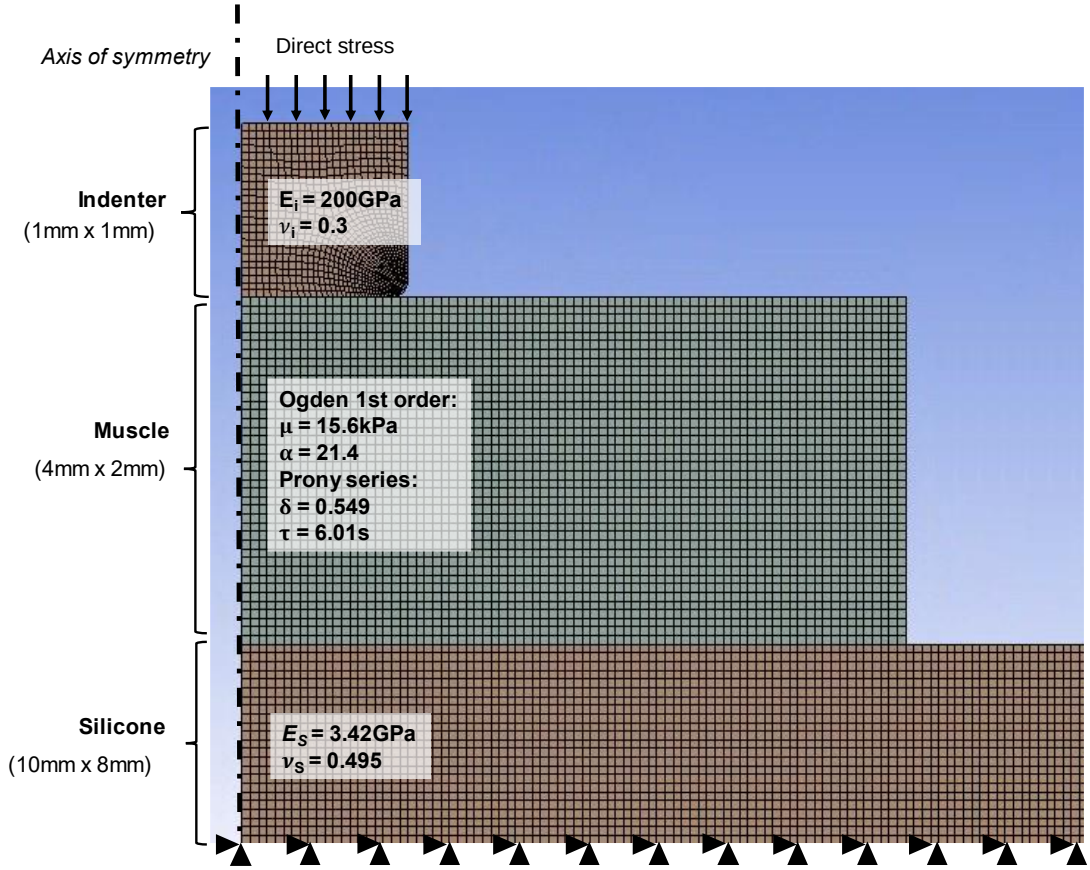

Figure 7-4: Finite element model of static indentation experiment. Axisymmetric model of indenter, muscle, and silicone layer (dimensions in image not representative of real model). The mesh of each component as well as the material properties are shown.

7.3.7. Definition of stress-time cell death thresholds for *ex vivo* skeletal muscle tissue

The results from the categorisation of samples into "cell death" and "no death" groups were combined with the internal stress values calculated through FEA into a stress-time plot. From this, stress-threshold functions for samples categorised as "cell death" and "no damage" were compiled. Their shape was estimated by four-parameter decreasing single-step Boltzmann-Type sigmoid functions, to be able to compare to muscle-damage-thresholds used by Linder-Ganz et al. [34] and Gefen et al. [33] in *in vivo* and *in vitro* studies:

$$\sigma_{compressive} = \frac{K}{1+e^{\alpha(t-t_0)}} + C \qquad (7\text{-}1)$$

where σ is the compressive stress, K [kPa] is the range of the function, α [min^{-1}] is the "slope coefficient" [392], t_0 [min] is the time at midrange, and C [kPa] represents the minimum compressive stress asymptote. Each dataset was analysed in Minitab (Vers.

19.2020.1), according to the least-square-method. Parameter estimates for *K* (maximum compressive stress minus minimum compressive stress) and *C* (minimum compressive stress) were calculated from the dataset, *α* and t_0 were taken from Linder-Ganz et al.'s study [34] (**Table 7-2**). To adapt a conservative approach to threshold estimates, the *C* parameter of each sigmoid was restricted in a way that the graphs were below all "cell death" and above all "no death" datapoints. The resulting threshold curves were assessed for their fit and compared with those from Linder-Ganz et al.'s study [34].

Table 7-2: Parameter estimates for non-linear regression analysis. Sigmoid Boltzmann functions were fitted with the least-square-method to a dataset from experimental indentation studies on skeletal muscle tissue to obtain "cell death" and "no damage" stress-time threshold curves. The functions were estimated based on the starting parameters K, C, α, t_0, (**Eq 7-1**) that were taken from the datasets and relevant literature [34]. The C-value was restricted to ensure that each threshold curve encompasses all data points of the respective dataset.

	K [kPa]	C [kPa]			α [min^{-1}]	t_0 [min]
		original value	parameter estimate	restriction condition		
Cell death threshold	16.2	6.3	5.5	C < 6	0.5	90
No damage threshold	13.1	3.4	4.2	C > 3.7	0.5	90

7.4. Results of static loading experiment

7.4.1. Comparison of direct stress with principal compressive stress within the muscle layer

Finite element (FE) modelling was performed to assess potential differences between the direct stress and computed principal compressive stresses within the muscle layer. The internal compressive stress was predicted to be 33.1% below the external direct stress (R^2 = 99.96%, **Figure 7-5**). This differs from other studies that predicted higher internal stresses as opposed to the interface stress [29, 34]. However, differences in geometry and the addition of a silicone layer underneath the muscle samples might have influenced the overall behaviour of this system as opposed to other models.

The stress-field in general was mostly uniform across the indentation zone. Localised stress concentrations were observed underneath the indenter edge. However, the majority of the stress field underneath the indenter was homogeneous. Based on

these results, computed values of the average internal stress in the homogeneous area (**Figure 7-6**) were used instead of direct stress (**Table 7-1**) to interpret data from the indentation study.

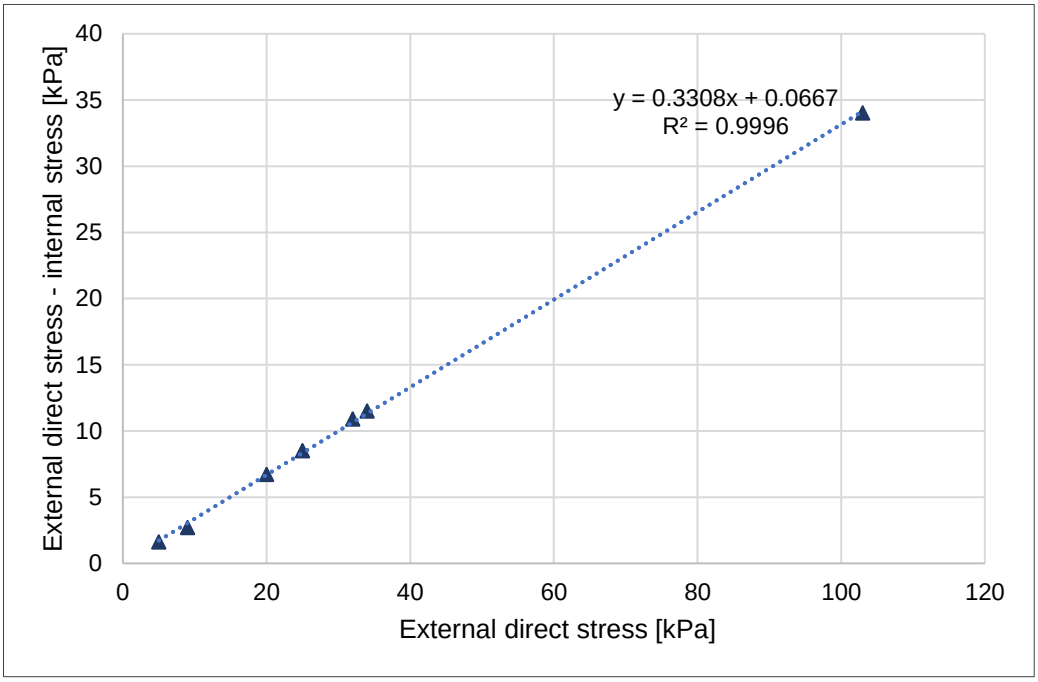

Figure 7-5: Difference between external direct stress and mean internal muscle stress applied by indentation experiment. Strong linear relationship (R^2 = 99.96%) between external direct stress and difference between external and internal stress as estimated through finite element analysis.

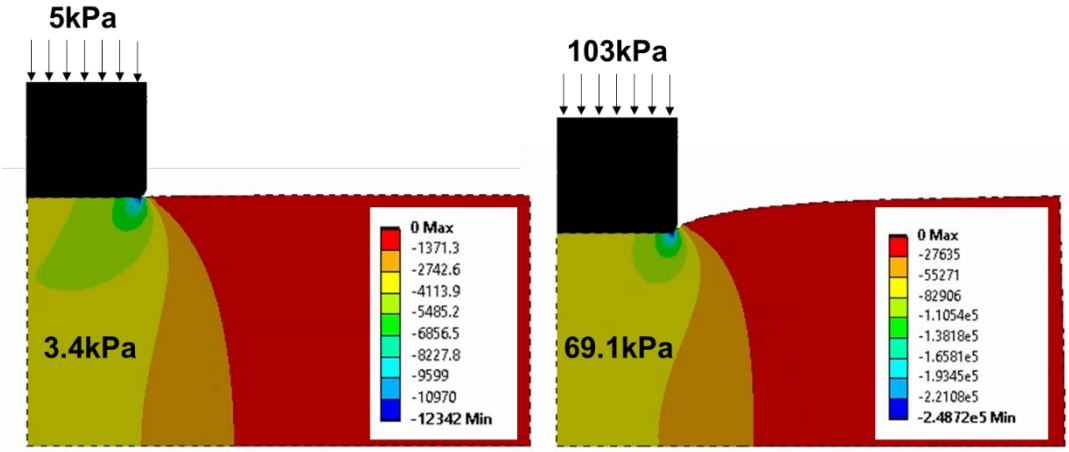

Figure 7-6: Representative finite element models of the *ex vivo* indentation experiments. Images demonstrate relationship between direct stress application (5kPa and 103kPa) and average compressive stress within the skeletal muscle layer (3.4kPa and 69.1kPa) when statically compressed with a flat indenter into a silicone layer (not shown in images).

7.4.2. Relationship between cell death counts, stress magnitude, and duration

The average cell death count obtained from statically indented samples ranged from n = 53 to n = 254 (**Table 7-3**). The lowest compressive stress for each duration corresponded with the lowest number of dead cells. For medium and high-level stress, however, cell death numbers were similar with n = 160 ± 70.56 at medium and n = 158 ± 58.09 at high stress levels. Unexpectedly, at three out of four time points, the number of dead cells after high stress was below that of the medium stress level. A longer duration of stress application on the other hand led to more dead cells for all but one stress level (69kPa for 30 – 60min).

Table 7-3: Average number of dead cells in skeletal muscle following mechanical loading. The time frame for the direct stress application ranged from 30min – 120min, the internal compressive stress from 3.4kPa to 69kPa. Each stress-duration combination was tested on one skeletal muscle sample from Sprague-Dawley rats.

Compressive stress [kPa]	**Time [min]**			
	30	**60**	**90**	**120**
69	229	162		
22.5	112	174		
21.1			87	153
16.5	72	109		
13.3			100	
6.3			53	254
3.4				54

7.4.3. Stress-time cell death threshold for *ex vivo* skeletal muscle tissue

A stress-time plot was generated with a differentiation between the “cell death” and “no damage” datapoints (**Figure 7-7**). A baseline cell death value was defined based on the visibility of a damage pattern (**Figure 7-3**). The lowest average number of dead cells in a sample with clear clustering of dead cells was n = 110. From this, sigmoid stress-threshold functions were determined for each category with the parameters for the graph (**Eq 7-1**) defined in **Table 7-4**. Both “cell death” and “no damage” functions encapsulate a region of uncertainty where the fate of a cell is not clearly destined. One outlier was observed at 90min loading with 21.1kPa. The sample was classified as “no damage” despite the compressive stress being above the proposed threshold function. This might be related to human error as the staining procedure for this

sample deviated from the protocol followed for the other samples, i.e. the sample was not “flipped” to ensure sufficient contact between the sample and the staining solution. Another potential explanation is biological variability. However, with only one sample analysed for each load-time-combination, no definitive conclusion could be drawn. With only few data points available, the outlier was excluded from the threshold curve analysis to avoid skewed results.

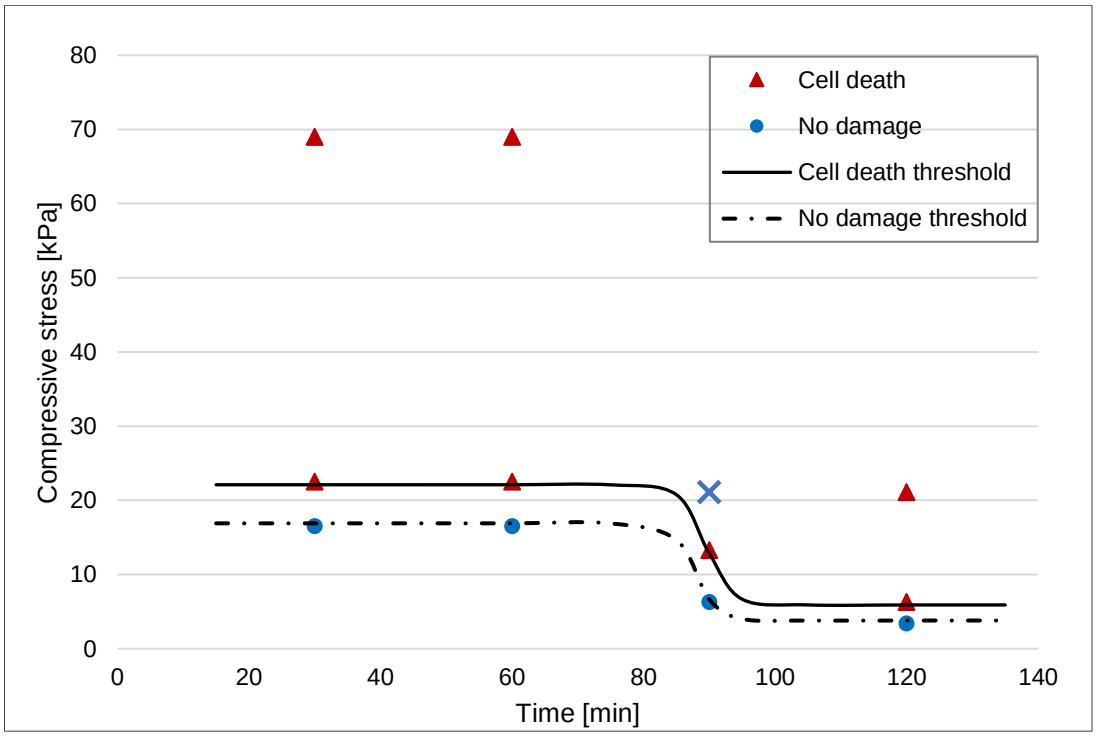

Figure 7-7: Static stress-time cell death thresholds for skeletal muscle tissue. Markers indicate data obtained from indentation of ex vivo skeletal muscle with triangles signalling “cell death”, circles marking “no damage” situations, as quantified through fluorescence dead cell staining. One outlier was observed at 90min, 21.1kPa loading, marked with a blue cross. The cell death number at this point classified the sample as “no damage” despite the compressive stress being above the proposed threshold.

The conformity of the threshold functions with the obtained data can be seen in more detail in **Figure 7-8**. A standard error of the regression could not be determined as the number of parameters was equal to the number of data points used in the analysis. However, the experimental data visually overlaps well with the determined threshold levels. The sums of the squared residuals (SSE) were calculated in Minitab to measure unexplained variability by the regression. The low values for both threshold curves (SSE_{death} = 0.72, $SSE_{no\ damage}$ = 0.62) support the observed good fit.

When comparing the results of this study to those of Linder-Ganz et al. [34], the parameters of the threshold functions were different (**Table 7-4**, **Figure 7-8**). The

loading level of both cell death and no damage scenarios was lower in the current study, with the stress range *K* reduced by 6.8kPa, the minimum stress *C* by 3.1kPa. On the contrary, the slope coefficient was higher in the current study with α_{death} = 0.54min^{-1} and $\alpha_{no\ damage}$ = 0.57min^{-1} compared to α = 0.15min^{-1} in Linder-Ganz et al.'s results, leading to a steeper sigmoid step. The time at midrange was similar across both studies with t_0 = 90min for Linder-Ganz et al.'s study, and t_0 = 89.5min and t_0 = 87.8min for the "cell death" and "no damage" thresholds of this experiment.

Table 7-4: Parameters for sigmoid stress-time threshold functions.

		K [kPa]	C [kPa]	α [min^{-1}]	t_0 [min]
Cell death threshold	Our data	16.2	5.9	0.54	89.46
	Linder-Ganz et al. [34]	23	9	0.15	90
No damage threshold	Our data	13.1	3.8	0.57	87.77
	Linder-Ganz et al. [34]	21	5	0.15	90

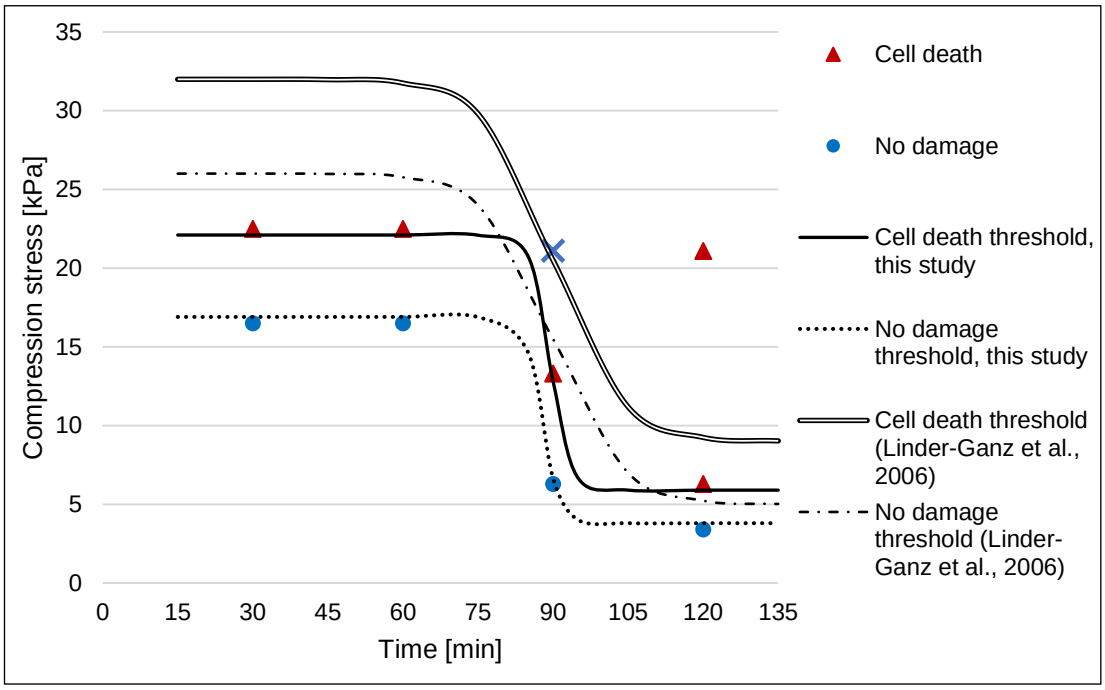

Figure 7-8: Comparison of stress-time cell death thresholds from ex vivo and in vivo studies. Markers indicate data from indentation of ex vivo skeletal muscle with triangles signalling "cell death", circles marking "no damage" situations, as quantified through fluorescence dead cell staining. One outlier was observed at 90min, 21.1kPa loading, marked with a blue cross. The threshold curves from in vivo studies performed by Linder-Ganz et al. **[34]** have a similar time step as those fitted to the data from this study but differ in stress magnitude and range, as well as the slope of the sigmoid step.

7.5. Discussion on the response of *ex vivo* skeletal muscle tissue to mechanical loading

In *Chapter 4* and *5*, a new *ex vivo* model of skeletal muscle was proposed together with an image analysis protocol to quantify sarcolemmal damage following mechanical loading. For validation, the performance of the model was measured against an established *in vivo* model by Linder-Ganz et al. [34]. They identified a sigmoid pressure-time cell death threshold, characterising the critical turning point where cells transit from “no damage” to “cell death”. Based on this study, a similar loading protocol was performed with the *ex vivo* model. The recorded stress-time cell death threshold thereby had a similar sigmoid shape that could differentiate undamaged and damaged samples for all but one scenario. The outlier might be explained by human error in the experimental procedure or biological variability.

One interesting observation from the image analysis was that cellular damage mostly occurred near the contact area between the muscle and indenter. A possible explanation is insufficient nutrient supply as superfusion with the buffer solution in this area is prohibited by the indenter. Although this theory was not tested as part of these experiments, other studies showed no effect of contact between an impermeable indenter and cells [388]. The damage observed in the here described experiments did also not extend all the way to the interface in some cases, making it less likely that the cell death pattern is caused by the impermeability of the indenter. Instead, a heterogeneous stress field might play a role. As described in “*6.4.3 Limitations of the finite element model and preliminary* studies”, a macro-level FE model as used in this study can only describe the mechanical environment within the tissue in general. This might differ from the environment experienced by single cells because of the complex anisotropic and heterogenous structure of skeletal muscle. It is hence possible that the compressive stress magnitude at cellular level differs from the calculated values, or additional tensile and shear stresses are present. Further multi-scale FE modelling would be necessary to explore this theory.

7.5.1. General response of skeletal muscle to compressive loading in *ex vivo*, *in vivo*, and *in vitro* models

The general threshold response of the developed *ex vivo* model overlapped with that reported by Linder-Ganz et al. [34] for *in vivo* scenarios. Other researchers have also

defined sigmoid threshold levels for skeletal muscle but with different model systems. Yao et al. [212] used monolayers of myoblasts, Gefen et al. [33] performed experiments on bioartificial muscle constructs (BAM). Muscle damage thereby always depended mainly on the magnitude of the compressive stress for short-term and long-term static pressure application. In between, the combination of loading duration and magnitude determined the onset of cellular damage. However, while all model systems exhibited this sigmoid threshold behaviour, the parameters of the threshold function varied significantly.

7.5.1.1. Influence of stress magnitude on skeletal muscle damage

In vivo tissue appears to be the model system with the highest stress magnitude tolerance. It needed a compressive stress of at least 30kPa within the first 30min of loading before being damaged [34], compared to 22.5kPa in *ex vivo* muscle (**Figure 7-7**). The stress tolerance of single myoblast layers was almost a hundred times lower with the maximum reached at 0.34kPa [212]. Similarly, single cells could only resist a minimum external direct stress of 9Pa for extended periods without damage [212], whereas the threshold of *ex vivo* tissue was at 5.9kPa, that of *in vivo* tissue at 9kPa [34]. For BAM, only strain values were readily available [33], making a comparison of stress magnitudes difficult.

The discrepancies between the different models might be explained by differences in hierarchical structure and cell morphology. In natural muscle, cells are arranged anisotropically in a fibrous pattern surrounded by connective tissue. When a compressive stress is applied, the fibrous arrangement of cells attached to sheets of connective tissue will take up some of the stress and distribute it across all fibre compartments. On the other hand, myoblast monolayers lack both the fibre arrangement and longitudinal cell shape and are therefore more likely to be subject to the high compressive stress.

Apart from the mechanical environment, the level of cellular maturity might play a role. Genetically modified cells like C2C12 myoblasts do not fully represent the structures and physiological processes that a mature, primary cell displays [212]. The mechanical stress response therefore might be different.

7.5.1.2. Influence of loading duration on skeletal muscle damage

Regarding the time component, myoblast monolayers seem most resistant to prolonged loading, followed by BAM and biological tissue. The sigmoid step time (point at which the decline of cell tolerance is at its maximum) was reached after 160min for myoblasts [212], 116min for BAM [33], and 90min for biological tissue (**Table 7-4**). Similarly, single myoblasts could resist their minimum pressure threshold for up to 300min without damage [212], whereas the minimum strain threshold of BAM was reached after 285min [33], the stress threshold of *in vivo* tissue after 120min [34] and *ex vivo* tissue after 100min (**Figure 7-7**).

The higher resistance of *in vitro* structures to extended loading might be explained by the prematurity of cells in comparison to fully developed biological tissue. Biological tissue depends on maintaining an intricate balance between many physiological processes to survive. As these processes rely on nutrients and oxygen, limiting their supply by load application, together with a build-up of waste products, might enhance the negative impact of loading on *in vivo* compared to *in vitro* models over time [393]. *Ex vivo* tissue is even more likely to lack nutrients and oxygen because of the missing connection to a functional vascular and lymphatic system.

Another possible explanation is the contribution of tensile forces and cellular deformation to the mechanical stress. When a compressive stress is applied to natural muscle, the fibrous arrangement of cells attached to sheets of connective tissue causes additional tensile forces [394], thereby increasing the mechanical load on the cell membrane. Over time, structural breakdown of the cytoskeleton and cellular membrane might accelerate. In comparison, the less mature connective tissue network of BAM and lack of fibre arrangement and longitudinal cell shapes in monolayers makes them less prone to tensile stress.

The last feature of the threshold behaviour to discuss is the significant decrease in stress endurance, calculated as $4\alpha^{-1}$ [33, 392, 395]. It lasted longest in BAM (111min) [33], compared to myoblasts (34min) [212], and biological tissue (8min) (**Table 7-4**). This might be explained by a combination of all the previously mentioned differences between the model systems, including their hierarchical structure as well as stages of cellular development.

7.5.1.3. Summary of parameters influencing cellular damage

Analysing the results of this *ex vivo* study in the context of other model systems, namely *in vivo* tissue [34], myoblast monolayers [212] and BAM [33], revealed that all of them displayed a sigmoid stress- or strain-time cell death threshold behaviour. For short-term and long-term loading, the magnitude of the loading condition was important, whereas in between, the combination of magnitude and time was relevant. However, the characteristics of the threshold curves differed significantly between the model systems, potentially because of differences in the level of cell maturity, cellular morphology, the extend of the hierarchical structure, as well as metabolic activity and need for nutrients and oxygen.

Besides the potential reasons for different responses of the model systems, not only the biological material used in each of the studies, but also the experimental setup, processing, and analysis steps to assess cellular damage differed. The comparison of absolute values should therefore be treated with caution.

Nevertheless, the response of the *ex vivo* model to static compression seems to closely resemble that of *in vivo* tissue, despite the lack of a functional blood and lymphatic supply. A study by Stekelenburg et al. [197] supports this observation, revealing that tissue damage from ischemia is minimal for the duration of the conducted experiments. It is therefore likely that for short-term mechanical loading experiments, like this study, the developed *ex vivo* model evokes a similar soft tissue response to external direct stress as an *in vivo* model. This confirms that the proposed *ex vivo* model and image analysis workflow presents a compelling alternative to explore the influence of mechanical loading on skeletal muscle health.

7.5.2. Benefits of quantitative information on the skeletal muscle response to mechanical loading

One main difference between the discussed threshold studies is the way the threshold is defined. Linder-Ganz et al. [34] determined cellular damage semi-qualitatively, assigning samples to “cell death” or “no damage” groups. Gefen et al. [33] used the relationship between the geometry of the indenter and the location of Propidium Iodide-positive cells. While these approaches are suitable for defining categorical threshold levels, they make it difficult to assess the influence of loading characteristics like magnitude and duration more specifically.

The developed *ex vivo* approach allows to obtain additional quantitative information (**Table 7-3**). In relation to the relevance of the direct stress magnitude on skeletal muscle health, one might expect that the higher the stress, the higher the number of dead cells. However, the results of this study did not support this hypothesis. On the contrary, at three out of four time points, the highest applied direct stress produced only the second highest cell death counts. Kosiak [187] reported a similar soft tissue response for an *in vivo* model. Like in this validation study, once cell damage was visible, its extent remained relatively constant with increasing stress magnitudes.

The duration of direct stress application, on the other hand, seems to influence the extent of cellular damage; the longer the load application, the more damage was visible at a constant stress in all but one cases. Other researchers observed comparable results in an *in vivo* [91] setup in rats as well as *in vitro* studies [212]: Once an initial threshold was exceeded, tissue damage spread with increased loading duration.

Overall, the results stress the importance of obtaining quantitative data in addition to defining "cell death" and “no damage” regions as it provides more information on the development of DTI. The similarities in the cellular response between the quantitative *in vivo* and *in vitro* studies and the performed *ex vivo* study are also another indication for the validity of the proposed setup.

7.5.3. Limitations of the validation study

The validation study has several limitations. Despite the importance of verification discussed in the introduction of this chapter, the accuracy of the load cell in the Bose Electroforce was not tested separately. However, regular maintenance and the absence of drifts or other artefacts in the recorded load data indicate a low likelihood of false results. On top of that, a calibration period was granted before every experiment to allow the system to stabilise.

Besides, sample numbers were low with only one muscle per direct stress-time-combination because of time restraints. This led to overfitting of the sigmoid threshold curve. The comparison between different model systems with the proposed one should therefore be interpreted with caution as the proposed threshold level for the *ex vivo* model is not a unique solution. The slope of the sigmoid step for example could change with the addition of further datapoints. Nevertheless, the proximity of the results at the 90min loading duration that differentiate between “cell death” and

“no damage” provides a level of confidence in the general shape of the curve. For future experiments, more samples should be included to account for biological variability and improve the significance of results.

Additional variability was introduced by using both SOL and EDL muscles. While EDL muscles consist mostly of type IIB fibres, the SOL muscle of Sprague-Dawley rats has mainly type I fibres [275]. Both fibre types differ in metabolic activity and cell organelles (s. “*3.3.2 Contractile function of skeletal muscle*”). It is therefore likely that they react differently to mechanical loading that is delivered in an environment with limited nutrient and missing oxygen supply. However, using as many muscles from one animal as possible reduced the number of animals needed. To minimise the variability, all animals were of similar age, same sex, and similar weight. Additionally, the processing and analysis steps were uniform across all samples.

Another shortcoming was the qualitative differentiation of visible damage patterns within samples before defining a baseline cell death count, which might have influenced the proposed threshold level. However, this categorisation was necessary to compare the *ex vivo* and *in vivo* model. To reduce potential bias, a second observer could be included to perform the same differentiation independently.

Last, compared with the *in vivo* model, the *ex vivo* setup is missing a live blood supply and lymphatic drainage. Considering that the response of both model systems to mechanical loading was similar, this seems negligible. Other researchers also found that ischemic damage has a later onset than direct deformation damage [105], making it less relevant for the comparably short experimentation times (< 24h) of this study.

7.6. Chapter summary

This study investigated the cellular response of an *ex vivo* skeletal muscle model to static loading. In the past, several researchers have assessed the relationship between mechanical stress and cellular damage with different model systems. Comparing the *in vitro*, *in vivo*, and *ex vivo* approaches, they all exhibited different cell responses. Varying degrees of hierarchical structure and cell maturity are probably the main drivers. Nevertheless, the same overall trends of a sigmoid threshold level were observed across all organisational levels.

The results from this *ex vivo* study thereby correlated most with those of an established *in vivo* approach [34]. Both approaches allow for the categorical

classification of the tissue's health status into "cell death" and "no damage". However, the developed staining and image analysis procedures that are part of the *ex vivo* setup provide additional quantitative information on the extent of cellular damage. This information facilitates comparative studies of aetiological factors and can further improve our understanding of the development process of pressure injuries.

To summarise, the results of this study indicate a successful validation of the proposed *ex vivo* model and image analysis workflow. It therefore seems a suitable approach for studying the influence of prosthesis-related loading on skeletal muscle health. The developed *ex vivo* model also expands the existing toolset of *in vivo* and *in vitro* studies for pressure injury research. Through this, the transferability of results between pressure injury, prosthetic, exercise science, and myopathic research can be improved.

CHAPTER 8

Influence of prosthesis-related loading on sarcolemmal integrity in an *ex vivo* skeletal muscle model

This chapter uses the established *ex vivo* animal model to investigate the effect of prosthesis-related loading on sarcolemmal integrity in skeletal muscle (**Objective 5**). Static and dynamic scenarios with different loading frequencies that mimic prosthetic use were thereby compared.

The study was conceptualised by the author and Dr. Arjan Buis. The experiments were setup and conducted by the author. Imaging and analysis were also performed by the author, with support from Dr. Alastair Wark.

8.1. Introduction to prosthetic socket fit

A lower limb prosthesis is an essential component in the rehabilitation process of many transtibial amputees. It adds the missing connection between the residual limb and the ground and thus allows for a return to functional movement and participation in everyday activities. In this coupling between body and prosthesis, the soft tissue of the residuum takes on the role of a weight-bearing part that transfers forces between the prosthesis and skeletal structures. This means that the soft tissue is constantly compressed and deformed between the rigid socket and the bone, from the point when the amputee dons the prosthesis, during everyday activities, until it is doffed.

The socket shape thereby strongly influences the degree of soft tissue deformation by defining the stress distribution across the residuum. As stress distribution has a major impact on comfort, soft tissue health, and rehabilitation success, its evaluation plays a critical role in assessing and defining a “good” prosthetic socket.

8.1.1. The biomechanics of prosthetic use and socket fit

Researchers have applied different methods to assess the biomechanical kinetics associated with prosthetic use. A common measurement is that of ground reaction forces (GRF), which are forces exerted between the prosthetic foot and the ground during stance phase [396, 397]. Information on general gait characteristics like step length, step frequency, or support time can be derived to assess the functional abilities of a prosthetic user with their prosthetic system.

Although gait analysis provides important information for the rehabilitation process, drawing conclusions on socket fit as one of many components in the prosthetic system is difficult. Another more targeted approach is taking interface pressure measurements. Numerous studies have estimated the direct stress distribution across the limb’s surface with pressure and shear sensors at the socket-limb interface [398]. However, researchers found that interface pressure measurements are inadequate to characterise direct stress distribution across the full soft tissue envelop [129, 130].

To gain a more comprehensive view on socket fit, the mechanical status of deep tissues could be investigated. Unfortunately, it is challenging to include internal loading conditions into socket assessment. The inaccessibility of deep tissues makes it impossible to measure deformations directly. While imaging techniques like MRI are an option for stand-still scenarios, the suitability for dynamic environments is limited.

Accordingly, researchers often use finite element analysis (FEA) to estimate stresses and strains within the residuum during locomotion, with input from either GRF or interface studies.

Portnoy et al. [77] for example modelled the force at a specific point within the residuum during a gait cycle as a sinusoidal wave with constant amplitude. The period of the sinewave can be estimated from the contact time of the prosthesis with the ground. The average walking frequency with a transtibial prosthesis on plane ground is around 1.4Hz (0.6 – 0.8s contact time) [77, 103, 399]. For the active amputee population, this frequency increases to around 4Hz (0.25-0.35 s contact time) when engaging in sports, assuming an average athlete running at a speed of 8-10km/h [400–402]. When considering the variety of terrain an amputee encounters during everyday activities – from plane walking to stairs, ramps, and uneven ground – the predictability of internal stresses and strains becomes even more complex [77] as force amplitudes and frequencies vary.

To summarise, assessing socket fit from a biomechanical point of view remains challenging. It often requires a combination of different techniques like GRF and interface pressure measurements with FEA to gain a comprehensive picture of loading conditions across the full soft tissue envelop. Even then, the high variability in gait scenarios is difficult to match with simplified models. Moreover, if a finite element (FE) model predicts internal loading conditions reasonably well, the question remains on how to interpret these numbers in a clinical context. Which loading conditions are harmful and which can be tolerated by the residual limb?

8.1.2. Mechanical load and its effect on soft tissue

To answer these questions, one must understand the connection between physical loading and its effect on soft tissue. The load itself has three main characteristics: magnitude, direction, time, i.e. the duration it is applied for. Under certain circumstances, specific combinations of these three factors can disturb the intricate balance between tissue damage and regeneration [63]. This may reflect in the frequent complaints about residual limb pain and reports on ulceration in the amputee population [21].

High-magnitude stress applied statically for a short duration as well as low-magnitude stress for a long duration can push the tissue above its damage threshold. This relationship between load magnitude, duration, and tissue viability is described as a

sigmoid pressure-cell death threshold for skeletal muscle [33, 34, 212]. Based on this response of muscle to transverse mechanical loading, researchers could estimate the risk for Deep Tissue Injury (DTI) in prosthetic users [76, 77] and developed a self-adjusting socket design [403]. Nevertheless, despite the efforts to broaden our understanding of the scientific basis of socket design, these developments have yet to find their way into clinical practice.

A potential reason is the sparsity in studies with a focus on prosthetics rather than pressure injuries (s. *Chapter 2* and *3*). Although the residual limb does experience static loading, as applies to many pressure-injury cases, a more common scenario is repetitive loading encountered during walking or running. This cyclic impact can offset the damage-regeneration balance of skeletal muscle [63] and may lower the established static threshold [23, 91, 98, 99]. However, as researchers pointed out repeatedly, information on how repetitive loading influences skeletal muscle health is still missing [22, 36, 76, 79, 404].

8.2. Aims of dynamic loading study

This study investigates the effect of dynamic loading on skeletal muscle health. Based on the developed *ex vivo* animal model, isolated muscle tissue was subjected to one of two loading scenarios: dynamic compression with a frequency representing walking with a prosthesis (1.42Hz), or a high-frequency compression equivalent to running (4Hz). The amount of cell death was quantified for each scenario. For comparison, the effect of a static load on skeletal muscle health was also tested under equal conditions. It was thereby hypothesised that:

1) cellular damage increases with longer load application for both static and dynamic cases.
2) dynamic loading will have a more detrimental effect on sarcolemmal integrity than static loading.
3) high-frequency loading is more damaging to skeletal muscle than a low frequency.

Gaining a more comprehensive understanding on the influence of prosthesis-specific loading conditions on skeletal muscle health has the potential to bridge the gap between existing knowledge on soft tissue behaviour and clinical practice of socket fitting.

8.3. Experimental design and methods for dynamic loading study

8.3.1. Collection and preparation of murine skeletal muscle tissue

The soleus (SOL) and extensor digitorum longus (EDL) muscles (n = 25) were collected from the hindlimbs of male Sprague Dawley rats as described in *"4.3.2 Collection and preparation of murine skeletal muscle tissue"*. The procedure followed ethical guidelines of the Biological Processing Unit of the University of Strathclyde. Following dissection, the muscles were pinned out separately in silicone covered Petri dishes and covered with MOPS buffer at 22°C.

8.3.2. Static and dynamic loading experiments

The experimental setups and procedures have been described in "*4.3 General materials and methods for ex vivo experiments*" and "*4.7.1 Method for Live-or-Dye and Procion Yellow MX4R staining*" but will be summarised for completeness. Five samples each were randomly assigned to one of the interventions listed in **Table 8-1**.

Table 8-1: Sample allocation for static and dynamic loading experiments. EDL and SOL muscles from Sprague-Dawley rats were assigned to one of the listed interventions for transverse mechanical indentation.

		dynamic compression	
	static compression	1.42Hz (walking)	4Hz (running)
1h loading	$n = 5$	$n = 5$	$n = 5$
2h loading	$n = 5$	$n = 5$	

The setup for static loading consisted of custom rigs, each fitted with a flat indenter (r = 1mm). The indenter was lowered onto the mid-belly region of the pinned-out muscle sample and rested on it with a weight of m = 33g for 1-2h. This comparably high interface direct stress of P = 103kPa exceeded the static pressure-cell death threshold (s. "*7.4.3 Stress-time cell death threshold for ex vivo skeletal muscle tissue*") to ensure cellular damage and thereby minimise the risk for skewed data.

For dynamic loading, a Bose Electroforce 3100 (TA instruments) was used. The instrument was fitted with a 22N load cell on the top, attached to an indenter identical

with the ones in the static setup. Once a contact force of 0.01N was established, the muscles were subjected to a sinusoidal load. The range was equal that of the static loading experiment (0.32N). The frequencies were either f_w = 1.42Hz for the “walking” condition or f_R = 4Hz for the “running” one, in line with existing prosthetic research. The cycle numbers were adjusted to cover a duration of 1-2h.

8.3.3. Fluorescent staining and tissue processing

After load application, the MOPS buffer was replaced with 0.1% Procion Yellow MX4R (Sigma Aldrich, St. Louis) for 1h before fixation in 10% NBF for 28h. The mechanically damaged area as well as peripheral control sections were processed separately into 4µm cross-sections as described in “*4.3.4 Tissue processing through formalin fixation and paraffin embedding*”.

8.3.4. Fluorescence image acquisition and quantification of sarcolemmal damage

Microscope slides were imaged on a Leica SP8 microscope equipped with an FITC (Ex 482/35nm, Em 536/40nm) and Y5 (Ex 620/60, DC 660, Em 700/75) filter (s. “*5.3.1.1 Microscope and software specifications*”). Twelve cross-sections were imaged from each sample, *n* = 6 from the indentation and *n* = 6 from the control areas. The images were acquired with both filter sets under identical conditions with 10x magnification (s. “*5.4.5 Summary of optimised image acquisition parameters for quantitative fluorescence imaging*”).

After automated stitching with the Leica Las X software, full cross-sections were analysed to obtain a quantitative cell death count for each indentation condition. A semi-automated workflow in FIJI/ImageJ was thereby employed (s.”*5.5.6 Overview over the image analysis* workflow”). In brief, the average intensity of each group of six control samples was determined. The resulting value was set as threshold for the corresponding indentation group to identify the number of dye-positive fibres.

8.3.5. Statistical analysis to compare intervention groups

Before assessing differences between groups, the distribution and skewness of the dataset were determined in Minitab (Vers. 19.2020.1). Firstly, the data were tested for normal distribution ($p \leq 0.05$, CI 95%). In three out of the six groups, the data was

non-normally distributed (**Table 8-2**). This is usually an indication for the need of a non-parametric test, like the Kruskal-Wallis test.

Table 8-2: Probability test for normal distribution of cell death counts. The cell death counts of each intervention group were tested for normal distribution with CI 95%. P-values marked with * indicate that the data is not normally distributed ($p \leq 0.05$).

	Mean	**StDev**	**p-value**
1h static	96.04	66.23	0.039*
2h static	238.3	119.6	0.307
1h 1.42Hz	98.21	45.12	0.946
2h 1.42Hz	232.3	125.9	0.018*
1h 4Hz	147.0	82.30	0.019*

Non-parametric tests are sensitive to differences in scale and symmetry within the data [405]. Accordingly, histograms were analysed for each dataset to determine skewness and symmetry. All but one intervention group had moderately right skewed data (**Table 8-3**); conversely, the 1h walking group had a symmetrical data distribution. Additionally, the scale of the data increased 2.5-fold from the 1h walking to the 2h walking group. Taken together, these characteristics of the dataset made non-parametric testing difficult. Nevertheless, the results of a non-parametric Kruskal-Wallis test can be found in **Appendix H**.

Table 8-3: Symmetry and scale of data from cell death counts. All measurements were performed in Minitab. Skewness was measured and described as symmetrical ($0 < s < 0.5$), moderately ($0.5 < s < 1.0$), or severely ($s > 1.0$) skewed. The direction of the skewness is described by the symmetry, which is calculated by subtracting the median from the mean. High positive numbers indicate right skewed, values close to zero symmetrical, and high negative numbers left skewed data. The scale was determined by subtracting the minimum from the maximum cell death count.

	Skewness		**Symmetry**		**Scale**
1h static	0.848	moderate	16.5	right skewed	232
2h static	0.539	moderate	19.9	right skewed	423
1h 1.42Hz	0.221	symmetrical	-0.8	symmetrical	179
2h 1.42Hz	0.742	moderate	29.8	right skewed	460
1h 4Hz	0.711	moderate	11.5	right skewed	289

Instead, ANOVA testing was performed. Although not ideal for nonnormally distributed data, this shortcoming can be overcome by a sufficiently large sample size ($n > 15$) [406]. With $n \geq 26$ across all intervention groups, this requirement was met. Unequal variances were assumed, based on tests of equal variance. Accordingly,

Welch's ANOVA tests were conducted with a significance level of α = 0.05. The Games-Howell method was used to compare the following groups:

(1) short duration vs long duration: 1h static vs 2h static; 1h dynamic walking vs 2h dynamic walking

(2) static vs dynamic: 1h static vs. 1h dynamic walking vs. 1h dynamic running; 2h static vs 2h dynamic walking

(3) low frequency dynamic vs high frequency dynamic: 1h dynamic walking vs 1h dynamic running

8.3.6. Finite element analysis of dynamic transverse mechanical loading setup

Preliminary studies revealed that the internal compressive stress within the skeletal muscle tissue differs from the externally applied direct stress (s. "*6.4 Finite element analysis of transverse mechanical loading of skeletal muscle tissue*"). Based on FEA, it was estimated that for static loading scenarios, an external direct stress of 103kPa generates a fairly uniform compressive stress field of 69kPa within the muscle layer. However, considering the viscoelastic properties of skeletal muscle tissue, static loading conditions might create a different mechanical environment than dynamic ones.

During the dynamic indentation experiments, the Bose Electroforce instrument recorded load and displacement data for the first seven minutes approximately. In the initial phase, the loading response of the muscle is considered unstable. The last few recorded cycles (4s) were therefore analysed to obtain data on the estimated displacement of the indenter following the prescribed loading protocol. This was compared with the indenter displacement predicted by the static FE model (s."*7.4.1 Comparison of direct stress with principal compressive stress within the muscle layer*") in Ansys (Workbench 2021 R2) to assess its capabilities to reproduce the internal loading conditions of the dynamic indentation experiment.

A maximum load of -0.324N was applied in a sinusoidal pattern with a frequency of either 1.42Hz (to n = 10 samples) or 4Hz (to n = 5 samples). Displacement and load data for each sample were recorded every 2s and exported as .csv file. Displacement data were normalised by addition or subtraction to account for calibration differences between the experiments (**Appendix I**).

The datasets were then analysed in Minitab. Non-linear regression models were fitted according to the general equation of:

$$\boldsymbol{y = A \times sin(\omega t + \varphi) + D} \qquad \textbf{(8-1)}$$

with *A* as the amplitude of the function, ω as the angular frequency (calculated as $2\pi f$), φ as the phase, and *D* describing the centre of the amplitude. Parameter estimates for all values but time were based on preliminary analysis of datasets. The standard error of regression (*S*) (standard deviations of the distance between data values and fitted values) were retrieved as an estimate for goodness-of-fit as R-values are less meaningful for non-linear regression [27]. Additionally, the amplitudes of the fitted deformation curves were compared to deformation values estimated by the static FE model.

8.4. Results of dynamic loading study

8.4.1. Comparison of dynamic deformation data to static finite element model

Deformation data from the dynamic indentation experiment were compared to predicted results from the static FE model to assess conformity. The parameters of a standard sinusoidal curve were thereby determined as described in **Table 8-4**.

Table 8-4: Curve-fitting parameters for estimation of load and displacement data from dynamic indentation experiments of skeletal muscle tissue. General sinusoidal equation (8-1) is described by A (amplitude), $\boldsymbol{\omega}$ (angular frequency), $\boldsymbol{\varphi}$ (phase), and D (centre of the amplitude).

		A	ω	φ	D
1.42Hz	Load	0.162	8.92	0.79	-0.162
	Displacement	0.168	8.92	0.62	-1.219
4Hz	Load	0.162	25.13	-0.18	-0.162
	Displacement	0.163	25.13	-0.41	-1.168

Looking at the fitted sinusoidal curves (**Figure 8-1**), they correspond reasonably well with the recorded data. For a frequency of 1.42Hz, the standard error of regression was *S* = 0.03N for loading data (10.01% of max. load) and *S* = 0.05mm for displacement (13.64% of overall displacement). The data for the 4Hz condition had a higher error for load with *S* = 0.04N (13.18% of max. load) and a lower error for displacement with *S* = 0.02mm (6.2% of overall displacement). Most datapoints

thereby fell within the 95%-prediction interval (± two standard errors of regression) with the largest deviations seen between the predicted and real values of displacement at a loading frequency of 1.42Hz.

The deviations in displacement data might be explained by the high biological variability between samples compared to the machine-controlled loading data. With fewer datapoints available for a loading frequency of 4Hz, the variability was also less visible for this configuration. The normalisation procedure might also have introduced an additional source of variability.

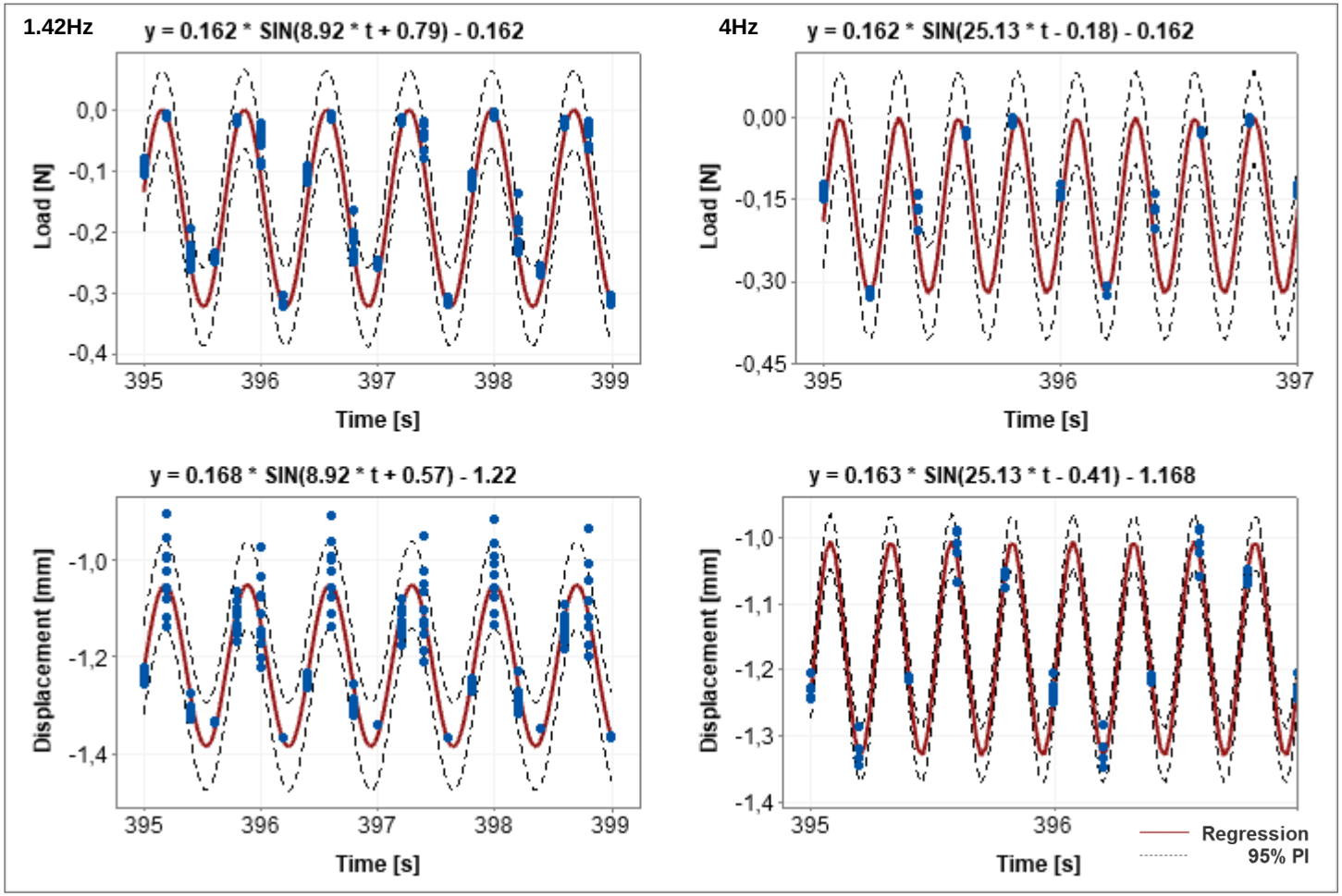

Figure 8-1: Load and displacement data for transverse indentation of skeletal muscle tissue. Muscles were loaded with a sinusoidal compression at a frequency of 1.42Hz (*n* = 10, column 1) or 4Hz (*n* = 5, column 2) with a maximum compressive force of 0.324N. All data showed a moderate agreement with the regression functions, according to the standard error of regression (load: $S_{1.42}$ = 0.03N, S_4 = 0.04N; displacement: $S_{1.42}$ = 0.05mm, S_4 = 0.02mm).

The overall displacement for samples compressed at a frequency of 1.42Hz was equal to 0.336mm, causing a maximum compressive strain of 16.8%. At a frequency of 4Hz, the maximum displacement was 0.326mm, equivalent to 16.3% compressive strain. The displacement predicted by the static FE model was slightly below these values (**Figure 8-2**) with a displacement of 0.276mm, causing a maximum compressive stress of 13.8%.

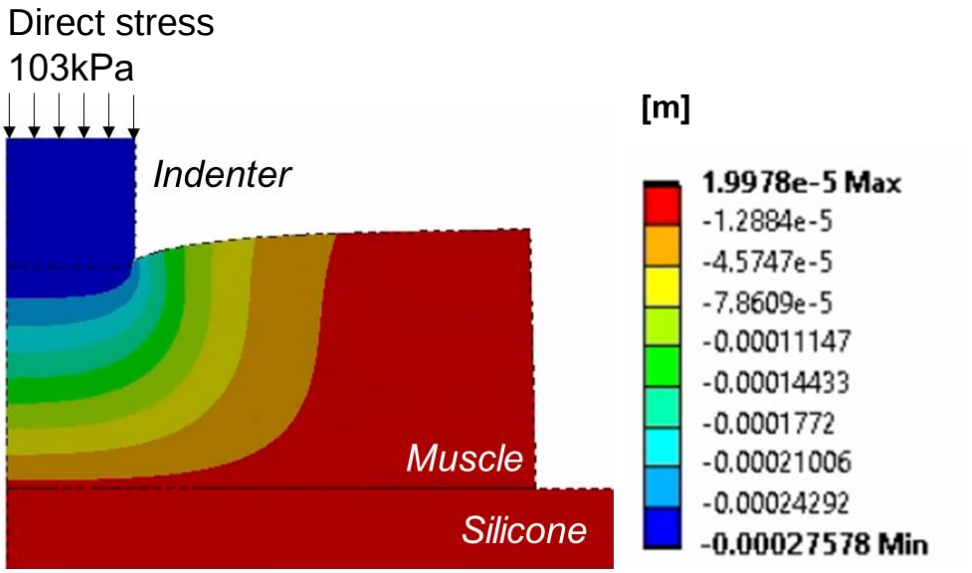

Figure 8-2: Axial displacement of an indenter compressing skeletal muscle tissue as predicted by an axisymmetric finite element model. A static direct stress of 103kPa (0.324N) was applied to the top of a flat indenter, leading to an axial displacement of 0.276mm. The silicone layer that the muscle is resting on is only partially shown for better visualisation.

For a more accurate prediction of the material response, a change of the model to dynamic loading would be necessary. Additionally, the material model would need to be adjusted to account for a dynamic, viscoelastic response. From the obtained load and deformation data, the deformation response lags the load application (**Figure 8-3**). This shift seems dependent on the frequency, with $\phi(t) = 0.025s$ for 1.42Hz loading, and $\phi(t) = 0.009s$ for 4Hz loading. Potential changes in the loading response over time would also need to be monitored. Accordingly, extensive material testing would need to be performed to characterise the mechanical response of skeletal muscle to the indentation tests.

Considering the time and effort needed to perform material testing on viscoelastic skeletal muscle tissue for a slightly more precise result, the static FE model was deemed sufficiently similar to the dynamic scenarios. Hence, a compressive stress of 69kPa was used for interpretation of both static and dynamic loading data.

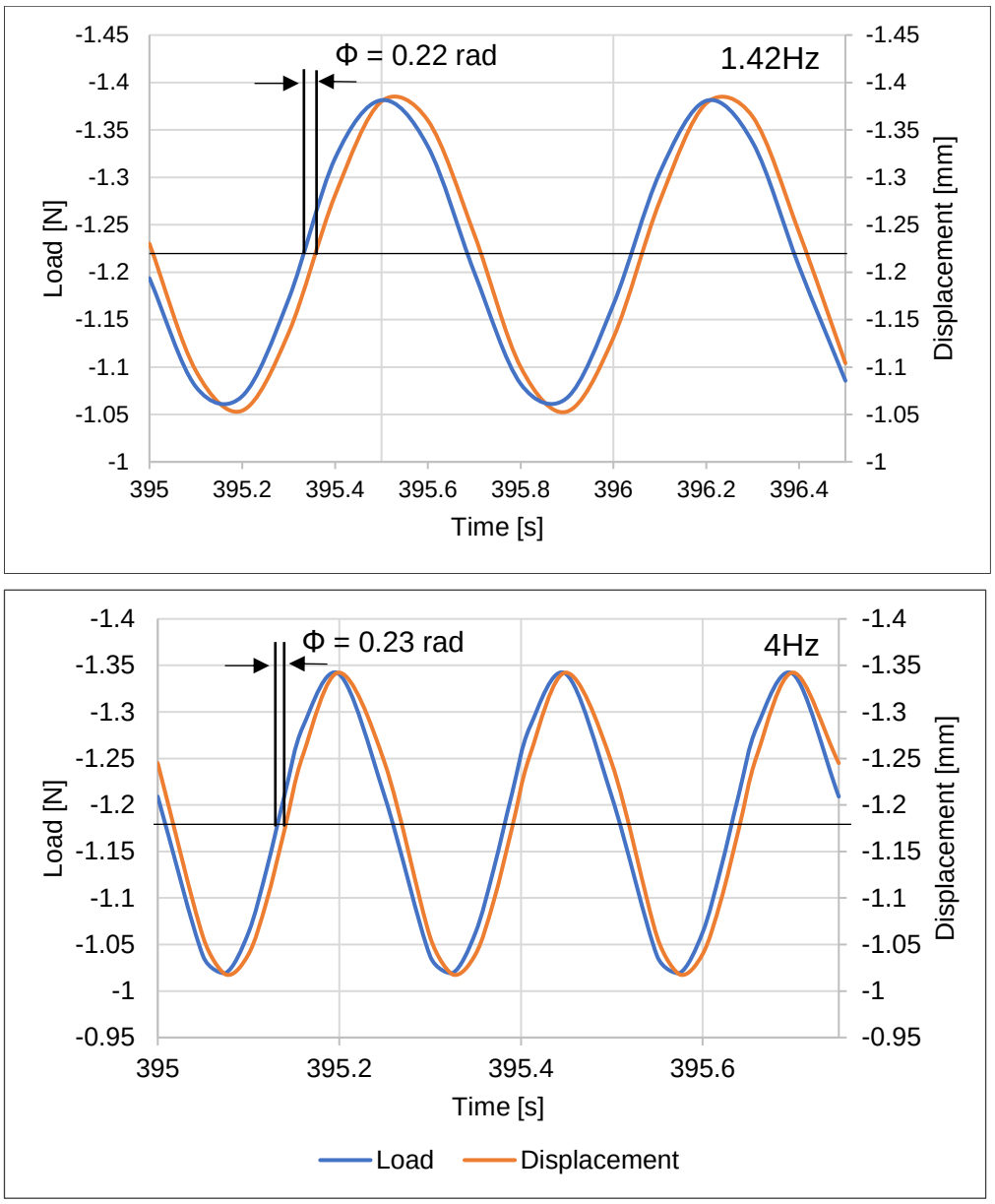

Figure 8-3: Phase-lag between load and displacement data from flat indentation experiments of skeletal muscle tissue. Displacement function lags Φ = 0.22 rad (0.025s) behind load function at a frequency of 1.42Hz and Φ = 0.23 rad (0.009s) at 4Hz. Centre of amplitude of load data was adjusted to the same level as displacement data for display purposes.

8.4.2. Difference in cell death counts between short and long duration loading

First, the cell death counts for short- and long-term compression were compared (**Figure 8-4**). For the static loading scenario, differences in cellular damage after 1h and 2h compression – resulting in a stress of σ = 69kPa – were investigated. The average cell death count thereby increased almost 2.5 times from $\bar{x}_{s,1h}$ = 96 ± 66.2

after 1h (95% CI [70.4; 121.7]) to $\bar{x}_{s,2h}$ = 238.3 ± 119.6 after 2h (95% CI [190.0; 286.7]). The corresponding significance level of p = 0.000 indicates a statistically significant difference. Additionally, a wider spread of the data was observed in the 2h compared to the 1h group with a wider scale (increase of 191) and wider confidence intervals (increase of 45.4). Last, in line with the previous results on data symmetry and skewness (Appendix H), a general tendency of right-skewness was noticeable in both groups with the median cell death numbers of $\tilde{x}_{s,1h}$ = 79.5 and $\tilde{x}_{s,2h}$ = 218.5 being lower than the corresponding means of $\bar{x}_{s,1h}$ = 96 and $\bar{x}_{s,2h}$ = 238.3.

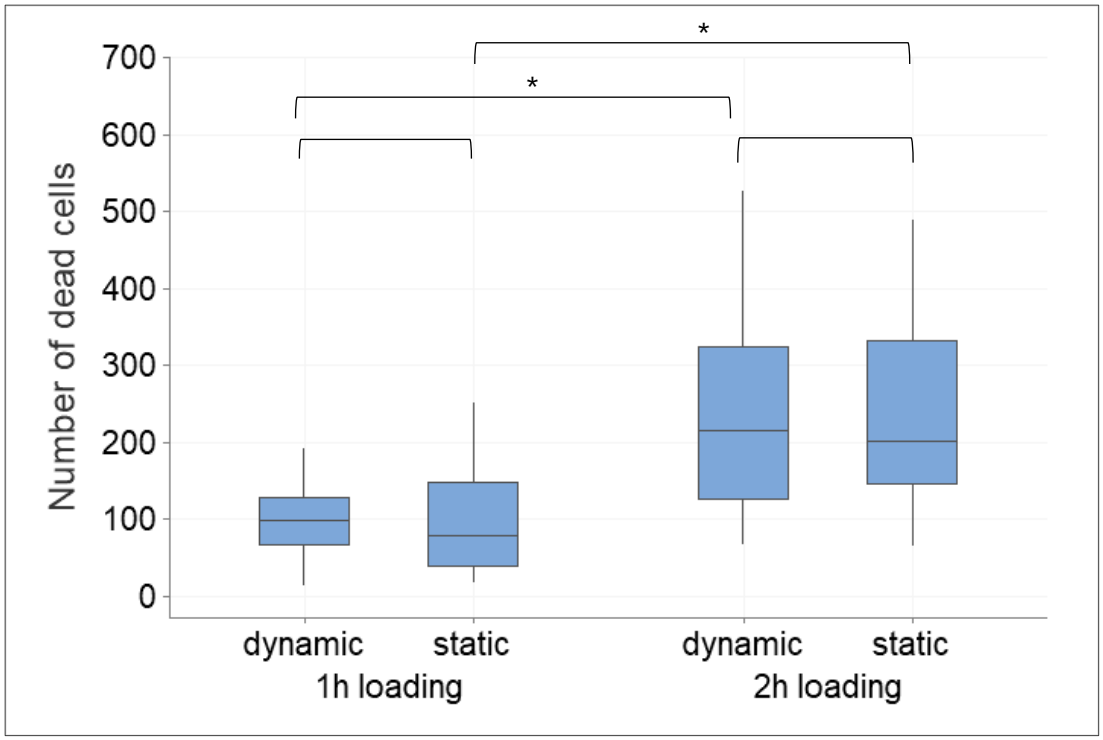

Figure 8-4: Boxplot of differences in cell death counts between 1h and 2h loading of *ex vivo* skeletal muscle tissue. Following compression of isolated murine EDL and SOL muscles with σ = 69kPa, the average number of dead cells after static loading increased between 1h ($\bar{x}_{s,1h}$ = 96 ± 66.2; 95% CI [70.4; 121.7]) and 2h loading duration ($\bar{x}_{s,2h}$ = 238.3 ± 119.6; 95% CI [190.0; 286.7]). Similarly, dynamic loading with a frequency of 1.42Hz caused a higher average cell death in the 2h group ($\bar{x}_{w,1h}$ = 232.3 ± 125.9; 95% CI [185.3; 279.3]) compared to the 1h group ($\bar{x}_{w,1h}$ = 98.21 ± 45.12; 95% CI [81.05; 115.37]). For both scenarios, the differences were statistically significant (p = 0.000). When comparing dynamic and static loading results with the same loading duration, no statistically significant differences were found (p_{1h} = 0.989, p_{2h} = 0.854).

For the dynamic loading scenario, differences in cell death counts were calculated after 1h and 2h compression with a stress of σ = 69kPa and frequency of f_w = 1.42Hz. The average number of dead cells increased by a factor of 2.37 from $\bar{x}_{w,1h}$ = 98.21 ± 45.12 after 1h (95% CI [81.05; 115.37]) to $\bar{x}_{w,2h}$ = 232.3 ± 125.9 after 2h (95% CI [185.3; 279.3]). This difference was statistically significant (p = 0.000). The variability

in the data from the 2h group was higher than in the 1h group, as indicated by a wider scale (increase of 281) and confidence intervals (increase of 59.68). As described in the symmetry data (**Table 8-3**), cell death counts from the 2h loading were right-skewed with the median of $\tilde{x}_{w,2h}$ = 202.5 below the mean of $\bar{x}_{w,2h}$ = 232.28, while the 1h loading group had a symmetrical distribution with similar median and mean values ($\tilde{x}_{w,1h}$ = 99, $\bar{x}_{w,1h}$ = 98.21).

8.4.3. Difference in cell death counts between static and dynamic loading

A main driver for this study was the missing information on how static and dynamic loading compare in terms of their influence on sarcolemmal damage. Average cell death counts were compared for two loading durations – 1h and 2h. For the 1h setup, samples were compressed with σ = 69kPa in a static, low-frequency (f_w = 1.42Hz), or high-frequency (f_R = 4Hz) dynamic environment. The results indicate that dynamic loading with f_R produced significantly more cell death compared with f_W (p = 0.018) and the static loading condition (p = 0.031) (**Figure 8-5**, **Figure 8-6**). The average cell death count of $\bar{x}_{R,1h}$ = 147 ± 82.3 after high-frequency loading (95% CI [116.3; 177.8]) was 1.5 times higher than the number of dead cells in the 1.42Hz group ($\bar{x}_{W,1h}$ = 98.21) and static loading group ($\bar{x}_{S,1h}$ = 96) for the same duration.

In comparison, no statistically significant increase could be found between the static loading and the dynamic walking scenario, both at a duration of 1h (**Figure 8-5,** p = 0.989) and a duration of 2h (**Figure 8-4**, p = 0.854). On the contrary, the number of dead cells was marginally higher in the static loading group after 2h, compared to the dynamic loading scenario (difference in means of 5), while dynamic loading caused a slightly higher cell death count at a duration of 1h (difference in means of 2.21).

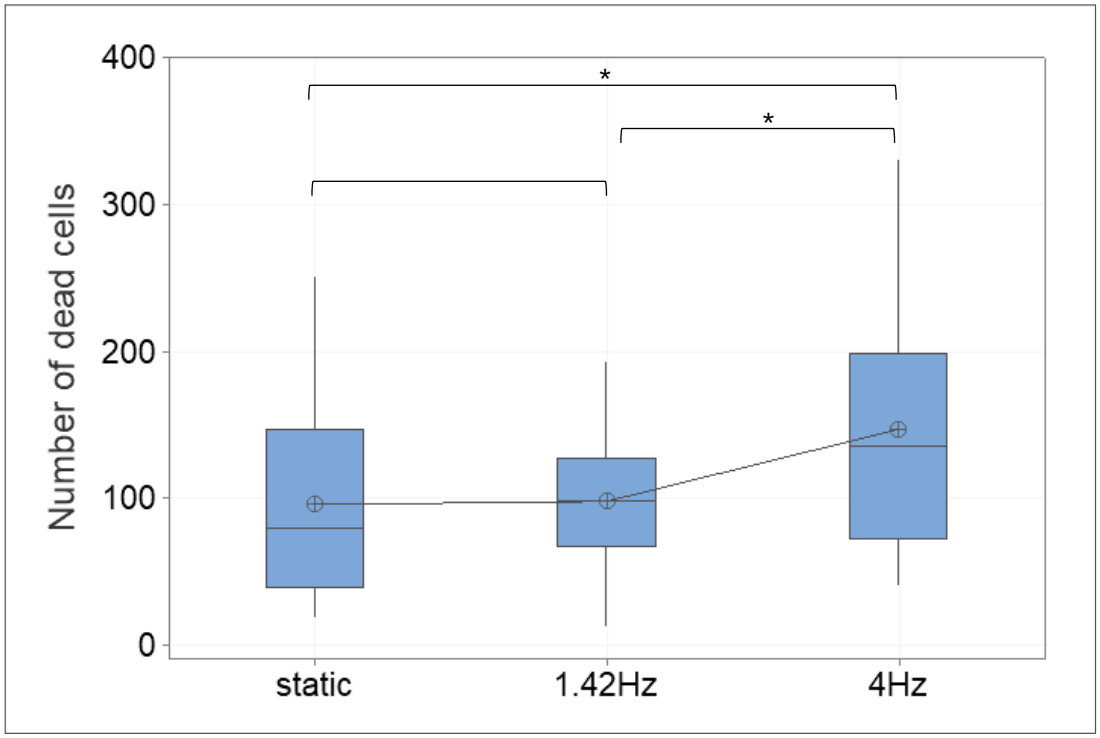

Figure 8-5: Boxplot of differences in cell death counts between static and dynamic loading of *ex vivo* skeletal muscle tissue. Compressive stress of σ = 69kPa was applied to isolated EDL and SOL muscles of Sprague-Dawley rats for 1h. Average cell death counts were $\bar{x}_{s,1h}$ = 96 ± 66.2 after static loading, $\bar{x}_{w,1h}$ = 98.21 ± 45.12 after sinusoidal compression with walking frequency (f_w = 1.42Hz), and $\bar{x}_{R,1h}$ = 147 ± 82.3 (95% CI [116.3; 177.8]) after loading with running frequency (f_R = 4Hz). The number of dead cells after the running scenario was significantly higher than the walking (p = 0.018) and the static loading group (p = 0.031). When comparing the static and walking scenario, the difference in the number of dead cells was not statistically significant (*p* = 0.989).

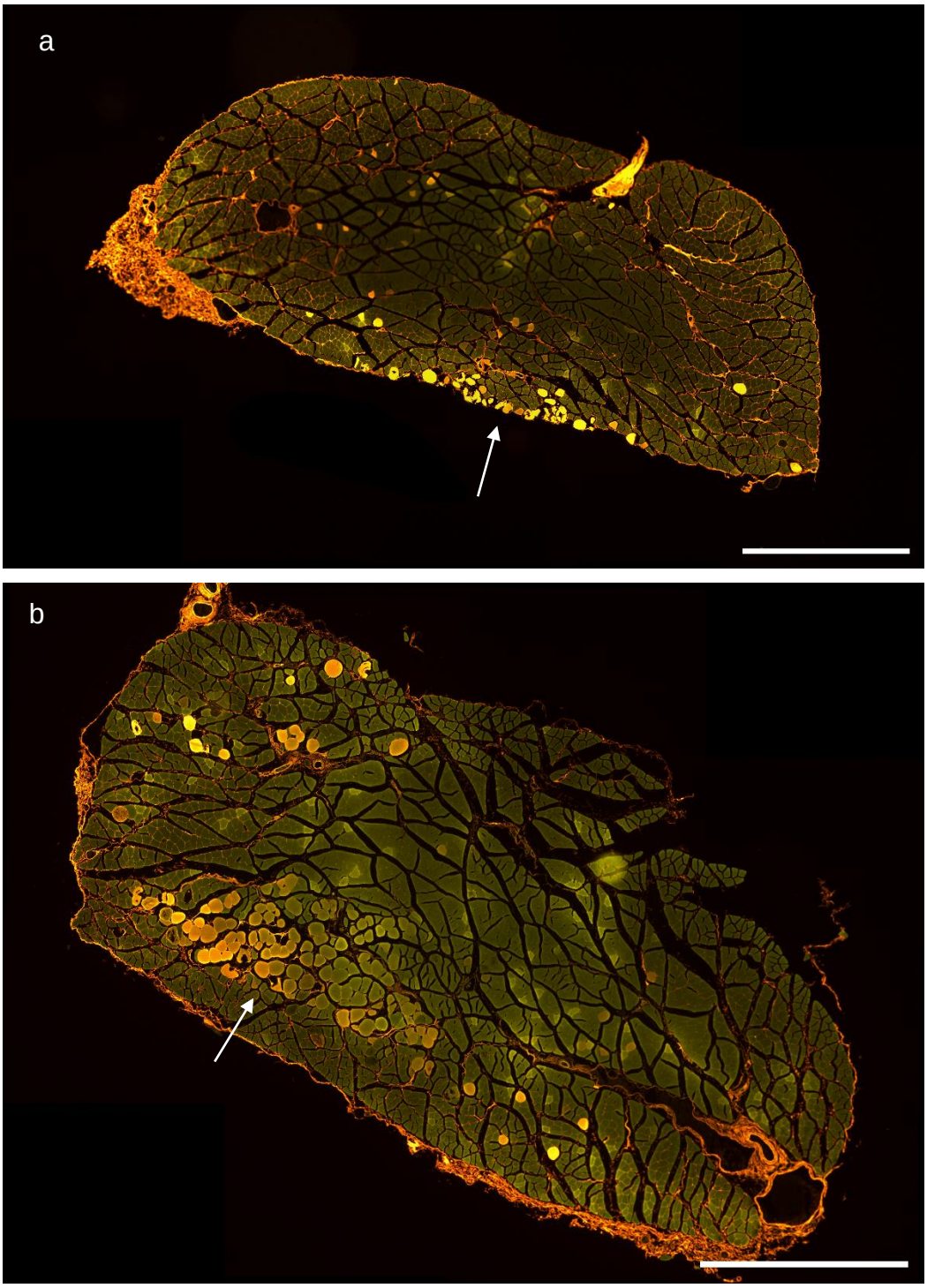

Figure 8-6: Representative images of sarcolemmal damage in *ex vivo* skeletal muscle tissue after static and dynamic loading as visualised through fluorescence ProY staining. Cross-sectional slices of 4µm thickness showing areas of high cell death indicated by white arrows (orange staining of cells with ProY). Characteristic rounded morphology of dead cells also visible. **(a)** Static loading with 0.324N for 1h led to an average of 96 ± 66.2 dead cells. **(b)** Dynamic, sinusoidal loading at a frequency of 4Hz with a maximum of 0.324N for 1h produced on average 147 ± 82.3 dead cells. Images captured through FITC filter (Ex 482/35, Em 536/40). Scale bar 1000µm.

8.5. Discussion of dynamic loading study

Understanding the effect of prosthetic loading on skeletal muscle health is an important aspect in fitting a prosthetic system. While it is well-known that high-amplitude and prolonged static compression can cause tissue damage, the tissue's reaction to a dynamic loading environment is unclear. This study explored potential differences between both scenarios by comparing varying combinations of load durations (1h and 2h) and frequencies (static, 1.42Hz, 4Hz) commonly seen in prosthetic settings. The main results were that:

1) cellular damage increased with extended time periods of loading, for both static and dynamic scenarios.
2) high-frequency dynamic loading was more damaging to skeletal muscle than static compression and low-frequency loading.

Cellular damage was thereby located either directly at or in close proximity to the contact area between indenter and muscle tissue (**Figure 8-6**). As discussed in the previous chapter ("*7.5 Discussion on the response of ex vivo skeletal muscle tissue to mechanical loading*"), this is likely an effect of the mechanical environment at cellular level, which differs from the homogeneous compressive stress field in the FE model on a macro-level. A more detailed multi-scale FE analysis of the performed experiments is therefore recommended.

Nevertheless, these results are a first step towards a more comprehensive understanding of the interaction between the prosthetic system and the residual limb. However, their impact on clinical care must be discussed carefully.

8.5.1. Prolonged static and dynamic loading increase cellular damage

A main concern when wearing a prosthesis is the duration for which the residual limb is loaded. The detrimental effect of time on soft tissue damage development has been documented by other researchers in the past. Both in *in vivo* murine skeletal muscle [91] and in *in vitro* skeletal myoblast monolayers [212], cell damage increased with the duration of static load application. The here presented study supports these observations in an *ex vivo* model. The cellular damage observed after inducing a static

compressive stress of σ = 69kPa increased significantly from the 1h to the 2h loading scenario (**Figure 8-4**).

Going one step further, the same tendency was seen for the dynamic loading scenario: Following cyclic loading that induced a compressive stress of 69kPa at a frequency of 1.42Hz, a statistically significant increase in cellular damage was apparent after 2h compared to 1h loading (**Figure 8-4**). Combined with the described studies on static loading, it is hypothesised that similar effects would be apparent at other frequencies.

Yao et al. [112] explored this phenomenon and found that prolonged compression lowers the damage threshold of cells for subsequent mechanical loading bouts. This may be initiated by apoptotic markers, cytokines, and reactive oxygen species (ROS) that the cells release as part of their stress response. The toxic waste products accumulate, creating a hostile environment that adds more stress to the cells. A study by Chapman et al. [407] supports this finding, showing that cyclic loading increased the production of ROS in epithelial cells over time. Besides the increasing toxicity of the cellular environment, cell death also causes a local stiffening of the tissue [85]. Consequently, mechanical loads are redistributed to the surrounding areas, inducing high stress concentrations. This accelerates the spread of the cellular damage further.

8.5.2. Dynamic loading at high frequencies is more damaging to the structural integrity of skeletal muscle than static loading

At the beginning of this chapter, it was hypothesised that dynamic loading has a more detrimental effect on cell death development than static loading. However, the results were ambiguous. While lower frequency loading with 1.42Hz produced slightly more cellular damage than static loading for a duration of both 1h and 2h, this difference was not statistically significant (**Figure 8-5**). In comparison, a significantly higher cell death count was observed when increasing the frequency from 1.42Hz to 4Hz. This supports the third hypothesis that high frequency loading is more damaging to skeletal muscle than low frequencies.

Explaining this phenomenon is difficult, considering that our understanding of how a cell converts physical cues into a biological response is still very limited. The cytoskeleton inside a cell consists mainly of filaments, like actin and myosin, and

microtubules. It is anchored to the surrounding extracellular matrix (ECM) by integrins and to other cells by cadherins [408, 409]. The interplay of these components with their different mechanical properties is often described through rheology, or the study of soft matter. In solids, the mechanical response to loading is independent from the loading frequency, i.e. stress and strain are proportional. Liquids on the other hand are frequency-dependent, with stress being proportional to the rate of strain. Cells in general are widely regarded as a viscoelastic material, exhibiting a mix of both behaviours [410–412]. The phase-lag between the load and deformation in the performed experiments is a testament to this (**Figure 8-3**).

8.5.2.1. Fatigue of structural cell components

One theory to describe the complex mechanical behaviour of cells is the tensegrity model [409, 413], which is based around a balance between tensile and compressive forces: contractile microfilaments administer tension, similar to a cable, which leads to constant compression of structural features like microtubules, similar to a rod. When tissue is compressed, the mechanical deformation is transmitted across the ECM to the cells. Within the cells, the anisotropic network of microtubules experiences tensile and compressive forces, depending on their orientation, and rearranges accordingly [414], which increases the stiffness of the cell. These forces might lead to structural damage, similar to crack formation, within the compressed support structures and a protein unfolding response [415] in those under tension. The small faults can accumulate and grow under repeated stress until the structures fail. Indeed, multiple computational studies have assessed the accumulation of microscopic tissue damage and microcrack-propagation in under repeated loading as a cause of skeletal muscle damage [416–418]. Thus, even at direct stress below the established static loading threshold, the repetitive nature of a cyclic load application may lead to tissue damage. This is in agreement with reports of ratchetting effects [418, 419], i.e. inelastic strain accumulation during cyclic load application, which shortens fatigue life for higher strain-rates like the 4Hz loading condition in comparison to lower strain rates like the 1.42Hz sinusoidal load.

8.5.2.2. Frequency-dependent change in mechanical properties of cells

Another popular mechanistic cell model is called soft glassy rheology (SGR) [410–412, 420]. SGR describes cell behaviour guided by a power law: an increased loading

frequency will increase the dynamic shear modulus of a cell, i.e. the ratio between shear stress and shear strain. Researchers found that at low frequencies and during short dynamic loading cycles, some cells display an elastic response where they return to their original shape after load application [414, 421]. This could explain the similarities in the cell death count between static and low-frequency dynamic loading observed in this study. Even more so, low frequency as well as low magnitude cyclic compression can prevent severe damage and stimulate skeletal muscle repair [205, 422–424].

At higher loading rates, the tissue exhibits a loading-rate dependent change in mechanical behaviour, i.e. a stiffening effect with increasing compression rates [425], which increases stress levels. Indeed, once frequencies rise above a certain threshold, cells seem to experience plastic deformation [414]. This manifests as permanent damage to the actin network, which can interfere with normal cellular function [426]. Cell-cell junctions, where cells adhere to one another, also seem to rupture more easily at high strain rates compared to lower ones [427]. A potential explanation is that remodelling of the cytoskeleton cannot keep up with the damage rate. Taken together, the significantly higher number of dead cells in the high-frequency loading group compared to the static and low-frequency situation might correspond with the frequency- and strain-rate dependent change in mechanical properties.

8.5.2.3. Self-heating of cells induced by cyclic loading

Another aspect that can affect cell death rates is energy transformation within cells. Cells are considered a viscoelastic material that can transform the energy transmitted from the deformation process in two ways [410, 420, 428]: First, energy can be stored within the support structures like the cytoskeleton and released as the load is removed; this is also known as elastic energy storage. Second, the energy might be converted into heat, a process known as energy dissipation, which is more pronounced following high-frequency loading. If the temperature rises beyond normal physiological levels, cellular homeostasis is at risk. The cellular membrane becomes progressively fluidic, which in turn increases cellular permeability [429].

8.5.2.4. Biochemical response of cells to deformation

Beside the described mechanical behaviour of cells, biochemical processes are activated in response to load application. Wu et al. [219] found that the molecular

messenger MAPK is activated after muscle compression, which initiates a cell death cascade. This process even precedes structural mechanical failure of cells. The researchers suggest that the activation depends on type, duration, and intensity of mechanical deformation. It is therefore likely that high-frequency, repetitive loading stimulates a more severe response of biochemical messenger systems than low frequency and static loading.

8.5.2.5. Summary of potential mechanisms for dynamic loading response of skeletal muscle and suggestions for future work

To summarise, increased fatigue, heat, changes in stiffness, and biochemical messengers are potential explanations for the significantly higher cell death observed after high-frequency cyclic loading compared with the static and low-frequency scenario. Moreover, the results of this study in combination with relevant literature suggest that the existing static pressure/stress-cell death threshold function needs to be extended by the variable of frequency for dynamic scenarios. To establish this multifactorial threshold that takes the relationship between frequency and duration, and frequency and direct stress into account, additional research is needed.

Besides expanding on the here presented research to obtain a multifactorial muscle damage threshold, further studies might elucidate the mechanisms that govern the observed frequency-dependency of cell death during mechanical loading. Firstly, the micro-structural effects of the macroscopic muscle behaviour modelled in this study could be assessed, i.e. through multi-scale FE analysis, to improve our understanding of force distribution and internal loading conditions at different organisational levels. Other computational modelling approaches like Peridynamics [430, 431] could be employed as well to assess the likelihood and dynamics of crack propagation in structural elements of skeletal muscle. These studies could be combined with scanning electron or atomic force microscopy to inform and validate the modelling efforts. Additional focus should be upon the role of connective tissue which has been shown to influence structural characteristics of skeletal muscle [383, 384, 389].

To assess the potential effect of temperature, measurements of samples and buffer solutions could be performed during different loading scenarios and compared. Additionally, the effect of an increased temperature on the mechanical damage resistance of cells could be evaluated by adjusting the experimental environment.

Lastly, biomarker analysis of buffer solutions might identify potential up- or down-regulation of biochemical messengers, inflammatory markers, and damage markers after different loading conditions. An overview over potential target biomarkers can be found in "*9.5 Biomarker for skeletal muscle damage*".

8.5.3. Implications of dynamic loading for prosthetic users

Relating the results of this study back to prosthetic users needs great care. The tested scenarios considered prolonged loading. This is representative of real-life situations, considering that the confined shape of a socket does not allow for repositioning of the residual limb, which would be necessary to reduce the risk for damage [91]. With prolonged loading producing significantly higher cell death numbers for both static and dynamic scenarios, doffing of the prosthesis between extended periods of use would therefore be necessary to allow for true stress removal and to avoid tissue damage from prolonged loading. Whether the common practice of short-term doffing during sitting is sufficient needs to be evaluated further.

It should also be stressed that not only the duration but also the magnitude of the load is important. The experimental setup described in this study applied compressive stresses above the static pressure-cell death threshold. Mechanical stress below the threshold on the other hand is tolerable for extended periods of time without causing any damage [33, 34]. This means that extended use of a prosthesis can still be safe if the prosthetic system applies sufficiently low direct stress. Minimising large deformation of the residual limb by the socket is therefore paramount.

The results also indicate a general tendency of higher tissue damage with high-frequency loading like running. Yet, standing, walking, and running are also naturally different in terms of the loading rate and impact forces for example, which have not been considered in this study. The choice of prosthetic componentry and support surface add another variable [36, 78]. Rather than defining generalised guidelines, the personalised prediction of soft tissue loads, i.e. through real-time interface pressure measurements combined with FEA [36, 76–78], seems like a more suitable approach to provide robust estimations of soft tissue risk across different activities.

Another aspect deserving attention is that all experiments were performed on healthy muscle, whereas prosthetic users often suffer from muscular atrophy [20, 432]. It is likely that this loss in muscle mass will shorten the time of onset for tissue damage because of an increase in strain levels, similar to individuals with spinal cord injury

[66]. However, epidemiological research is needed to back this theory. Additionally, atrophic changes and intramuscular fat infiltration might also influence physiological processes within the tissue [64], including the response to dynamic loading.

Last, the potential effect of self-heating on soft tissue damage has been discussed. An insufficient blood supply worsens this problem. The temperature of avascular tissue like cartilage for example increases significantly after dynamic loading, i.e. from physical activity [433, 434]. Similarly, prosthetic users might not only have a limited blood supply as a side effect of pressure-related tissue deformation but also often suffer from peripheral vascular diseases. The rise in temperature might be further alleviated by the enclosed environment around the residual limb which hampers heat dissipation. Accordingly, the elevated temperatures measured at residual limbs after physical activity [435] might be partly caused by self-heating. However, some of these temperature changes will also be related to a higher metabolic rate and contractile activity of muscles during exercise [436, 437]. The role of self-heating in relation to deformation of skeletal muscle cells with prosthesis-related loading frequencies therefore needs to be explored further.

8.5.4. Effects of dynamic loading on the vascular and lymphatic system

So far, the discussion revolved around the effect of dynamic loading on direct deformation damage. For a holistic view of pressure-related tissue damage, implications for lymphatic activity and vascular supply also need to be considered. However, literature on the lymphatic system is sparse. Researchers found that an obstructed lymphatic flow can lead to the accumulation of toxic waste products, which reduces the cells' capabilities to withstand mechanical loading [111, 112]. Yet, potential effects of cyclic compared to static loading scenarios are widely unknown.

The vascular system on the other hand is better researched. If the magnitude of the direct stress is sufficiently high to obstruct blood flow (fully or partially), then dynamic loading might induce cycles of ischaemia and reperfusion (IR). Generally, ischaemia leads to mitochondrial dysfunction [107, 438–442]. Low ATP levels disrupt the electron transport chain within the mitochondria, which in turn release reactive oxygen species (ROS) that can damage cell organelles upon reperfusion. Additionally, apoptotic messengers might be released. Besides mitochondria, the endoplasmic

reticulum initiates a stress response, which disrupts protein folding and the Ca^{2+} homeostasis within the cell [107, 441, 443].

However, the majority of studies on pressure injuries has been designed without repeated cycles of ischaemia and reperfusion. To the author's knowledge, the few existing experiments induced IR cycles at skin level rather than on muscle and only with extended IR times of ≥ 30min [99, 102]. In how far the observed damage accumulation is applicable to short frequency loading as applied in this study is therefore uncertain. Nevertheless, studies on pre- and postconditioning give a first indication on potential effects of severity, duration, and frequency of IR on skeletal muscle health. Researchers found that mild mitochondrial damage can pre-condition tissue against future IR events, both in cardiac [107, 439, 440] and skeletal muscle [444]. Similarly, repetitive intermittent ischaemia at modest levels might cause cellular adaption to low oxygen levels, as observed in cardiomyocytes [107, 445]. The literature on post-conditioning on the other hand is less conclusive. One study by Mansour et al. showed that brief cycles of IR before extensive reperfusion minimised damage on skeletal muscle cells [446]. Another study by the same authors found an increase in damage when changing IR cycles at a higher frequency [447]. These discrepancies stress that the effects of severity, duration, and frequency of loading on skeletal muscle health need to be addressed not only for direct deformation damage but also for IR scenarios.

8.5.5. Limitations of the static and dynamic loading experiments

Limitations of this study are mainly associated with the experimental design. The isolated EDL and SOL muscles, which are dominated by type IIB and type I fibres respectively, might respond differently to compressive loading, as discussed in "*7.5.3 Limitations of the validation study*". The positive effect of reducing the number of animals, however, outweighed the potential increase in variability.

Additionally, the circular shape of the indenter meant that the indentation area and therefore the potential number of dead cells decreased when moving away from the centre line. With more cross-sections analysed from these peripheral areas then at the centre line (s. "*4.3.4 Tissue processing through formalin fixation and paraffin embedding*"), the collected data is likely to underestimate the number of dead cells. This is reflected by the right-skew of the average cell death numbers per group (**Figure 8-4**, **Figure 8-5**). However, with the same collection principles applied to all

samples, these shortcomings affect groups equally, therefore minimising negative effects on the statistical analysis.

Another important aspect is the limited transferability of results from a murine model to humans. While general trends might be similar, absolute values can and should not be adapted, based on differences in structure and physiological processes. This study also only tested the response of passive muscle. This might be relevant for prolonged static loading, i.e. during sitting. Dynamic loading scenarios, however, always involve muscle contraction. Although not included in this study for better comparability, changes in stiffness and metabolic activity associated with muscle contraction could be considered in future research.

Last, the FE model used to predict the compressive stress within the muscle layer comes with limitations. Data recorded during dynamic experiments showed a higher indenter displacement than predicted by the static FE model. Although the stress in the dynamic loading scenario might be underestimated with a static model, the influence should be small with an overall difference in strain of 3%. For better accuracy, added material testing of skeletal muscle tissue under dynamic loading conditions and an adjustment of the FE model to accommodate sinusoidal loading could be considered in the future.

8.6. Chapter summary

This study explored the effect of prosthesis-related loading on sarcolemmal integrity in skeletal muscle. According to the results, frequency has a major influence on cell death numbers, with high frequency compression (4Hz) being more damaging than low frequency (1.42Hz) or static compression with the same amplitude. Potential explanations are fatigue of structural intra- and extracellular components, frequency-dependent changes in material properties, self-heating, and the release of biochemical messengers. However, further research is needed to elucidate the underlying mechanisms.

The significant difference in cell death counts between the tested scenarios also demonstrates that the established pressure-cell death curve for static loading cannot simply be transferred to dynamic situations. Instead, the frequency behaviour needs to be investigated further to create a multifactorial threshold that considers the relationship between all three factors of magnitude, duration, and frequency of direct stress application.

Translating these results to the prosthetic user is difficult. The experimental design and animal model system can unveil general tendencies on the effect of loading but are unsuitable for directly deducing clinical guidance. One can assume that fast walking or running, and extended loading periods might cause higher levels of direct deformation damage in the muscles of the residual limb. However, multiple other factors need to be considered alongside, like the vascular and lymphatic system, as well as variations in cadence, the nature of the support surface, and the choice of prosthetic componentry. Nevertheless, expanding the baseline knowledge on how prosthesis-related loading affects skeletal muscle health is an important steppingstone towards successful risk assessment and future advances in prosthetic use and care.

CHAPTER 9

Alternative methodological approaches for future work

The response of skeletal muscle to mechanical loading is a complex interplay of processes that can be detected across all organisational levels. For future work, the current experimental setup could be expanded by 3D fluorescence imaging and detecting Raman signals from *ex vivo* tissue samples, as described in this Chapter. The role of biomarker detection is also discussed.

This chapter is a collaborative work. The author and Dr. Arjan Buis conceptualised the studies. The clearing and confocal microscopy process was advised by Prof. Gail McConnell, who also performed the Mesolens imaging. Dr. Alastair Wark supported the author in the Raman-specific preparation of samples and performed Raman spectroscopy and microscopy. The following analysis as well as the overview of biomarkers were composed by the author.

9.1. Introduction to alternative methodologies for muscle damage analysis

When skeletal muscle fibres are mechanically damaged, they lose their sarcolemmal integrity. Without an intact outer barrier, extracellular material like ions and molecules can enter the cell. Staining with membrane impermeable dyes uses this circumstance and is hence a popular way to tag damaged cells. The developed *ex vivo* pressure injury model for example quantifies cell damage after transverse mechanical loading through ProY staining. However, many other assays and markers are available that target different aspects of cell damage. By combining them, a holistic picture of pathological changes in cellular processes can be drawn.

9.1.1. Optical clearing to enable 3D imaging of whole tissue samples

When working with tissue samples, inner cell layers need to be uncovered to gain information on the whole specimen. One way is through formalin fixation and paraffin embedding (FFPE) and microtoming, as described in ”*4.3.4 Tissue processing through formalin fixation and paraffin embedding*”. The associated processing, embedding, and cutting is laborious and requires considerable hands-on time. Over the last decades, different ways to image full tissue have been explored to make these steps obsolete. Like with single slices, whole mounts can be fluorescently stained to gain three-dimensional information.

Unlike conventional microscopy, a confocal microscope allows for 3D-imaging. The field of view depends on the setup – standard confocal microscopes illuminate micrometre-sized sections of a sample; for samples up to the millimetre-scale, a Mesolens can be used [282]. However, scattering, absorption, defraction and refraction may hinder high quality imaging [448]. Additional clearing to increase the tissue’s transparency can alleviate a few of these problems. Decolourisation of the samples i.e. with H_2O_2 limits absorption. The replacement of intra- and extra-cellular fluids with a clearing agent like BABB (benzyl alcohol, benzyl benzoate) eliminates strong scattering effects caused by a mismatch in refractive indices between fluids and cellular components like lipids found in the membrane [448, 449]. This makes imaging of whole tissues possible, even with conventional confocal microscopes.

9.1.2. Principles of Raman imaging as label-free alternative to fluorescence imaging

An alternative to fluorescence microscopy is label-free imaging with Raman microscopy, a form of biochemical mapping. This technique can visualise the cross-striational appearance of skeletal muscle [450] and support the diagnosis of cardiovascular disease [451] without the need for staining. It is based on light scattering influenced by molecular bonds. A monochromatic light source, usually a laser, is targeted at a sample, where the incoming photons scatter in two ways (**Figure 9-1**). Usually, the wavelength of the scattered photons stays the same, meaning that no energy is lost to the targeted molecules. This elastic scattering is called Rayleigh scattering. However, with an efficiency of $1:10^8$ [452], the photon loses a part of its energy to the molecules and is emitted at a lower wavelength. The energy of the excitation photon changes according to the vibrational state of the chemical bonds within the specimen, either increasing (Stokes) or reducing (anti-Stokes) [452, 453]. This inelastic response is called Raman scattering. The change in wavelength or Raman shift is commonly expressed in wavenumbers (units of cm^{-1}) and plotted against its intensity. The resulting Raman spectrum provides a unique fingerprint of the biochemical composition of the substrate.

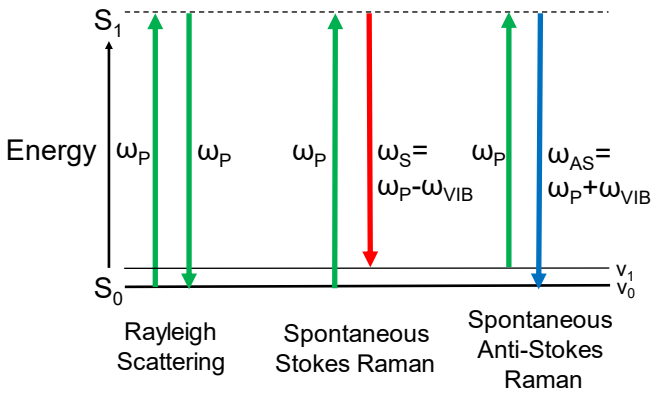

Figure 9-1: Perrin-Jablonski Diagram of Rayleigh and Spontaneous Raman Scattering. S_0 and S_1 are virtual electronic energy levels. **(1)** Rayleigh Scattering: Light with an excitation frequency ω_P is scattered with the same frequency. **(2)** Spontaneous Stokes Raman: Light with an excitation frequency ω_P is scattered with a lower frequency ω_S. The molecule in the sample absorbs part of the incident photons energy, reducing the energy of the scattered photon by ω_{VIB}. **(3)** Spontaneous Anti-Stokes Raman: Light excitation of a molecule with a frequency ω_P is scattered with a higher frequency ω_{AS}. When the molecule has a higher excitation, it loses part of its energy to the incident photon, which increases the scattered photons energy by ω_{VIB}.

When combining Raman spectroscopy with microscopy, biochemical images can be generated with subcellular resolution. To improve the low spontaneous Raman signal intensity, different variations of Raman microscopes have been invented. Stimulated Raman Scattering (SRS) uses two lasers at separate frequencies, a pump and a stokes beam (**Figure 9-2**). When the energy difference between those lasers matches the molecular vibrational mode of interest, the Stokes emission signal is amplified [454, 455]. SRS therefore measures the intensity gain and loss in the incident beams.

Coherent Anti-Stokes Raman Scattering (CARS) has four frequency components: pump, stokes, probe, and anti-Stokes (**Figure 9-2**) [455, 456]. The pump beam and probe beam are mixed with the stokes beam. The difference between the pump and stokes beam thereby needs to match the vibrational mode of the molecule of interest. This generates an intensified emitted anti-stokes signal at a new optical frequency. Both SRS and CARS are time-gated techniques, meaning that they can focus on a specific spectroscopic wavelength to visualise structures that return this signal, i.e. C-H bonds to image lipids.

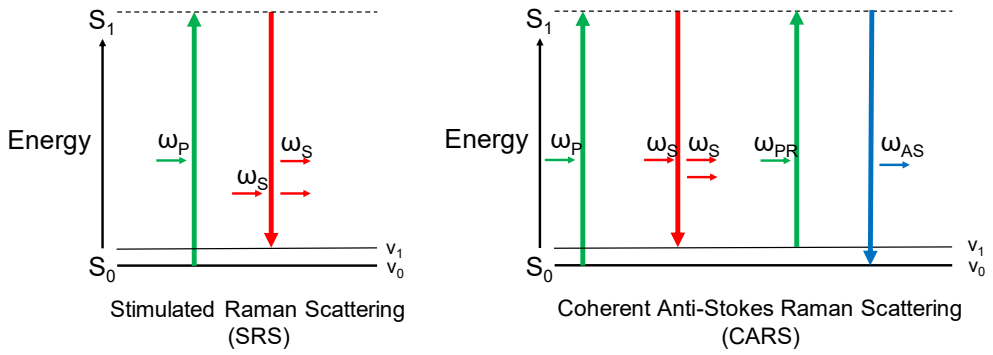

Figure 9-2: Perrin-Jablonski Diagram of CARS and SRS. (1) SRS: The excitation pulse with frequency ω_P is mixed with a Stokes light (ω_S). If the frequency difference between the two beams matches that of the molecular vibration in the sample, the photonic emission is amplified. (2) CARS: The excitation pulse with frequency ω_P is mixed with a probe pulse (ω_{PR}) and a Stokes pulse (ω_S). This configuration creates a new, intensified anti-stokes signal (ω_{AS}).

9.1.3. Biomarker analysis to complement optical imaging

Besides the optical identification of cellular damage, changes at the micro- and meso-level can be detected through biomarkers. Biomarkers represent direct physiological messengers of cells in response to loading. In pressure injury research, the successful measurement and identification of biomarkers is key to effective risk assessment and diagnosis.

So far, researchers have collected biofluids like sweat [457–460], sebum [459, 461, 462], urine [215, 463], or blood [215, 464–466], as well as soluble proteins through skin blotting [467, 468] to detect changes in biomarker concentrations. They identified multiple inflammatory markers, muscle damage markers, metabolites, and purines as biomarkers for pressure injuries. Recently, the detection of inflammatory biomarkers has also found its way into the assessment of prosthetics [214].

Apart from systemic analyses, biomarkers can also be found in *ex vivo* and *in vitro* experiments. Tissues, cells, and artificial constructs secrete biomarkers into the surrounding medium *in vitro* when under physical stress. By analysing the medium, various studies identified mediators of the immediate cell response to mechanical loading [112, 469, 470].

Additionally, biomarker-based assays are available that uncover messenger pathways and (patho-)physiological processes within the cells of a tissue compound, like membrane damage [471] or the onset of apoptosis [472] after mechanical loading. Instead of fluorescent staining of samples for microscopic imaging, cells can be separated from the extracellular matrix (ECM) by enzymatic digestion. The acquired cell lysate can then be analysed in numerous ways. Examples include cytometric staining and flow cytometry [473, 474], immunoblotting [219, 472], or the use of immunoassays on microplate readers [470–472].

The direct analysis of medium or cell lysate is usually more sensitive to cell-level changes than biomarker analysis in body fluids. Nevertheless, detecting systemic biomarkers is relevant for clinical diagnostics. Research indicates that biomarker analysis might even detect skeletal muscle injury more readily than histopathology [472]. By combining both approaches, a more comprehensive understanding of the cell and tissue response across multiple organisational levels can be achieved.

9.2. Aims of preliminary studies for future work

The current approach to quantifying sarcolemmal damage after mechanical loading requires formalin fixation and paraffin embedding (FFPE) and epifluorescence imaging. Although achieving the intended results, this method could be combined with other techniques to gain a more complete picture of the complex cellular behaviour. Two alternative ways of sample preparation and imaging were therefore explored, namely clearing and confocal imaging, as well as dewaxing and Raman imaging. Their suitability to integrate into the experimental setup was tested. Additionally,

several potential biomarkers were identified from literature and reviewed in the discussion section. The purpose is to highlight the possibilities for future research into the response of skeletal muscle to transverse mechanical loading.

9.3. Experimental design and methods for confocal fluorescence and label-free imaging of tissue samples

9.3.1. Collection and preparation of murine skeletal muscle tissue

As described in previous chapters, extensor digitorum longus (EDL) and soleus (SOL) muscles were isolated from the hindlimbs of male Sprague Dawley rats, following ethical guidelines by the University of Strathclyde (s. "*4.3.2 Collection and preparation of murine skeletal muscle tissue*"). Muscle samples were assigned either to whole mount imaging (*n* = 16) or Raman imaging (*n* = 7).

9.3.2. Optical tissue clearing method

A clearing protocol was explored to allow for confocal imaging of whole tissue samples. Seven samples (*n* = 2 EDL, *n* = 5 SOL) were mechanically damaged in a static loading setup (s. "*4.3.3 Mechanical loading* "). The setup consisted of a flat indenter with a weight of 11g or 25g lowered onto the samples for 1.5h. Additional control samples (*n* = 2) were stored in MOPS buffer for 1.5h or 3h. All muscles were stained with 0.1% ProY for 5 - 30min before following the clearing protocol. The remaining samples (*n* = 7) had to be excluded from analysis because of limited availability of microscopic equipment.

Before clearing, the muscles were washed 3 x 5 minutes in PBS to remove any residue and transferred to 4% (w/v) paraformaldehyde (PFA) solution for at least 6h at ambient temperature. To bleach the tissue and aid clearing, the specimens were then placed in 35% H_2O_2 for 18h. Next, the tissues were dehydrated through an anhydrous methanol and BABB series, each step lasting 1 hour. BABB is a 1:2 mixture of benzyl alcohol and benzyl benzoate, which was introduced in a 1:1 by volume mixture of BABB and MeOH in the first step. The amount of BABB in the next steps increased from 50% to 75% and 2 x 100%. The specimens were then removed from the MeOH/BABB mixture and placed in 100% BABB for at least 24h before imaging. All materials were acquired from Sigma Aldrich (St. Louis).

Imaging was conducted in two ways: Standard confocal microscopy was performed on a laser scanning system (Olympus FV1000) coupled with an IX81 inverted microscope (Olympus, Japan). Magnification was set to 10x, step size to 5µm, and excitation and emission wavelengths (488nm and 530nm) were taken from literature [475].

For a larger field of view, a Mesolens system was used, which allows for a 6mm field size and 3mm thickness to be captured with sub-cellular detail [282]. Laser power was set to 70mW. The excitation wavelength was identical to confocal microscopy and emission was collected through a GFP (540/10nm) and a PI (600/10nm) filter in two channels. A total depth of 1277µm was imaged with a step size of 5µm.

9.3.3. Raman microscopy method

For Raman microscopy, six samples (*n* = 5 EDL, *n* = 1 SOL) were processed. Two of them were mechanically indented in a static setup for 2h with 60g (s. *"4.3.3 Mechanical loading setup"*). Without any staining, the samples were fixed, processed, and sectioned into longitudinal and cross-sectional slices of a thickness of either 4µm or 10µm, as described previously (s."*4.3.4 Tissue processing through formalin fixation and paraffin embedding*").

To investigate the interference of paraffin with the Raman signal, paraffin embedded slides were compared with dewaxed samples. The dewaxing procedure included two baths of Histoclear (5min and 4min), two baths of EtOH (3min and 2min) and 1min in 95% industrial methylated spirits. The samples were then either mounted in DPX or PBS to test the interference of DPX with Raman signals.

Spontaneous Raman spectra of *n* = 3 undamaged tissue samples were obtained from randomly selected ROI as well as wax-only areas, utilising a WITEC Alpha300 instrument employing a 514 nm, 633 nm and 785 nm excitation laser. The microscope objective used was 20x (Nikon, S Plan Fluor, NA 0.45, ELWD) and data processing was performed using the WITEC project 2.1 software. The associated excitation wavelength and laser power are stated alongside the presented data.

After characterising the Raman spectra of skeletal muscle tissue, preliminary Raman multiphoton images were obtained with a confocal Leica Microsystems TCS SP8 system. In addition to the features described in "*5.3.1.1 Microscope and software*

specifications", the system has a fully integrated SRS module featuring a picoEmeraldTM S picosecond laser (APE). The SRS module provides two temporally and spatially overlapped beams operating at a pulse repetition rate of 80 MHz and ~2 pS pulse width. The fundamental Stokes beam is at 1031.4 nm, a portion of which is passed into an optical parametric oscillator (OPO) with the wavelength tuning of the second infrared (pump) beam fully automated between 700–960 nm with <1 nm (10 cm-1) spectral bandwidth. For SRS measurements, an electro-optic modulator (EOM) operating at a frequency of 20 MHz is integrated into the 1031 nm beam path, with the forward scattered SRS signal reflected into a photodiode detection module. The photodiode signal is passed to a lock-in amplifier (UHFLI, Zurich Instruments) before returning to the SP8 scan head. The incident laser powers are typically 10 - 30 mW for the pump beam and 10 – 50 mW for the Stokes beam, and are software controlled via half-wave plate polarisation rotation.

SRS images were acquired using a 40x water immersion objective (HC PL IRAPO, N.A. 1.1) and the forward scattered light collected via a condenser lens (S1 oil, NA 1.3). All images were acquired at 12-bit image depth and typically at a resolution of 1024 × 1024 pixels and a pixel dwell time of 48mS unless otherwise stated. Line averaging (x3) was typically used to reduce image noise. All measurements were performed using the LAS X software with further data analysis also performed upon exporting to FIJI/ImageJ.

9.3.4. Data analysis for optically cleared and label-free samples

Cleared samples were visually inspected for the success of the BABB protocol. Images were also reviewed for signal across different depths with both the Mesolens and normal confocal fluorescence microscopy. The feasibility of combining fluorescent ProY-staining and BABB clearing was assessed by looking for dye-positive fibres in mechanically damaged samples.

Prior to Raman imaging, spontaneous Raman spectra from undamaged and wax samples were corrected for background signal before peak wavenumbers were identified and compared to known wavenumbers from the literature. For Raman imaging, the dewaxing protocol was verified by comparing images from paraffin-embedded slices to dewaxed ones. Both longitudinal and cross-sectional slices of indented samples were also inspected for signs of mechanical damage like disorganised fibres and loss of cross-striation.

9.4. Results and discussion of alternative methods to detect cell death

Currently, cellular damage in mechanically loaded skeletal muscle cells is visualised through fluorescent staining and FFPE processing. To achieve a more comprehensive picture of the mechanisms initiated at a cellular level, complementary methods could be integrated. Alternative processing, imaging, and analysis techniques were therefore identified. For a direct adaption of the current *ex vivo* model, preliminary experiments were conducted using optical tissue clearing (OTC) with confocal micro- and mesoscopy, or label-free Raman imaging. All approaches showed promise, but a number of limitations will need to be addressed before reliable results can be obtained.

Several alternative markers for tissue damage were also identified and will be discussed in the last section. These biomarkers, including inflammatory markers, muscle damage markers, metabolites, and purines, are potential targets for cell and tissue assays or extracellular fluid analysis.

9.4.1. Optical tissue clearing and confocal imaging

By combining OTC with confocal imaging, spatial information on fibre structure and mechanically induced tissue damage can be obtained. Compared with the current FFPE protocol, the labour-intensive cutting process with its risk of introducing artefacts would be eliminated while gaining additional spatial information. Thus, factors influencing damage distribution and severity could be identified more easily, including indenter shapes and load directions, or tissue thickness and myofiber size.

Additionally, cleared tissue images can feed into sophisticated Finite Element (FE) models by visualising three-dimensional cellular orientations. Comparing damage locations in real samples to internal loading conditions of the corresponding FE models could improve the predictive power and validate these models.

9.4.1.1. Detection of mechanically induced fibre damage in cleared skeletal muscle

To gauge the success of BABB clearing for skeletal muscle tissue, the macroscopic light transmission of cleared samples was tested first. The transparency of n = 12 out

of *n* = 16 samples increased noticeably after completing the BABB protocol **(Figure 9-3**). The other four samples remained cloudy after the first clearing procedure but were salvaged by storage in MeOH for 12h before repeating the BABB protocol. Confocal fluorescence imaging on the standard microscope as well as with the Mesolens confirmed these results as autofluorescence signal could be recorded across the full depth of the samples (**Figure 9-4**).

While clearing was successful, clear detection of ProY-positive fibres indicating mechanical damage was difficult. Both microscope and Mesolens images revealed increased signal on fibres that also appeared disorganised (**Figure 9-4**). On the large-scale images from the Mesolens, the irregularities were located towards the central belly region of the muscle, which coincides with the typical area of indentation. Although fibre damage was also visible with the confocal microscope, the limited field of view was a hindrance to establishing a similar connection.

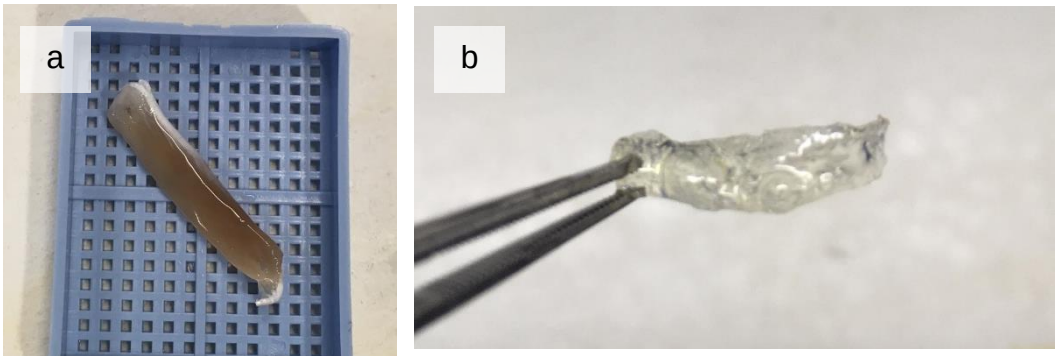

Figure 9-3: Clearing of skeletal muscle tissue. **(a)** Isolated soleus muscle of Sprague Dawley with distinct red colour and high opacity; **(b)** Transparent muscle after clearing with BABB.

9.4.1.2. Limitations of optical clearing

The preliminary results on the suitability of clearing and fluorescent staining need to be interpreted with caution. First, time and other restrictions lead to a small sample size. Additionally, several technical issues arose with the experimental setup: Tissue samples were not pinned out during indentation and initial fixation, and the indentation site was not marked. This made it difficult to relate fibre damage to the loading protocol. The applied loads also may have been insufficient to inflict mechanical damage (s. ”*7.4.3 Stress-time cell death threshold for ex vivo skeletal muscle tissue*”).

Last, ProY might not be compatible with BABB clearing as it could be quenched in the process [449]. Alternative clearing protocols like iDISCO [476], 3DISCO [449], or SeeDB [477] could be tested. The microscopic settings were also not yet adjusted to the optimised imaging parameters defined in "*5.4.5 Summary of optimised image acquisition parameters for quantitative fluorescence imaging*". Consequently, the fluorescence signal of ProY might have been partially masked by the strong autofluorescence of the tissue.

Considering these limitations, the preliminary study should be repeated with careful control of the experimental setup. This includes proper fixation of the tissue during loading, clear demarcation of the indentation site, application of a damage-inducing mechanical load, and appropriate microscope settings. Additional positive and negative controls need to be included as well.

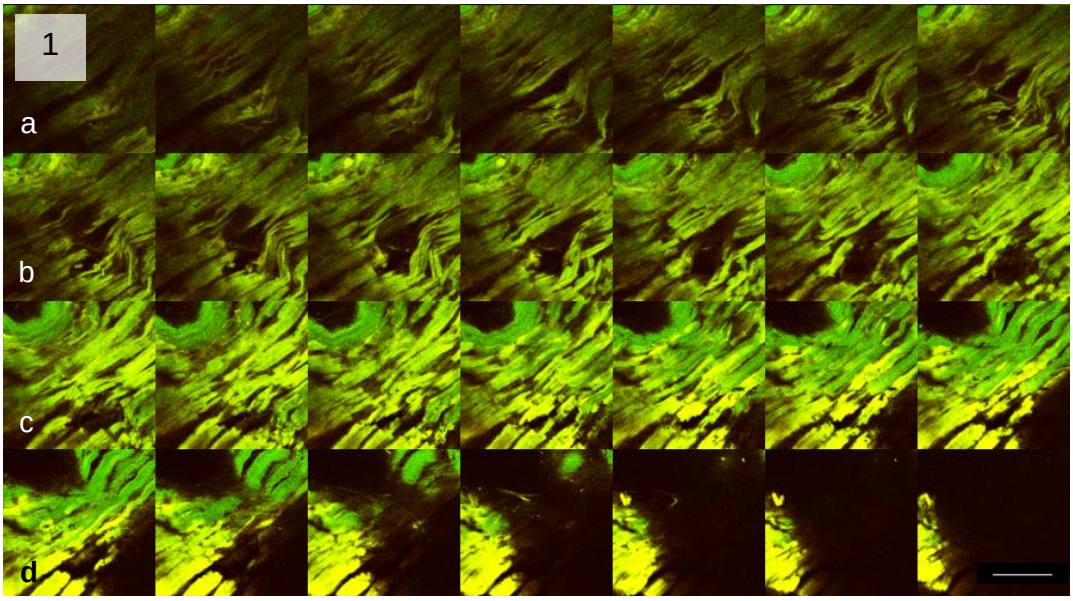

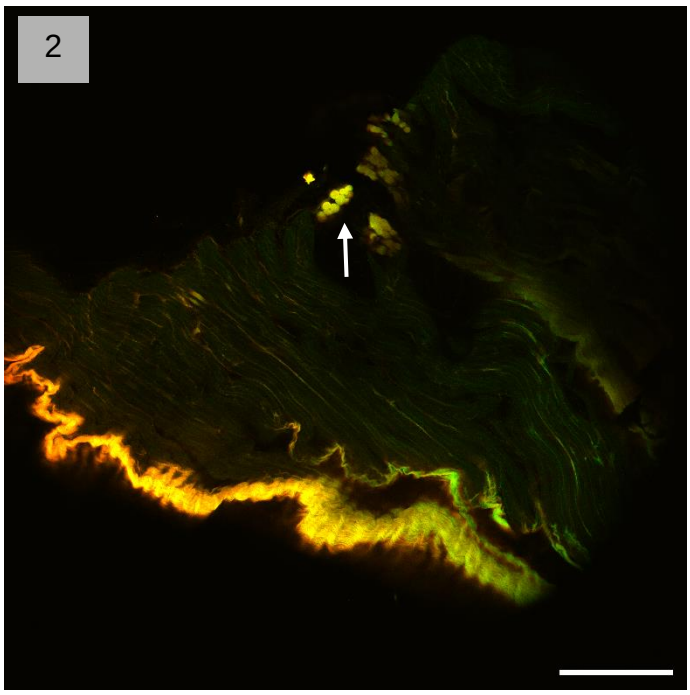

Figure 9-4: Confocal fluorescence imaging of mechanically damaged skeletal muscle tissue. **(1)** Montage of image stack from confocal microscopy (5µm steps). Longitudinal fibres have typical green autofluorescence. Disorganised fibre structure and increased intensity visible in rows b – d. Images were acquired at ex 488nm, em 530nm with 10x magnification. Scale bar 50µm. **(2)** Confocal Mesoscopy of approximately half of a skeletal muscle. Clear longitudinal fibre arrangement and stain accumulation at outer tendon area. Arrow marking internal damage with disturbed fibre orientation. Image acquired with 488nm em, 540nm ex. Scale bar 1mm.

9.4.1.3. Suitability of confocal fluorescence microscopy and mesoscopy

Despite the limitations, the preliminary results indicate that the Mesolens can provide clear spatial information on damage location based on its large field of view (6mm x 6mm), covering half of the hindlimb muscle. Standard confocal imaging on the other hand has a limited field of view (0.13 x 0.13mm) and would need multiple imaging and stitching to attain full cross-sectional or longitudinal images. However, the imaging

time and amount of data produced with confocal fluorescence microscopy are easier to handle. Imaging a full EDL or SOL with the Mesolens would take approximately three days and another 6 - 8h to transfer the vast dataset onto a computer for analysis. The trade-off between the extensive information and the feasibility of analysing the created dataset therefore needs to be considered carefully when choosing a method.

Overall, combining OTC and confocal fluorescence imaging is a promising way to visualise the spatial distribution of cellular damage within a muscle after mechanical loading. To reach its full potential, existing limitations in the method still need to be addressed. Once successfully set up, it can expand our current understanding of the effect of physical stress on skeletal muscle.

9.4.2. Skeletal muscle analysis with Raman signals

Compared with fluorescence imaging techniques, Raman microscopy visualises changes in molecular structure following mechanical tissue damage without the risk of toxic effects and photobleaching of fluorophores. This makes it an attractive alternative for biomedical applications, including studies on skeletal muscle [450, 478].

9.4.2.1. Setup for Raman spectroscopy and imaging

The background fluorescence associated with standard microscope glass slides and coverslips was an issue in acquiring Raman spectra of thin tissue sections. Background fluorescence from tissue at 532 and 633 nm excitation also interfered with Raman signals. This is not surprising, based on the fluorescence measurements that were acquired previously. Similar to reports from other researchers [479], the best results were achieved for 785 nm excitation, providing a good balance between scattering efficiency and influence of fluorescence that could hide Raman signals.

Besides the tissue itself, paraffin wax from the FFPE preparation also interfered with Raman signals. Spectral analysis of wax-only areas of microscope slides revealed a strong spectral response (**Figure 9-5**). Similarly, shifts in the spectra were observed when analysing DPX-mounted tissue. Hence, dewaxing and PBS mounting were necessary.

For thin sections (4µm), it was also difficult to get good signal-to-noise ratio (SNR) from the samples when acquiring spontaneous Raman. Thicker sample preparations

(10µm) were therefore preferred. Incident laser powers between 10 mW and the maximum available of 45 mW were also explored. There was no evidence of significant laser damage affecting the spectral response on repeat spontaneous Raman measurements on the same sample spot at 785 nm excitation.

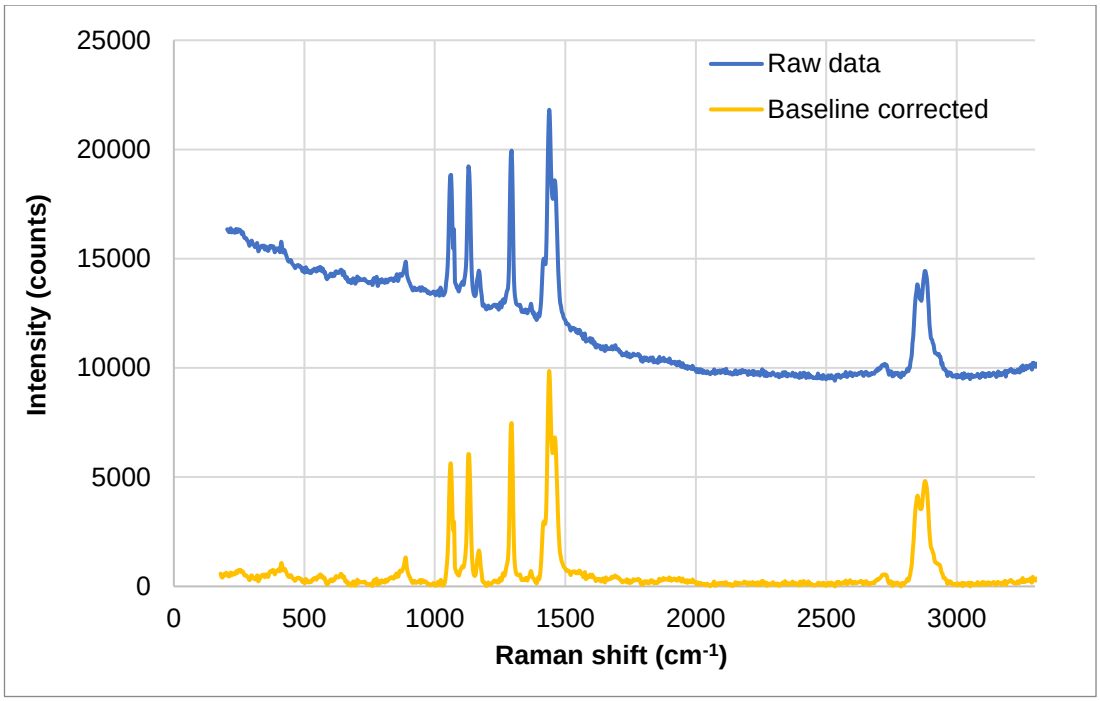

Figure 9-5: Representative Raman spectrum of paraffin wax. Data was obtained with at 785 nm ex with 3mW laser power and 60s integration time. Raw data (blue) was baseline corrected (yellow) using an adaptive multipoint fitting (Spectrogryph 1.2).

9.4.2.2. Spectral Raman analysis of skeletal muscle tissue

A spontaneous Raman spectrum was obtained from multiple dewaxed skeletal muscle samples to obtain a spectral profile. The most notable peaks are annotated in **Figure 9-6**. The peaks overlapped well with data from other studies on skeletal muscle tissue [479, 480], with peak intensities at 856, 940, 1044, 1243, 1320, 1450, and 1659 cm^{-1} reported to belong to collagen and other proteins, based on amino acid building blocks like proline and amide III. The peak at 1659 cm^{-1} represents lipids (C=C bonds). The high-wavenumber region around 2900 cm^{-1} has multiple overlapping peaks with 2930 cm^{-1} (CH_3 bonds) associated with proteins and 2851 cm^{-1} (CH_2 bonds) associated with lipid structures like the membrane. Other studies also reported on spontaneous Raman signals from skeletal muscle and other tissues but with different preparations and hence slight variations [481–484].

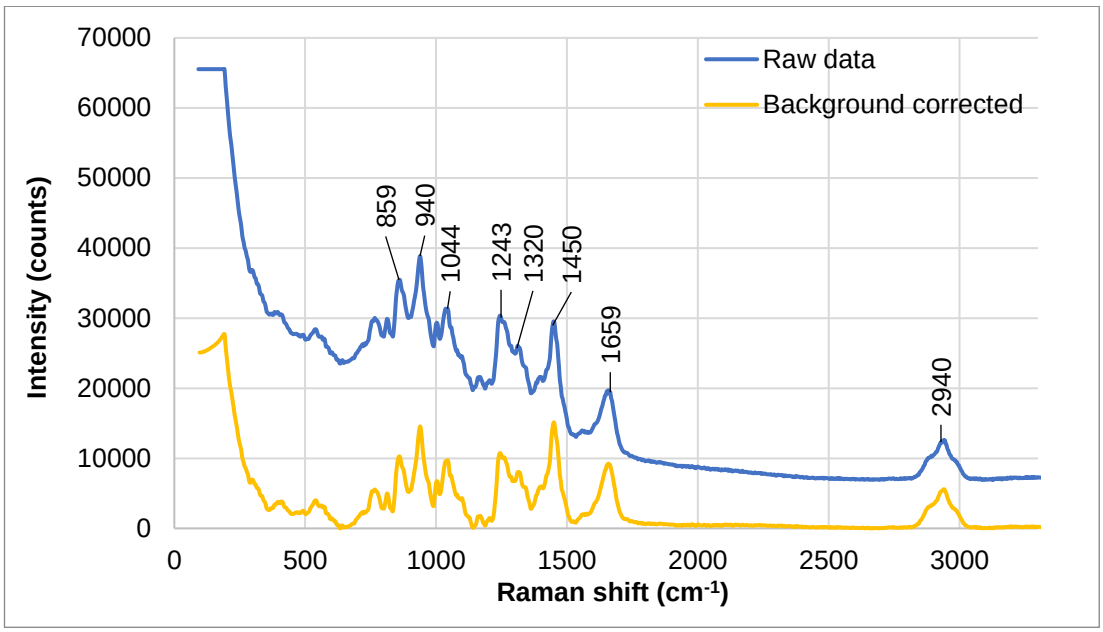

Figure 9-6: Representative Raman spectrum of skeletal muscle tissue. Raman spectrum of dewaxed, thick cross-section of skeletal muscle tissue. Data was obtained at 785 nm ex with 45mW laser power and 30s integration time. Raw data (blue) was background corrected (yellow).

Researchers recently compared shifts and intensity changes in Raman peaks between healthy and pathological tissue for example between normal and atrophic muscle [479], and healthy and ischemic limbs [478]. Thus, they identified molecular processes that are involved in the abnormal function, like sarcoplasmic reticulum stress, which leads to perturbation of the protein folding process, or increased apoptosis and changes in metabolic activity. Similarly, spectroscopic studies on cardiovascular disease have been used to identify biomarkers like Tn-1, myoglobin, and CK-MB to aid clinical diagnostics [451]. Comparing the spectral information of mechanically damaged and control tissue could therefore reveal molecular changes and target muscle damage-specific biomarkers, which are described in ”*9.5 Biomarker for skeletal muscle damage*”.

9.4.2.3. Raman microscopy of skeletal muscle tissue

The spectral analysis of Raman signals from skeletal muscle tissue can also be combined with imaging to create biochemical maps. Pfeffer et al. [450] imaged the typical cross-striation of skeletal muscle and cell organelles like mitochondria and nuclei with Raman microscopy. They targeted C-H groups in the high-wavenumber region (2845cm^{-1}, CH_2 symmetric stretch, visualising lipids) with CARS. Unlike Pfeffer

et al. [450], quality images with CARS could not be obtained in this preliminary study because of high signal interference from non-resonant background effects [485, 486].

Instead, muscle fibres were clearly distinguishable in Raman images taken at 2930cm^{-1} (CH_3 symmetric stretch, visualising proteins) with SRS. As expected, the typical cross-striational pattern was visible (**Figure 9-7**), with proteins like myosin abundant in skeletal muscle ("*3.3.1 Hierarchical structure of skeletal muscle*"). Peripheral nuclei were also distinguishable.

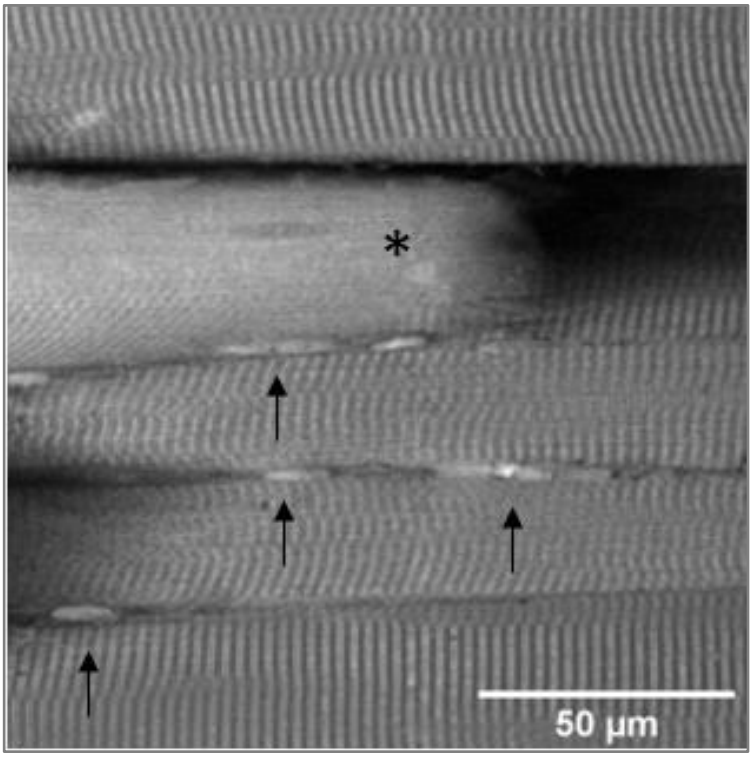

Figure 9-7: Longitudinal SRS-Raman image of skeletal muscle tissue. Clearly visible cross-striation of individual skeletal muscle fibres. (*) indicates damaged fibre with loss of striation pattern. Arrows mark peripherally placed nuclei. Image was taken with excitation lasers tuned to 2930cm^{-1}.

When comparing images across the high-wavenumber region from 2750–3150nm^{-1}, the difference between nuclei and the protein structures of myofibrils was even more distinct. Mainly nuclei were visible outside of the main CH_2-CH_3 band that ranged from 2850 – 3025 nm^{-1} (**Figure 9-8**). This indicates that the off-resonance signal for nuclei might not be from Raman scattering but other multiphoton processes giving off a broad luminescent signal that is received because of the different molecular composition. However, the exact relationship of different cellular components and their appearance in Raman images needs to be evaluated further.

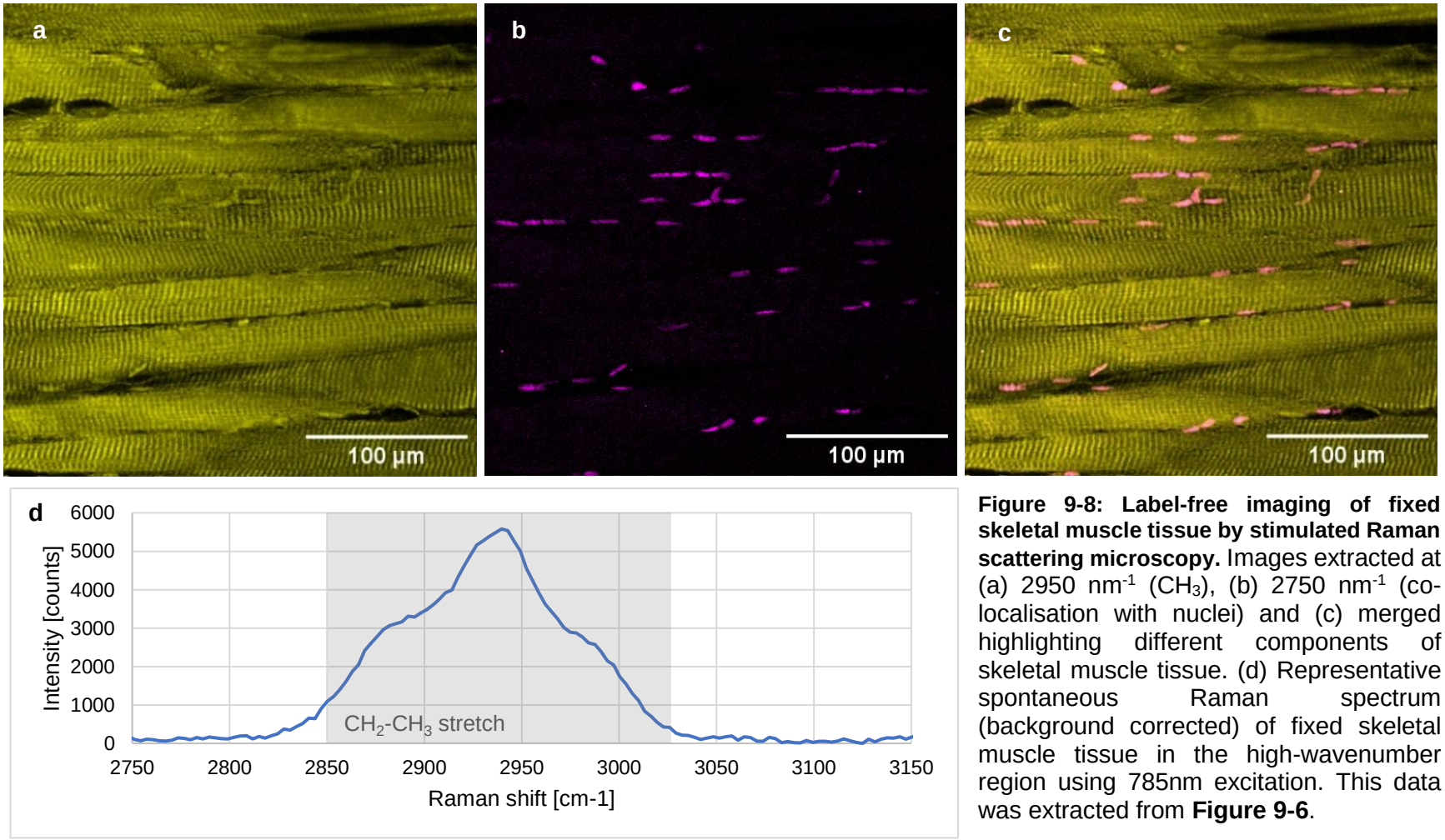

Figure 9-8: Label-free imaging of fixed skeletal muscle tissue by stimulated Raman scattering microscopy. Images extracted at (a) 2950 nm^{-1} (CH_3), (b) 2750 nm^{-1} (co-localisation with nuclei) and (c) merged highlighting different components of skeletal muscle tissue. (d) Representative spontaneous Raman spectrum (background corrected) of fixed skeletal muscle tissue in the high-wavenumber region using 785nm excitation. This data was extracted from **Figure 9-6**.

9.4.2.4. Alternative Raman-based approaches

One advantage of Raman spectroscopy and microscopy is that it makes labelling obsolete, which might otherwise interfere with cells and tissues. This makes it an ideal analysis approach not only for fixed but also *in vivo* specimen, which could be explored in the future. One way could be to monitor cells or cell constructs throughout the process of mechanical damage development to identify sub-cellular processes involved.

Apart from the high-wavenumber region assessed in the preliminary experiments, recording images in the so-called fingerprint region (400 – 1800cm^{-1}) could also be of interest. The fingerprint region contains a wide variety of overlapping signals from biomolecules like proteins, lipids, and DNA [454, 479, 487]. Bergholt et al. [487] describe how they used this stretch to focus on the ECM rather than intracellular components. The ECM is an intricate biomolecular network that provides structural function. Excessive mechanical loading of the ECM therefore might induce focal stresses and strains on cells. Monitoring potential changes in the ECM structure could therefore provide insight into the development of deformation-related cellular damage.

Similar to the preliminary studies on fluorescent staining and clearing, Raman can also be combined with OTC. Wei et al. [488] achieved a 10-fold increase in imaging depth with SRS on brain tissue, which is known to have high scattering effects. Their clearing protocol was tailored to preserve the high-wavenumber region of the Raman spectrum that was targeted in the experiments. Likewise, Sdobnov et al. [489] modified their clearing protocol of skin to allow for confocal Raman imaging in the fingerprint region. Both approaches could be an addition to the developed fluorescent staining and clearing route to gain spatial information on biochemical changes.

9.5. Biomarker for skeletal muscle damage

Biomarkers play an important role in pressure injury and prosthetic research, where they are used to detect damage and understand the underlying pathophysiological processes. So far, biomarkers have been identified in a clinical context as well as in bench top experiments [214, 215, 460, 464, 466]. Their carriers range from biofluids like sweat, sebum, urine, or blood, to tissue sections, cell lysates, and extracellular medium. This overview covers four types of biomarkers – inflammatory markers,

muscle damage markers, metabolites, and purines – and discusses their role in DTI research.

9.5.1. Inflammatory marker

Mechanical loading of muscle tissue triggers an inflammatory response, which can be detected through inflammatory markers. One class are inflammatory cytokines like tumour necrosis factor alpha (TNF- α), interleukin 1 alpha (IL-1α) and interleukin 6 (IL-6). These cytokines recruit neutrophils to the damage site, which in turn initiate phagocytosis and generate free radicals [165]. This initial response is non-selective and may damage not only to the affected cells but also the surrounding tissue [490].

When skeletal muscle is structurally damaged, the inflammatory response seems to be dependent on the mechanical loading scenario. According to Tsivitse et al. [491], neutrophil chemotaxis is relative to the magnitude of the applied strain rather than initiated by muscle injury. The priming of neutrophils to produce free radicals also seems to be sensitive to a strain threshold. However, elucidating the role of specific cytokines in the muscle damage process is difficult. While Tsivitse et al. [491] found that TNF-α-levels remained constant in medium surrounding mechanically compressed myotubes, others observed an increase associated with muscle damage [492]. Many markers also play an ambiguous role of promoting destruction but also regenerating damaged cells and tissues [490, 492, 493].

Cytokines also stimulate the production of other inflammatory markers, like C-reactive protein (CRP). CRP binds to damaged cells and promotes their phagocytosis, the secretion of pro-inflammatory cytokines, and the release of reactive oxygen species (ROS) [490]. It comes in two isoforms: pro-inflammatory monomer CRP (mCRP) and anti-inflammatory pentamer CRP (pCRP). Multiple studies found an association between an increase in CRP serum levels and pressure injuries [466, 494–496]. However, Del Giudice et al. [490] pointed out that the pro-inflammatory mCRP is not soluble in plasma and remains localised in the tissue. Analysing serum samples therefore measures pCRP concentrations, which is likely to be an indicator of acute inflammation but not pro-inflammatory in itself. Additionally, a clear relationship between tissue strain and CRP levels is yet to be defined.

Another challenge is correlating isolated bench-top experiments with clinical biomarker measurements. A popular method to gauge inflammation is through sebum analysis at the skin surface. The concentration of IL1- α has been shown to increase

significantly under pressure and shear of 30mmHg and 5.9kPa respectively [461]. As the collection of sebum or sweat is non-invasive, these methods are ideal for clinical settings [214, 462]. Nevertheless, the significance of superficially collected samples to characterise deep muscle damage needs further investigation.

9.5.2. Muscle damage marker

The second group of biomarkers discussed here is specific to muscle tissue. When muscles are damaged, they release intracellular contents that can be identified in serum, urine, and exudate. The most popular muscle damage marker is creatine phosphokinase (CPK), with its isozyme CK-MM predominating in skeletal muscle. Following pressure injury, CK-MM is released from damaged skeletal muscle cells, leading to an increased concentration in serum and exudate [463–465, 497]. Similarly, the systemic concentration of other molecules might rise, including myoglobin [215, 463], myosin [463], troponin-I (TnI) [215, 463], and heart-type fatty acid binding protein (H-FABP) [463, 466].

Despite the specificity of the mentioned markers to muscular damage, they are not exclusive to DTI but commonly increase during normal daily activity like exercise [498–501]. Thus, a direct correlation between pressure injury and biomarkers can be difficult. The collection procedure of serum and exudate is also often invasive, limiting their routine application in clinical settings.

A potential alternative to collect muscle damage markers is skin blotting [502]. Through the application of a saline-soaked nitrocellulose membrane, large soluble proteins can be captured on the skin surface. Tamai et al. [503] have used this technique to identify increased CK-MM and IL-6 levels in wheelchair basketball athletes after training. Biomarker collection through skin blotting therefore seems like a promising non-invasive approach to obtain information on the status of deep soft tissues, making it relevant for pressure injury and prosthetics research.

9.5.3. Metabolites

The third group of biomarkers for pressure injuries is metabolites. When tissue deformation occludes the vascular supply, the cells are deprived of oxygen and their metabolism switches from aerobic to anaerobic, which relies on glycolysis for energy production. A by-product of glycolysis is lactic acid, which will accumulate in the cells. Once the acidification reaches a threshold of pH 5.3, cell death rates might increase

[105]. The increase in lactate can be measured through sweat and sebum analysis [459, 462, 504] and rises significantly once the transcutaneous oxygen pressure ($tcPO_2$) is reduced by > 60% [213]. Other metabolites like urea, urate, pyruvate, and chloride were also found to increase in sweat and sebum after pressure application [213, 457–459]. However, it is not clear whether pressure exposure time [462] or pressure magnitude [213] are related to the metabolite concentrations. High variability in individual responses to loading further complicates the interpretation of results [459, 504]. Additionally, the focus on ischemia-related processes at the cutaneous level makes the current techniques of metabolite analysis less suitable for deep tissue assessment.

9.5.4. Purines

The last group of biomarkers, purines, is mainly associated with ischaemia-reperfusion. During an ischaemic event, the metabolism not only switches from aerobic to anaerobic, but ATP synthesis is reversed as an additional source of energy [442, 505, 506]. One side effect is the deposition of purines like xanthine and hypoxanthine. When the blood supply is restored, purines are oxidised into ROS. ROS have an unpaired electron on the outer shell, making them highly reactive. Their interference with lipids, proteins, and the DNA, can lead to dysfunction of cellular processes and an increased membrane permeability in cellular organelles and the cell itself [107, 505, 507, 508]. The damage potential of ROS is also not restricted to the skeletal muscle cell but extends to the microvasculature where they might activate platelets that aggregate at the vessel wall and promote oedema formation [107].

The described purine response has been observed in muscle biopsy and blood samples after strenuous exercise [509, 510], as well as in sweat and sebum samples after loading-unloading regimes [460]. However, to evaluate the suitability of these purines as biomarker for DTI, the relation of concentration levels to deep tissue damage still needs to be studied. The role of ischaemia in dynamically induced pressure injuries needs to be investigated as well. Lastly, ischaemia-reperfusion is only a secondary factor in DTI development, making it potentially less indicative of pressure-induced muscle damage in general.

9.5.5. Summary of biomarkers for tissue injury

The presented biomarkers only outline the exhaustive list of potential markers for pressure injuries. Their identification and analysis can improve our understanding of the aetiology of DTI, and their measurement is an important step towards effective risk assessment and diagnosis. However, there are four major drawbacks: First, while all biomarkers seem relevant for DTI diagnosis and monitoring, not all are suited for predictive purposes. They represent different levels of severity in tissue damage, have different aetiological origins, and might only be detectable with a long delay. Second, many biomarkers are systemic, making it difficult to differentiate localised DTI from damage elsewhere in the body. Third, high inter-patient variability and potential diurnal changes in biomarker concentrations [466] make repeated sampling and continuous monitoring necessary to detect potential deviations from base level biomarker concentrations. Last, samples for biomarker analysis are inherently difficult to collect. Invasive tissue sampling is ethically questionable and provides only systemic information. Serum and sebum samples on the other hand can be collected non-invasively but are only diffusely related to DTI. New sampling methods like skin blotting or biophysical markers like subepidermal moisture measurement [511] should therefore be explored to combine ease and clinical applicability with full-depth information about soft tissue status.

9.6. Chapter summary

This section has highlighted potential pathways for future research into DTI and prosthetic use. Both areas share the common denominator of mechanical loading of skeletal muscle tissue beyond its restorative capabilities. Loss of sarcolemmal integrity is thereby one of many processes initiated by the physical stress.

So far, FFPE and membrane impermeable fluorescence dyes were used to quantify skeletal muscle damage (s. *Chapter 7* and *8*). The preliminary studies described in this chapter demonstrated that for micro- and mesoscale studies, confocal imaging and Raman microscopy and spectroscopy are promising techniques that, once optimised, can complement the existing experimental approach.

These techniques can also be used to further explore the field of biomarkers. Apart from identifying potential biomarkers, comparing biomarker concentrations after different mechanical loading protocols could provide an insight into the multifaceted

response mechanisms on the microlevel. This may allow us to find new ways to measure and predict muscular damage with a potential to up-scale to clinical studies. In a wider context, biomarkers can not only aid in risk assessment, but also serve as a surrogate to measure the success of an intervention, for example the suitability of different prosthetic socket designs. After all, improving health care for prosthetic users and other groups experiencing abnormal mechanical loads is at the heart of this research.

CHAPTER 10

General Discussion and Conclusion

10.1. Context of research

Prosthetic socket design is a major challenge in the rehabilitation procedure of people with lower limb loss. The main problem is that generally set and agreed upon criteria characterising a good socket fit are missing. However, it is understood that the mechanical load applied via the socket to the residual limb needs to be balanced against the physical stress on the soft tissue to avoid pain and tissue injury [63].

A literature review was conducted as part of this project (*Chapter 2* and *3*). It revealed that although the effect of static loading on the mechanical integrity of skeletal muscle cells is reasonably well understood, the influence of dynamic loading is largely unknown. With this – for prosthetics relevant – information missing, the aim of this thesis was to investigate the influence of prosthesis-related loading on skeletal muscle health, considering both static and dynamic loading scenarios.

Based on the link between tissue injuries and prosthetic use, a mechanobiological approach was followed to relate the mechanical environment during prosthetic use to the biological effects within the soft tissue. The focus was on direct deformation damage as the main aetiological factor for Deep Tissue Injury (DTI). To investigate both the static and dynamic loading response of skeletal muscle, the following objectives were defined:

1) Designing an experimental setup with the potential to quantify cellular damage to skeletal muscle following mechanical loading representative of prosthetic use.
2) Developing a robust microscopic setup and image analysis workflow to quantify sarcolemmal damage within the skeletal muscle model.
3) Replicating the experimental setup in computational models to estimate the loading conditions within the samples.
4) Validating the experimental setup and analysis process for static loading scenarios.
5) Quantifying sarcolemmal damage in skeletal muscle in response to static and dynamic loading.

By starting from the cell and tissue level, the fundamental behaviour of skeletal muscle was assessed on a micro-scale, with the potential to be up-scaled to the meso- and macro-scale and translated into clinical studies.

10.2. Summary of the main findings

10.2.1. *Ex vivo* model is successful method to study direct deformation damage in skeletal muscle after transverse mechanical loading

To perform fundamental mechanobiological research on the cell and tissue level, a suitable model system was needed. For the design of the experimental setup, methods from pressure injury research as well as adjacent areas of exercise-related injury and myopathic research were considered.

First, existing *in vitro*, *in vivo*, and *ex vivo* approaches were identified [224, 225, 512]. After deliberating their advantages and disadvantages, an *ex vivo* approach was most favourable. Skeletal muscle tissue was isolated from Sprague Dawley rats and pinned out in a Petri dish for transverse mechanical loading by indentation. Although auxiliary systems stop functioning after dissection, the nutrient supply can be maintained *in vitro*; superfusion with MOPS buffer kept the samples alive for 3-4h without major damage (s. "*4.5.2 Suitability of skeletal muscle storage in MOPS-based buffer solution*"), even without oxygenation. The suitability of the *ex vivo* model was further supported by the results of a validation study (*Chapter 7*). The static stress-cell death threshold from *in vivo* studies was in good agreement with that of the developed *ex vivo* model, despite the loss of interstitial pressure in *ex vivo* tissue. The *ex vivo* setup is therefore a suitable model to investigate cell death after mechanical loading.

10.2.2. Fluorescence imaging and analysis provides robust, quantitative results on cell death

Optical imaging techniques are widely used to visualise cell death in pressure injury models, exercise-related, and myopathic research. For this project, live-cell staining with propidium iodide, histology with haematoxylin and eosin, and fluorescent staining with the membrane impermeable dyes Procion Yellow MX4R (ProY) and Live-or-Dye were tested. Thereof, cell death was quantified most reliably with fluorescent staining in combination with fixation. ProY was the stain of choice with ProY-positive, dead cells readily distinguishable after mechanical and chemical insults (s. "*4.7.3 Suitability of Procion Yellow to detect cell damage*").

A reoccurring challenge during the analysis of ProY-stained muscles was the high biological variability between the samples, leading to differences in autofluorescence signal intensity between samples. When following analysis methods described in the literature, ProY-positive staining was difficult to detect across samples. After optimising the microscopic settings, additional normalisation methods were therefore introduced to the image analysis workflow, together with background subtraction, segmentation, thresholding, and particle analysis. By integrating these analysis steps into a semi-automated workflow (s. "*5.5.6 Overview over the image analysis* workflow"), consistent results were achieved across mildly, moderately, and heavily damaged samples with minimal risk for bias.

10.2.3. Prolonged loading is more damaging to skeletal muscle tissue than short loading durations under both static and dynamic conditions

The seminal work by Linder-Ganz et al. [34] and Gefen et al. [33] revealed that prolonged and/or high magnitude direct stress and strain are damaging to soft tissues. Accordingly, governing bodies like the National Pressure Injury Advisory Panel define these loading conditions as the main cause for pressure injuries [24]. In agreement, the validation study for the *ex vivo* model developed for this project produced a sigmoid stress-cell death threshold curve when compressing isolated muscle samples statically (s. "*7.4.3 Stress-time cell death threshold for ex vivo skeletal muscle tissue*").

The following dynamic loading study revealed similar tendencies: The cell death count increased significantly when the load was applied for a two-hour period compared to the one-hour group (s. "*8.4.2 Difference in cell death counts between short and long duration loading*"). However, only two time points with identical loading magnitudes were compared. For a conclusion about whether cyclic loading initiates the same sigmoid stress-cell death behaviour as static loading, further experiments are necessary.

10.2.4. Extent of skeletal muscle damage is frequency-dependent with more damage after high-frequency loading compared to low-frequency or static conditions

The results of the dynamic loading study indicated that loading frequency influences cell death rates, in addition to magnitude and duration. Compared with static and low frequency loading with 1.42Hz, high frequency loading at 4Hz produced significantly higher cell death counts at equal external stress magnitude and duration (s. "*8.4.3 Difference in cell death counts between static and dynamic loading*"). Potential explanations are fatigue behaviour, self-heating, changes in mechanical properties of structural cell components, and the activation of biochemical cell-death messengers. Further research will be necessary to explore these theories. Nevertheless, frequency needs to be factored into the existing pressure-cell death threshold for dynamic loading scenarios.

10.3. Contributions to knowledge

This thesis produced several original contributions to the existing research on pressure injury development and tissue damage from prosthetic use. Most notably, the effect of transverse, cyclic compression on cell sarcolemmal damage was documented for the first time and contrasted with the skeletal muscle response to static loading. For this, an *ex vivo* setup for tissue injury research was developed in combination with a semi-automated analysis workflow to quantify cell death in fluorescently stained skeletal muscle tissue.

The foundation of this work lies in the link between pressure injuries and prosthetic use that was established in *Chapter 2*. The conducted scoping review demonstrated that the aetiology and risk factors for DTI development coincide with prosthetic use. Examples are the mechanical environment of the prosthesis-limb-complex, soft tissue changes of the residuum, and co-morbidities commonly found in amputees. Pressure-related DTI is therefore a notable risk for prosthetic users. Accordingly, this thesis highlights the importance of considering deep tissue deformation not only in the ongoing discussions on how to design a prosthetic socket but also for ways to evaluate the fit.

The scoping review also signposted that the current knowledge on the effect of mechanical loading on soft tissue health needs to be expanded to understand

potential impact of prosthetic use on the residual limb. For this, suitable model systems are needed. The evaluation of existing *in vitro* and *in vivo* pressure injury models revealed several shortcomings. Hence, an *ex vivo* approach was adapted, presenting a new method for pressure injury as well as prosthetic research. This improves the comparability of results to related research areas where *ex vivo* models are common practice, like exercise science or myopathies. *Ex vivo* models are also easily adaptable to future research endeavours, like the application of shear forces.

To obtain quantifiable data from the *ex vivo* model, an image acquisition and analysis workflow was developed. Compared with existing protocols on Procion-stained tissue that were difficult to replicate, the developed analysis presents a robust protocol to count ProY-positive cells. A major improvement is the integration of the different analysis steps into a semi-automated workflow, which reduces the risk for bias significantly. Additionally, the workflow can not only be used for ProY-stained tissues but also adapted for other fluorescent stains and dyes that require thresholding to convert images into quantitative data.

With the *ex vivo* model and analysis workflow in place, the effect of dynamic loading on sarcolemmal damage was compared with that of static loading. Up to now, stress or strain cell death threshold were based on static loading conditions [33, 34, 212]. This thesis provides new insights into the effect of dynamic conditions: the frequency of the load application seems to play a crucial role with significantly higher cellular damage in samples compressed with a high frequency of 4Hz compared to a lower frequency of 1.42Hz and static compression.

Accordingly, frequency might be just as important for the development of cellular damage in dynamic loading scenarios as loading magnitude and duration. In turn, frequency should be considered during the design and risk assessment of any dynamic body-device interaction, be it the prosthetic or orthotic system with the (residual) limb, the interaction of diabetic feet with shoes [513], or even that of stents with arterial walls [514]. However, further research is needed to validate the observed relationship and create a wider evidence base.

10.4. Implications of the results for the field of prosthetics

Animal or cell-based studies are not directly relatable to humans [327], yet their results can reveal general tendencies, like potentially harmful loading scenarios at the body-device interface. This thesis confirmed that, even for a short period of time, severe

deformation of soft tissues poses a high risk for cellular damage. Thus, producing a uniform stress and strain distribution throughout a prosthetic socket should be favoured over aggressive rectifications that induce high pressure points. Additionally, prolonged loading of the same type, like standing or walking for long periods, seems to lower the capacity of the soft tissues within the residual limb to withstand deformation damage. It might therefore be advisable to change activities or doff the prosthesis after extended use to avoid tissue injury. Last, activities that induce high-frequency loading like running might be more harmful to tissues than low frequency or static activities like walking or standing. However, the exact tissue response still needs to be explored further before clinical recommendations can be made.

This thesis also revealed a strong link between prosthetic use and deep soft tissue damage at the residual limb in general. It is common practice in prosthetic research to perform interface pressure measurements to understand body-device interactions [128, 364]. However, according to research from the field of pressure injuries [130], internal strain levels are more relevant for tissue damage development than interface pressure. Hence, awareness and understanding for this mechanobiological phenomenon should be raised amongst prosthetists, clinicians, surgeons, and researchers. The dissemination of this thesis through publications and conference presentations marks one step towards this goal and will hopefully guide future research and clinical practice.

Owing to this missing awareness, only few researchers have considered the biological effects of deep tissue deformation when they developed monitoring devices [31, 76, 77], new socket design concepts [403, 515], or FE models of prosthetic use [135]. Even more so, all these studies integrated existing static stress-time-cell death thresholds [33]. However, the results of this thesis indicate that static thresholds are insufficient when describing the dynamic loading environment during locomotion. The conclusions drawn from existing studies might therefore need reconsideration, once a more extensive evidence base is created around dynamic loading scenarios.

10.5. Recommendations for future work

A main result of this thesis is that high-frequency loading appears to be more damaging to skeletal muscle than static or low-frequency loading. However, the underlying mechanisms remain unclear. Different explanations were hypothesised (s.”*8.5.2 Dynamic loading at high frequencies is more damaging to the structural*

integrity of skeletal muscle than static loading"), which could be explored further. Fatigue behaviour for example could be monitored by visualising the cell's structural components, like the cytoskeleton and membrane, and comparing it to computational modelling of fracture formation, like Peridynamics [430, 431]. Once the mechanisms behind dynamic, structural cell failure are understood, potential preventative measures, diagnostic tools, and suitable risk assessment methods can be developed.

In addition to the experiments described in this thesis, further research can widen our knowledgebase on body-device interactions. Different combinations of stress magnitude, loading duration, and frequency could be tested to compile a multi-factorial cell death threshold for dynamic loading scenarios. Further, the effect of cyclic loading with varying magnitudes could be investigated as research indicates that changing magnitudes might increase the metabolic demand as well as alter the structural organisation of cell organelles [170].

Every pressure application at the skin causes tension and shear forces within the underlying tissue [11–13]. In skin for example, an upregulation of inflammatory and hyperaemic biomarkers was noted when pressure and shear were applied in combination, compared to pressure alone [461]. Similarly, shear seems to increase direct deformation damage in myoblasts compared to compression alone [516]. Besides the compressive loads tested in this thesis and other studies [33, 34, 212], tensile and shear forces should therefore be considered in future research.

The *ex vivo* setup described in this thesis also allows to test tissues other than healthy murine skeletal muscle. Risk-group specific characteristics like muscular atrophy, intramuscular fat infiltration [517], or diabetes could be integrated by using different murine strains. Additionally, the methodology could be applied to human skeletal muscle biopsies to obtain comparable data that can aid the translation of the laboratory research to clinically relevant outcomes. It is also possible to adapt the experimental setup proposed in this thesis to an entirely different tissue type like adipose tissue or skin to characterise loading effects of the full soft tissue envelop.

Apart from direct mechanical damage to cells, the vascular and lymphatic system also play an important role in tissue injury. In how far a dynamic load application might hamper or, on the contrary, enhance their function is beyond the scope of this thesis. However, other researchers have designed and conducted studies on both the vascular and lymphatic system [90, 90, 105, 111, 194], which could be expanded by a dynamic loading scenario.

The recommended future work will improve our understanding of the biological effect of body-device interactions. Once a wider evidence base is established, existing prosthetic socket design, amputation surgery procedures, and rehabilitation plans can be reviewed under the premise of the effect of deep tissue deformation.

10.6. Conclusion

Body-device interactions remain the crux of prosthetic rehabilitation. A major drawback is our limited understanding of the biological and physiological effects that prosthetic use has on the residual limb. This thesis sought to shed light onto the soft tissue response to mechanical loading. A main result was that in dynamic loading scenarios, frequency plays an important role in determining the extent of skeletal muscle damage beside the already known factors of magnitude and loading duration. Further research into the response of cells as well as ancillary systems to dynamic loading is therefore strongly advised as a simple translation of static conditions appears to be insufficient.

It also became clear that mechanobiological research methods have great potential when evaluating body-device interactions. Drawing upon techniques from adjacent fields like pressure injury, exercise science, or myopathic research will enhance our understanding of the biological and pathophysiological response of the residual limb to prosthesis-related loading. The vision is that by combining this knowledge with advances in digitalisation, material sciences, and manufacturing, proactive design and monitoring can be implemented into routine rehabilitation procedures to provide a step change in prosthetic care for persons with limb loss. Ultimately, this clinical translation could help to prevent tissue damage not only for prosthetic users but anyone at risk of dynamic pressure injuries.

References

1. University of Salford. Limbless Statistics. A repository for quantitative information on the UK limbless population referred for prosthetic treatment. Annual report 2011 - 2012. U.-U.N.I.f.P.O. Development; 2015.

2. Fajardo-Martos I, Roda O, Zambudio-Periago R, Bueno-Cavanillas A, Hita-Contreras F, Sánchez-Montesinos I. Predicting successful prosthetic rehabilitation in major lower-limb amputation patients: a 15-year retrospective cohort study. Brazilian Journal of Physical Therapy. 2018;22:205–14.

3. Taylor SM, Kalbaugh CA, Blackhurst DW, Hamontree SE, Cull DL, Messich HS, et al. Preoperative clinical factors predict postoperative functional outcomes after major lower limb amputation: An analysis of 553 consecutive patients. Journal of Vascular Surgery. 2005;42:227–34.

4. Diabetes UK. The future of diabetes. 2017.

5. International Diabetes Federation, International Working Group on the Diabetic Foot. Diabetes and foot care. 2005.

6. Chatterji S, Byles J, Cutler D, Seeman T, Verdes E. Health, functioning and disability in older adults – current status and future implications. Lancet. 2015;385:563–75.

7. World Health Organisation. World report on ageing and health. 2015.

8. Walsh NE, Walsh WS. Rehabilitation of landmine victims--the ultimate challenge. Bull World Health Organ. 2003;81:665–70.

9. Anti-Personnel Mine Ban Convention. History and Text. Convention on the Prohibition of the Use, Stockpiing, Production and Transfer of Anti-Personnel Mines and Their Destruction. 2018. https://www.apminebanconvention.org/en/the-convention/history-and-text/. Accessed 13 Jun 2022.

10. International Committee of the Red Cross. Myanmar: Living with the rising risk of landmines and other explosive devices. 2022.

11. Ukraine: Russia Uses Banned Antipersonnel Landmines. Human Rights Watch. 2022. https://www.hrw.org/news/2022/03/29/ukraine-russia-uses-banned-antipersonnel-landmines. Accessed 14 Jun 2022.

12. Ham R (Rosalind). Limb amputation: from aetiology to rehabilitation. 1st ed.. London: Springer; 1991.

13. Tisi PV, Than MM. Type of incision for below knee amputation. Cochrane Database of Systematic Reviews. 2014. https://doi.org/10.1002/14651858.CD003749.pub3.

14. Marshall C, Barakat T, Stansby G. Amputation and rehabilitation. Surgery (Oxford). 2016;34:188–91.

15. Bowker JH, Goldberg B, Poonekar PD. Transtibial Amputation: Surgical Procedures and Immediate Postsurgical Management. In: Atlas of Limb Prosthetics: Surgical, Prosthetic and Rehabilitation Principles. Rosemont, IL: American Academy of Orthopedic Surgeons; 2002.

16. Robinson V, Sansam K, Hirst L, Neumann V. Major lower limb amputation – what, why and how to achieve the best results. Orthopaedics and Trauma. 2010;24:276–85.

17. Devinuwara K, Dworak-Kula A, O'Connor RJ. Rehabilitation and prosthetics post-amputation. Orthopaedics and Trauma. 2018;32:234–40.

18. Fenton K. The human cost of falls. UK Health Security Agency. 2014. https://ukhsa.blog.gov.uk/2014/07/17/the-human-cost-of-falls/. Accessed 14 Jun 2022.

19. Bennett G. The cost of pressure ulcers in the UK. Age and Ageing. 2004;33:230–5.

20. Sanders J. Stump-Socket Interface Conditions. In: Pressure Ulcer Research. Berlin/Heidelberg: Springer-Verlag; 2005. p. 129–47.

21. Morgan SJ, Friedly JL, Amtmann D, Salem R, Hafner BJ. A cross-sectional assessment of factors related to pain intensity and pain interference in lower limb prosthesis users. Arch Phys Med Rehabil. 2017;98:105–13.

22. Paterno L, Ibrahimi M, Gruppioni E, Menciassi A, Ricotti L. Sockets for Limb Prostheses: A Review of Existing Technologies and Open Challenges. IEEE Transactions on Biomedical Engineering. 2018;65:1996–2010.

23. Mak AFT, Zhang M, Boone DA. State-of-the-art research in lower-limb prosthetic biomechanics- socket interface: A review. Journal of Rehabilitation Research and Development. 2001;38:161–74.

24. National Pressure Injury Advisory Panel. NPIAP Pressure Injury Stages. 2016.

25. Bouten CVC, Colin D, Oomens CWJ, editors. Pressure Ulcer Research. Berlin/Heidelberg: Springer-Verlag; 2005.

26. Gefen A, Brienza DM, Cuddigan J, Haesler E, Kottner J. Our contemporary understanding of the aetiology of pressure ulcers/pressure injuries. International Wound Journal. 2022;19:692–704.

27. Linder-Ganz E, Shabshin N, Itzchak Y, Gefen A. Assessment of mechanical conditions in sub-dermal tissues during sitting: A combined experimental-MRI and finite element approach. Journal of Biomechanics. 2007;40:1443–54.

28. Elsner JJ, Gefen A. Is obesity a risk factor for deep tissue injury in patients with spinal cord injury? Journal of Biomechanics. 2008;41:3322–31.

29. Portnoy S, Yizhar Z, Shabshin N, Itzchak Y, Kristal A, Dotan-Marom Y, et al. Internal mechanical conditions in the soft tissues of a residual limb of a trans-tibial amputee. J Biomech. 2008;41:1897–909.

30. Linder-Ganz E, Gefen A. Stress analyses coupled with damage laws to determine biomechanical risk factors for Deep Tissue Injury during sitting. J Biomech Eng. 2009;131.

31. Portnoy S, Siev-Ner I, Yizhar Z, Kristal A, Shabshin N, Gefen A. Surgical and morphological factors that affect internal mechanical loads in soft tissues of the transtibial residuum. Ann Biomed Eng. 2009;37:2583–605.

32. Gefen A, Farid KJ, Shaywitz I. A review of deep tissue injury development, detection, and prevention: shear savvy. Ostomy/wound management. 2013;59:26–35.

33. Gefen A, van Nierop B, Bader DL, Oomens CW. Strain-time cell-death threshold for skeletal muscle in a tissue-engineered model system for deep tissue injury. Journal of Biomechanics. 2008;41:2003–12.

34. Linder-Ganz E, Engelberg S, Scheinowitz M, Gefen A. Pressure–time cell death threshold for albino rat skeletal muscles as related to pressure sore biomechanics. Journal of Biomechanics. 2006;39:2725–32.

35. Committee on Prosthetics Research and Development. The effect of pressure on soft tissues. Washington, D.C.: National Academy of Sciences; 1972.

36. Portnoy S, Yarnitzky G, Yizhar Z, Kristal A, Oppenheim U, Siev-Ner I, et al. Real-time patient-specific finite element analysis of internal stresses in the soft tissues of a residual limb: a new tool for prosthetic fitting. Ann Biomed Eng. 2007;35:120–35.

37. Safari MR, Meier MR. Systematic review of effects of current transtibial prosthetic socket designs--Part 1: qualitative outcomes. Journal of Rehabilitation Research & Development. 2015;52:491–508.

38. Dickinson AS, Steer JW, Worsley PR. Finite element analysis of the amputated lower limb: A systematic review and recommendations. Medical Engineering & Physics. 2017;43:1–18.

39. Graser M, Day S, Buis AWP. Exploring the role of transtibial prosthetic use in deep tissue injury development: a scoping review. BMC Biomedical Engineering. 2020;2:2–18.

40. Ziegler-Graham K, MacKenzie EJ, Ephraim PL, Travison TG, Brookmeyer R. Estimating the Prevalence of Limb Loss in the United States: 2005 to 2050. Archives of Physical Medicine and Rehabilitation. 2008;89:422–9.

41. Information Services Division NHSScotland. The Amputee Statistical Database for the United Kingdom 2004/2005. Edinburgh: National Amputee Statistical Database (NASDAB); 2005.

42. Marshall HM, Jensen MP, Ehde DM, Campbell KM. Pain site and impairment in individuals with amputation pain. Archives of Physical Medicine and Rehabilitation. 2002;83:1116–9.

43. Darnall BD, Ephraim P, Wegener ST, Dillingham T, Pezzin L, Rossbach P, et al. Depressive symptoms and mental health service utilization among persons with limb loss: Results of a national survey. Archives of Physical Medicine and Rehabilitation. 2005;86:650–8.

44. Ephraim PL, Wegener ST, MacKenzie EJ, Dillingham TR, Pezzin LE. Phantom Pain, Residual Limb Pain, and Back Pain in Amputees: Results of a National Survey. Archives of Physical Medicine and Rehabilitation. 2005;86:1910–9.

45. Dudek NL, Marks MB, Marshall SC, Chardon JP. Dermatologic conditions associated with use of a lower-extremity prosthesis. Archives of Physical Medicine and Rehabilitation. 2005;86:659–63.

46. Meulenbelt HE, Geertzen JH, Jonkman MF, Dijkstra PU. Determinants of Skin Problems of the Stump in Lower-Limb Amputees. Archives of Physical Medicine and Rehabilitation. 2009;90:74–81.

47. Colgecen E, Korkmaz M, Ozyurt K, Mermerkaya U, Kader C. A clinical evaluation of skin disorders of lower limb amputation sites. International Journal of Dermatology. 2016;55:468–72.

48. Ehde DM, Czerniecki JM, Smith DG, Campbell KM, Edwards WT, Jensen MP, et al. Chronic phantom sensations, phantom pain, residual limb pain, and other regional pain after lower limb amputation. Archives of Physical Medicine and Rehabilitation. 2000;81:1039–44.

49. Hsu E, Cohen SP. Postamputation pain: epidemiology, mechanisms, and treatment. J Pain Res. 2013;6:121–36.

50. Zheng YP, Mak AF, Leung AK. State-of-the-art methods for geometric and biomechanical assessments of residual limbs: a review. Journal of rehabilitation research & development. 2001;38:487–504.

51. Manucharian SR. An Investigation of Comfort Level Trend Differences Between the Hands-On Patellar Tendon Bearing and Hands-Off Hydrocast Transtibial Prosthetic Sockets. JPO: Journal of Prosthetics and Orthotics. 2011;23:124–40.

52. Guest JF, Ayoub N, McIlwraith T, Uchegbu I, Gerrish A, Weidlich D, et al. Health economic burden that different wound types impose on the UK's National Health Service. International Wound Journal. 2017;14:322–30.

53. Gould LJ, Bohn G, Bryant R, Paine T, Couch K, Cowan L, et al. Pressure ulcer summit 2018: An interdisciplinary approach to improve our understanding of the risk of pressure-induced tissue damage. Wound Repair and Regeneration. 2019. https://doi.org/10.1111/wrr.12730.

54. Bouten CVC, Oomens CW, Baaijens FP, Bader DL. The etiology of pressure ulcers: Skin deep or muscle bound? Archives of Physical Medicine and Rehabilitation. 2003;84:616–9.

55. Black J, Baharestani MM, Cuddigan J, Dorner B, Edsberg L, Langemo D, et al. National Pressure Ulcer Advisory Panel's Updated Pressure Ulcer Staging System. Advances in Skin & Wound Care. 2007;20:269–74.

56. Oomens CWJ, Bader DL, Loerakker S, Baaijens F. Pressure Induced Deep Tissue Injury Explained. Annals of Biomedical Engineering. 2015;43:297–305.

57. Kottner J, Balzer K, Dassen T, Heinze S. Pressure Ulcers: A Critical Review of Definitions and Classifications. Ostomy Wound Manage. 2009;55:22–9.

58. Mak AFT, Zhang M, Tam EWC. Biomechanics of Pressure Ulcer in Body Tissues Interacting with External Forces during Locomotion. Annu Rev Biomed Eng 2010. 2010;12:29–53.

59. Aoi N, Yoshimura K, Kadono T, Nakagami G, Iizuka S, Higashino T, et al. Ultrasound Assessment of Deep Tissue Injury in Pressure Ulcers: Possible Prediction of Pressure Ulcer Progression. Plastic and Reconstructive Surgery. 2009;124:540–50.

60. Berlowitz D, Brienza DM. Are All Pressure Ulcers the Result of Deep Tissue Injury? A Review of the Literature. Ostomy Wound Manage. 2007;53:34–8.

61. Bouten C, Oomens C, Colin D, Bader D. The Aetiopathology of Pressure Ulcers: A Hierarchical Approach. In: Bader DL, Bouten CVC, Colin D, Oomens CWJ, editors. Pressure Ulcer Research. Berlin/Heidelberg: Springer-Verlag; 2005. p. 1–9.

62. Shoham N, Gefen A. Deformations, mechanical strains and stresses across the different hierarchical scales in weight-bearing soft tissues. Journal of Tissue Viability. 2012;21:39–46.

63. Mueller MJ, Maluf KS. Tissue Adaption to Physical Stress: A Proposed “Physical Stress Theory” to Guide Physical Therapist Practice, Education, and Research. Physical Therapy. 2002;82:383–403.

64. Sopher R, Nixon J, Gorecki C, Gefen A. Effects of Intramuscular Fat Infiltration, Scarring, and Spasticity on the Risk for Sitting-Acquired Deep Tissue Injury in Spinal Cord Injury Patients. J Biomech Eng. 2011;133.

65. Lin F, Pandya A, Cichowski A, Modi M, Reprogle B, Lee D, et al. Deep tissue injury rat model for pressure ulcer research on spinal cord injury. Journal of Tissue Viability. 2010;19:67–76.

66. Gefen A. The biomechanics of sitting-acquired pressure ulcers in patients with spinal cord injury or lesions. International Wound Journal. 2007;4:222–31.

67. Bogie K, Bader D. Susceptibility of Spinal Cord-Injured Individuals to Pressure Ulcers. In: Pressure Ulcer Research. Berlin/Heidelberg: Springer-Verlag; 2005. p. 73–88.

68. Linder-Ganz E, Shabshin N, Itzchak Y, Yizhar Z, Siev-Ner I, Gefen A. Strains and stresses in sub-dermal tissues of the buttocks are greater in paraplegics than in healthy during sitting. Journal of Biomechanics. 2008;41:567–80.

69. Black J, Fawcett D, Scott S. Ten top tips: preventing pressure ulcers in the surgical patient. Wounds International. 2014;5:14–8.

70. Tescher AN, Thompson SL, McCormack HE, Bearden BA, Christopherson MW, Mielke CL, et al. A Retrospective, Descriptive Analysis of Hospital-acquired Deep Tissue Injuries. Wound Management & Prevention. 2018;64:30–41.

71. Levac D, Colquhoun H, O'Brien KK. Scoping studies: advancing the methodology. Implementation Science. 2010;5.

72. Arksey H, O'Malley L. Scoping studies: towards a methodological framework. International Journal of Social Research Methodology. 2005;8:19–32.

73. Peters M, Godfrey C, McInerey P, Baldini Soares C, Kahlil H, Parker D. Chapter 11: Scoping reviews. In: Aromataris E, Munn Z, editors. Joanna Briggs Institute Reviewer's Manual. The Joanna Briggs Institute; 2017.

74. Tricco AC, Lillie E, Zarin W, O'Brien KK, Colquhoun H, Levac D, et al. PRISMA Extension for Scoping Reviews (PRISMA-ScR): Checklist and Explanation. Ann Intern Med. 2018;169:467–85.

75. Kosasih JB, Silver-Thorn MB. Sensory changes in adults with unilateral transtibial amputation. Journal of Rehabilitation Research and Development. 1998;35:85–90.

76. Portnoy S, Siev-Ner I, Shabshin N, Kristal A, Yizhar Z, Gefen A. Patient-specific analyses of deep tissue loads post transtibial amputation in residual limbs of multiple prosthetic users. J Biomech. 2009;42:2686–93.

77. Portnoy S, van Haare J, Geers RPJ, Kristal A, Siev-Ner I, Seelen HAM, et al. Real-time subject-specific analyses of dynamic internal tissue loads in the residual limb of transtibial amputees. Med Eng Phys. 2010;32:312–23.

78. Portnoy S, Kristal A, Gefen A, Siev-Ner I. Outdoor dynamic subject-specific evaluation of internal stresses in the residual limb: Hydraulic energy-stored prosthetic foot compared to conventional energy-stored prosthetic feet. Gait & Posture. 2012;35:121–5.

79. Portnoy S, Siev-Ner I, Shabshin N, Gefen A. Effects of sitting postures on risks for deep tissue injury in the residuum of a transtibial prosthetic-user: a biomechanical case study. Comput Methods Biomech Biomed Engin. 2011;14:1009–19.

80. Buis AWP, Guarato F, Law J, Ralston Z, Courtney A. A feasibility study to investigate if there is a correlation between soft tissue deformation and acoustic emission. Can Prosthet Orthot J. 2018. https://doi.org/10.33137/cpoj.v1i1.30354.

81. Portnoy S, Atlas E, Gefen A. Influence of bony prominence sharpness and underlying tissue stiffness on the susceptibility to pressure-related deep tissue injury: Biomechanical computer model studies. L'escarre. 2007;36:4–7.

82. Lenz AL. A synergistic approach to transtibial socket interface mechanics: experiments and modeling [dissertation]. Michigan State University; 2017.

83. Bader DL, Worsley PR, Gefen A. Bioengineering considerations in the prevention of medical device-related pressure ulcers. Clinical Biomechanics. 2019;67:70–7.

84. Henrot P, Stines J, Walter F, Martinet N, Paysant J, Blum A. Imaging of the Painful Lower Limb Stump. RadioGraphics. 2000;20:219–35.

85. Gefen A, Gefen N, Linder-Ganz E, Margulies SS. In Vivo Muscle Stiffening Under Bone Compression Promotes Deep Pressure Sores. Journal of Biomechanical Engineering. 2005;127:512–24.

86. Yang F. Asymptotic solution to axisymmetric indentation of a compressible elastic thin film. Thin Solid Films. 2006;515:2274–83.

87. Gefen A, editor. Bioengineering research of chronic wounds: a multidisciplinary study approach. Berlin: Springer; 2009.

88. Bliss M. Aetiology of pressure sores. Reviews in Clinical Gerontology. 1993;3:379.

89. Sopher R, Nixon J, Gorecki C, Gefen A. Exposure to internal muscle tissue loads under the ischial tuberosities during sitting is elevated at abnormally high or low body mass indices. Journal of Biomechanics. 2010;43:280–6.

90. Loerakker S, Manders E, Strijkers GJ, Nicolay K, Baaijens FPT, Bader DL, et al. The effects of deformation, ischemia, and reperfusion on the development of muscle damage during prolonged loading. Journal of Applied Physiology. 2011;111:1168–77.

91. Loerakker S, Stekelenburg A, Strijkers GJ, Rijpkema JJM, Baaijens FPT, Bader DL, et al. Temporal Effects of Mechanical Loading on Deformation-Induced Damage in Skeletal Muscle Tissue. Ann Biomed Eng. 2010;38:2577–87.

92. Buis AWP, Dumbleton T, Murray KD, McHugh BF, McKay G, Sexton S. Measuring the Daily Stepping Activity of People with Transtibial Amputation Using the ActivPAL™ Activity Monitor. Journal of Prosthetics and Orthotics. 2014;26:43–7.

93. Dou P, Jia X, Suo S, Wang R, Zhang M. Pressure distribution at the stump/socket interface in transtibial amputees during walking on stairs, slope and non-flat road. Clinical Biomechanics. 2006;21:1067–73.

94. Klasson B, Buis AWP. Advanced Prosthetic Science - Prosthetic Socket fit; Implications of basic engineering principles. University of Strathclyde, Glasgow: National Centre for Training and Education in Prosthetics and Orthotics; 2006.

95. Lilja M, Johansson T, Öberg T. Movement of the tibial end in a PTB prosthesis socket: A sagittal X-ray study of the PTB prosthesis. Prosthetics and Orthotics International. 1993;17:21–6.

96. Papaioannou G, Mitrogiannis C, Nianios G, Fiedler G. Assessment of amputee socket–stump–residual bone kinematics during strenuous activities using Dynamic Roentgen Stereogrammetric Analysis. Journal of Biomechanics. 2010;43:871–8.

97. Wounds International. International review: Pressure ulcer prevention: pressure, shear, friction and microclimate in context. A consensus document. London: Wounds International; 2010.

98. Tam EWC, Mak AFT, Evans JH, Chow YYN. Post occlusive hyperaemic effect of tissue under static and dynamic loading conditions [using laser perfusion imager]. In: Biomedical Engineering Towards the Year 2000 and Beyond. IEEE; 1998. p. 2294–6.

99. Tsuji S, Ichioka S, Sekiya N, Nakatsuka T. Analysis of ischemia-reperfusion injury in a microcirculatory model of pressure ulcers. Wound Repair and Regeneration. 2005;13:209–15.

100. Linder-Ganz E, Gefen A. The effects of pressure and shear on capillary closure in the microstructure of skeletal muscles. Annals of Biomedical Engineering. 2007;35:2095–107.

101. Manorama A, Meyer R, Wiseman R, Bush TR. Quantifying the effects of external shear loads on arterial and venous blood flow: Implications for pressure ulcer development. Clinical Biomechanics. 2013;28:574–8.

102. Peirce SM, Skalak TC, Rodeheaver GT. Ischemia-reperfusion injury in chronic pressure ulcer formation: A skin model in the rat. Wound Repair and Regeneration. 2000;8:68–76.

103. Sanders JE, Daly CH, Burgess EM. Clinical measurement of normal and shear stresses on a trans-tibial stump: Characteristics of wave-form shapes during walking. Prosthet Orthot Int. 1993;17:38–48.

104. Goldstein B, Sanders J. Skin response to repetitive mechanical stress: A new experimental model in pig. Archives of Physical Medicine and Rehabilitation. 1998;79:265–72.

105. Gawlitta D, Oomens CWJ, Bader DL, Baaijens FPT, Bouten CVC. Temporal differences in the influence of ischemic factors and deformation on the metabolism of engineered skeletal muscle. Journal of Applied Physiology. 2007;103:464–73.

106. Hagisawa S, Shimada T. Skin Morphology and Its Mechanical Properties Associated with Loading. In: Pressure Ulcer Research. Berlin/Heidelberg: Springer-Verlag; 2005. p. 161–85.

107. Kalogeris T, Baines CP, Krenz M, Korthuis RJ. Cell Biology of Ischemia/Reperfusion Injury. Int Rev Cell Mol Biol. 2012;298:229–317.

108. Margaris KN, Black RA. Modelling the lymphatic system: challenges and opportunities. J R Soc Interface. 2012;9:601–12.

109. Miller GE, Seale J. Lymphatic Clearance during Compressive Loading. Lymphology. 1981;14:161–6.

110. Reddy NP, Cochran GVB, Krouskop TA. Interstitial fluid flow as a factor in decubitus ulcer formation. Journal of Biomechanics. 1981;14:879–81.

111. Gray RJ, Voegeli D, Bader DL. Features of lymphatic dysfunction in compressed skin tissues – Implications in pressure ulcer aetiology. Journal of Tissue Viability. 2016;25:26–31.

112. Yao Y, Da Ong LX, Li X, Wan K, Mak AFT. Effects of Biowastes Released by Mechanically Damaged Muscle Cells on the Propagation of Deep Tissue Injury: A Multiphysics Study. Annals of Biomedical Engineering. 2017;45:761–74.

113. Kasuya A, Sakabe J, Tokura Y. Potential application of in vivo imaging of impaired lymphatic duct to evaluate the severity of pressure ulcer in mouse model. Scientific Reports. 2014;4.

114. Ruocco V, Brunetti G, Puca RV, Ruocco E. The immunocompromised district: a unifying concept for lymphoedematous, herpes-infected and otherwise damaged sites. Journal of the European Academy of Dermatology and Venereology. 2009;23:1364–73.

115. Bouch E, Burns K, Geer E, Fuller M, Rose A, Broomhead P. Guidance for the multi disciplinary team on the management of post operative residuum oedema in lower limb amputees. Bradford: British Association of Chartered Physiotherapists in Amputee Rehabilitation; 2012.

116. Prompers JJ, Jeneson JAL, Drost MR, Oomens CCW, Strijkers GJ, Nicolay K. Dynamic MRS and MRI of skeletal muscle function and biomechanics. NMR in Biomedicine. 2006;19:927–53.

117. Barnay J, Joussain C, Orta C, Tourlonias B, Laroche D, Morard M, et al. Use of near-infrared spectroscopy (NIRS) in the evaluation of tissular oxygenation of under knee limb amputation from arteriopathy. Ann Phys Rehabil Med. 2014;57 Suppl 1:120.

118. Ferrari M, Muthalib M, Quaresima V. The use of near-infrared spectroscopy in understanding skeletal muscle physiology: recent developments. Philosophical Transactions of the Royal Society A: Mathematical, Physical and Engineering Sciences. 2011;369:4577–90.

119. Ertl J. Über Amputationsstümpfe. Der Chirurg. 1949;20:218–24.

120. Brückner L. A standardised trans-tibial amputation method following chronic occlusive arterial disease. 1992.

121. Burgess EM. The management of lower-extremity amputations: surgery, immediate postsurgical prosthetic fitting, patient care. Washington: Prosthetic and Sensory Aids Service, Veterans Administration; 1969.

122. Lilja M, Hoffmann P, Öberg T. Morphological changes during early trans-tibial prosthetic fitting. Prosthet Orthot Int. 1998;22:115–22.

123. Vocke AK, Schmid A. Osseous overgrowth after post-traumatic amputation of the lower extremity in childhood. Arch Orthop Trauma Surg. 2000;120:452–4.

124. Lineham B, Harwood P, Giannoudis P. Case study: Correction of angular deformity post-trans-tibial amputation to improve prosthesis fit and comfort. Prosthet Orthot Int. 2015;39:157–60.

125. Stewart CPU. Synopsis of Causation Lower Limb Amputation. United Kongdom: Ministry of Defence; 2008.

126. Marino M, Pattni S, Greenberg M, Miller A, Hocker E, Ritter S, et al. Access to prosthetic devices in developing countries: Pathways and challenges. In: 2015 IEEE Global Humanitarian Technology Conference (GHTC). 2015. p. 45–51.

127. Eide AH, Øderud T. Assistive Technology in Low-Income Countries. In: Disability & International Development. New York, NY: Springer US; 2009. p. 149–60.

128. Al-Fakih EA, Abu Osman NA, Mahmad Adikan FR. Techniques for Interface Stress Measurements within Prosthetic Sockets of Transtibial Amputees: A Review of the Past 50 Years of Research. Sensors. 2016;16:1119.

129. Oomens C, Bressers O, Bosboom E, Bouten C, Bader D. Can loaded interface characteristics influence strain distributions in muscle adjacent to bony prominences? Comput Methods Biomech Biomed Engin. 2003;6:171–80.

130. Oomens CWJ, Loerakker S, Bader DL. The importance of internal strain as opposed to interface pressure in the prevention of pressure related deep tissue injury. Journal of Tissue Viability. 2010;19:35–42.

131. Aritan S, Oyadiji SO, Bartlett RM. The in vivo mechanical properties of muscular bulk tissue. In: Annual International Conference of the IEEE Engineering in Medicine and Biology Society. Minneapolis: IEEE; 2009. p. 5259–62.

132. Robi K, Jakob N, Matevz K, Matjaz V. The Physiology of Sports Injuries and Repair Processes. In: Hamlin M, editor. Current Issues in Sports and Exercise Medicine. InTech; 2013.

133. Linder-Ganz E, Gefen A. Mechanical compression-induced pressure sores in rat hindlimb: muscle stiffness, histology, and computational models. Journal of Applied Physiology. 2004;96:2034–49.

134. Lacroix D, Ramírez Patiño JF. Finite Element Analysis of Donning Procedure of a Prosthetic Transfemoral Socket. Ann Biomed Eng. 2011;39:2972–83.

135. Ramasamy E, Okan A, Dorow B, Chong S-Y, Gizzi L, Steidle G, et al. An Efficient Modelling-Simulation-Analysis Workflow to Investigate Stump-Socket Interaction Using Patient-Specific, Three-Dimensional, Continuum-Mechanical, Finite Element Residual Limb Models. Frontiers in Bioengineering and Biotechnology. 2018;6:1–17.

136. Bader DL, Worsley PR. Technologies to monitor the health of loaded skin tissues. BioMedical Engineering OnLine. 2018;17.

137. Strijkers GJ, Araujo ECA, Azzabou N, Bendahan D, Blamire A, Burakiewicz J, et al. Exploration of New Contrasts, Targets, and MR Imaging and Spectroscopy

Techniques for Neuromuscular Disease – A Workshop Report of Working Group 3 of the Biomedicine and Molecular Biosciences COST Action BM1304 MYO-MRI. Journal of Neuromuscular Diseases. 2019;6:1–30.

138. Nelissen JL, de Graaf L, Traa WA, Schreurs TJL, Moerman KM, Nederveen AJ, et al. A MRI-Compatible Combined Mechanical Loading and MR Elastography Setup to Study Deformation-Induced Skeletal Muscle Damage in Rats. PLOS ONE. 2017;12.

139. Sigrist RMS, Liau J, Kaffas AE, Chammas MC, Willmann JK. Ultrasound Elastography: Review of Techniques and Clinical Applications. Theranostics. 2017;7:1303–29.

140. Ceelen KK, Stekelenburg A, Mulders JLJ, Strijkers GJ, Baaijens FPT, Nicolay K, et al. Validation of a Numerical Model of Skeletal Muscle Compression With MR Tagging: A Contribution to Pressure Ulcer Research. J Biomech Eng. 2008;130:061015.

141. Gefen A, Cornelissen LH, Gawlitta D, Bader DL, Oomens CWJ. The free diffusion of macromolecules in tissue-engineered skeletal muscle subjected to large compression strains. Journal of Biomechanics. 2008;41:845–53.

142. Sekino M, Kaneko A, Ueno S. Mapping of strain-induced diffusivity changes in biological tissues using magnetic resonance. IEEE Transactions on Magnetics. 2005;41:4176–8.

143. Kottner J, Sigaudo-Roussel D, Cuddigan J. From bed sores to skin failure: Linguistic and conceptual confusion in the field of skin and tissue integrity. International Journal of Nursing Studies. 2019;92:58–9.

144. Ousey K, Schoonhoven L, Moore Z, Fletcher J. Should the EPUAP adopt the NPUAP's new pressure ulcer terminology and definitions? Wounds UK. 2017;13:8–14.

145. Li D, Wang Y. Chapter 14 - Mechanobiology, tissue development, and tissue engineering. In: Lanza R, Langer R, Vacanti JP, Atala A, editors. Principles of Tissue Engineering (Fifth Edition). Academic Press; 2020. p. 237–56.

146. Martini F. Fundamentals of anatomy & physiology. 10th edition. Harlow, Essex: Pearson; 2014.

147. Abmayr SM, Pavlath GK. Myoblast fusion: lessons from flies and mice. Development. 2012;139:641–56.

148. Encyclopaedia Britannica. Skeletal muscle. Encyclopaedia Britannica. 2015. https://www.britannica.com/science/skeletal-muscle. Accessed 12 Oct 2022.

149. Cadot B, Gache V, Gomes ER. Moving and positioning the nucleus in skeletal muscle – one step at a time. Nucleus. 2015;6:373–81.

150. Yin H, Price F, Rudnicki MA. Satellite Cells and the Muscle Stem Cell Niche. Physiol Rev. 2013;93:23–67.

151. Sanger JW, Wang J, Fan Y, White J, Sanger JM. Assembly and Dynamics of Myofibrils. J Biomed Biotechnol. 2010;2010.

152. Scott W, Stevens J, Binder–Macleod SA. Human Skeletal Muscle Fiber Type Classifications. Physical Therapy. 2001;81:1810–6.

153. Biga LM, Dawson S, Harwell A, Hopkins R, Kaufmann J, LeMaster M, et al. 10.5 Types of Muscle Fibers. In: Anatomy & Physiology. OpenStax/Oregon State University; 2019.

154. Bouten CVC, Knight MM, Lee DA, Bader DL. Compressive Deformation and Damage of Muscle Cell Subpopulations in a Model System. Annals of Biomedical Engineering. 2001;29:153–63.

155. Slomka N, Or-Tzadikario S, Sassun D, Gefen A. Membrane-Stretch-Induced Cell Death in Deep Tissue Injury: Computer Model Studies. Cellular and Molecular Bioengineering. 2009;2:118–32.

156. Slomka N, Gefen A. Relationship between strain levels and permeability of the plasma membrane in statically stretched myoblasts. Annals of Biomedical Engineering. 2012;40:606–18.

157. Peeters EAG, Oomens CWJ, Bouten CVC, Bader DL, Baaijens FPT. Mechanical and failure properties of single attached cells under compression. Journal of Biomechanics. 2005;38:1685–93.

158. Allen DG, Whitehead NP, Yeung EW. Mechanisms of stretch-induced muscle damage in normal and dystrophic muscle: role of ionic changes. The Journal of Physiology. 2005;567:723–35.

159. Bansal D, Miyake K, Vogel SS, Groh S, Chen C-C, Williamson R, et al. Defective membrane repair in dysferlin-deficient muscular dystrophy. Nature. 2003;423:168–72.

160. Clarke MSF, Khakee R, McNeil PL. Loss of cytoplasmic basic fibroblast growth factor from physiologically wounded myofibers of normal and dystrophic muscle. Journal of Cell Science. 1993;106:121–33.

161. McNeil PL, Steinhardt RA. Plasma Membrane Disruption: Repair, Prevention, Adaptation. Annual Review of Cell and Developmental Biology. 2003;19:697–731.

162. McNeil PL, Terasaki M. Coping with the inevitable: how cells repair a torn surface membrane. Nature Cell Biology. 2001;3:124–9.

163. Miyake K. Vesicle accumulation and exocytosis at sites of plasma membrane disruption. The Journal of Cell Biology. 1995;131:1737–45.

164. Steinhardt RA, Bi G, Alderton JM. Cell Membrane Resealing by a Vesicular Mechanism Similar to Neurotransmitter Release. Science. 1994;263:390–3.

165. Stevens A, Lowe JS, Scott I. Cell injury and death. In: Core Pathology. 3rd edition. Mosby/Elsevier; 2008. p. 19–34.

166. Deprez J-F, Brusseau E, Fromageau J, Cloutier G, Basset O. On the potential of ultrasound elastography for pressure ulcer early detection. Med Phys. 2011;38:1943–50.

167. Quintavalle PR, Lyder CH, Mertz PJ, Phillips-Jones C, Dyson M. Use of High-Resolution, High-Frequency Diagnostic Ultrasound to Investigate the Pathogenesis of Pressure Ulcer Development. Advances in Skin & Wound Care. 2006;19:498–505.

168. Dao TT, Tho M-CHB. A Systematic Review of Continuum Modeling of Skeletal Muscles: Current Trends, Limitations, and Recommendations. Applied Bionics and Biomechanics. 2018;2018:e7631818. https://www.hindawi.com/journals/abb/2018/7631818/. Accessed 11 Jan 2021.

169. Nagel T, Loerakker S, Oomens CWJ. A theoretical model to study the effects of cellular stiffening on the damage evolution in deep tissue injury. Computer Methods in Biomechanics and Biomedical Engineering. 2009;12:585–97.

170. Bartolák-Suki E, Imsirovic J, Parameswaran H, Wellman TJ, Martinez N, Allen PG, et al. Fluctuation-driven mechanotransduction regulates mitochondrial-network structure and function. Nature Materials. 2015;14:1049–57.

171. Bosboom EMH, Hesselink MKC, Oomens CWJ, Bouten CVC, Drost MR, Baaijens FPT. Passive transverse mechanical properties of skeletal muscle under in vivo compression. Journal of Biomechanics. 2001;34:1365–8.

172. Maas SA, Ellis BJ, Ateshian GA, Weiss JA. FEBio: Finite Elements for Biomechanics. J Biomech Eng. 2012;134:11005_1-11005_10.

173. Radcliff CW, Foort J. The patellar-tendon-bearing below-knee prosthesis. Berkeley: Biomechanics Laboratory, Dept. of Engineering, University of California; 1961.

174. Lee WC, Zhang M, Mak AF. Regional differences in pain threshold and tolerance of the transtibial residual limb: Including the effects of age and interface material. Archives of Physical Medicine and Rehabilitation. 2005;86:641–9.

175. Hsu C-H, Ou C-H, Hong W-L, Gao Y-H. Comfort level discussion for prosthetic sockets with different fabricating processing conditions. Biomed Eng Online. 2018;17 Suppl 2.

176. Wu C, Chang C, Hsu A, Lin C, Chen S, Chang G. A proposal for the pre-evaluation protocol of below-knee socket design - integration pain tolerance with finite element analysis. Journal of the Chinese Institute of Engineers. 2003;26:853–60.

177. Ogawa A, Obinata G, Hase K, Dutta A, Nakagawa M. Design of lower limb prosthesis with contact pressure adjustment by MR fluid. In: 2008 30th Annual International Conference of the IEEE Engineering in Medicine and Biology Society. 2008. p. 330–3.

178. Safari MR, Tafti N, Aminian G. Socket Interface Pressure and Amputee Reported Outcomes for Comfortable and Uncomfortable Conditions of Patellar Tendon Bearing Socket: A Pilot Study. Assistive Technology. 2015;27:24–31.

179. Neumann ES. Measurement of Socket Discomfort—Part I: Pressure Sensation. JPO: Journal of Prosthetics and Orthotics. 2001;13:99–110.

180. Katz K, Suska Z, Seliktar R, Najenson T. End-bearing characteristics of patellar-tendon-bearing prostheses - a preliminary report. Bulletin of Prosthetics Research. 1979;16:55–68.

181. Lee WCC, Zhang M. Using computational simulation to aid in the prediction of socket fit: A preliminary study. Medical Engineering & Physics. 2007;29:923–9.

182. Seo J-H, Lee H-J, Seo D-W, Lee D-K, Kwon O-W, Kwak M-K, et al. A Prosthetic Socket with Active Volume Compensation for Amputated Lower Limb. Sensors (Basel). 2021;21.

183. Dakhil N, Evin M, Llari M, Mo F, Thefenne L, Liu T, et al. Is skin pressure a relevant factor for socket assessment in patients with lower limb amputation? Technology and Health Care. 2019;27:669–77.

184. Kazamel M, Dyck PJ. Sensory manifestations of diabetic neuropathies: Anatomical and clinical correlations. Prosthet Orthot Int. 2015;39:7–16.

185. Groth K-E. Clinical observations and experimental studies of the pathogenesis of decubitus ulcers. Acta Chir Scand. 1942;87 76 (Suppl.):1–209.

186. Husain T. An experimental study of some pressure effects on tissues, with reference to the bed-sore problem. The Journal of Pathology and Bacteriology. 1953;66:347–58.

187. Kosiak M. Etiology of decubitus ulcers. Archives of physical medicine and rehabilitation. 1961;42:19–29.

188. Reswick JB, Rogers JE. Experience at Rancho Los Amigos Hospital With Devices and Techniques to Prevent Pressure Sores. In: Kenedi RM, Cowden JM, editors. Bed Sore Biomechanics: Proceedings of a seminar on Tissue Viability and Clinical Applications organised in association with the Department of Biomedical Engineering, the Institute of Orthopaedics (University of London), Royal National Orthopaedic Hospital, Stanmore, London, and held at the University of Strathclyde, Glasgow, in August, 1975. London: Macmillan Education UK; 1976. p. 301–10.

189. Gefen A. Reswick and Rogers pressure-time curve for pressure ulcer risk. Part 1. Nursing Standard. 2009;23:64–74.

190. Peeters EA, G, Bouten CV, C, Oomens CW, J, et al. Anisotropic, Three-Dimensional Deformation of Single Attached Cells Under Compression. Annals of Biomedical Engineering; New York. 2004;32:1443–52.

191. Peeters EA, G, Bouten CV, C, Oomens CW, J, et al. Monitoring the biomechanical response of individual cells under compression: A new compression

device. Medical and Biological Engineering and Computing; Heidelberg. 2003;41:498–503.

192. Wang Y-N, Bouten CVC, Lee DA, Bader DL. Compression-induced damage in a muscle cell model *in vitro*. Proceedings of the Institution of Mechanical Engineers, Part H: Journal of Engineering in Medicine. 2005;219:1–12.

193. Breuls RG, M, Bouten CV, C, Oomens CW, J, et al. Compression Induced Cell Damage in Engineered Muscle Tissue: An In Vitro Model to Study Pressure Ulcer Aetiology. Annals of Biomedical Engineering; New York. 2003;31:1357–64.

194. Gawlitta D, Li W, Oomens CWJ, Baaijens FPT, Bader DL, Bouten CVC. The Relative Contributions of Compression and Hypoxia to Development of Muscle Tissue Damage: An In Vitro Study. Ann Biomed Eng. 2007;35:273–84.

195. Bosboom EMH, Bouten CVC, Oomens CWJ, van Straaten HWM, Baaijens FPT, Kuipers H. Quantification and localisation of damage in rat muscles after controlled loading; a new approach to study the aetiology of pressure sores. Medical Engineering & Physics. 2001;23:195–200.

196. Stekelenburg A, Oomens CWJ, Strijkers GJ, Nicolay K, Bader DL. Compression-induced deep tissue injury examined with magnetic resonance imaging and histology. Journal of Applied Physiology. 2006;100:1946–54.

197. Stekelenburg A, Strijkers G, Parusel H, Bader D. Role of ischemia and deformation in the onset of compression-induced deep tissue injury: MRI-based studies in a rat model. Journal of Applied Physiology. 2007;102:2002–11.

198. Ceelen KK, Stekelenburg A, Loerakker S, Strijkers GJ, Bader DL, Nicolay K, et al. Compression-induced damage and internal tissue strains are related. Journal of Biomechanics. 2008;41:3399–404.

199. Traa WA, van Turnhout MC, Nelissen JL, Strijkers GJ, Bader DL, Oomens CWJ. There is an individual tolerance to mechanical loading in compression induced deep tissue injury. Clinical Biomechanics. 2019;63:153–60.

200. Birke JA, Patout CA, Foto JG. Factors Associated With Ulceration and Amputation in the Neuropathic Foot. Journal of Orthopaedic & Sports Physical Therapy. 2000;30:91–7.

201. Guyton GP, Saltzman CL. The diabetic foot: Basic mechanisms of the disease. Journal of Bone and Joint Surgery, American volume; Needham. 2001;83:1083–96.

202. Gefen A. Plantar soft tissue loading under the medial metatarsals in the standing diabetic foot. Medical Engineering & Physics. 2003;25:491–9.

203. Gefen A. The biomechanics of heel ulcers. Journal of Tissue Viability. 2010;19:124–31.

204. Liu J, Zou L, Zheng Y, Zhao Z, Li Y, Yang P, et al. NF-κB responds to mechanical strains in osteoblast-like cells, and lighter strains create an NF-κB response more readily. Cell Biology International. 2007;31:1220–4.

205. Yao Y, Mak AF. Strengthening of C2C12 mouse myoblasts against compression damage by mild cyclic compressive stimulation. Journal of Biomechanics; Kidlington. 2016;49:3956–61.

206. Gaskell P, Krisman AM. Critical Closing Pressure of Vessels Supplying the Capillary Loops of the Nailfold. Circulation Research. 1958;6:461–7.

207. Landis EM. Microinjection studies of capillary blood pressure in human skin. Heart. 1930;15:209–28.

208. Salcido R, Lee A, Ahn C. Heel Pressure Ulcers: Purple Heel and Deep Tissue Injury. Advances in Skin & Wound Care. 2011;24:374–80.

209. Barnett RI, Ablarde JA. Skin vascular reaction to standard patient positioning on a hospital mattress. Adv Wound Care. 1994;7:58–65.

210. Shilo M, Gefen A. Identification of capillary blood pressure levels at which capillary collapse is likely in a tissue subjected to large compressive and shear deformations. Computer Methods in Biomechanics and Biomedical Engineering. 2012;15:59–71.

211. Bosboom EMH, Bouten CVC, Oomens CWJ, Baaijens FPT, Nicolay K. Quantifying pressure sore-related muscle damage using high-resolution MRI. Journal of Applied Physiology. 2003;95:2235–40.

212. Yao Y, Xiao Z, Wong S, Hsu Y-C, Cheng T, Chang C-C, et al. The Effects of Oxidative Stress on the Compressive Damage Thresholds of C2C12 Mouse Myoblasts: Implications for Deep Tissue Injury. Annals of Biomedical Engineering. 2015;43:287–96.

213. Knight SL, Taylor RP, Polliack AA, Bader DL. Establishing predictive indicators for the status of loaded soft tissues. Journal of Applied Physiology. 2001;90:2231–7.

214. Bramley JL, Worsley PR, Bostan LE, Bader DL, Dickinson AS. Establishing a measurement array to assess tissue tolerance during loading representative of prosthetic use. Medical Engineering & Physics. 2020;78:39–47.

215. Traa WA, Strijkers GJ, Bader DL, Oomens CWJ. Myoglobin and troponin concentrations are increased in early stage deep tissue injury. Journal of the Mechanical Behavior of Biomedical Materials. 2019;92:50–7.

216. Hagblad J, Lindberg L-G, Kaisdotter Andersson A, Bergstrand S, Lindgren M, Ek A-C, et al. A technique based on laser Doppler flowmetry and photoplethysmography for simultaneously monitoring blood flow at different tissue depths. Med Biol Eng Comput. 2010;48:415–22.

217. Stekelenburg A, Gawlitta D, Bader DL, Oomens CW. Deep Tissue Injury: How Deep is Our Understanding? Archives of Physical Medicine and Rehabilitation. 2008;89:1410–3.

218. Peeters EAG, Oomens CWJ, Bouten CVC, Bader DL, Baaijens FPT. Viscoelastic Properties of Single Attached Cells Under Compression. J Biomech Eng. 2005;127:237–43.

219. Wu Y, van der Schaft DWJ, Baaijens FP, Oomens CWJ. Cell death induced by mechanical compression on engineered muscle results from a gradual physiological mechanism. Journal of Biomechanics. 2016;49:1071–7.

220. van der Schaft DWJ, van Spreeuwel ACC, Boonen KJM, Langelaan MLP, Bouten CVC, Baaijens FPT. Engineering Skeletal Muscle Tissues from Murine Myoblast Progenitor Cells and Application of Electrical Stimulation. J Vis Exp. 2013;73:e4267.

221. Langelaan MLP, Boonen KJM, Rosaria-Chak KY, Schaft DWJ van der, Post MJ, Baaijens FPT. Advanced maturation by electrical stimulation: Differences in response between C2C12 and primary muscle progenitor cells. Journal of Tissue Engineering and Regenerative Medicine. 2011;5:529–39.

222. Dennis RG, Kosnik PE, Gilbert ME, Faulkner JA. Excitability and contractility of skeletal muscle engineered from primary cultures and cell lines. American Journal of Physiology-Cell Physiology. 2001;280:288–95.

223. Kawamoto Y, Nakajima Y, Kuranaga E. Apoptosis in Cellular Society: Communication between Apoptotic Cells and Their Neighbors. Int J Mol Sci. 2016;17.

224. Salcido R, Popescu A, Ahn C. Animal Models In Pressure Ulcer Research. The Journal of Spinal Cord Medicine. 2007;30:107–16.

225. Gawlitta D, Bouten C. In Vitro Muscle Model Studies. In: Pressure Ulcer Research. Berlin/Heidelberg: Springer-Verlag; 2005. p. 287–300.

226. Stekelenburg A, Oomens C, Bader D. Compression-Induced Tissue Damage: Animal Models. In: Pressure Ulcer Research. Berlin/Heidelberg: Springer-Verlag; 2005. p. 187–204.

227. Hashimoto M, Kurose T, Kawamata S. Comparison between a weight compression and a magnet compression for experimental pressure ulcers in the rat. Histological studies and effects of anesthesia. Arch Histol Cytol. 2008;71:303–16.

228. Moorwood C, Liu M, Tian Z, Barton ER. Isometric and Eccentric Force Generation Assessment of Skeletal Muscles Isolated from Murine Models of Muscular Dystrophies. J Vis Exp. 2013;:e50036.

229. Howl JD, Publicover SJ. Permeabilisation of the sarcolemma in mouse diaphragm exposed to Bay K 8644 in vitro: time course, dependence on Ca2+ and effects of enzyme inhibitors. Acta Neuropathol. 1990;79:438–43.

230. Ferry CB, Cullen MJ. Myopathic changes in indirectly stimulated mouse diaphragm after ecothiopate in vitro. Int J Exp Pathol. 1991;72:329–43.

231. Bannister NJ, Publicover SJ. Immediate and delayed effects of a brief period of calcium loading, induced by the calcium channel agonist Bayer K 8644, on the ultrastructure and sarcolemmal integrity of murine diaphragm in vitro. Acta Neuropathol. 1993;86.

232. Lynch GS, Fary CJ, Williams DA. Quantitative measurement of resting skeletal muscle [Ca2+]i following acute and long-term downhill running exercise in mice. Cell Calcium. 1997;22:373–83.

233. Yeung EW, Bourreau J-P, Allen DG, Ballard HJ. Effect of eccentric contraction-induced injury on force and intracellular pH in rat skeletal muscles. Journal of Applied Physiology. 2002;92:93–9.

234. McBride TA, Stockert BW, Gorin FA, Carlsen RC. Stretch-activated ion channels contribute to membrane depolarization after eccentric contractions. Journal of Applied Physiology. 2000;88:91–101.

235. Balnave CD, Allen DG. Intracellular calcium and force in single mouse muscle fibres following repeated contractions with stretch. The Journal of Physiology. 1995;488:25–36.

236. Blaisdell FW. The pathophysiology of skeletal muscle ischemia and the reperfusion syndrome: a review. Cardiovasc Surg. 2002;10:620–30.

237. Brooks JW. Postmortem Changes in Animal Carcasses and Estimation of the Postmortem Interval. Veterinary Pathology. 2016;53:929–40.

238. Van Ee CA. Quantifying Skeletal Muscle Properties in Cadaveric Test Specimens: Effects of Mechanical Loading, Postmortem Time, and Freezer Storage. Journal of Biomechanical Engineering. 1999;122:9–14.

239. Van Loocke M, Lyons CG, Simms CK. A validated model of passive muscle in compression. Journal of Biomechanics. 2006;39:2999–3009.

240. Heinrichs A. Stains and fluorescent dyes. Nat Cell Biol. 2009;11:7.

241. Hammers DW, Merritt EK, Matheny W, Adamo ML, Walters TJ, Estep JS, et al. Functional deficits and insulin-like growth factor-I gene expression following tourniquet-induced injury of skeletal muscle in young and old rats. J Appl Physiol (1985). 2008;105:1274–81.

242. Gosker HR, Kubat B, Schaart G, van der Vusse GJ, Wouters EFM, Schols AMWJ. Myopathological features in skeletal muscle of patients with chronic obstructive pulmonary disease. European Respiratory Journal. 2003;22:280–5.

243. Ceelen KK, Oomens CWJ, Stekelenburg A, Bader DL, Baaijens FPT. Changes in Intracellular Calcium during Compression of C2C12 Myotubes. Experimental Mechanics. 2009;49:25–33.

244. Schindelin J, Arganda-Carreras I, Frise E, Kaynig V, Longair M, Pietzsch T, et al. Fiji: an open-source platform for biological-image analysis. Nat Methods. 2012;9:676–82.

245. Carpenter AE, Jones TR, Lamprecht MR, Clarke C, Kang IH, Friman O, et al. CellProfiler: image analysis software for identifying and quantifying cell phenotypes. Genome Biology. 2006;7:R100.

246. Haustein E, Schwille P. Trends in fluorescence imaging and related techniques to unravel biological information. HFSP Journal. 2007;1:169–80.

247. Sanderson MJ, Smith I, Parker I, Bootman MD. Fluorescence Microscopy. Cold Spring Harb Protoc. 2014;2014:pdb.top071795.

248. Conchello J-A, Lichtman JW. Optical sectioning microscopy. Nature Methods; New York. 2005;2:920–31.

249. Engelbrecht L, Ollewagen T, de Swardt D. Advances in fluorescence microscopy can reveal important new aspects of tissue regeneration. Biochimie. 2022;196:194–202.

250. Danial JSH, Aguib Y, Yacoub MH. Advanced fluorescence microscopy techniques for the life sciences. Glob Cardiol Sci Pract. 2016;2016:e201616.

251. Larson AM. Multiphoton microscopy. Nature Photon. 2011;5.

252. Borile G, Sandrin D, Filippi A, Anderson KI, Romanato F. Label-Free Multiphoton Microscopy: Much More Than Fancy Images. IJMS. 2021;22:2657.

253. Rehberg M, Krombach F, Pohl U, Dietzel S. Label-Free 3D Visualization of Cellular and Tissue Structures in Intact Muscle with Second and Third Harmonic Generation Microscopy. PLoS One. 2011;6:e28237.

254. Caorsi V, Toepfer C, Sikkel MB, Lyon AR, MacLeod K, Ferenczi MA. Non-Linear Optical Microscopy Sheds Light on Cardiovascular Disease. PLOS ONE. 2013;8:e56136.

255. Monici M. Cell and tissue autofluorescence research and diagnostic applications. In: Biotechnology Annual Review. Elsevier; 2005. p. 227–56.

256. Jackson KA, Snyder DS, Goodell MA. Skeletal Muscle Fiber-Specific Green Autofluorescence: Potential for Stem Cell Engraftment Artifacts. Stem Cells. 2004;22:180–7.

257. Baschong W, Suetterlin R, Laeng RH. Control of Autofluorescence of Archival Formaldehyde-fixed, Paraffin-embedded Tissue in Confocal Laser Scanning Microscopy (CLSM). J Histochem Cytochem. 2001;49:1565–71.

258. Oliveira VC, Carrara RCV, Simoes DLC, Saggioro FP, Carlotti CG, Covas DT, et al. Sudan Black B treatment reduces autofluorescence and improves resolution of in situ hybridization specific fluorescent signals of brain sections. Histol Histopathol. 2010;25:1017–24.

259. Schnell SA, Staines WA, Wessendorf MW. Reduction of Lipofuscin-like Autofluorescence in Fluorescently Labeled Tissue. J Histochem Cytochem. 1999;47:719–30.

260. Bradley WG, Fulthorpe JJ. Studies of sarcolemmal integrity in myopathic muscle. Neurology. 1978;28:670–670.

261. Echeverría OM, Vázquez-Nin GH, Ninomiya JG. Structural Alterations and Changes in the Distribution of Markers in Transected Skeletal Muscle Fibers of the Guinea Pig. CTO. 1983;116:358–65.

262. Whitehead NP, Streamer M, Lusambili LI, Sachs F, Allen DG. Streptomycin reduces stretch-induced membrane permeability in muscles from mdx mice. Neuromuscular Disorders. 2006;16:845–54.

263. Horn A, Meulen JHV der, Defour A, Hogarth M, Sreetama SC, Reed A, et al. Mitochondrial redox signaling enables repair of injured skeletal muscle cells. Sci Signal. 2017;10.

264. Sreetama SC, Chandra G, Van der Meulen JH, Ahmad MM, Suzuki P, Bhuvanendran S, et al. Membrane Stabilization by Modified Steroid Offers a Potential Therapy for Muscular Dystrophy Due to Dysferlin Deficit. Molecular Therapy. 2018;26:2231–42.

265. Vila MC, Rayavarapu S, Hogarth MW, Van der Meulen JH, Horn A, Defour A, et al. Mitochondria mediate cell membrane repair and contribute to Duchenne muscular dystrophy. Cell Death Differ. 2017;24:330–42.

266. Palacio J, Gāldiz JB, Alvarez FJ, Orozco-Levi M, Lloreta J, Gea J. Procion orange tracer dye technique vs. identification of intrafibrillar fibronectin in the assessment of sarcolemmal damage. European Journal of Clinical Investigation. 2002;32:443–7.

267. Petrof BJ, Shrager JB, Stedman HH, Kelly AM, Sweeney HL. Dystrophin protects the sarcolemma from stresses developed during muscle contraction. Proceedings of the National Academy of Sciences. 1993;90:3710–4.

268. Billin AN, Honeycutt SE, McDougal AV, Kerr JP, Chen Z, Freudenberg JM, et al. HIF prolyl hydroxylase inhibition protects skeletal muscle from eccentric contraction-induced injury. Skeletal Muscle. 2018;8:35.

269. Oprescu SN, Yue F, Kuang S. Single-Cell Isolation from Regenerating Murine Muscles for RNA-Sequencing Analysis. STAR Protocols. 2020;1.

270. Maeshige N, Langston PK, Yuan Z-M, Kondo H, Fujino H. High-intensity ultrasound irradiation promotes the release of extracellular vesicles from C2C12 myotubes. Ultrasonics. 2021;110.

271. Hamer PW, McGeachie JM, Davies MJ, Grounds MD. Evans BlackwellScienceLtd Blue Dye as an in vivo marker of myofibre damage: optimising parameters for detecting initial myofibre membrane permeability. 2002;:11.

272. Wooddell CI, Zhang G, Griffin JB, Hegge JO, Huss T, Wolff JA. Use of evans blue dye to compare limb muscles in exercised young and old mdx mice. Muscle & Nerve. 2010;41:487–99.

273. Sun C-C, Li S-J, Yang C-L, Xue R-L, Xi Y-Y, Wang L, et al. Sulforaphane Attenuates Muscle Inflammation in Dystrophin-deficient mdx Mice via NF-E2-related Factor 2 (Nrf2)-mediated Inhibition of NF-κB Signaling Pathway. Journal of Biological Chemistry. 2015;290:17784–95.

274. Yao L, Xue X, Yu P, Ni Y, Chen F. Evans Blue Dye: A Revisit of Its Applications in Biomedicine. Contrast Media & Molecular Imaging. 2018;2018:e7628037.

275. Eng CM, Smallwood LH, Rainiero MP, Lahey M, Ward SR, Lieber RL. Scaling of muscle architecture and fiber types in the rat hindlimb. Journal of Experimental Biology. 2008;211:2336–45.

276. Barclay CJ. Modelling diffusive O2 supply to isolated preparations of mammalian skeletal and cardiac muscle. J Muscle Res Cell Motil. 2005;26:225–35.

277. Segal SS, Faulkner JA. Temperature-dependent physiological stability of rat skeletal muscle in vitro. American Journal of Physiology-Cell Physiology. 1985;248:265–70.

278. National Centre for the Replacement Refinement & Reduction of Animal Research. The 3Rs. NC3Rs. https://nc3rs.org.uk/who-we-are/3rs. Accessed 20 Dec 2022.

279. Patil A, Anand R, Mahajan P. Comparative Study of Acrylic Color and India Ink for Their Use as a Surgical Margin Inks in Oral Squamous Cell Carcinoma. World Journal of Dentistry. 2015;6:26–30.

280. Kosemehmetoglu K, Guner G, Ates Ozdemir D. Indian ink vs tissue marking dye: A quantitative comparison of two widely used macroscopical staining tool. Virchows Archiv : an international journal of pathology. 2010;457:21–5.

281. Milgroom A, Ralston E. Clearing Skeletal Muscle with CLARITY for Light Microscopy Imaging. Cell Biol Int. 2016;40:478–83.

282. McConnell G, Trägårdh J, Amor R, Dempster J, Reid E, Amos WB. A novel optical microscope for imaging large embryos and tissue volumes with sub-cellular resolution throughout. eLife. 2016;5:e18659.

283. Gropp KE. Skeletal Muscle Toolbox. Toxicol Pathol. 2017;45:939–42.

284. Chatterjee S. Artefacts in histopathology. J Oral Maxillofac Pathol. 2014;18 Suppl 1:S111–6.

285. Taqi SA, Sami SA, Sami LB, Zaki SA. A review of artifacts in histopathology. J Oral Maxillofac Pathol. 2018;22:279.

286. Anderson JR. Recommendations for the biopsy procedure and assessment of skeletal muscle biopsies. Virchows Archiv. 1997;431:227–33.

287. Hack AA, Cordier L, Shoturma DI, Lam MY, Sweeney HL, McNally EM. Muscle degeneration without mechanical injury in sarcoglycan deficiency. PNAS. 1999;96:10723–8.

288. Martino F, Varricchio S, Russo D, Merolla F, Ilardi G, Mascolo M, et al. A Machine-learning Approach for the Assessment of the Proliferative Compartment of Solid Tumors on Hematoxylin-Eosin-Stained Sections. Cancers. 2020;12.

289. Bedrick AE, Painter JL, Bonitz DL. Spectral properties and relative quantum yields of new fluorescent stains. Immunopharmacology. 1979;2:33–7.

290. Rost FWD. Fluorescence Microscopy. Cambridge University Press; 1992.

291. PROCION YELLOW MX4R AldrichCPR | Sigma-Aldrich. http://www.sigmaaldrich.com/. Accessed 13 Jul 2022.

292. PubChem. Reactive Orange 14. https://pubchem.ncbi.nlm.nih.gov/compound/114432. Accessed 13 Jul 2022.

293. Live-or-Dye™ Fixable Viability Staining Kits. Biotium. 2022. https://biotium.com/product/live-or-dye-fixable-viability-staining-kit/. Accessed 5 Jan 2022.

294. Anversa P, Leri A, Rota M, Hosoda T, Bearzi C, Urbanek K, et al. Concise Review: Stem Cells, Myocardial Regeneration, and Methodological Artifacts. Stem Cells. 2007;25:589–601.

295. Câmara-Pereira E, Campos L, Vannier-Santos M, Mermelstein C, Costa M. Distribution of cytoskeletal and adhesion proteins in adult zebrafish skeletal muscle. Histology and histopathology. 2009;24:187–96.

296. Schuchmann S, Kovacs R, Kann O, Heinemann U, Buchheim K. Monitoring NAD(P)H autofluorescence to assess mitochondrial metabolic functions in rat hippocampal–entorhinal cortex slices. Brain Research Protocols. 2001;7:267–76.

297. Schilders SP, Gu M. Three-dimensional autofluorescence spectroscopy of rat skeletal muscle tissue under two-photon excitation. Appl Opt, AO. 1999;38:720–3.

298. Verma M, Murkonda BS, Asakura Y, Asakura A. Skeletal Muscle Tissue Clearing for LacZ and Fluorescent Reporters, and Immunofluorescence Staining. In: Kyba M, editor. Skeletal Muscle Regeneration in the Mouse: Methods and Protocols. New York, NY: Springer; 2016. p. 129–40.

299. Wright Cell Imaging Facility TWRI. Autofluorescence: Causes and Cures.

300. Bornø A, Ploug T, Bune LT, Rosenmeier JB, Thaning P. Purinergic receptors expressed in human skeletal muscle fibres. Purinergic Signalling. 2012;8:255–64.

301. Neikirk K, Vue Z, Katti P, Rodriguez BI, Omer SA, Shao J, et al. Systematic Transmission Electron Microscopy-Based Identification and 3D Reconstruction of Cellular Degradation Machinery. 2022.

302. Lin J, Lin W, Hong W, Hung W, Nowotarski SH, Gouveia SM, et al. Morphology and organization of tissue cells in 3D microenvironment of monodisperse foam scaffolds. Soft Matter. 2011;7:10010–6.

303. Arribas SM, Daly CJ, González MC, McGrath JC. Imaging the vascular wall using confocal microscopy. J Physiol. 2007;584 Pt 1:5–9.

304. Csapo R, Gumpenberger M, Wessner B. Skeletal Muscle Extracellular Matrix – What Do We Know About Its Composition, Regulation, and Physiological Roles? A Narrative Review. Frontiers in Physiology. 2020;11.

305. Rehman A ul, Qureshi SA. Quantitative auto-fluorescence quenching of free and bound NADH in HeLa cell line model with Carbonyl cyanide-p-Trifluoromethoxy phenylhydrazone (FCCP) as quenching agent. Photodiagnosis and Photodynamic Therapy. 2022;39.

306. Rich RM, Stankowska DL, Maliwal BP, Sørensen TJ, Laursen BW, Krishnamoorthy RR, et al. Elimination of autofluorescence background from fluorescence tissue images by use of time-gated detection and the AzaDiOxaTriAngulenium (ADOTA) fluorophore. Anal Bioanal Chem. 2013;405:2065–75.

307. Chorvat D, Kirchnerova J, Cagalinec M, Smolka J, Mateasik A, Chorvatova A. Spectral Unmixing of Flavin Autofluorescence Components in Cardiac Myocytes. Biophysical Journal. 2005;89:55–7.

308. Zimmermann T, Rietdorf J, Pepperkok R. Spectral imaging and its applications in live cell microscopy. FEBS Letters. 2003;546:87–92.

309. Shehadul Islam M, Aryasomayajula A, Selvaganapathy PR. A Review on Macroscale and Microscale Cell Lysis Methods. Micromachines (Basel). 2017;8:83.

310. Lewalle A, Campbell KS, Campbell SG, Milburn GN, Niederer SA. Functional and structural differences between skinned and intact muscle preparations. Journal of General Physiology. 2022;154:e202112990.

311. Lou J, Bi W, Li W, Zhao Y, Liu S, Zheng J, et al. Muscle injury induced by different types of contractions in dystrophic mdx mice. J Muscle Res Cell Motil. 2012;32:411–9.

312. Defour A, Medikayala S, Van der Meulen JH, Hogarth MW, Holdreith N, Malatras A, et al. Annexin A2 links poor myofiber repair with inflammation and adipogenic replacement of the injured muscle. Human Molecular Genetics. 2017;26:1979–91.

313. Consolino CM, Brooks SV. Susceptibility to sarcomere injury induced by single stretches of maximally activated muscles of mdx mice. Journal of Applied Physiology. 2004;96:633–8.

314. Grange RW, Gainer TG, Marschner KM, Talmadge RJ, Stull JT. Fast-twitch skeletal muscles of dystrophic mouse pups are resistant to injury from acute mechanical stress. American Journal of Physiology-Cell Physiology. 2002;283:1090–101.

315. Nguyen HX, Tidball JG. Expression of a muscle-specific, nitric oxide synthase transgene prevents muscle membrane injury and reduces muscle inflammation during modified muscle use in mice. J Physiol. 2003;550 Pt 2:347–56.

316. Dumont N, Bouchard P, Frenette J. Neutrophil-induced skeletal muscle damage: a calculated and controlled response following hindlimb unloading and

reloading. American Journal of Physiology-Regulatory, Integrative and Comparative Physiology. 2008;295:1831–8.

317. Greelish JP, Su LT, Lankford EB, Burkman JM, Chen H, Konig SK, et al. Stable restoration of the sarcoglycan complex in dystrophic muscle perfused with histamine and a recombinant adeno-associated viral vector. Nat Med. 1999;5:439–43.

318. Zanou N, Iwata Y, Schakman O, Lebacq J, Wakabayashi S, Gailly P. Essential role of TRPV2 ion channel in the sensitivity of dystrophic muscle to eccentric contractions. FEBS Letters. 2009;583:3600–4.

319. Steenhuis J. Use of Live-or-Dye on tissue. 2021.

320. Lin M-C, Ebihara S, Dwairi QE, Hussain SNA, Yang L, Gottfried SB, et al. Diaphragm Sarcolemmal Injury Is Induced by Sepsis and Alleviated by Nitric Oxide Synthase Inhibition. Am J Respir Crit Care Med. 1998;158:1656–63.

321. Park KH, Brotto L, Lehoang O, Brotto M, Ma J, Zhao X. Ex Vivo Assessment of Contractility, Fatigability and Alternans in Isolated Skeletal Muscles. J Vis Exp. 2012;69:e4198.

322. Lee J-Y, Kitaoka M. A beginner's guide to rigor and reproducibility in fluorescence imaging experiments. Mol Biol Cell. 2018;29:1519–25.

323. North AJ. Seeing is believing? A beginners' guide to practical pitfalls in image acquisition. J Cell Biol. 2006;172:9–18.

324. Ogama T. A beginner's guide to improving image acquisition in fluorescence microscopy. The Biochemist. 2020;42:22–7.

325. Montero Llopis P, Senft RA, Ross-Elliott TJ, Stephansky R, Keeley DP, Koshar P, et al. Best practices and tools for reporting reproducible fluorescence microscopy methods. Nat Methods. 2021;18:1463–76.

326. Ettinger A, Wittmann T. Fluorescence Live Cell Imaging. Methods Cell Biol. 2014;123:77–94.

327. Festing MFW. The design of animal experiments. In: The UFAW Handbook on the Care and Management of Laboratory and Other Research Animals. John Wiley & Sons; 2010.

328. Klaus B. Statistical relevance—relevant statistics, part I. EMBO J. 2015;34:2727–30.

329. Minitab LLC. Overview for Power and Sample Size for One-Way ANOVA. 2022. https://support.minitab.com/en-us/minitab/19/help-and-how-to/statistics/power-and-sample-size/how-to/linear-models/power-and-sample-size-for-one-way-anova/before-you-start/overview/. Accessed 18 Jul 2022.

330. Deconinck N, Rafael JA, Beckers-Bleukx G, Kahn D, Deconinck AE, Davies KE, et al. Consequences of the combined deficiency in dystrophin and utrophin on the mechanical properties and myosin composition of some limb and respiratory muscles of the mouse. Neuromuscular Disorders. 1998;8:362–70.

331. Minitab LLC. Methods and formulas for Power and Sample Size for One-Way ANOVA. 2022. https://support.minitab.com/en-us/minitab/19/help-and-how-to/statistics/power-and-sample-size/how-to/linear-models/power-and-sample-size-for-one-way-anova/methods-and-formulas/methods-and-formulas/#calculating-sample-size-and-maximum-difference. Accessed 18 Jul 2022.

332. Minitab LLC. Interpret all statistics and graphs for Power and Sample Size for 2-Sample t. 2022. https://support.minitab.com/en-us/minitab/19/help-and-how-to/statistics/power-and-sample-size/how-to/hypothesis-tests/power-and-sample-size-for-2-sample-t/interpret-the-results/all-statistics-and-graphs/. Accessed 5 May 2022.

333. Burger W, Burge MJ. Histograms and Image Statistics. In: Burger W, Burge MJ, editors. Digital Image Processing: An Algorithmic Introduction Using Java. London: Springer; 2016. p. 37–56.

334. Cromey DW. Avoiding Twisted Pixels: Ethical Guidelines for the Appropriate Use and Manipulation of Scientific Digital Images. Sci Eng Ethics. 2010;16:639–67.

335. Pistilli EE, Bogdanovich S, Goncalves MD, Ahima RS, Lachey J, Seehra J, et al. Targeting the Activin Type IIB Receptor to Improve Muscle Mass and Function in the mdx Mouse Model of Duchenne Muscular Dystrophy. Am J Pathol. 2011;178:1287–97.

336. Bittel DC, Sreetama SC, Chandra G, Ziegler R, Nagaraju K, Meulen JHV der, et al. Secreted acid sphingomyelinase as a potential gene therapy for limb girdle muscular dystrophy 2B. J Clin Invest. 2022;132.

337. Moens P, Baatsen PHWW, Marschal G. Increased susceptibility of EDL muscles from mdx mice to damage induced by contractions with stretch. J Muscle Res Cell Motil. 1993;14:446–51.

338. Shihan MH, Novo SG, Le Marchand SJ, Wang Y, Duncan MK. A simple method for quantitating confocal fluorescent images. Biochem Biophys Rep. 2021;25.

339. Noller CM, Boulina M, McNamara G, Szeto A, McCabe PM, Mendez AJ. A Practical Approach to Quantitative Processing and Analysis of Small Biological Structures by Fluorescent Imaging. J Biomol Tech. 2016;27:90–7.

340. Spaepen P, De Boodt S, Aerts J-M, Sloten JV. Digital Image Processing of Live/Dead Staining. In: Stoddart MJ, editor. Mammalian Cell Viability: Methods and Protocols. Totowa, NJ: Humana Press; 2011. p. 209–30.

341. Graf J, Cho S, McDonough E, Corwin A, Sood A, Lindner A, et al. FLINO: a new method for immunofluorescence bioimage normalization. Bioinformatics. 2022;38:520–6.

342. Hoffman R, Kothari S, Wang M. Comparison of Normalization Algorithms for Cross-Batch Color Segmentation of Histopathological Images. Conf Proc IEEE Eng Med Biol Soc. 2014;2014:194–7.

343. Nyul LG, Udupa JK, Zhang X. New variants of a method of MRI scale standardization. IEEE Transactions on Medical Imaging. 2000;19:143–50.

344. Chang YH, Chin K, Thibault G, Eng J, Gray JW. RESTORE: Robust intEnSiTy nORmalization mEthod for Multiplexed Imaging. Communications Biology. 2020;3:18.

345. Johnson S, Rabinovitch P. Ex-vivo imaging of excised tissue using vital dyes and confocal microscopy. Curr Protoc Cytom. 2012. https://doi.org/10.1002/0471142956.cy0939s61.

346. Resch-Genger U, DeRose PC. Fluorescence standards: Classification, terminology, and recommendations on their selection, use, and production (IUPAC Technical Report). Pure and Applied Chemistry. 2010;82:2315–35.

347. Majumder S, Fisk HA. Quantitative Immunofluorescence Assay to Measure the Variation in Protein Levels at Centrosomes. J Vis Exp. 2014;:e52030.

348. Nichele L, Persichetti V, Lucidi M, Cincotti G. Quantitative evaluation of ImageJ thresholding algorithms for microbial cell counting. OAS Continuum. 2020;3:1417–27.

349. MyofibrilJ. ImageJ Wiki. https://imagej.github.io/plugins/myofibrilj. Accessed 1 Jun 2022.

350. Encarnacion-Rivera L, Foltz S, Hartzell HC, Choo H. Myosoft: An automated muscle histology analysis tool using machine learning algorithm utilizing FIJI/ImageJ software. PLOS ONE. 2020;15:e0229041.

351. Smith LR, Barton ER. SMASH – semi-automatic muscle analysis using segmentation of histology: a MATLAB application. Skeletal Muscle. 2014;4:21.

352. Kastenschmidt JM, Ellefsen KL, Mannaa AH, Giebel JJ, Yahia R, Ayer RE, et al. QuantiMus: A Machine Learning-Based Approach for High Precision Analysis of Skeletal Muscle Morphology. Front Physiol. 2019;10.

353. Lau YS, Xu L, Gao Y, Han R. Automated muscle histopathology analysis using CellProfiler. Skelet Muscle. 2018;8.

354. MyoVision: automatic image quantification platform | University of Kentucky College of Health Sciences. https://www.uky.edu/chs/center-for-muscle-biology/myovision. Accessed 1 Jun 2022.

355. Babcock LW, Hanna AD, Agha NH, Hamilton SL. MyoSight—semi-automated image analysis of skeletal muscle cross sections. Skeletal Muscle. 2020;10:33.

356. Desgeorges T, Liot S, Lyon S, Bouvière J, Kemmel A, Trignol A, et al. Open-CSAM, a new tool for semi-automated analysis of myofiber cross-sectional area in regenerating adult skeletal muscle. Skeletal Muscle. 2019;9:2.

357. Reyes-Fernandez PC, Periou B, Decrouy X, Relaix F, Authier FJ. Automated image-analysis method for the quantification of fiber morphometry and fiber type population in human skeletal muscle. Skeletal Muscle. 2019;9.

358. Stringer C, Wang T, Michaelos M, Pachitariu M. Cellpose: a generalist algorithm for cellular segmentation. Nat Methods. 2021;18:100–6.

359. Matteo C. Running cellpose in colab with a GPU. 2022.

360. Principles of Scientific Imaging. ImageJ Wiki. https://imagej.github.io/imaging/principles. Accessed 2 Jun 2022.

361. Waisman A, Norris AM, Elías Costa M, Kopinke D. Automatic and unbiased segmentation and quantification of myofibers in skeletal muscle. Sci Rep. 2021;11.

362. Jost AP-T, Waters JC. Designing a rigorous microscopy experiment: Validating methods and avoiding bias. J Cell Biol. 2019;218:1452–66.

363. Tasker L.H., Shapcott N.G., Watkins A.J., Holland P.M. The effect of seat shape on the risk of pressure ulcers using discomfort and interface pressure measurements. Prosthet Orthot Int. 2014;38:46–53.

364. Armitage L, Turner S, Sreenivasa M. Human-device interface pressure measurement in prosthetic, orthotic and exoskeleton applications: A systematic review. Medical Engineering & Physics. 2021;97:56–69.

365. Cheng L, Xia X, Yu W, Scriven LE, Gerberich WW. Flat-punch indentation of viscoelastic material. Journal of Polymer Science Part B: Polymer Physics. 2000;38:10–22.

366. Lin DC, Horkay F. Nanomechanics of polymer gels and biological tissues: A critical review of analytical approaches in the Hertzian regime and beyond. Soft Matter. 2008;4:669–82.

367. Argatov I, Daniels AU, Mishuris G, Ronken S, Wirz D. Accounting for the thickness effect in dynamic spherical indentation of a viscoelastic layer: Application to non-destructive testing of articular cartilage. European Journal of Mechanics - A/Solids. 2013;37:304–17.

368. Hertz H. Ueber die Berührung fester elastischer Körper. Journal für die reine und angewandte Mathematik (Crelles Journal). 1882;1882:156–71.

369. Boussinesq J. Application des potentiels à l'étude de l'équilibre et du mouvement des solides élastiques: principalement au calcul des déformations et des pressions que produisent, dans ces solides, des efforts quelconques exercés sur une petite partie de leur surface ou de leur intérieur : mémoire suivi de notes étendues sur divers points de physique, mathematique et d'analyse. Gauthier-Villars; 1885.

370. Popov VL. Rigorous Treatment of Contact Problems – Hertzian Contact. In: Contact Mechanics and Friction. Berlin, Heidelberg: Springer Berlin Heidelberg; 2010. p. 55–70.

371. Ning X, Lovell M, Slaughter WS. Asymptotic solutions for axisymmetric contact of a thin, transversely isotropic elastic layer. Wear. 2006;260:693–8.

372. Sneddon IN. The relation between load and penetration in the axisymmetric boussinesq problem for a punch of arbitrary profile. International Journal of Engineering Science. 1965;3:47–57.

373. Popov VL, Heß M, Willert E. Normal Contact Without Adhesion. In: Popov VL, Heß M, Willert E, editors. Handbook of Contact Mechanics: Exact Solutions of Axisymmetric Contact Problems. Berlin, Heidelberg: Springer; 2019. p. 5–66.

374. Zhang M, Zheng YP, Mak AFT. Estimating the effective Young's modulus of soft tissues from indentation tests—nonlinear finite element analysis of effects of friction and large deformation. Medical Engineering & Physics. 1997;19:512–7.

375. Hayes WC, Keer LM, Herrmann G, Mockros LF. A mathematical analysis for indentation tests of articular cartilage. Journal of Biomechanics. 1972;5:541–51.

376. Kabir W, Di Bella C, Choong PFM, O'Connell CD. Assessment of Native Human Articular Cartilage: A Biomechanical Protocol. Cartilage. 2021;13 2 Suppl:427–37.

377. Keenan KE, Pal S, Lindsey DP, Besier TF, Beaupre GS. A Viscoelastic Constitutive Model Can Accurately Represent Entire Creep Indentation Tests of Human Patella Cartilage. J Appl Biomech. 2013;29:292–302.

378. Dourte LM, Pathmanathan L, Jawad AF, Iozzo RV, Mienaltowski MJ, Birk DE, et al. Influence of Decorin on the Mechanical, Compositional, and Structural Properties of the Mouse Patellar Tendon. J Biomech Eng. 2012;134:31005_1-31005_8.

379. Ling H, Choi P, Zheng Y, Lau K. Extraction of mechanical properties of foot plantar tissues using ultrasound indentation associated with genetic algorithm. J Mater Sci: Mater Med. 2007;18:1579–86.

380. ANSYS, Inc. Mechanical User's Guide. 2021.

381. Lamsfuss J, Bargmann S. Skeletal muscle: Modeling the mechanical behavior by taking the hierarchical microstructure into account. Journal of the Mechanical Behavior of Biomedical Materials. 2021;122:104670.

382. Kuravi R, Leichsenring K, Trostorf R, Morales-Orcajo E, Böl M, Ehret AE. Predicting muscle tissue response from calibrated component models and histology-based finite element models. Journal of the Mechanical Behavior of Biomedical Materials. 2021;117:104375.

383. Spyrou LA, Agoras M, Danas K. A homogenization model of the Voigt type for skeletal muscle. Journal of Theoretical Biology. 2017;414:50–61.

384. Spyrou LA, Brisard S, Danas K. Multiscale modeling of skeletal muscle tissues based on analytical and numerical homogenization. Journal of the Mechanical Behavior of Biomedical Materials. 2019;92:97–117.

385. Bleiler C, Ponte Castañeda P, Röhrle O. A microstructurally-based, multi-scale, continuum-mechanical model for the passive behaviour of skeletal muscle tissue. Journal of the Mechanical Behavior of Biomedical Materials. 2019;97:171–86.

386. Takaza M, Cooney GM, McManus G, Stafford P, Simms CK. Assessing the microstructural response to applied deformation in porcine passive skeletal muscle. Journal of the Mechanical Behavior of Biomedical Materials. 2014;40:115–26.

387. Kuravi R, Leichsenring K, Böl M, Ehret AE. 3D finite element models from serial section histology of skeletal muscle tissue – The role of micro-architecture on mechanical behaviour. Journal of the Mechanical Behavior of Biomedical Materials. 2021;113:104109.

388. Breuls RGM, Sengers BG, Oomens CWJ, Bouten CVC, Baaijens FPT. Predicting Local Cell Deformations in Engineered Tissue Constructs: A Multilevel Finite Element Approach. Journal of Biomechanical Engineering. 2002;124:198.

389. Kohn S, Leichsenring K, Kuravi R, Ehret AE, Böl M. Direct measurement of the direction-dependent mechanical behaviour of skeletal muscle extracellular matrix. Acta Biomaterialia. 2021;122:249–62.

390. Jafari M, Guan Y, Wedge DC, Ansari-Pour N. Re-evaluating experimental validation in the Big Data Era: a conceptual argument. Genome Biology. 2021;22:71.

391. J. Rykiel Jr. E. Testing ecological models: the meaning of validation. Ecological Modelling. 1996;:229–44.

392. Heusser K, Heusser R, Jordan J, Urechie V, Diedrich A, Tank J. Baroreflex Curve Fitting Using a WYSIWYG Boltzmann Sigmoidal Equation. Frontiers in Neuroscience. 2021;15.

393. Rouwkema J, Gibbs S, Lutolf M, Martin I, Vunjak-Novakovic G, Malda J. In vitro platforms for tissue engineering: implications to basic research and clinical translation. J Tissue Eng Regen Med. 2011;5:164–7.

394. Böl M, Ehret AE, Leichsenring K, Weichert C, Kruse R. On the anisotropy of skeletal muscle tissue under compression. Acta Biomaterialia. 2014;10:3225–34.

395. Aguiar J, Carpena P, Molina-Bolívar JA, Carnero Ruiz C. On the determination of the critical micelle concentration by the pyrene 1:3 ratio method. Journal of Colloid and Interface Science. 2003;258:116–22.

396. Su P-F, Gard SA, Lipschutz RD, Kuiken TA. Gait characteristics of persons with bilateral transtibial amputations. JRRD. 2007;44:491–502.

397. Vickers DR, Palk C, McIntosh AS, Beatty KT. Elderly unilateral transtibial amputee gait on an inclined walkway: A biomechanical analysis. Gait & Posture. 2008;27:518–29.

398. Safari R. Lower limb prosthetic interfaces: Clinical and technological advancement and potential future direction. Prosthet Orthot Int. 2020;44:384–401.

399. Sanderson DJ, Martin PE. Lower extremity kinematic and kinetic adaptations in unilateral below-knee amputees during walking. Gait & Posture. 1997;6:126–36.

400. Groothuis A, Houdijk H. The Effect of Prosthetic Alignment on Prosthetic and Total Leg Stiffness While Running With Simulated Running-Specific Prostheses. Frontiers in Sports and Active Living. 2019;1:1–10.

401. Oudenhoven LM, Boes JM, Hak L, Faber GS, Houdijk H. Regulation of step frequency in transtibial amputee endurance athletes using a running-specific prosthesis. Journal of Biomechanics. 2017;51:42–8.

402. Beck ON, Taboga P, Grabowski AM. How do prosthetic stiffness, height and running speed affect the biomechanics of athletes with bilateral transtibial amputations? J R Soc Interface. 2017;14:20170230.

403. Mbithi FM, Chipperfield AJ, Steer JW, Dickinson AS. Developing a control framework for self-adjusting prosthetic sockets incorporating tissue injury risk estimation and generalized predictive control. Biomed Eng Lett. 2021;12.

404. Safari MR, Meier MR. Systematic review of effects of current transtibial prosthetic socket designs—Part 2: Quantitative outcomes. Journal of Rehabilitation Research and Development. 2015;52:509–26.

405. Minitab LLC. Data considerations for Kruskal-Wallis Test. Minitab 18 Support. 2022. https://support.minitab.com/en-us/minitab/18/help-and-how-to/statistics/nonparametrics/how-to/kruskal-wallis-test/before-you-start/data-considerations/. Accessed 29 Jul 2022.

406. Minitab LLC. Data considerations for One-Way ANOVA. Minitab 19 Support. 2022. https://support.minitab.com/en-us/minitab/19/help-and-how-to/statistical-modeling/anova/how-to/one-way-anova/before-you-start/data-considerations/. Accessed 29 Jul 2022.

407. Chapman KE, Sinclair SE, Zhuang D, Hassid A, Desai LP, Waters CM. Cyclic mechanical strain increases reactive oxygen species production in pulmonary epithelial cells. American Journal of Physiology-Lung Cellular and Molecular Physiology. 2005;289:L834–41.

408. Humphrey JD, Dufresne ER, Schwartz MA. Mechanotransduction and extracellular matrix homeostasis. Nat Rev Mol Cell Biol. 2014;15:802–12.

409. Ingber DE, Wang N, Stamenović D. Tensegrity, cellular biophysics, and the mechanics of living systems. Rep Prog Phys. 2014;77:046603.

410. Hoffman BD, Crocker JC. Cell Mechanics: Dissecting the Physical Responses of Cells to Force. Annual Review of Biomedical Engineering. 2009;11:259–88.

411. Janmey PA, Weitz DA. Dealing with mechanics: mechanisms of force transduction in cells. Trends in Biochemical Sciences. 2004;29:364–70.

412. Kasza KE, Rowat AC, Liu J, Angelini TE, Brangwynne CP, Koenderink GH, et al. The cell as a material. Current Opinion in Cell Biology. 2007;19:101–7.

413. Wang N, Naruse K, Stamenović D, Fredberg JJ, Mijailovich SM, Tolić-Nørrelykke IM, et al. Mechanical behavior in living cells consistent with the tensegrity model. Proc Natl Acad Sci U S A. 2001;98:7765–70.

414. Bonakdar N, Gerum R, Kuhn M, Spörrer M, Lippert A, Schneider W, et al. Mechanical plasticity of cells. Nature Mater. 2016;15:1090–4.

415. Höhfeld J, Benzing T, Bloch W, Fürst DO, Gehlert S, Hesse M, et al. Maintaining proteostasis under mechanical stress. EMBO reports. 2021;22:e52507.

416. Lamsfuss J, Bargmann S. Computational modeling of damage in the hierarchical microstructure of skeletal muscles. Journal of the Mechanical Behavior of Biomedical Materials. 2022;134:105386.

417. Ito D, Tanaka E, Yamamoto S. A novel constitutive model of skeletal muscle taking into account anisotropic damage. Journal of the Mechanical Behavior of Biomedical Materials. 2010;3:85–93.

418. Zhu Y, Kang G, Yu C, Poh LH. Logarithmic rate based elasto-viscoplastic cyclic constitutive model for soft biological tissues. Journal of the Mechanical Behavior of Biomedical Materials. 2016;61:397–409.

419. Kang G, Wu X. Ratchetting of porcine skin under uniaxial cyclic loading. Journal of the Mechanical Behavior of Biomedical Materials. 2011;4:498–506.

420. Kollmannsberger P, Fabry B. Linear and Nonlinear Rheology of Living Cells. Annual Review of Materials Research. 2011;41:75–97.

421. Ho KKY, Wang YL, Wu J, Liu AP. Advanced Microfluidic Device Designed for Cyclic Compression of Single Adherent Cells. Frontiers in Bioengineering and Biotechnology. 2018;6:1–12.

422. Butterfield TA, Zhao Y, Agarwal S, Haq F, Best TM. Cyclic compressive loading facilitates recovery after eccentric exercise. Med Sci Sports Exerc. 2008;40:1289–96.

423. Haas C, Best TM, Wang Q, Butterfield TA, Zhao Y. In vivo passive mechanical properties of skeletal muscle improve with massage-like loading following eccentric exercise. J Biomech. 2012;45:2630–6.

424. Seo BR, Payne CJ, McNamara SL, Freedman BR, Kwee BJ, Nam S, et al. Skeletal muscle regeneration with robotic actuation–mediated clearance of neutrophils. Sci Transl Med. 2021;13:eabe8868.

425. Van Loocke M, Simms CK, Lyons CG. Viscoelastic properties of passive skeletal muscle in compression—Cyclic behaviour. Journal of Biomechanics. 2009;42:1038–48.

426. Onal S, Alkaisi MM, Nock V. A Flexible Microdevice for Mechanical Cell Stimulation and Compression in Microfluidic Settings. Frontiers in Physics. 2021;9.

427. Esfahani AM, Rosenbohm J, Safa BT, Lavrik NV, Minnick G, Zhou Q, et al. Characterization of the strain-rate–dependent mechanical response of single cell–cell junctions. Proceedings of the National Academy of Sciences. 2021;118:e2019347118.

428. Nasrollahzadeh N, Karami P, Wang J, Bagheri L, Guo Y, Abdel-Sayed P, et al. Temperature evolution following joint loading promotes chondrogenesis by synergistic cues via calcium signaling. eLife. 2022;11:e72068.

429. Bowler K, Laudien H, Laudien I. Cellular heat injury. Journal of Thermal Biology. 1983;8:426–30.

430. Lejeune E, Linder C. Chapter 12 - Modeling biological materials with peridynamics. In: Oterkus E, Oterkus S, Madenci E, editors. Peridynamic Modeling, Numerical Techniques, and Applications. Elsevier; 2021. p. 249–73.

431. Taylor M, Gözen I, Patel S, Jesorka A, Bertoldi K. Peridynamic Modeling of Ruptures in Biomembranes. PLOS ONE. 2016;11:e0165947.

432. Pröbsting E, Blumentritt S, Kannenberg A. Veränderungen am Bewegungsapparat als Folge von Amputationen an der unteren Extremität. Z Orthop Unfall. 2017;12:77–91.

433. Abdel-Sayed P, Moghadam MN, Salomir R, Tchernin D, Pioletti DP. Intrinsic viscoelasticity increases temperature in knee cartilage under physiological loading. Journal of the Mechanical Behavior of Biomedical Materials. 2014;30:123–30.

434. Becher C, Springer J, Feil S, Cerulli G, Paessler HH. Intra-articular temperatures of the knee in sports – An in-vivo study of jogging and alpine skiing. BMC Musculoskeletal Disorders. 2008;9:46.

435. Peery JT, Ledoux WR, Klute GK. Residual-limb skin temperature in transtibial sockets. The Journal of Rehabilitation Research and Development. 2005;42:147–54.

436. Kenny GP, Reardon FD, Zaleski W, Reardon ML, Haman F, Ducharme MB. Muscle temperature transients before, during, and after exercise measured using an intramuscular multisensor probe. Journal of Applied Physiology. 2003;94:2350–7.

437. Kenny GP, McGinn R. Restoration of thermoregulation after exercise. Journal of Applied Physiology. 2017;122:933–44.

438. Baines CP. The mitochondrial permeability transition pore and ischemia-reperfusion injury. Basic Res Cardiol. 2009;104:181–8.

439. Di Lisa F, Canton M, Carpi A, Kaludercic N, Menabo R, Menazza S, et al. Mitochondrial injury and protection in ischemic pre- and postconditioning. Antioxidants & Redox Signaling. 2011;14:881–91.

440. Honda HM, Korge P, Weiss JN. Mitochondria and Ischemia/Reperfusion Injury. Annals of the New York Academy of Sciences. 2005;1047:248–58.

441. Zhou H, Wang S, Hu S, Chen Y, Ren J. ER–Mitochondria Microdomains in Cardiac Ischemia–Reperfusion Injury: A Fresh Perspective. Front Physiol. 2018;9.

442. Paradis S, Charles A-L, Meyer A, Lejay A, Scholey JW, Chakfé N, et al. Chronology of mitochondrial and cellular events during skeletal muscle ischemia-reperfusion. Am J Physiol Cell Physiol. 2016;310:968–82.

443. Cui F-F, Pan Y-Y, Xie H-H, Wang X-H, Shi H-X, Xiao J, et al. Pressure Combined with Ischemia/Reperfusion Injury Induces Deep Tissue Injury via Endoplasmic Reticulum Stress in a Rat Pressure Ulcer Model. Int J Mol Sci. 2016;17:284.

444. Martou G, O'Blenes CA, Huang N, McAllister SE, Neligan PC, Ashrafpour H, et al. Development of an in vitro model for study of the efficacy of ischemic preconditioning in human skeletal muscle against ischemia-reperfusion injury. Journal of Applied Physiology. 2006;101:1335–42.

445. Vaidya Y, Dhamoon AS. Myocardial Stunning and Hibernation. In: StatPearls. Treasure Island (FL): StatPearls Publishing; 2019.

446. Charles A-L, Guilbert A-S, Bouitbir J, Goette-Di Marco P, Enache I, Zoll J, et al. Effect of postconditioning on mitochondrial dysfunction in experimental aortic cross-clamping. British Journal of Surgery. 2011;98:511–6.

447. Mansour Z, Charles AL, Bouitbir J, Pottecher J, Kindo M, Mazzucotelli J-P, et al. Remote and local ischemic postconditioning further impaired skeletal muscle mitochondrial function after ischemia-reperfusion. Journal of Vascular Surgery. 2012;56:774–82.

448. Yu T, Zhu J, Li D, Zhu D. Physical and chemical mechanisms of tissue optical clearing. iScience. 2021;24:102178.

449. Decroix L, Van Muylder V, Desender L, Sampaolesi M, Thorrez L. Tissue clearing for confocal imaging of native and bio-artificial skeletal muscle. Biotechnic & Histochemistry. 2015;90:424–31.

450. Pfeffer CP, Olsen BR, Ganikhanov F, Légaré F. Imaging skeletal muscle using second harmonic generation and coherent anti-Stokes Raman scattering microscopy. Biomed Opt Express. 2011;2:1366–76.

451. Chaichi A, Prasad A, Gartia M. Raman Spectroscopy and Microscopy Applications in Cardiovascular Diseases: From Molecules to Organs. Biosensors. 2018;8:107.

452. Butler HJ, Ashton L, Bird B, Cinque G, Curtis K, Dorney J, et al. Using Raman spectroscopy to characterize biological materials. Nat Protoc. 2016;11:664–87.

453. Lockwood DJ. Rayleigh and Mie Scattering. In: Luo MR, editor. Encyclopedia of Color Science and Technology. New York, NY: Springer New York; 2016. p. 1097–107.

454. Lee M, Simon Herrington C, Ravindra M, Sepp K, Davies A, N. Hulme A, et al. Recent advances in the use of stimulated Raman scattering in histopathology. Analyst. 2021;146:789–802.

455. Jones RR, Hooper DC, Zhang L, Wolverson D, Valev VK. Raman Techniques: Fundamentals and Frontiers. Nanoscale Res Lett. 2019;14:231.

456. Shipp DW, Sinjab F, Notingher I. Raman spectroscopy: techniques and applications in the life sciences. Adv Opt Photon. 2017;9.

457. Polliack A, Taylor R, Bader D. Analysis of sweat during soft tissue breakdown following pressure ischemia. Journal of Rehabilitation Research and Development. 1993;30:250–9.

458. Polliack A, Taylor R, Bader D. Sweat analysis following pressure ischaemia in a group of debilitated subjects. J Rehabil Res Dev. 1997;34:303–8.

459. Soetens JFJ, Worsley PR, Herniman JM, Langley GJ, Bader DL, Oomens CWJ. The expression of anaerobic metabolites in sweat and sebum from human skin subjected to intermittent and continuous mechanical loading. Journal of Tissue Viability. 2019;28:186–93.

460. Bader DL, Wang Y-N, Knight S, Polliack A, James T, Taylor R. Biochemical Status of Soft Tissues Subjected to Sustained Pressure. In: Pressure Ulcer Research. Berlin/Heidelberg: Springer-Verlag; 2005. p. 109–27.

461. de Wert LA, Bader DL, Oomens CWJ, Schoonhoven L, Poeze M, Bouvy ND. A new method to evaluate the effects of shear on the skin: The effects of shear on the skin. Wound Repair and Regeneration. 2015;23:885–90.

462. Hemmes B, de Wert LA, Brink PRG, Oomens CW, Bader DL, Poeze M. Cytokine IL1α and lactate as markers for tissue damage in spineboard immobilisation. A prospective, randomised open-label crossover trial. Journal of the Mechanical Behavior of Biomedical Materials. 2017;75:82–8.

463. Makhsous M, Lin F, Pandya A, Pandya MS, Chadwick CC. Elevation in the Serum and Urine Concentration of Injury-Related Molecules After the Formation of Deep Tissue Injury in a Rat Spinal Cord Injury Pressure Ulcer Model. PM&R. 2010;2:1063–5.

464. Minematsu T, Nakagami G, Sari Y, Akase T, Sugama J, Nagase T, et al. Candidate biomarkers for deep tissue damage from molecular biological and biochemical aspects. Journal of Tissue Viability. 2010;19:77–83.

465. Sari Y, Nakagami G, Kinoshita A, Huang L, Ueda K, Iizaka S, et al. Changes in serum and exudate creatine phosphokinase concentrations as an indicator of deep tissue injury: a pilot study. International Wound Journal. 2008;5:674–80.

466. Loerakker S, Huisman ES, Seelen HAM, Glatz JFC, Baaijens FPT, Oomens CWJ, et al. Plasma variations of biomarkers for muscle damage in male nondisabled and spinal cord injured subjects. JRRD. 2012;49:361–72.

467. Kimura N, Nakagami G, Minematsu T, Sanada H. Non-invasive detection of local tissue responses to predict pressure ulcer development in mouse models. Journal of Tissue Viability. 2020;29:51–7.

468. Nakai A, Minematsu T, Tamai N, Sugama J, Urai T, Sanada H. Prediction of healing in Category I pressure ulcers by skin blotting with plasminogen activator inhibitor 1, interleukin-1α, vascular endothelial growth factor C, and heat shock protein 90α: A pilot study. Journal of Tissue Viability. 2019;28:87–93.

469. Bronneberg D, Bouten CVC, Oomens CWJ, van Kemenade PM, Baaijens FPT. An in vitro Model System to Study the Damaging Effects of Prolonged Mechanical Loading of the Epidermis. Ann Biomed Eng. 2006;34:506–14.

470. Cornelissen LH, Bronneberg D, Bader DL, Baaijens FPT, Oomens CWJ. The Transport Profile of Cytokines in Epidermal Equivalents Subjected to Mechanical Loading. Ann Biomed Eng. 2009;37:1007–18.

471. Tam BT, Yu AP, Tam EW, Monks DA, Wang XP, Pei XM, et al. Ablation of Bax and Bak protects skeletal muscle against pressure-induced injury. Sci Rep. 2018;8.

472. Teng BT, Pei XM, Tam EW, Benzie IF, Siu PM. Opposing responses of apoptosis and autophagy to moderate compression in skeletal muscle. Acta Physiologica. 2011;201:239–54.

473. Gimble JM, Frazier T, Wu X, Uquillas AA, Llamas C, Brown T, et al. A Novel, Sterilized Microvascular Tissue Product Improves Healing in a Murine Pressure Ulcer Model. Plast Reconstr Surg Glob Open. 2018;6:e2010.

474. Motegi S, Sekiguchi A, Uchiyama A, Uehara A, Fujiwara C, Yamazaki S, et al. Protective effect of mesenchymal stem cells on the pressure ulcer formation by the regulation of oxidative and endoplasmic reticulum stress. Sci Rep. 2017;7.

475. Horobin RW, Kiernan JA, Conn HJ, Biological Stain Commission. Conn's biological stains: a handbook of dyes, stains and fluorochromes for use in biology and medicine. 2020.

476. Azaripour A, Lagerweij T, Scharfbillig C, Jadczak AE, Willershausen B, Van Noorden CJF. A survey of clearing techniques for 3D imaging of tissues with special reference to connective tissue. Progress in Histochemistry and Cytochemistry. 2016;51:9–23.

477. Calve S, Ready A, Huppenbauer C, Main R, Neu CP. Optical Clearing in Dense Connective Tissues to Visualize Cellular Connectivity In Situ. PLoS One. 2015;10:e0116662.

478. Cluff K, Kelly AM, Koutakis P, He XN, Huang X, Lu YF, et al. Surface-enhanced Raman spectral biomarkers correlate with Ankle Brachial Index and characterize leg muscle biochemical composition of patients with peripheral arterial disease. Physiol Rep. 2014;2.

479. Azeem M, Qaisar R, Karim A, Ranade A, Elmoselhi A. Signature molecular changes in the skeletal muscle of hindlimb unloaded mice. Biochem Biophys Rep. 2021;25:100930.

480. Y. Lau CP, Ma W, Yau Law K, D. Lacambra M, Chuen Wong K, Wei Lee C, et al. Development of deep learning algorithms to discriminate giant cell tumors of bone from adjacent normal tissues by confocal Raman spectroscopy. Analyst. 2022;147:1425–39.

481. Krafft C, Schie IW, Meyer T, Schmitt M, Popp J. Developments in spontaneous and coherent Raman scattering microscopic imaging for biomedical applications. Chem Soc Rev. 2016;45:1819–49.

482. Al-Rifai R, Tournois C, Kheirallah S, Bouland N, Poitevin G, Nguyen P, et al. Subcutaneous and transcutaneous monitoring of murine hindlimb ischemia by in vivo Raman spectroscopy. Analyst. 2019;144:4677–86.

483. Plesia M, Stevens OA, Lloyd GR, Kendall CA, Coldicott I, Kennerley AJ, et al. In Vivo Fiber Optic Raman Spectroscopy of Muscle in Preclinical Models of Amyotrophic Lateral Sclerosis and Duchenne Muscular Dystrophy. ACS Chem Neurosci. 2021;12:1768–76.

484. P. Alix JJ, Plesia M, R. Lloyd G, P. Dudgeon A, A. Kendall C, Hewamadduma C, et al. Rapid identification of human muscle disease with fibre optic Raman spectroscopy. Analyst. 2022;147:2533–40.

485. Tipping WJ, Lee M, Serrels A, Brunton VG, Hulme AN. Stimulated Raman scattering microscopy: an emerging tool for drug discovery. Chem Soc Rev. 2016;45:2075–89.

486. Bégin S, Bélanger E, Laffray S, Vallée R, Côté D. In vivo optical monitoring of tissue pathologies and diseases with vibrational contrast. Journal of Biophotonics. 2009;2:632–42.

487. Bergholt MS, Serio A, Albro MB. Raman Spectroscopy: Guiding Light for the Extracellular Matrix. Front Bioeng Biotechnol. 2019;7.

488. Wei M, Shi L, Shen Y, Zhao Z, Guzman A, Kaufman LJ, et al. Volumetric chemical imaging by clearing-enhanced stimulated Raman scattering microscopy. PNAS. 2019;116:6608–17.

489. Sdobnov AY, Tuchin VV, Lademann J, Darvin ME. Confocal Raman microscopy supported by optical clearing treatment of the skin—influence on collagen hydration. J Phys D: Appl Phys. 2017;50.

490. Del Giudice M, Gangestad SW. Rethinking IL-6 and CRP: Why they are more than inflammatory biomarkers, and why it matters. Brain, Behavior, and Immunity. 2018;70:61–75.

491. Tsivitse SK, Mylona E, Peterson JM, Gunning WT, Pizza FX. Mechanical loading and injury induce human myotubes to release neutrophil chemoattractants. American Journal of Physiology-Cell Physiology. 2005;288:721–9.

492. Renström L, Stål P, Song Y, Forsgren S. Bilateral muscle fiber and nerve influences by TNF-alpha in response to unilateral muscle overuse – studies on TNF receptor expressions. BMC Musculoskeletal Disorders. 2017;18.

493. Rogeri PS, Gasparini SO, Martins GL, Costa LKF, Araujo CC, Lugaresi R, et al. Crosstalk Between Skeletal Muscle and Immune System: Which Roles Do IL-6 and Glutamine Play? Frontiers in Physiology. 2020;11.

494. Frost F, Roach MJ, Kushner I, Schreiber P. Inflammatory C-reactive protein and cytokine levels in asymptomatic people with chronic spinal cord injury. Archives of Physical Medicine and Rehabilitation. 2005;86:312–7.

495. Scivoletto G, Fuoco U, Morganti B, Cosentino E, Molinari M. Pressure sores and blood and serum dysmetabolism in spinal cord injury patients. Spinal Cord. 2004;42:473–6.

496. Morse LR, Stolzmann K, Nguyen HP, Jain NB, Zayac C, Gagnon DR, et al. Association Between Mobility Mode and C-Reactive Protein Levels in Men With Chronic Spinal Cord Injury. Archives of Physical Medicine and Rehabilitation. 2008;89:726–31.

497. Hagisawa S, Ferguson-Pell MW, Palmieri VR, Cochran GV. Pressure sores: a biochemical test for early detection of tissue damage. Arch Phys Med Rehabil. 1988;69:668–71.

498. Apple FS, Rogers MA, Sherman WM, Costill DL, Hagerman FC, Ivy JL. Profile of creatine kinase isoenzymes in skeletal muscles of marathon runners. Clin Chem. 1984;30:413–6.

499. Evans WJ, Meredith CN, Cannon JG, Dinarello CA, Frontera WR, Hughes VA, et al. Metabolic changes following eccentric exercise in trained and untrained men. Journal of Applied Physiology. 1986;61:1864–8.

500. Sorichter S, Mair J, Koller A, Pelsers MM, Puschendorf B, Glatz JF. Early assessment of exercise induced skeletal muscle injury using plasma fatty acid binding protein. British Journal of Sports Medicine. 1998;32:121–4.

501. Koskinen SOA, Lehti M. Molecular and Cellular Markers in Skeletal Muscle Damage after Acute Voluntary Exercise Containing Eccentric Muscle Contractions. In: Muscle Cell and Tissue - Current Status of Research Field. InTech; 2018. p. 19–32.

502. Minematsu T, Horii M, Oe M, Sugama J, Mugita Y, Huang L, et al. Skin Blotting: A Noninvasive Technique for Evaluating Physiological Skin Status. Advances in Skin & Wound Care. 2014;27:272–9.

503. Tamai N, Minematsu T, Maeda T, Yabunaka K, Sanada H. The relationship between skin ultrasound images and muscle damage using skin blotting in wheelchair basketball athletes. Spinal Cord. 2020;58:1022–9.

504. Luo T-T, Sun Z-H, Li C-X, Feng J-L, Xiao Z-X, Li W-D. Monitor for lactate in perspiration. The Journal of Physiological Sciences. 2021;71.

505. Phaniendra A, Jestadi DB, Periyasamy L. Free Radicals: Properties, Sources, Targets, and Their Implication in Various Diseases. Indian Journal of Clinical Biochemistry. 2015;30:11–26.

506. Sakellariou GK, Jackson MJ, Vasilaki A. Redefining the major contributors to superoxide production in contracting skeletal muscle. The role of NAD(P)H oxidases. Free Radical Research. 2014;48:12–29.

507. Boya P, Kroemer G. Lysosomal membrane permeabilization in cell death. Oncogene. 2008;27:6434–51.

508. Serrano-Puebla A, Boya P. Lysosomal membrane permeabilization in cell death: new evidence and implications for health and disease. Annals of the New York Academy of Sciences. 2016;1371:30–44.

509. Sutton JR, Toews CJ, Ward GR, Fox IH. Purine metabolism during strenuous muscular exercise in man. Metabolism. 1980;29:254–60.

510. Hellsten Y, Richter EA, Kiens B, Bangsbo J. AMP deamination and purine exchange in human skeletal muscle during and after intense exercise. The Journal of Physiology. 1999;520:909–20.

511. Moore Z, Patton D, Rhodes SL, O'Connor T. Subepidermal moisture (SEM) and bioimpedance: a literature review of a novel method for early detection of pressure-induced tissue damage (pressure ulcers). International Wound Journal. 2017;14:331–7.

512. Nguyen PKT, Smith A-L, Reynolds KJ. A literature review of different pressure ulcer models from 1942-2005 and the development of an ideal animal model. Australasian Physical & Engineering Sciences in Medicine; Dordrecht. 2008;31:223–5.

513. Call E, Groberg DF, Santamaria N. Chapter 19 - What makes a good device for the diabetic foot. In: Gefen A, editor. The Science, Etiology and Mechanobiology of Diabetes and its Complications. Academic Press; 2021. p. 327–45.

514. Early M, Kelly DJ. The role of vessel geometry and material properties on the mechanics of stenting in the coronary and peripheral arteries. Proc Inst Mech Eng H. 2010;224:465–76.

515. Mbithi FM, Chipperfield AJ, Steer JW, Dickinson AS. Predictive Control for an Active Prosthetic Socket informed by FEA-based Tissue Damage Risk Estimation. In: 2019 41st Annual International Conference of the IEEE Engineering in Medicine and Biology Society (EMBC). 2019. p. 2073–6.

516. Hong YL, Yao Y, Wong S, Bian L, Mak AFT. Change in viability of C2C12 myoblasts under compression, shear and oxidative challenges. Journal of biomechanics. 2016;49:1305–10.

517. Bramley JL, Worsley P, Bader D, Everitt C, Darekar A, King L, et al. Changes in tissue composition and load response after transtibial amputation indicate biomechanical adaptation. 2021. https://doi.org/10.31224/osf.io/b3y4h.

518. Tabas I, Ron D. Integrating the mechanisms of apoptosis induced by endoplasmic reticulum stress. Nat Cell Biol. 2011;13:184–90.

519. Ron D, Walter P. Signal integration in the endoplasmic reticulum unfolded protein response. Nature Reviews Molecular Cell Biology. 2007;8:519–29.

520. Szegezdi E, Logue SE, Gorman AM, Samali A. Mediators of endoplasmic reticulum stress-induced apoptosis. EMBO Rep. 2006;7:880–5.

521. Dupont-Versteegden EE. Apoptosis in skeletal muscle and its relevance to atrophy. World J Gastroenterol. 2006;12:7463–6.

522. Wang WZ, Fang X-H, Stephenson LL, Khiabani KT, Zamboni WA. Ischemia/reperfusion-induced necrosis and apoptosis in the cells isolated from rat skeletal muscle. Journal of Orthopaedic Research. 2008;26:351–6.

523. Chouchani ET, Pell VR, Gaude E, Aksentijevi[c acute] D, Sundier SY, Robb EL, et al. Ischaemic accumulation of succinate controls reperfusion injury through mitochondrial ROS. Nature. 2014;515:431.

524. Tran TP, Tu H, Liu J, Muelleman RL, Li Y-L. Mitochondria-Derived Superoxide Links to Tourniquet-Induced Apoptosis in Mouse Skeletal Muscle. PLoS ONE. 2012;7:e43410.

525. Olszewski WL. Physiology – Lymph Flow. In: Lee B-B, Bergan J, Rockson SG, editors. Lymphedema. London: Springer London; 2011. p. 69–74.

526. Bergan J, Bunke N. General Considerations. In: Lee B-B, Bergan J, Rockson SG, editors. Lymphedema: A Concise Compendium of Theory and Practice. London: Springer London; 2011. p. 3–10.

527. Olszewski WL. Pathology and Histochemistry. In: Lee B-B, Bergan J, Rockson SG, editors. Lymphedema. London: Springer London; 2011. p. 75–80.

528. Rockson SG. Physiology, Pathophysiology, and Lymphodynamics: General Overview. In: Lee B-B, Bergan J, Rockson SG, editors. Lymphedema: A Concise Compendium of Theory and Practice. London: Springer London; 2011. p. 59–61.

529. Zampell JC, Aschen S, Weitman ES, Yan A, Elhadad S, De Brot Andrade M, et al. Regulation of Adipogenesis by Lymphatic Fluid Stasis Part I: Adipogenesis, Fibrosis, and Inflammation. Plast Reconstr Surg. 2012;129:825–34.

530. Krouskop TA, Reddy NP, Spencer WA, Secor JW. Mechanisms of decubitus ulcer formation — An hypothesis. Medical Hypotheses. 1978;4:37–9.

531. Proske U, Morgan DL. Muscle damage from eccentric exercise: mechanism, mechanical signs, adaptation and clinical applications. The Journal of Physiology. 2001;537:333–45.

532. Wong JKF, Alyouha S, Kadler KE, Ferguson MWJ, McGrouther DA. The cell biology of suturing tendons. Matrix Biol. 2010;29:525–36.

533. Slomka N, Oomens CWJ, Gefen A. Evaluating the effective shear modulus of the cytoplasm in cultured myoblasts subjected to compression using an inverse finite element method. Journal of the Mechanical Behavior of Biomedical Materials. 2011;4:1559–66.

534. Davies PF, Tripathi SC. Mechanical stress mechanisms and the cell. An endothelial paradigm. Circulation Research. 1993;72:239–45.

535. Ingber D. Integrins as mechanochemical transucers. Current Opinion in Cell Biology. 1991;3:841–8.

536. Kaye D, Pimental D, Prasad S, Mäki T, Berger HJ, McNeil PL, et al. Role of transiently altered sarcolemmal membrane permeability and basic fibroblast growth

factor release in the hypertrophic response of adult rat ventricular myocytes to increased mechanical activity in vitro. Journal of Clinical Investigation. 1996;97:281–91.

537. Nakamura TY, Iwata Y, Sampaolesi M, Hanada H, Saito N, Artman M, et al. Stretch-activated cation channels in skeletal muscle myotubes from sarcoglycan-deficient hamsters. American Journal of Physiology-Cell Physiology. 2001;281:690–9.

538. Yeung EW, Whitehead NP, Suchyna TM, Gottlieb PA, Sachs F, Allen DG. Effects of stretch-activated channel blockers on [Ca2+]i and muscle damage in the mdx mouse. The Journal of Physiology. 2005;562:367–80.

539. Pimentel DR, Amin JK, Xiao L, Miller T, Viereck J, Oliver-Krasinski J, et al. Reactive Oxygen Species Mediate Amplitude-Dependent Hypertrophic and Apoptotic Responses to Mechanical Stretch in Cardiac Myocytes. Circulation Research. 2001;89:453–60.

540. Hervé J-C. Reciprocal influences between cell cytoskeleton and membrane channels, receptors and transporters. Biochimica et Biophysica Acta (BBA) - Biomembranes. 2014;1838:511–3.

541. Burkholder TJ. Mechanotransduction in skeletal muscle. Front Biosci. 2007;12:174–91.

A. Pressure-related damage mechanisms explained

1. Ischemia

When a mechanical load is applied to soft tissue, small capillaries and vessels might get obstructed (**Figure A-1**). The following paragraphs provide an overview over the mechanisms activated as a result of ischemia.

All cellular activities are based on the availability of energy. This energy is usually provided by adenosine triphosphate (ATP), which is produced during aerobic metabolism, where carbohydrates, amino acids, and fat are converted into ATP in the presence of oxygen (O_2). When the tissue is deformed and the blood supply occluded, the cell is deprived of the oxygen that this system relies on. Subsequently, it switches to an anaerobic metabolism, where glucose is now broken down without the aid of oxygen in a much less efficient way. By-products of anaerobic metabolism are lactic acid and hydrogen ions (H^+), which accumulate in the cytosol and decrease the cellular pH. To buffer the acidosis, a chain of pumps transports some of the hydrogen ions across the cell membrane in exchange for calcium ions (Ca^{2+}). Mechanisms to reduce the cytosolic calcium fail due to the shortage of ATP, including membrane pumps in the cell membrane and endoplasmic reticulum. The subsequent calcium overload activates a variety of enzymes and proteases that weaken the cytoskeleton: calpains disassemble cytoskeletal proteins; phosopholipases attack membrane lipids; protein kinase phosphorylates proteins [107, 165, 439, 442]. All these activities lead to a degradation of the cell membrane, a loss of cellular integrity and a decreased viability. The cell is then more prone to mechanical damage i.e. by direct deformation. Calcium ions also increase the expression of inflammatory metabolites and signalling proteins like cytokines and chemokines, which trigger inflammatory processes [107].

The deprivation of oxygen also increases the number of ROS within the cell. They are produced by the endoplasmic reticulum as part of its stress response [518], as well as within the mitochondria as a result of the disrupted electron transport chain, which is part of the aerobic metabolism and strongly dependent on the availability of oxygen [442]. The mitochondria's permeability transmission pore (PTP), an unselective channel, starts to leak due to this increase in ROS, calcium influx, the subsequent fall in its membrane potential, and additional stimuli by the endoplasmic reticulum's stress

response [440, 442, 519, 520]. ROS can therefore leave the mitochondria and accumulate in the cytosol. As ROS have an unpaired electron on the outer shell, they are highly reactive and cause changes in lipids, proteins, and the DNA, leading to dysfunction of cellular processes, and permeability of membranes of cellular organelles and the cell itself. [107, 505, 507, 508].

The PTP releases not only ROS but also apoptosis inducing factor (AIF) and cytochrome C, which activate a chain of caspase reactions. These cascades lead to the dissolution of the nuclear membrane and cleavage of the DNA, and ultimately apoptosis [165, 520–522]. So overall, ischemia may lead to an increased cell fragility, inflammation, and apoptosis.

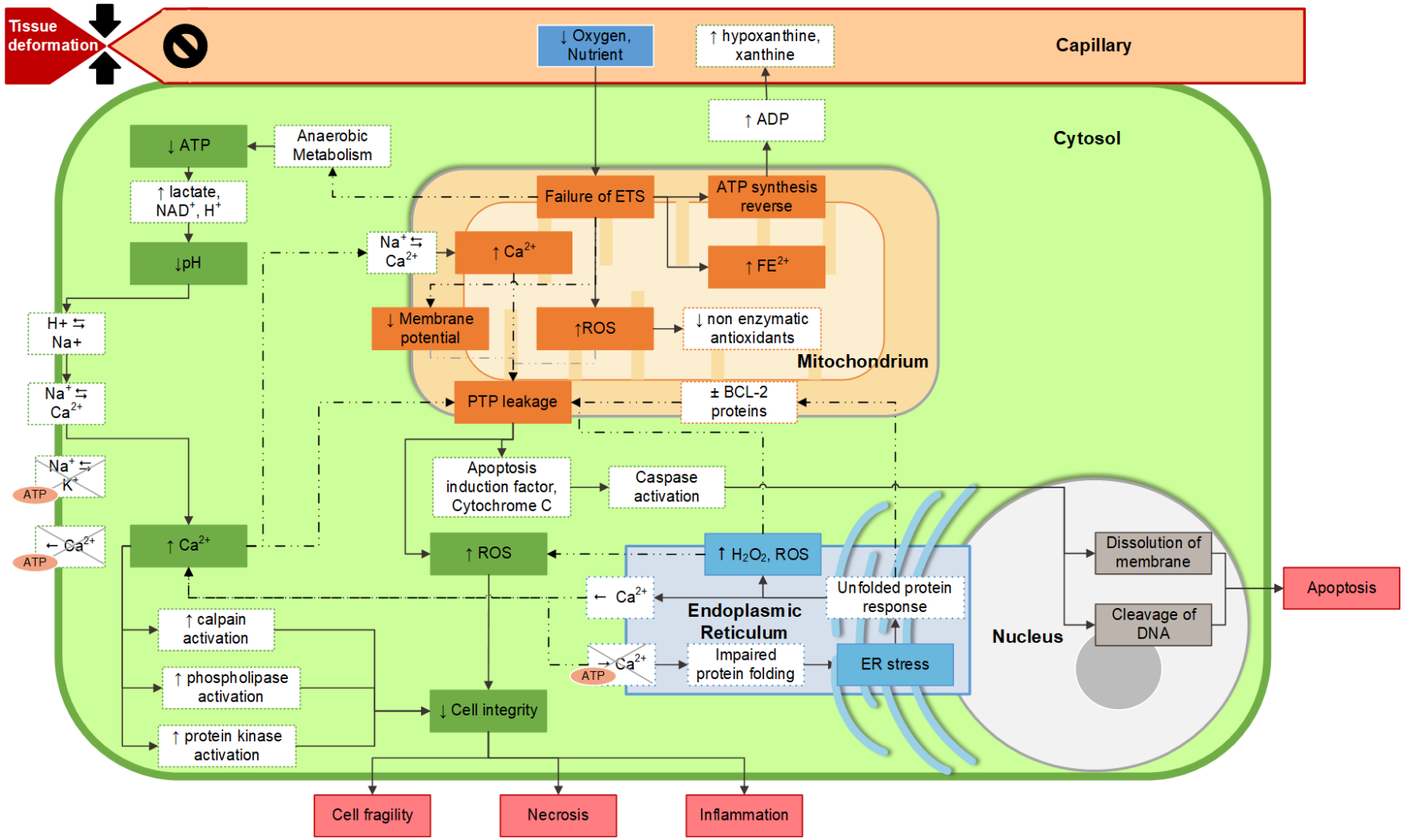

Figure A-1: Overview over intracellular processes during Ischemia. Blood vessel in red, cell in green, nucleus grey, endoplasmic reticulum blue, mitochondrion orange.

2. Ischemia Reperfusion

During reperfusion (**Figure A-3**), the damage initiated by ischemia is exacerbated. Once the blood flow is restored, the hydrogen ions that accumulated around the anaerobic cell during its attempt to balance out the decreased intracellular pH level, are transported away. The following increase in the proton gradient between the cell and its environment leads to a further uptake of calcium ions into the cell to regain homeostasis, rapidly increasing cellular damage. Another imbalance arises from the osmotic gradient between the cell and its environment. During ischemia, molecules excreted by the cell aggregate in its surrounding. When these molecules are taken up by the blood recirculation, the resulting osmotic gradient leads to water uptake and cell swelling (**Figure A-2**), reducing cellular integrity [442].

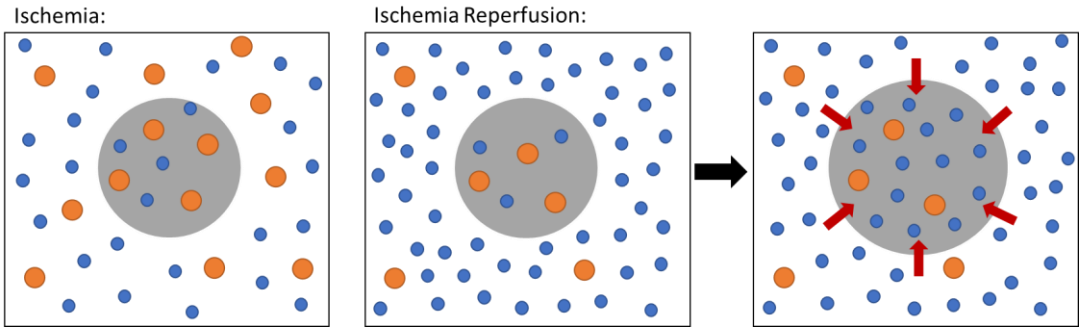

Figure A-2: Osmotic gradient. During Ischemia, the water (blue) and solute (orange) concentration of the cell (grey) and its environment are at equilibrium. As the solutes are removed in the event of reperfusion, the cellular environment now has a higher water concentration than the cell. Subsequently, water molecules move down the concentration gradient into the cell, causing an increase in cellular volume and therefore cell swelling.

As the blood supply is restored, oxygen becomes available and the cell switches back to an aerobic metabolism. However, the defect of the electron transport chain of the mitochondria due to the insufficient ATP supply results in a continuous ROS production [107, 505, 523, 524]. The amount of mitochondrial ROS is further increased by the accumulation of iron ions (Fe^{2+}) [505]. Whilst nonenzymatic antioxidants would usually contain ROS, their decrease in number during ischemia enhances the severity of ROS destruction at reperfusion.

The other main source of ROS is the oxidation of xanthine and hypoxanthine. Both are deposited during ischemia, when ATP synthesis is reversed to get an additional source of energy [442, 505, 506]. As they can cross the cell membrane, their damage potential is not restricted to the skeletal muscle cell but extends to the microvasculature, including endothelial and parenchymal cells, where they can also

activate platelets that aggregate at the vessel wall, and enhance oedema formation [107].

To worsen the calcium ion and ROS overload even more, the mitochondrial membrane pore might open. During ischemia, the cellular acidosis kept its leakage to a minimum. The combination of the radically increased calcium ion and ROS levels that depolarise the mitochondrial membrane potential, together with the regaining of a normal pH level now drastically increase the likelihood of a PTP opening [440, 442].

Subsequently, all the calcium ions and ROS that were contained in the mitochondria might be released to the cytosol, together with proapoptotic factors. The damaged mitochondria can then no longer synthesise ATP, causing a further energy depletion. A prolonged opening may lead to excessive water entry, matrix swelling, and outer membrane rupture. [440]

Overall, reperfusion results in a burst of ROS and calcium ions. Together with the restoration of the pH level, the mitochondrial PTP might be opened. The results will be further cell damage, swelling, cell death, endothelial dysfunction, and inflammation.

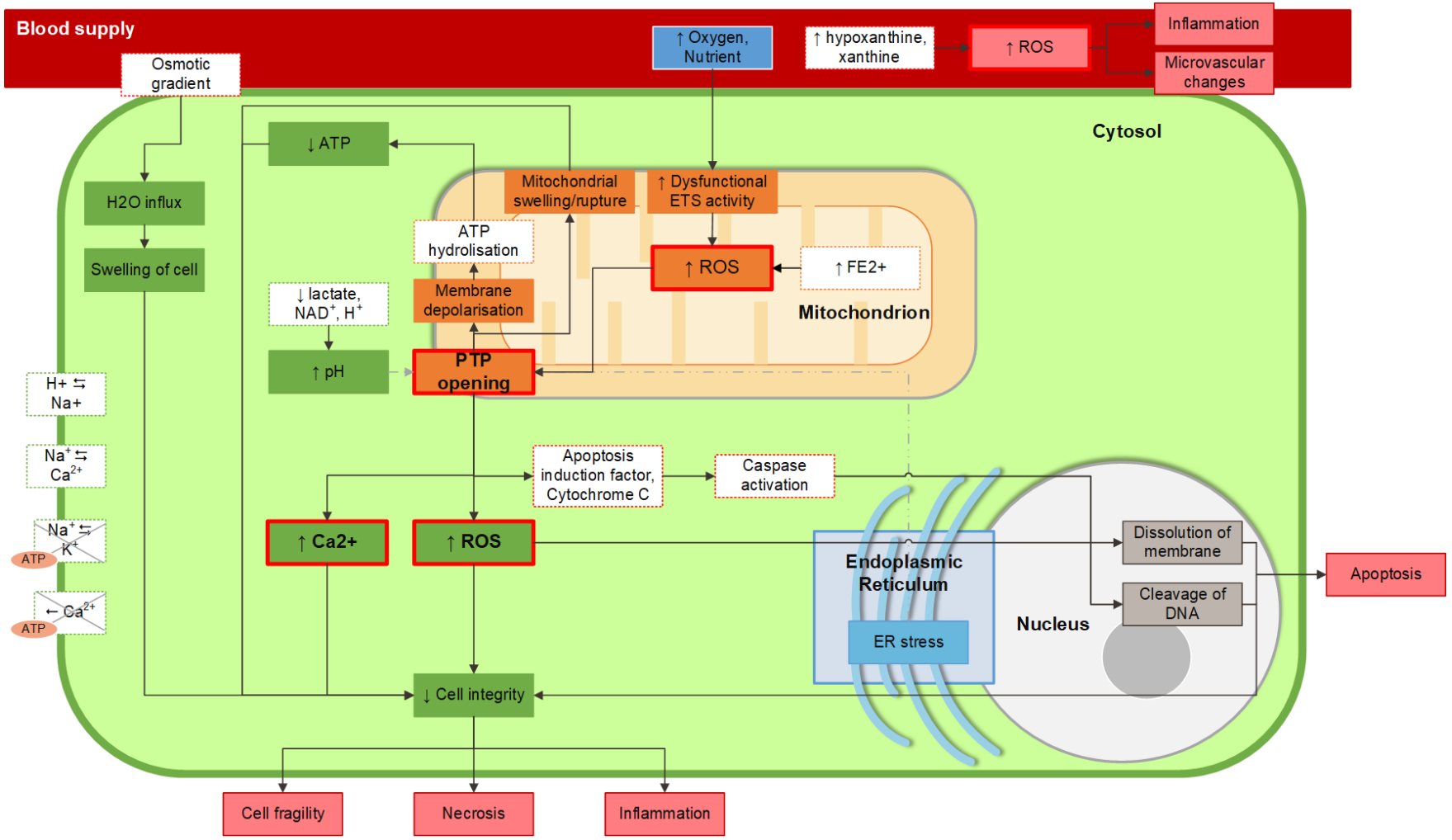

Figure A-3: Overview over intracellular processes during ischemia-reperfusion. Blood vessel in red, cell in green, nucleus grey, endoplasmic reticulum blue, mitochondrion orange.

3. Impaired Lymphatic Drainage

The lymphatic system is a network of vessels that regulates fluid homeostasis and is responsible for immune defence. It maintains the fluid balance by clearing the interstitial spaces of excess water, cellular debris, and metabolic waste products, including large molecules, lipids, antigens, and immune cells. This system relies heavily on pressure gradients and muscular contractions that propel these excess substances through lymphatic ducts [525]. During DTI, lymphedema may arise from the obliteration of lymphatic vessels by mechanical loading, causing an immune response and inflammation, aided by the expression of cytokines, raised ROS levels, and the stimulation of macrophages [526–529].

These inflammatory factors, together with biowastes like ROS that are excreted by the cell in response to mechanical loading, are believed to generate a toxic environment [112, 530]. This may affect the mechanical properties of surrounding muscle cells, thereby increasing cellular damage and reducing the capability to withstand further mechanical loading. Yao et al. [112] investigated this process by collecting biowastes from skeletal muscle cells in agarose that were exposed to various load-duration combinations. Different lines of myoblasts where then cultured in the biowaste medium to determine its toxicity. Additionally, the influence of biowaste accumulation on the damage stress threshold was investigated. The results indicated a significant release of toxic biowastes after two hours, as prolonged, low compressive stress lead to a weakening of skeletal muscle cells, whilst short-term, high compressive stress yielded no difference. Successive Finite Element simulation showed that a higher release rate of biowastes was seen under prolonged loading conditions due to gradual breakdown of cell membranes, which can increase the expansion of, and worsen tissue damage, if not cleared. The damage propagation might be enhanced by increased diffusion coefficients, resulting from lymphedema.

Overall, accumulated biowastes like cytokines and ROS might affect mechanical properties of surrounding muscle cells and create a toxic cell environment, which supports the progression of cellular damage under subsequent loading by weakening cellular capabilities to withstand compressive stress. For the lymphatic system, prolonged loading might be most dangerous, as significant amounts of biowastes can be generated before cell damage, whilst high stress may cause early rupture of cell membranes. However, an identification and quantification of the main toxins in biowastes is still missing.

4. Direct deformation

The last mechanism to be discussed is direct deformation. This is the most recently developed theory of cell damage and death in DTI, first proposed by Bouten et al. in 2001. Their idea was that mechanical loading may not only impair the blood and lymphatic system, but also damage the cell directly. Similar observations have been made for eccentric contractions of skeletal muscle during exercise, or when suturing wounds [531, 532]. Large deformation of the tissue thereby deforms the outer and inner membranes of cells, leading to stretch under tensile loads and folding under compression [155, 533]. Bouten et al. observed that compression of up to 60% strain of mouse muscle cells in agarose and in a myotube structure caused buckling and bursting of the membrane at the cell equator, where tension is the highest.

When a load is applied, the external forces are transmitted through the ECM via integrins, which are mechanotransducers within the cell membrane that connect to the cytoskeleton. The cytoskeleton is the cell's framework that usually counteracts these external forces, thereby controlling the cell's shape, growth, and migration. Under extensive external loads, these support structures for force transmission may be altered either directly, via associated proteins, or via changes in other proteins within the plasma membrane, like ion channels or enzymes. [534, 535] Cell organelles, like the nucleus, might be damaged directly by the subsequent deformation [535, 536], or indirectly due to an increased membrane permeability.

The exact pathways of extensive membrane permeability are not fully understood yet. One explanation might be a mechanical damage to the surface membrane, leading to a rapid equilibrium between the intracellular and extracellular space [158]: Natrium and calcium ions enter the cell through membrane tears, whilst soluble proteins are lost to the extracellular space. This interference of the natural ion gradients depolarises the membrane potential, disrupting the cell's homeostasis. Despite giving a reason for the high calcium and natrium ion levels after mechanical insults, it seems unlikely that this theory is the actual cause as membrane tears are usually repaired by the cell: The leaky areas are sealed either by intracellular vesicles, activated by a calcium overload, by membrane fusion, or by reduction of the membrane tension [159–164]. Another plausible cause could be the activation of calcium ion leak channels. They are opened by proteolysis that is initiated by localised calcium accumulation due to membrane tears, and further boost calcium overload and proteolysis [158, 537]. Lastly, the membrane might become permeable because of

stretch activated ion channels [158, 161, 538]. Following this would be an increased, non-selective ion influx i.e. of natrium, potassium, and calcium. The subsequent membrane depolarisation may open voltage dependent calcium ion channels and exacerbate the influx. [537]

Although calcium overload is often named as stimulator of cell death, Ceelen et al. [198] challenged this idea, as they could not clearly assign a causality of elevated calcium ion levels to cell death in their experiments on cultured myotubes. The observed high calcium levels could have resulted from an increased membrane permeability following lethal cell damage, rather than inducing it. An alternative process to explain cell death might be the release of factors for neutrophil chemotaxis, and ROS, provoking inflammation and oxidative stress [491, 539].

Overall, loading alters the mechanotransduction of cells, influencing their structural elements and activating secondary messengers [534, 540]. The result is a stimulation of kinases, proteases, nucleases, and ROS that breakdown cellular components, leading to the loss of homeostasis, inflammation and ultimately cell death [155, 158, 541].

B. PRISMA-ScR Checklist

Preferred Reporting Items for Systematic reviews and Meta-Analyses extension for Scoping Reviews (PRISMA-ScR) Checklist

SECTION	ITEM	PRISMA-ScR CHECKLIST ITEM	REPORTED ON PAGE #
TITLE			
Title	1	Identify the report as a scoping review.	8
ABSTRACT			
Structured summary	2	Provide a structured summary that includes (as applicable): background, objectives, eligibility criteria, sources of evidence, charting methods, results, and conclusions that relate to the review questions and objectives.	1-2 (published paper)
INTRODUCTION			
Rationale	3	Describe the rationale for the review in the context of what is already known. Explain why the review questions/objectives lend themselves to a scoping review approach.	9-14
Objectives	4	Provide an explicit statement of the questions and objectives being addressed with reference to their key elements (e.g., population or participants, concepts, and context) or other relevant key elements used to conceptualize the review questions and/or objectives.	14
METHODS			
Protocol and registration	5	Indicate whether a review protocol exists; state if and where it can be accessed (e.g., a Web address); and if available, provide registration information, including the registration number.	Not applicable
Eligibility criteria	6	Specify characteristics of the sources of evidence used as eligibility criteria (e.g., years considered, language, and publication status), and provide a rationale.	15-16
Information sources*	7	Describe all information sources in the search (e.g., databases with dates of coverage and contact with authors to identify additional sources), as well as the date the most recent search was executed.	14-15
Search	8	Present the full electronic search strategy for at least 1 database, including any limits used, such that it could be repeated.	15
Selection of sources of evidence†	9	State the process for selecting sources of evidence (i.e., screening and eligibility) included in the scoping review.	16-17
Data charting process‡	10	Describe the methods of charting data from the included sources of evidence (e.g., calibrated forms or forms that have been tested by the team before their use, and whether data charting was done independently or in duplicate) and any	15-16

SECTION	ITEM	PRISMA-ScR CHECKLIST ITEM	REPORTED ON PAGE #
		processes for obtaining and confirming data from investigators.	
Data items	11	List and define all variables for which data were sought and any assumptions and simplifications made.	15
Critical appraisal of individual sources of evidence§	12	If done, provide a rationale for conducting a critical appraisal of included sources of evidence; describe the methods used and how this information was used in any data synthesis (if appropriate).	Not applicable
Synthesis of results	13	Describe the methods of handling and summarizing the data that were charted.	16
RESULTS			
Selection of sources of evidence	14	Give numbers of sources of evidence screened, assessed for eligibility, and included in the review, with reasons for exclusions at each stage, ideally using a flow diagram.	16-17
Characteristics of sources of evidence	15	For each source of evidence, present characteristics for which data were charted and provide the citations.	18-32
Critical appraisal within sources of evidence	16	If done, present data on critical appraisal of included sources of evidence (see item 12).	Not relevant
Results of individual sources of evidence	17	For each included source of evidence, present the relevant data that were charted that relate to the review questions and objectives.	18-32
Synthesis of results	18	Summarize and/or present the charting results as they relate to the review questions and objectives.	18-32
DISCUSSION			
Summary of evidence	19	Summarize the main results (including an overview of concepts, themes, and types of evidence available), link to the review questions and objectives, and consider the relevance to key groups.	32-38
Limitations	20	Discuss the limitations of the scoping review process.	38
Conclusions	21	Provide a general interpretation of the results with respect to the review questions and objectives, as well as potential implications and/or next steps.	39
FUNDING			
Funding	22	Describe sources of funding for the included sources of evidence, as well as sources of funding for the scoping review. Describe the role of the funders of the scoping review.	27 (published paper)

JBI = Joanna Briggs Institute; PRISMA-ScR = Preferred Reporting Items for Systematic reviews and Meta-Analyses extension for Scoping Reviews.

* Where *sources of evidence* (see second footnote) are compiled from, such as bibliographic databases, social media platforms, and Web sites.

† A more inclusive/heterogeneous term used to account for the different types of evidence or data sources (e.g., quantitative and/or qualitative research, expert opinion, and policy documents) that may

be eligible in a scoping review as opposed to only studies. This is not to be confused with *information sources* (see first footnote).
‡ The frameworks by Arksey and O'Malley (6) and Levac and colleagues (7) and the JBI guidance (4, 5) refer to the process of data extraction in a scoping review as data charting.
§ The process of systematically examining research evidence to assess its validity, results, and relevance before using it to inform a decision. This term is used for items 12 and 19 instead of "risk of bias" (which is more applicable to systematic reviews of interventions) to include and acknowledge the various sources of evidence that may be used in a scoping review (e.g., quantitative and/or qualitative research, expert opinion, and policy document).

From: Tricco AC, Lillie E, Zarin W, O'Brien KK, Colquhoun H, Levac D, et al. PRISMA Extension for Scoping Reviews (PRISMA-ScR): Checklist and Exp lanation. Ann Intern Med. ;169:467–473. doi: 10.7326/M18-0850

C. Explanation of criteria for decision analysis of possible pressure injury models

Representation of true morphology and physiology

A model system should mimic a disease or injury procedure as closely as possible to ensure results are relevant and reliable. Thus, the potential model systems were rated according to how well they represent the highly hierarchical cellular structure of skeletal muscle (fibrous cell shape and additional structures like ECM relevant for pressure distribution and cellular interactions) as well as its supply systems, including lymphatic and vascular networks (necessary for fully functional physiological processes). Single cells without any supply systems, fibrous structure, or ECM scored lowest, followed by BAM with a premature hierarchical structure, then *ex vivo* studies with full hierarchical structure but impaired supply systems, and the best representation by *in vivo* models with both hierarchical structure and supply system intact.

Controllability of damage mechanisms

The focus of the proposed study was on investigating direct deformation as main damage mechanism. It was therefore important to differentiate deformation-induced damage from other factors such as ischemia, ischemia-reperfusion, and an impaired lymphatic drainage. With all of these processes being inevitably interlinked to ensure the functioning of a cell, none of the model systems allow for perfect separation. However, single cells and BAM naturally do not have a vascular or lymphatic supply, making it more likely that true deformation damage can be measured. *Ex vivo* studies can have artificial nutrient and oxygen supply to avoid ischemia and biowaste accumulation, allowing to separate deformation damage to a certain extent. In *in vivo* scenarios, it is virtually impossible to separate each of the damage mechanisms.

Feasibility of preparation and testing

To make the whole project feasible, the available equipment, training, and the expertise of the author needed to be considered. Although the author herself had no previous experience in working with biological material, simple cell cultures are commonly studied within the department of biomedical engineering at Strathclyde. In comparison, greater expertise is needed to culture bioartificial muscle constructs, which has to the author’s knowledge not been done within the University of Strathclyde. Handling of BAM is also more intricate than for the other model systems.

Animal experiments on the other hand are often performed in the Strathclyde Institute of Pharmacy and Biomedical Sciences, making necessary equipment and training easily accessible.

Fulfilment of 3Rs and ease of ethical procedures

Whenever working with animals for medical experiments is considered, the decision on a suitable procedure should be guided by the 3R principles of replacement, reduction, and refinement. Working with cells and cell constructs obviously avoids the use of animals, making it the best method regarding 3R. It also requires no additional ethical approval. For *ex vivo* studies, so-called “partial replacement” can be achieved as no procedures would be performed on the animal prior to euthanisation. This also minimises the need for ethical approval. Additionally, animals can be “shared” with other research groups to minimise the number of animals needed for studies within the University. *In vivo* studies on the other hand require the time-consuming application for a home office licence and conform least with the 3R principles.

Low cost

Although not the main priority, the cost of the experiment should be considered. Animals and solutions related to the dissection are comparably cheap, especially when resources are shared with other research groups, making *ex vivo* studies a cost-effective option. Performing *in vivo* studies on the other hand needs additional equipment and facilities, making it more expensive than *ex vivo* approaches. Single cell studies were rated similar to *ex vivo* studies with more specific consumables being required as well as the acquisition of a suitable cell line, which can be used for an extensive number of experiments. In comparison, growing BAM requires further differentiation and development than single cells, making it more expensive.

Low variability

Lastly, variability introduced by biological variability as well as the environment of the samples was considered as it might influence sample sizes needed for meaningful results. *In vitro* studies thereby have the lowest variability as they are based on cell lines grown in a controllable environment. *Ex vivo* studies on the other hand have a much higher biological variability but the environment during the experimental studies is controllable. The highest variability is to be expected from *in vivo* studies with high biological variability and very limited influence on the experimental environment.

D. Materials and method for *ex vivo* experiments

D-1: Materials for *ex vivo* experiments

Solutions

- MOPS buffer
- ProY solution
- 10% Neutral buffered formalin
- PBS
- EtOH
- Histoclear
- Deionised water
- DPX

Consumables

- Gloves
- 5ml vials
- Petri dishes with Sylgard or medical grade silicone layer
- Glassware
- Pipettes
- Dissection tools (forceps, scissors, pins)
- Insect pins

Equipment

- Bose Electroforce 3200
- Flat indenter
- pH meter
- Magnetic stirrer
- Automatic tissue processor
- Wax embedder
- Microtome
- Water bath
- Drying oven
- Epifluorescence microscope
- Aluminium foil
- Histology cassettes
- Microscope slides
- Coverslips
- Microtome blades
- Brushes
- India ink pen
- Tape
- Pencil
- Sharpie
- Lab coats

D-2: Preparation protocols for solutions

MOPS buffer:

Prepare 25ml of 10x stock solution (freezable)

145mM	Sodium chloride	21.8g
2mM	MOPS	1.046g
4.7mM	Potassium chloride	0.876g
1.2mM	Monosodium phosphate	0.486g
1.2mM	Magnesium chloride	3ml

Defrost stock solution and combine with the following ingredients no more than one day in advance:

5mM	Glucose	0.2252g
0.02mM	EDTA	1.4615mg
2mM	Sodium pyruvate	5ml
2mM	Calcium chloride	0.5ml

Add enough deionised water to get 250ml before adjusting pH to 7.4. Store at 5°C until usage.

ProY staining solution:

Prepare 5ml of 0.1% ProY solution per muscle. For a total of 4 muscles (2 x EDL, 2 x SOL), dissolve 0.02g of Procion Yellow MX4R in 19.98g of PBS. Keep solution covered with aluminium foil to minimse light exposure and use within a few hours.

D-3: General Method

1. Isolate EDL and SOL from male Sprague-Dawley rats. (see D-4)
2. Pin out samples in separate petri-dishes with medical-grade silicone base with insect pins and submerge in MOPS buffer.
3. Transverse mechanical loading by compressing the mid-belly region of the muscle with a flat indenter attached to custom device or Bose Electroforce.
4. Remove indenter and MOPS buffer. Replace with 0.5ml of 0.1% ProY in PBS for 1h. Flip the muscle halfway through to ensure even penetration and keep covered to avoid photobleaching.
5. Remove ProY solution and wash sample 3 x 5min with PBS.
6. Blot sample to remove excess PBS and mark the indentation site with India ink. Let it dry for 10min to avoid smudging.
7. Cover pinned out muscle with few drops of 10% NBF for 10min to avoid shrinkage
8. Transfer each sample into a pre-labelled vial tube with 10% NBF overnight (26h)
9. If storing sample, transfer into 70% EtOH until further processing.
10. Gross each sample before placing it into histology cassettes. Cut the sample transversely with a surgical blade into 3mm wide slices. Cassette 1: Indentation site split into two; Cassette 2: Three CTRL sections from outside of indentation area. Label each cassette with pencil.
11. Process tissues overnight in automated processor with graded series of EtOH, Histoclear, and Paraffin. (see D-5)

12. Remove samples from processor and embed in Paraffin. Ensure that cross-sectional sides are facing up.
13. Cut each block into 3-4um cross-sections on rotary microtome (blade set to 4° angle).
14. Keep three slices every 120µm and spread onto warm water bath (30°C). Pick up slices with microscope slides and let them dry overnight.
15. Bake microscope slides in slide oven for up to 1h at 60°C.
16. Remove slides and cover samples with DPX before adding coverslip. Avoid bubbles and excessive pressure on the coverslip to avoid distortion of the sample.
17. Wait at least 20min for DPX to dry. Then store in covered container until imaging.

D-4: Protocol for isolation of extensor digitorum longus and soleus muscles from rat hindlimbs

Preparation

- Fixation of limbs with pushpins on cork board or aluminium covered styrofoam
- Lateral positioning of animal
- Starting with one hindlimb, superficial skin incision and removal of skin and fascia starting from the ankle until above knee joint
- Keep tissues moist by adding MOPS buffer ad libitum

Isolation of EDL:

- Localise four distal tendons that insert into middle and distal phalanges (digits 2-5). Test if EDL tendon is correctly identified by pulling gently on it – should flex the toes
- Hold tendon with forceps and cut
- Gently peel up muscle whilst cutting perimysium surrounding EDL and other surrounding muscles. Take care not to damage the EDL.
- Peel up to the proximal end where the ligament is connected to the lateral condyle of the tibia
- Cut ligament with scissors as distally as possible from muscle, releasing proximal origin of EDL
- Transfer isolated EDL into vial containing MOPS solution
- Repeat for EDL on contralateral limb
- Remove pins and position animal frontally, followed by fixation of the limbs

Isolation of SOL:

- Remove remaining skin from posterior lateral side of hindlimbs
- Hold achilles tendon with forceps
- Carefully rub gap open between Achilles tendon and other tendons
- When gap is visible, cut Achilles tendon as close as possible to foot
- Carefully continue to open gap by peeling of muscle group. Cut further fascia as you go, taking care not to injure SOL
- The SOL becomes visible when the gap is open up to the knee (darker pink than overlying gastrocnemius)
- When the knee joint is reached, cut ligaments at the proximal origin
- Separate SOL from gastrocnemius
- Transfer separated SOL into vial containing MOPS solution
- Repeat for SOL on contralateral limb

D-5: Automated tissue processing protocol

70%	EtOH in distilled water	2h
80%	EtOH in distilled water	2h
95%	EtOH in distilled water	2h
95%	EtOH in distilled water	2h
100%	EtOH	1.5h
100%	EtOH	1.5h
100%	EtOH	1h
100%	Histoclear	1.5h
100%	Histoclear	1h
100%	Paraffin	1h
100%	Paraffin	1h
Total		16.5h

D-6: Haematoxylin and Eosin staining protocol

Histoclear	2 x 5 min
100% EtOH	10 min
90% EtOH	10 min
70% EtOH	10 min
Running tap water	5 min
Haematoxylin	5 min
Running tap water	5min
Acid Alcohol	2 dips
Running tap water	5 min
Lukewarm tap water	2 min
Running tap water	5 min
Eosin	1 min
70% EtOH	10 min
90% EtOH	10 min
100% EtOH	10 min
Histoclear	2 x 5min
DPX mounting	

E. Data management plan

Administrative Data

Creator

Marisa Sargent

Creator Department

Biomedical Engineering

ID

mfb16160

Co-investigator(s)

Arjan Buis

Co-investigator(s) contact details

Arjan.Buis@strath.ac.uk (University of Strathclyde)

Project title

Prosthetic mechanobiology: How prosthesis-related loading influences skeletal muscle health

Project Description

An ex vivo model for transverse mechanical loading of skeletal muscle tissue was developed, based on murine tissue samples. These samples were fluorescently stained and prepared into cross-sections for optical analysis.
Full sections will be imaged on a widefield microscope in epifluorescence mode and processed further with ImageJ to be able to quantify the amount of damaged cells within each sample.

Funder

University of Strathclyde

Data Collection

What data will be collected or created?

Image files in .tif format will be created with Leica LAS X software (V.3.1.5.16308). These images are merged images of fluorescently stained skeletal muscle cross-sections.

How will the data be collected or created?

All samples will be given a unique name prior to being processed. This includes the type of muscle (EDL or SOL), a serial experiment number, as well as number 1 or 2 to differentiate between the two muscles taken from contralateral hindlimbs. Notes of this in combination with the intervention will be taken manually in a lab book.

The sample name will be carried forward to the sectioning process where it will be noted on the outer case of histology cassettes. When slicing samples to be transferred to microscope slides, microscope slides will gain an additional number (consecutively for each sample) as an indication of the position of the slices within the sample.
When imaging, each file is given the complete name from the processing steps, as well as TileScan"number", which is added automatically by the software. Notes will be taken in a lab book to document the imaging conditions of each TileScan, indicating the microscopic filter and integration time.

Documentation and Metadata

What documentation or metadata will accompany the data?

The following documentation and metadata will accompany the data in a lab book:

For sample preparation:
1. Date
2. Sample name
3. Duration of each preparation step
4. Additional comments on preparation (i.e. salience with regards to rats or preparation)
5. Intervention (indentation or control, details on indentation incl. weight, amount of time, static or dynamic)

For imaging:
1. Date
2. Sample name
3. Filter set (FITC or Y5)
4. Integration time in seconds

Ethics and Legal Compliance

How will ethical issues relating to data be managed?

There are no ethical issues expected.

How will copyright and Intellectual property (IPR) issues be managed?

Copyright belongs to the PI. However, commercially exploitable Intellectual Property (IP) rights belong to the University. Contact with the legal compliance team will be sought in case of arising issues.

Storage and Backup

How will data be stored, backed up and shared during the research project?

Imaging data will be stored on the initial computer where data was acquired for the duration of the PhD project. It will also be transferred to the OneDrive Strathclyde acount of the PI as well as an external hard drive for backup. Access is available for the PI and will be shared online with supervisors/collaborates as needed.

How will access and security to data be managed during the research project?

Access to data will be controlled by the PI. High security of data is not relevant as there are no ethical concerns related to the type of data generated. However, password protection of computer devices and private settings of the cloud files are in place.

Selection and Preservation

Which data should be retained, shared, preserved and destroyed

Data used in the final studies to assess the influence of different dynamic loading conditions should be preserved for later access. Additionally, all data that has been part of a publication will need to be maintained to be available to share with the public when required.
Preliminary data can be destroyed once the project is completed.

What is the long-term preservation plan for data?

Data will be preserved for a minimum of 10 years following completion of the project. They will be added to the pure network as well as made available to the supervisor for storage and ongoing communication in case of published data, unless otherwise required by the publisher.

Data Sharing

How will the data be shared?

1. Data will be published in a data journal or as supplementary information to an article
2. Data will be shared via the repository deposit (Pure portal)
3. Data will be made available to supervisor for personal communication

Are any restrictions on data sharing required?

IPR of the university is to be observed.

Responsibilities and Resources

Who will be responsible for data management?

Marisa Sargent will be responsible for data management.

What resources will you require to deliver your plan?

Access to the Pure portal as well as USB sticks to transfer data will be necessary.

F. Image analysis workflow FIJI/ImageJ

1. Pre-process for all images:

- Set global scale to 16px per 10 µm
- Convert images to 8bit greyscale
- Set measurements > mean intensity

2. Establish threshold from CTRLS (x6):

2.1. Subtract background

- Open FITC-filtered and Y5-filtered image of same cross-section
- Remove tendon manually on one of the images
- Measure background of 5 ROIs & average (both images)
- Subtract average background value from whole image (both images)
- Safe files as “CTRLX_FITC” or “CTRLX_Y5”
- Divide “CTRLX_FITC” by “CTRLX_Y5” image, gives “Result” image (32bit flow)
- Safe file as “CTRLX_combined”

2.2. Create mask of cells in Cellpose (Google Colab)

- Upload grayscale images “CTRLX_FITC” to Google drive folder
- Add file names to Cellpose
- Select settings “Cytoplasm”, “greyscale (0,0)”, “diameter 55.8”
- Run Cellpose
- Download result files as .npy
- Open masks in Cellpose (GUI) & save as .png with name “CTRLX_combined_label.tiff”
- Delete .npy and move .pngs to image folder

2.3. ImageJ analysis to identify threshold

- In FIJI, run “Labels to ROI” plugin of whole image folder with “CTRLX_combined_label.tiff” files, erode 2px
- Open overall excel file generated and retrieve mean intensity of “CTRLX_combined” images (= threshold)

3. Count number of dead cells from Indent (x6):

3.1. Subtract background

- Open FITC-filtered and Y5-filtered image of same cross-section
- Measure background of 5 ROIs & average (both images)
- Subtract average background value from whole image (both images)
- Safe file as “IndentX_FITC” or “IndentX_Y5”

3.2. Create mask of cells in Cellpose

- Upload grayscale images of “IndentX_FITC” to Google drive folder
- Add file names to Cellpose
- Select “Cytoplasm”, “greyscale (0,0)”, “diameter 55.8”
- Run Cellpose
- Download result files as .npy
- Open masks in Cellpose (GUI) & save as .png
- Delete npy and move pngs to desktop

3.3. ImageJ analysis to count number of dead cells

- Open “IndentX_FITC” and “IndentX_Y5” in FIJI/ImageJ
- Run “Labels to ROI” with corresponding Cellpose mask (individual image)
- Open new image (black background, dimensions identical to IndentX)
- Show all ROIs on new image > flatten > make binary > fill holes
- Save ROI image as “IndentX_mask”
- Image calculator > “IndentX_FITC” divided by “IndentX_Y5” (32-bit flow)
- Threshold new image by value from CTRLs (see 2.3) and convert to 8-bit mask
- Image calculator > “Result X” MIN “IndentX_mask”
- Analyse particles > size 250-infinity, circularity 0.3-1
- save area & No. of cells to excel

G. Calculation of Young's modulus for silicone layer

For the calculation of the Young's modulus, the following factors need to be known:

Young's modulus: $\boldsymbol{E = \frac{\sigma}{\varepsilon}}$ (stress over strain)

1. Stress: $\boldsymbol{\sigma = \frac{F}{A}}$ (force over area)

Stress was calculated from the maximum load of -0.324N divided by the area of the indenter (circular with r = 1mm).

$$\boldsymbol{\sigma = \frac{0.324N}{3.14 \times 10^{-6}} = 103kPa}$$

2. Strain: $\boldsymbol{\varepsilon = \frac{\Delta L}{L}}$ (change in thickness over original thickness)

Strain was calculated from deformation measurements taken with a Bose Electroforce 3100 during static indentation tests. For this, a maximum compressive load of 0.324N was applied with an indenter (r = 1mm) to an 8mm thick silicone layer (original thickness). The change in thickness was calculated from the displacement at the end of the test subtracted by displacement at the beginning of the test (**Figure G-1**).

With all values known for both the stress and strain formulas, the average Young's modulus could be calculated:

Sample	1.1	1.2	1.3	2.1	2.2	2.3	3.1	3.2	3.3	**Average**
L [m]	0.008	0.008	0.008	0.008	0.008	0.008	0.008	0.008	0.008	
ΔL [m]	$2.2E^{-4}$	$2.7E^{-4}$	$2.4E^{-4}$	$2.31E^{-4}$	$2.6E^{-4}$	$2.2E^{-4}$	$2.5E^{-4}$	$2.4E^{-4}$	$2.4E^{-4}$	
ε	$2.8E^{-2}$	$3.4E^{-2}$	$3.0E^{-2}$	$2.89E^{-2}$	$3.3E^{-2}$	$2.8E^{-2}$	$3.1E^{-2}$	$3.0E^{-2}$	$3.0E^{-2}$	
E [Pa]	$3.7E^{6}$	$3.0E^{6}$	$3.4E^{6}$	$3.57E^{6}$	$3.2E^{6}$	$3.7E^{6}$	$3.3E^{6}$	$3.4E^{6}$	$3.4E^{6}$	**3.42MPa**

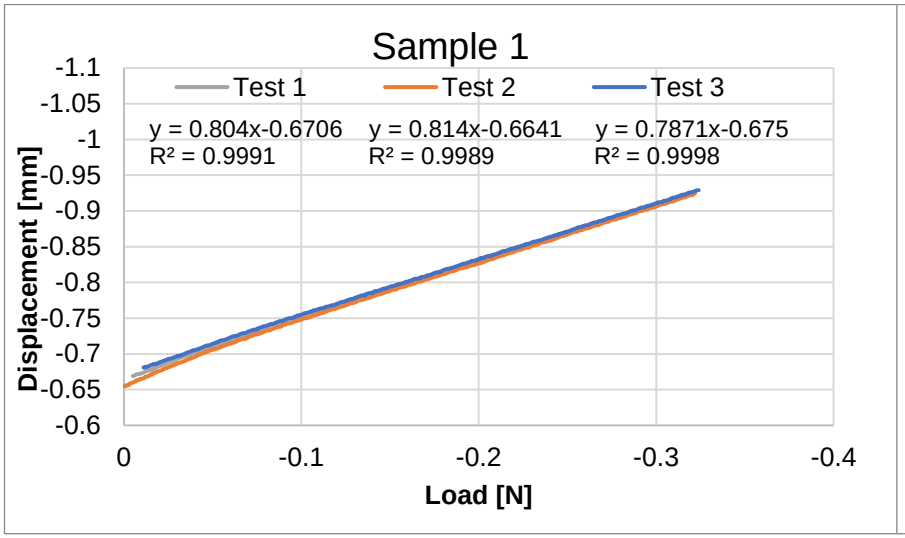

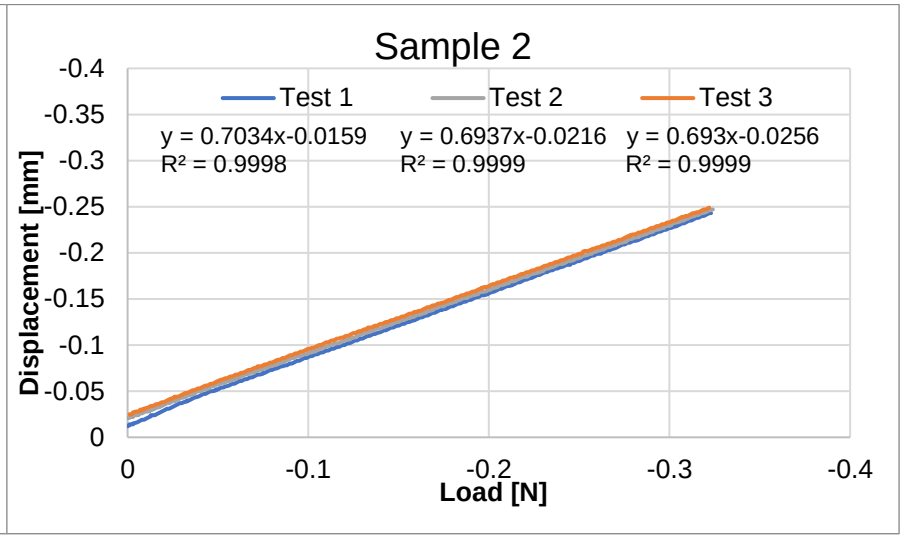

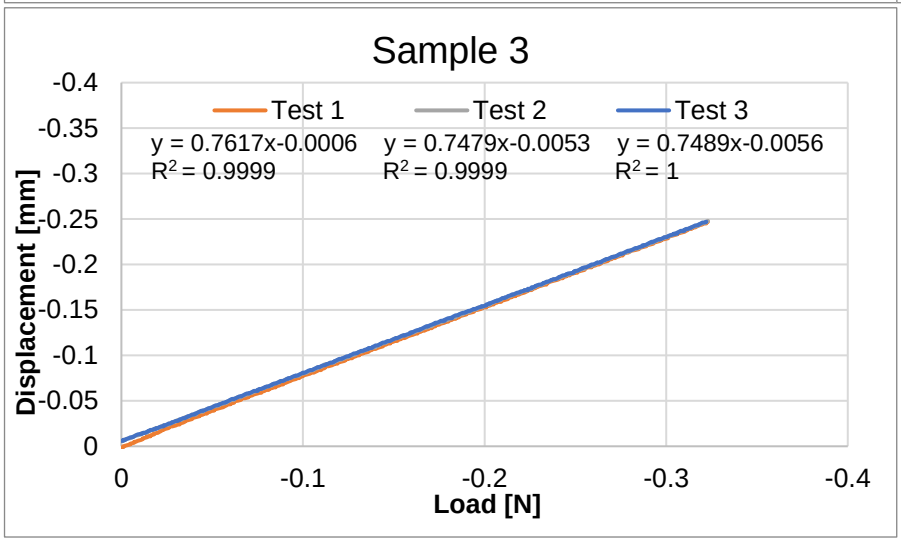

Figure G-1: Load-Displacement data of silicone layer. Medical grade silicone was filled into bottom of plastic petri dishes (thickness 8mm) and set. Indentation tests were performed with a Bose Electroforce 3100 fitted with a flat punch (r = 1mm). Loading rate was 0.001mm/s up to a maximum compressive force of 0.324N. Differences in displacement scale originate from differences in taring of displacement measurement during recording. However, this does not influence Young's modulus calculations.

H. Non-parametric testing for comparison between static and dynamic loading experiments

In addition to the parametric ANOVA tests, non-parametric Kruskal-Wallis tests were performed to ensure that non-normality had no effect on the significance of results. The null hypothesis H_0 was that “all medians are equal”, the alternative hypothesis H_1 that “at least one median is different. The significance level was $\alpha = 0.05$ in line with the ANOVA test. The test was performed in Minitab (Vers. 19.2020.1).

The results showed a median number of dead cells of $n = 79.5$ for the static scenario, $n = 99.0$ for the 1.42Hz loading, and $n = 135.5$ for loading at 4Hz. The significance level of $p = 0.024$ indicates a significant difference between at least two of the experimental groups. A post-hoc Dunn’s test was performed for multiple comparisons. Corresponding with the results of the ANOVA test, a statistically significant difference was found between the static and 4Hz loading group ($p = 0.0089$) and the 1.42Hz and 4Hz loading group ($p = 0.0475$). The difference between static and 1.42Hz loading was not statistically significant ($p = 0.51$).

I. Data normalisation procedure dynamic loading

During loading experiments, the indenter attached to the Bose Electroforce 3100 was lowered onto muscle samples until a force of -0.001N was recorded. Subsequently, a monotonous sinusoidal load with a maximum of -0.324N was applied with a frequency of either 1.42Hz or 4Hz. During this process, displacement data was recorded. However, minor differences in calibration of the starting position the indenter during displacement recordings were observed in the raw data (**Figure I-1**). To be able to compare the maximum displacement across different muscle samples, data needed to be normalised.

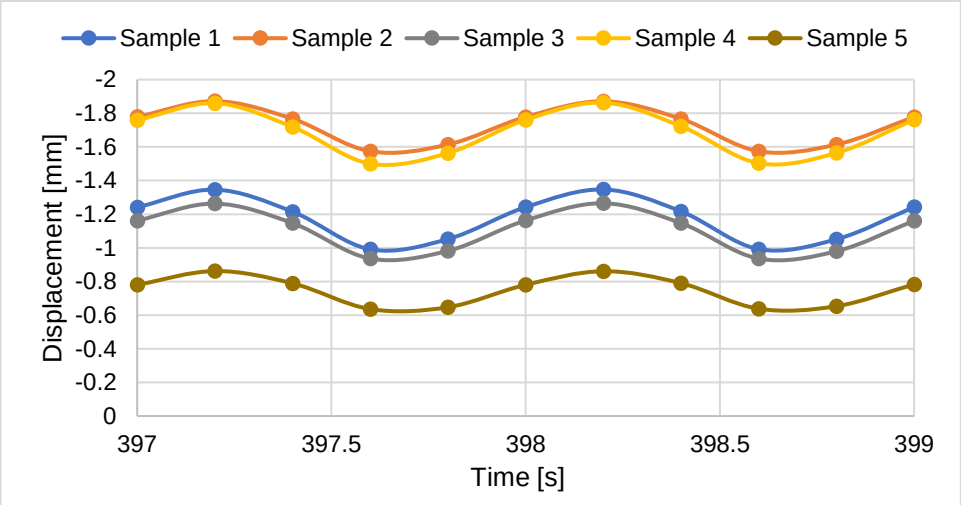

Figure I-1: Raw deformation data from dynamic loading. The deformation of five different samples was recorded across the same timeframe during monotonous sinusoidal indentation. Data shows calibration issues with differences in the centre lines of the amplitude, causing a relative shift of the data in reference to each other.

The general approach to data normalisation was to fit sinusoidal functions to the displacement data from each sample and align the centre lines of their amplitudes. However, undersampling of displacement data led to aliasing. Displacement data was recorded every 0.2s; accordingly, the "frequency" displayed in the raw data (**Figure I-1**) was approximately 1Hz, compared to the 1.42Hz and 4Hz loading frequency tested in the experiments.

To correct this error, a sinusoidal function with the known frequency of 1.42Hz or 4Hz was fitted to the displacement dataset of each sample first. Non-linear regression analysis was performed in Minitab to fit data to the general equation of:

$$\mathbf{y = A \times \mathit{sin}(\omega t + \varphi) + D}$$

with *A* as the amplitude of the function, ω as the angular frequency, φ as the phase and *D* describing the centre of the amplitude. Starting parameters were set to *A* = 0.15, φ = -1, *D* = 0.18 based on estimates from the dataset. The angular frequency was added as a fixed value, based on the formula $\omega = 2\pi f$, of ω = 8.92 (1.42Hz) or ω = 25.13 (4Hz).

Based on the corrected sinusoidal equations, the centre line of the amplitude was determined for each sample. The centre line of the amplitude of the first sample was established as reference value. The difference in centre lines between the reference sample and each following sample was then added or subtracted from the original displacement data of the respective sample for normalisation (**Figure I-2**).

With all displacement data normalised, the average sinusoidal displacement function could be estimated for each loading frequency as described in *Chapter 8, "8.3.1. Finite element analysis of dynamic transverse mechanical loading setup".*

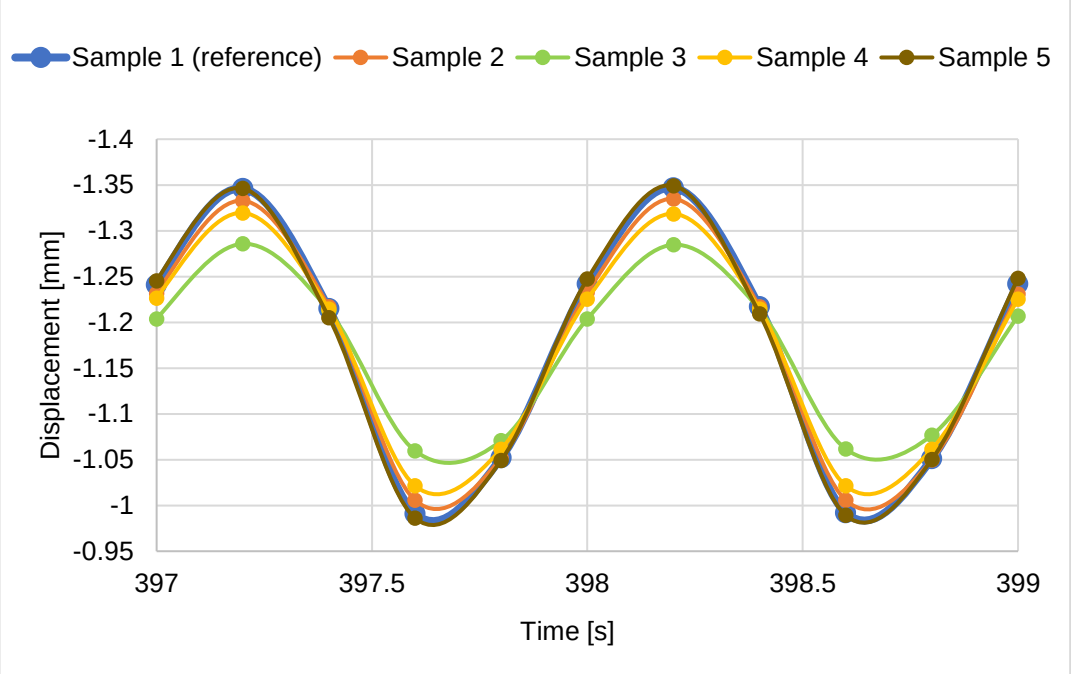

Figure I-2: Normalised deformation data from dynamic loading. The deformation of five different samples was recorded across the same timeframe during monotonous sinusoidal indentation. Graph shows normalised data after alignment of the centre lines of the amplitudes in reference to the first sample.